REPORT DOCUMENTATION PAGE

Form Approved
OMB No. 0704-0188

1. REPORT DATE *(DD-MM-YYYY)*
02/26/2003

2. REPORT TYPE **Final Technical Report**

3. DATES COVERED *(From - To)*
8/1/2000 - 1/31/2002

4. TITLE AND SUBTITLE

Multifunctional Mechatronic Materials

5a. CONTRACT NUMBER

5b. GRANT NUMBER
N00014-00-1-0885

5c. PROGRAM ELEMENT NUMBER

5d. PROJECT NUMBER
PR03303

5e. TASK NUMBER

5f. WORK UNIT NUMBER

6. AUTHOR(S)

Anthony Evans, Principal Investigator

7. PERFORMING ORGANIZATION NAME(S) AND ADDRESS(ES)

Princeton University
Office of Research & Project
Administration
4 New South Building
Princeton, NJ 08544-0036

8. PERFORMING ORGANIZATION REPORT NUMBER

9. SPONSORING / MONITORING AGENCY NAME(S) AND ADDRESS(ES)

Office of Naval Research
Ballston Centre
800 North Qunicy Street
Arlington, VA 22217-5660

Office of Naval Research
495 Summer Street, Room 627
Boston, MA 02210-2109

10. SPONSOR/MONITOR'S ACRONYM(S)

11. SPONSOR/MONITOR'S REPORT NUMBER(S)

12. DISTRIBUTION / AVAILABILITY STATEMENT

Approved for Public Release; Distribution is Unlimited

13. SUPPLEMENTARY NOTES

14. ABSTRACT

Contributions have been made in two basic areas:

1. Ultralight structures based on sandwich panels with truss and textile cores

2. High authority actuating structures based on the properties of the Kagone syste.

15. SUBJECT TERMS

16. SECURITY CLASSIFICATION OF:

a. REPORT

b. ABSTRACT

c. THIS PAGE

17. LIMITATION OF ABSTRACT

18. NUMBER OF PAGES

19a. NAME OF RESPONSIBLE PERSON
Michelle D. Christy

19b. TELEPHONE NUMBER *(include area code)609-258-3090*

University of California, Santa Barbara

Materials Department
Engineering II, Room 1355
Santa Barbara, CA 93106-5050

February 21, 2003

To: Lynn Failla
Princeton University
Office of Research and Project Administration
New South Building
Princeton, NJ 08544-0036

From: Anthony Evans
Principal Investigator
Materials Department

Please find enclosed the annual report for ONR Award entitled Mechatronic Materials & Systems

Thank you.

Table of Contents

SYNOPSIS

Contributions have been made in two basic areas:

- (i) Ultralight structures based on sandwich panels with truss and textile cores.
- (ii) High authority actuating structures based on the properties of the Kagome system.

A variety of core designs have been explored that achieve lightweight objectives, while also having structural robustness and are amenable to straightforward manufacturing. The cores included trusses with tetrahedral, pyramidal and 3D-Kagome topologies as well as plain weave textiles in 0/90,±45 configurations. The basic design principle is that, when incorporated into a panel and subjected to shear, the core members stretch/compress without bending. The basic attributes can be ascertained by analyzing the minimum weight needed to support specified loads without failure in either bending or compression. Progress has been achieved by a combination of fabrication, testing, modeling and simulation. The outcome has been a consistent representation of structural performance culminating in a comparison between these new designs and the benchmark system, consisting of a hexagonal, honeycomb core (figure 1). The results reveal that the benefits of the truss/textile cores over honeycombs do not reside in their structural performance, but in their potential for lower manufacturing cost, especially in curved configurations, and when their multifunctionality is exploited.

A class of actuating plate structures has been introduced, based on a planar truss having the Kagome weave pattern. The two planar manifestations explored both consist of faces connected by a tetrahedral truss core comprise: (a) a Kagome plane and a solid skin and (b) two Kagome faces. The feature rendering the Kagome planar truss exceptional for actuation is that its members can be actuated (elongated or contacted) to achieve arbitrary in-plane nodal displacements with minimal internal resistance. This attribute arises because the infinite, pin-jointed version satisfies most of the requirements for static determinacy, permitting minimal elastic energy storage (in bending) even when the joints are welded. These benefits become apparent upon comparing with a highly redundant planar truss, exemplified by identical triangular units with equal length members. If such a truss replaces the Kagome, axial deformation of the members would be required upon actuation, storing substantial energy. The Kagome truss is the only example known of an infinite planar truss amenable to assembly from repeat units having both isotropic stiffness and the properties desired for actuation. Analysis and experimentation on this concept is continuing.

Effective properties of the octet-truss lattice material

V. S. Deshpande, N. A. Fleck* and M. F. Ashby
Cambridge University Engineering Department, Trumpington Street, Cambridge, CB2 1PZ, U.K.

Submitted to Journal of Mechanics and Physics of Solids

July 2000

Abstract

The effective mechanical properties of the octet-truss lattice structured material have been investigated both experimentally and theoretically. Analytical and FE calculations of the elastic properties and plastic yielding collapse surfaces are reported. The intervention of elastic buckling of the struts is also analysed in an approximate manner. Good agreement is found between the predictions of the strength and experimental observations from tests on the octet-truss material made from a casting aluminium alloy. Moreover, the strength and stiffness of the octet-truss material are stretching-dominated and compare favourably with the corresponding properties of metallic foams. Thus, the octet-truss lattice material can be considered as a promising alternative to metallic foams in lightweight structures.

Keywords: lattice materials, collapse surfaces, porous solids, buckling, finite elements

---

*Author to whom all correspondence should be addressed. Fax: + 44 1223 332662; email: nafl@eng.cam.ac.uk

1 Introduction

Over the past few years, a variety of metallic and polymeric foams have been produced for a wide range of potential applications such as the cores of sandwich panels and various automotive parts. A typical aim is to develop lightweight structures that are adequately stiff and strong. Numerous studies on metallic and polymer foams have shown that the strength of the foams is governed by cell wall bending for all loading conditions and scales as $\bar{\rho}^{1.5}$, where $\bar{\rho}$ is the relative density of the foam; see Gibson and Ashby (1997). On the other hand, the strength of a structure that deforms by cell wall stretching scales with $\bar{\rho}$. Thus, for a relative density of $\bar{\rho} = 0.1$ the stretching-governed structure is expected to be about three times as strong as the bending governed structure. The aim of this study is to investigate the mechanical properties of a stretching-governed cellular material and compare them with those of traditional foamed materials.

Deshpande et al. (2000) have recently analysed the criteria for the construction of stretching-dominated cellular materials. A sufficient condition for the deformation of a periodic structure to be stretching-dominated is that the unit cell of the structure satisfies Maxwell's criterion for static determinacy. This criterion in three dimensions is given by:

$$b - 3j + 6 \geq 0 \tag{1}$$

where b and j are the number of struts and nodes respectively in the unit cell. It identifies several classes of unit cells from which stretching-dominated cellular materials (referred to as lattice materials in the following) can be synthesised. In order to give a more definite prescription for constructing lattice materials, Deshpande et al. also analysed a special class of structures with nodes which are all *similarly situated*- nodes are said to be similarly situated if the remainder of the structure appears the same and in the same orientation when viewed from any of the nodes. For this case they showed that the necessary and sufficient condition for the structure to be stretching-dominated is that the connectivity at each node is $Z = 12$ (or $Z = 6$ if the material is two dimensional).

Recent developments in manufacturing techniques have allowed for the manufacture of lattice materials at length scales ranging from millimetres to tens of centimeters. For example, the injection moulding of polymeric structures and subsequent assembly into complex lattice materials is a cheap way to manufacture materials whose constituent struts have aspect ratios less than about 5. These polymeric materials can then be used as sacrificial patterns for investment casting of metallic lattice materials. Rapid prototyping techniques can be used to fabricate materials with lattice parameters on the order of 0.5 mm. Recently, Brittain et al. (2000) have reported an electro-deposition technique to manufacture truss structures with strut diameters as small as 50 μm.

Along with advances in manufacturing methods for these materials, efforts are underway to investigate their mechanical properties. Wallach and Gibson (2000) have recently reported a combined experimental and finite element (FE) investigation of the strength and stiffness of a truss plate. They find that the properties compare favourably with those of metallic foams. Wicks and Hutchinson (2000) show that optimised truss panels are exceptionally weight-efficient for carrying bending and compression loads, as compared to alternatives such as honeycomb core sandwich panels or stringer stiffened plates. Although the properties of truss plates have been analysed, analytical studies on the properties of full 3D lattice materials are lacking.

In this paper we shall investigate the properties of the octet-truss (Fuller, 1961) lattice material. The nodes of the octet-truss are configured in a "Face Centred Cubic" arrangement, such that each node has a similar situation and a connectivity of $Z = 12$. We report analytical and FE calculations of the elastic-plastic properties as well as collapse surfaces due to elastic buckling. The predictions are compared with experimental observations from tests on an octet-truss material made from an aluminium casting alloy (LM25).

1.1 Description of microstructure

A unit cell of the lattice structure is sketched in Figure 1 and clearly shows its FCC nature. Octahedral cells can be stacked to synthesise the octet-truss structure, with each strut of an octahedral cell shared between two neighbouring cells. Thus, for the purposes of structural calculations it suffices to analyse the octahedral cell. An isometric sketch of a typical octahedral cell, with the associated Cartesian co-ordinate system (x, y, z) is shown in Figure 2.

An alternative repeating unit which can be stacked in the same orientation to construct the octet-truss lattice material is a regular tetrahedron. One such tetrahedral cell with nodes labelled p1 through p4 is shown in Figure 1. An isometric sketch of this tetrahedral cell with the associated global co-ordinate system $(1, 2, 3)$ of the octet-truss is included in Figure 2. Here, the 1-2 plane is parallel to the base plane p1-p2-p3 and the 2-axis is parallel to the strut between the nodes p2 and p3. The $(1, 2, 3)$ co-ordinate system corresponds to the 3-fold symmetry of the octet-truss material about the 3-axis. Note that the 1-2 plane is a close-packed plane of the FCC structure and constitutes a fully triangulated layer in the lattice material. Thus, the octet-truss material can be constructed by the successive packing of the triangulated layers in "ABCABC..." positions with each layer separated by a tetrahedral core.

In the remainder of this paper an octet-truss lattice material constructed from identical circular cylindrical struts is analysed. The conclusions drawn can easily be generalised for the case of hollow or solid struts of arbitrary cross-section. The relative density $\bar{\rho}$ of the octet-truss lattice material (ratio of the density of the lattice material to the density of the solid material from which it is made) is given by

$$\bar{\rho} = 6\sqrt{2}\pi \left(\frac{a}{l}\right)^2 \tag{2}$$

where a and l are the radius and length of a strut respectively. This formula is a first order approximation and overestimates the relative density due to double counting of the volume of the nodes. A higher order approximation of the relative density is given by

$$\bar{\rho} = 6\sqrt{2}\pi\left(\frac{a}{l}\right)^2 - C\left(\frac{a}{l}\right)^3 \tag{3}$$

where C depends on the detailed geometry of the nodes. For small a/l, the first order approximation suffices and is used in the remainder of the analysis presented in this paper.

2 Effective elastic properties

The cubic symmetry of the octet-truss lattice material dictates that the form of the linear elastic stress versus strain relationship is

$$\begin{pmatrix} \epsilon_x \\ \epsilon_y \\ \epsilon_z \\ \epsilon_{yz} \\ \epsilon_{xz} \\ \epsilon_{xy} \end{pmatrix} = \begin{pmatrix} s_1 & -s_2 & -s_2 & 0 & 0 & 0 \\ & s_1 & -s_2 & 0 & 0 & 0 \\ & & s_1 & 0 & 0 & 0 \\ & & & s_3 & 0 & 0 \\ & \text{sym} & & & s_3 & 0 \\ & & & & & s_3 \end{pmatrix} \begin{pmatrix} \sigma_x \\ \sigma_y \\ \sigma_z \\ \sigma_{yz} \\ \sigma_{xz} \\ \sigma_{xy} \end{pmatrix}, \tag{4}$$

where the principal material axes (x, y, z) are defined in Figure 2 and s_1, s_2 and s_3 are three independent compliances. Note that an isotropic material has only two independent elastic constants with $s_3 = 2(s_1 + s_2)$.

For small a/l, the contribution to overall stiffness from the bending of the struts is negligible compared to stretching of the struts. Thus, the struts are assumed to be pin-jointed at the nodes, and analytical expressions for the compliances follow as

$$\frac{1}{s_1} = \frac{2\sqrt{2}\pi}{3}\left(\frac{a}{l}\right)^2 E_s = \frac{\bar{\rho}}{9}E_s, \tag{5a}$$

$$\frac{1}{s_2} = 2\sqrt{2}\pi\left(\frac{a}{l}\right)^2 E_s = \frac{\bar{\rho}}{3}E_s, \quad \text{and} \tag{5b}$$

$$\frac{1}{s_3} = \frac{\pi}{\sqrt{2}}\left(\frac{a}{l}\right)^2 E_s = \frac{\bar{\rho}}{12}E_s \tag{5c}$$

where E_s is the Young's modulus of the solid material. The macroscopic elastic stress versus strain relationship in the $(1, 2, 3)$ co-ordinate system is of practical interest and is obtained by transforming (4):

$$\begin{pmatrix}\epsilon_1\\ \epsilon_2\\ \epsilon_3\\ \epsilon_{23}\\ \epsilon_{13}\\ \epsilon_{12}\end{pmatrix} = \frac{1}{E_s\bar{\rho}}\begin{pmatrix}6 & -2 & -1 & 0 & -2\sqrt{2} & 0\\ & 6 & -1 & 0 & 2\sqrt{2} & 0\\ & & 5 & 0 & 0 & 0\\ & \text{sym} & & 20 & 0 & 2\sqrt{2}\\ & & & & 20 & 0\\ & & & & & 16\end{pmatrix}\begin{pmatrix}\sigma_1\\ \sigma_2\\ \sigma_3\\ \sigma_{23}\\ \sigma_{13}\\ \sigma_{12}\end{pmatrix}. \tag{6}$$

This stress versus strain relationship displays a coupling between the normal components of stress and the shear components of strain in the $(1,2,3)$ co-ordinate system as these directions are not aligned with the principal material directions (x, y, z).

For clarity, in the following we shall refer to the various moduli as either a Young's modulus E or a shear modulus G and subscript them with their respective directions. For example, the Young's modulus in the x and 3 directions will be denoted by E_{xx} and E_{33}, respectively, while the shear modulus in the $x-y$ direction will be referred to as G_{xy}. It is worth mentioning here that $E_{33} = \frac{\bar{\rho}}{5}E_s$ is the maximum value of Young's modulus of the octet-truss lattice material over all orientations.

2.1 Comparison with the FE predictions

The accuracy of the approximate analytical expressions for the moduli was checked against FE calculations performed using the general purpose finite element package ABAQUS (HKS, 1997). In these FE calculations the pin-jointed strut assumption was relaxed. Here, we briefly describe details of the FE calculations.

The octahedral cell with each cylindrical strut modelled by between 20 and 40 Timoshenko beam elements (B32 element of ABAQUS) depending on its length was analysed to extract the 3 cubic moduli. The displacements of the nodes at the vertices of the cell were constrained so as to prevent rigid body translation and rotation of the cell. Further, the rotations of the nodes at vertices were constrained as dictated by symmetry. Two stress states, uniaxial tension σ_{zz} and simple shear τ_{xz} were prescribed and the moduli extracted from the resulting nodal displacements. We performed calculations for three values of the solid material elastic Poisson's ratio $\nu_s = 0.2$, 0.3 and 0.49. However, ν_s had a negligible effect on the octet-truss material moduli. Thus, for the sake of brevity only results for $\nu_s = 0.3$ are presented.

A comparison between the analytical and FE predictions of the moduli E_{xx}, G_{xy} and E_{33} is shown in Figure 3 for $\bar{\rho}$ ranging from 0.01 to 0.5. Excellent agreement between the FE and analytical calculations is seen, in support of the pin-jointed strut assumption made in the analytical calculations.

3 Collapse criteria

The octet-truss lattice material can fail either by plastic yielding or elastic buckling of the struts. In this section the collapse of the lattice material by these two competing mechanisms is explored. We shall calculate plastic collapse surfaces of the material under various combinations of loading and then proceed to propose an anisotropic yield criterion.

3.1 Plastic collapse

In the analytical calculations it is assumed that the struts are pin-jointed and made from a rigid, ideally plastic solid. The macroscopic collapse stress is calculated by equating the external work with the plastic dissipation in stretching the struts for kinematically-admissible modes of collapse; that is, an upper bound approach is adopted. The accuracy of these analytical calculations was checked through FE calculations in which the pin-jointed strut assumption was relaxed.

In the FE analysis each cylindrical strut was again modelled by between 20 and 40 Timoshenko beam elements (B32 element of ABAQUS) depending on its length. J_2 flow theory was employed and the strut material was assumed to be elastic-plastic with the uniaxial stress versus strain law:

$$\frac{\epsilon}{\epsilon_Y} = \left\{ \begin{array}{ll} \sigma/\sigma_Y & \text{for } \sigma \leq \sigma_Y \\ (\sigma/\sigma_Y)^m & \text{for } \sigma > \sigma_Y \end{array} \right\} \tag{7}$$

where σ_Y and ϵ_Y are the material yield stress and strain respectively. The elastic Poisson's ratio ν_s of the material was assumed to be 0.3, the yield strain ϵ_Y of the strut material was taken equal to 0.1 % and the hardening co-efficient $m = 80$ (this small degree of hardening was required to get convergence of the FE calculations). An imperfection in the shape of the plastic buckling mode was imposed on each strut to ensure a unique equilibrium path in the FE calculations. The imperfection is described by the initial transverse deflection w:

$$w(x) = \frac{\zeta a}{2}\left[1 - \cos\left(\frac{2\pi x}{l}\right)\right], \tag{8}$$

where ζ is a dimensionless imperfection parameter, a the strut radius, l the strut length and x the axial co-ordinate along the strut measured from one end. This imperfection is not expected to affect the plastic limit load values; see section 3.4 for details. For the calculations presented in this section ζ was taken equal to 0.01.

The collapse surfaces in $(\sigma_{zz},\ \sigma_{xz})$ and $(\sigma_{xx},\ \sigma_{yy})$ space were calculated by analysing the octahedral cell while the tetrahedral cell was used to calculate the collapse surface in $(\sigma_{33},\ \sigma_{13})$ space. The displacements of the nodes at the vertices of the cell were constrained so as to prevent rigid body translation and rotation of the cell; and the rotations of the nodes at the vertices were set to zero. The macroscopic yield stresses (defined by the peak of the macroscopic the stress versus strain curve) were calculated for a variety of proportional stress paths and plotted in the relevant stress space to give the plastic collapse surface.

3.1.1 Collapse surface calculations

The overall yield surface in macroscopic stress space consists of intersecting collapse surfaces which are associated with particular collapse modes. Plastic strain increments are normal to the relevant collapse surface. In this section we detail calculations of the collapse surfaces for three important practical combinations of macroscopic stressing viz. $(\sigma_{zz},\ \sigma_{xz})$, $(\sigma_{xx},\ \sigma_{yy})$ and $(\sigma_{33},\ \sigma_{13})$.

Collapse surface in $(\sigma_{zz},\ \sigma_{xz})$ space

The collapse modes for this combination of macroscopic stressing are sketched in side views of the octahedral cell in Figure 4. In the sketches dashed and solid lines struts are at yield and in the rigid state, respectively, while a solid circle represents a plastic hinge. However, the plastic dissipation at the hinges is neglected in comparison with the dissipation in axial stretching of the yielded struts. As the struts yield either in compression or tension, two collapse locii exist for each yield pattern. Thus, for collapse Mode I, the struts labelled p5-p2, p5-p3, p6-p2 and p6-p3 are yielding and the collapse planes are given by

$$\text{Mode Ia}: \qquad \frac{\sigma_{xz}}{\sigma_Y} = \frac{\sigma_{zz}}{2\sigma_Y} + \sqrt{2}\pi\left(\frac{a}{l}\right)^2, \text{ and} \tag{9a}$$

$$\text{Mode Ib}: \qquad \frac{\sigma_{xz}}{\sigma_Y} = \frac{\sigma_{zz}}{2\sigma_Y} - \sqrt{2}\pi\left(\frac{a}{l}\right)^2 \tag{9b}$$

where σ_Y is the yield stress of the solid material. In Mode II, struts p5-p1, p5-p4, p6-p1 and p6-p4 are yielding and the collapse plane equations are

$$\text{Mode IIa}: \qquad \frac{\sigma_{xz}}{\sigma_Y} = -\frac{\sigma_{zz}}{2\sigma_Y} - \sqrt{2}\pi\left(\frac{a}{l}\right)^2, \text{ and} \tag{10a}$$

$$\text{Mode IIb}: \qquad \frac{\sigma_{xz}}{\sigma_Y} = -\frac{\sigma_{zz}}{2\sigma_Y} + \sqrt{2}\pi\left(\frac{a}{l}\right)^2. \tag{10b}$$

A comparison between the analytical and FE predictions of the uniaxial yield strength σ_{zz}^Y is shown in Figure 3 for $\bar{\rho}$ ranging from 0.01 to 0.5. The good agreement between the two sets of calculations confirms that the plastic dissipation in the hinges is negligible. FE and analytical calculations of the collapse surface in (σ_{zz}, σ_{xz}) space are shown in Figure 4 for $a/l = 0.1$. Again, results from the analytical and FE calculations are in good agreement. It is worth mentioning that the symmetry of the octet-truss lattice material is such that the set of collapse surfaces (σ_{mm}, σ_{nm}) are identical, where m and n represent any pair of the x, y or z directions.

The octet-truss is periodic with respect to rotations of period 90 ° about the z-axis. FE calculations show that the shear strength σ_{xz} varies by approximately 10 % as the octet-truss is rotated about the z axis with the shear strength being minimum at a 45 ° rotation. This suggests that the collapse surface in (σ_{zz}, σ_{xz}) space is almost invariant with respect to rotations of the co-ordinate system about the z axis.

Collapse surface in (σ_{xx}, σ_{yy}) space

The collapse modes under combinations of applied stresses (σ_{xx}, σ_{yy}) are sketched in plan views of the octahedral cell in Figure 5. In Mode III the struts labelled p5-p1, p5-p3, p6-p1 and p6-p3 yield, with the collapse planes described by the equations

$$\text{Mode IIIa}: \quad \frac{\sigma_{yy}}{\sigma_Y} = \frac{\sigma_{xx}}{\sigma_Y} + 2\sqrt{2}\pi\left(\frac{a}{l}\right)^2, \quad \text{and} \tag{11a}$$

$$\text{Mode IIIb}: \quad \frac{\sigma_{yy}}{\sigma_Y} = \frac{\sigma_{xx}}{\sigma_Y} - 2\sqrt{2}\pi\left(\frac{a}{l}\right)^2. \tag{11b}$$

In Mode IV, the struts p1-p2, p2-p3, p3-p4 and p1-p4 yield and the collapse planes corresponding to this mode are given by

$$\text{Mode IVa}: \quad \frac{\sigma_{yy}}{\sigma_Y} = -\frac{\sigma_{xx}}{\sigma_Y} - 2\sqrt{2}\pi\left(\frac{a}{l}\right)^2 \quad \text{and} \tag{12a}$$

$$\text{Mode IVb}: \quad \frac{\sigma_{yy}}{\sigma_Y} = -\frac{\sigma_{xx}}{\sigma_Y} + 2\sqrt{2}\pi\left(\frac{a}{l}\right)^2. \tag{12b}$$

The FE calculations of the collapse surface are included in Figure 5; good agreement is noted with the above analytical predictions. Note that symmetry dictates that the set of collapse surfaces (σ_{mm}, σ_{nn}) are identical where m and n represent any pair of x, y or z directions.

Collapse surface in (σ_{33}, σ_{13}) space

For the combinations (σ_{33}, σ_{13}) of macroscopic stress, it is convenient to analyse the tetrahedral cell. The various collapse modes are sketched in side views of the tetrahedral cell, see Figure 6. In Mode V, the two struts p4-p2 and p4-p3 yield while in Mode VI the strut p4-p1 yields. The equations of the collapse planes corresponding to these modes are given by

$$\text{Mode Va}: \quad \frac{\sigma_{13}}{\sigma_Y} = \frac{\sigma_{33}}{\sqrt{2}\sigma_Y} + 2\pi\left(\frac{a}{l}\right)^2, \quad \text{and} \tag{13a}$$

$$\text{Mode Vb}: \quad \frac{\sigma_{13}}{\sigma_Y} = \frac{\sigma_{33}}{\sqrt{2}\sigma_Y} - 2\pi\left(\frac{a}{l}\right)^2 \tag{13b}$$

for Mode V and

$$\text{Mode VIa}: \quad \frac{\sigma_{13}}{\sigma_Y} = -\frac{\sigma_{33}}{2\sqrt{2}\sigma_Y} - \pi\left(\frac{a}{l}\right)^2, \quad \text{and} \tag{14a}$$

$$\text{Mode VIb}: \quad \frac{\sigma_{13}}{\sigma_Y} = -\frac{\sigma_{33}}{2\sqrt{2}\sigma_Y} + \pi\left(\frac{a}{l}\right)^2 \tag{14b}$$

for Mode VI. Comparisons between the analytical and FE calculations for $a/l = 0.1$ are shown in Figure 6: good agreement again confirms the accuracy of the analytical calculations.

The collapse surface in $\sigma_{33} - \sigma_{13}$ space is approximately invariant with respect to rotations of the co-ordinate system about the 3-axis, by the following argument. Consider shear loading with $\sigma_{33} = 0$. The shear strength σ_{13} of the octet-truss is periodic with respect to rotations of period 60 ° about the 3-axis; FE calculations reveal that the shear strength σ_{13} varies by less than 10 % as the octet-truss is rotated about the 3-axis, with the shear strength a maximum for a 30 ° rotation.

3.2 Anisotropic yield criterion

While the collapse surfaces presented in the previous section are useful for displaying the yield stress under specific load paths, a closed-form expression for the yield surface would be advantageous in summarising the collapse response of the octet-truss lattice material. In this section we shall make use of Hill's (1948) generalisation of the von Mises yield criterion for materials with orthotropic symmetry. An orthotropic material has 3 mutually perpendicular planes of symmetry at every point, with the intersections of these planes known as the principal axes of anisotropy. With respect to the principal axes of anisotropy (x, y, z), Hill's yield criterion has the form:

$$\Phi \equiv \sigma_d^2 - 1 = 0 \tag{15a}$$

where the applied macroscopic stress is characterised by the effective stress measure σ_d given by

$$\sigma_d^2 \equiv A(\sigma_x - \sigma_y)^2 + B(\sigma_y - \sigma_z)^2 + C(\sigma_z - \sigma_x)^2 + D\tau_{xz}^2 + E\tau_{yz}^2 + F\tau_{xy}^2. \tag{15b}$$

Here, A through F are parameters which characterise the degree of anisotropy.

The octet-truss lattice material also has 3 mutually perpendicular planes of symmetry passing through every node and the (x, y, z) axes as defined in Figure 2 correspond to the principal axes of anisotropy. Thus, it is appropriate to consider using Hill's criterion to describe the yielding of this material. However, Hill's anisotropic yield criterion assumes that plastic yielding is not influenced by hydrostatic pressure. This is clearly not the case for the cellular octet-truss lattice material. We therefore modify Hill's criterion by incorporating a mean stress dependence on yielding.

As the simplest extension of Hill's yield criterion we assume that the yield function Φ of the octet-truss lattice material is quadratic in mean stress $\sigma_m = \sigma_{kk}/3$, and in the deviatoric stress measure σ_d. Φ is then of the form

$$\begin{aligned}\Phi \equiv\ & \sigma_d^2 + G\sigma_m^2 = \\ & A(\sigma_x - \sigma_y)^2 + B(\sigma_y - \sigma_z)^2 + C(\sigma_z - \sigma_x)^2 + D\tau_{xz}^2 + E\tau_{yz}^2 + F\tau_{xy}^2 + G\sigma_m^2 = 0\end{aligned} \tag{16}$$

where A through G are material constants. The quadratic term $\sigma_m\sigma_d$ is rejected as it is assumed that the yield stresses under hydrostatic compression and tension are equal. It must be remembered that the yield criterion (16) only has the form shown when the principal axes of anisotropy co-incide with the reference axes; otherwise, the form of the yield condition changes in a way that can be found by rotating the co-ordinate system.

It remains to calibrate the yield criterion to determine the material constants A through G. The uniaxial and shear yield strengths with respect to the material principal axes and the hydrostatic yield strength σ_m^Y of the octet-truss lattice material are

$$\sigma_{xx}^Y = \sigma_{yy}^Y = \sigma_{zz}^Y = 2\sqrt{2}\pi \left(\frac{a}{l}\right)^2 \sigma_Y \tag{17a}$$

$$\sigma_{xy}^Y = \sigma_{xz}^Y = \sigma_{yz}^Y = \sqrt{2}\pi \left(\frac{a}{l}\right)^2 \sigma_Y, \text{ and} \tag{17b}$$

$$\sigma_m^Y = 2\sqrt{2}\pi \left(\frac{a}{l}\right)^2 \sigma_Y \tag{17c}$$

respectively. Upon substituting the above yield stresses into (16) and solving for A through G, the yield criterion for the octet-truss lattice material can be re-written as

$$\begin{aligned}\Phi \equiv\ & \frac{4}{9}\left[(\sigma_x - \sigma_y)^2 + (\sigma_y - \sigma_z)^2 + (\sigma_z - \sigma_x)^2\right] \\ & + 4\left[\tau_{xz}^2 + \tau_{yz}^2 + \tau_{xy}^2\right] + \sigma_m^2 - \left[2\sqrt{2}\pi \left(\frac{a}{l}\right)^2 \sigma_Y\right]^2 = 0,\end{aligned} \tag{18}$$

where $2\sqrt{2}\pi \left(\frac{a}{l}\right)^2 \sigma_Y$ is the uniaxial yield strength in a principal direction of anisotropy. Thus, to fully describe the state of anisotropy of the octet-truss lattice material we must know the orientations of the principal axes of anisotropy and the uniaxial yield strength in the principal directions.

Comparisons between the calculated collapse surfaces and the predictions of the above yield criterion are shown in Figures 4 to 6. In (σ_{zz}, σ_{xz}) space, good agreement is seen between the predictions of the proposed yield criterion both and the FE and analytical calculations. On the other hand, in (σ_{xx}, σ_{yy}) space the proposed yield criterion substantially overestimates the yield stresses under biaxial tension and compression. In (σ_{33}, σ_{13}) space, the yield criterion does not capture the form of the collapse surface accurately.

In an effort to propose a better functional form for the yield criterion we tried higher order functions of σ_m and σ_d (viz. 4th and 6th order functions). However, no improvements in the accuracy of the predictions were found. The authors' have been unable to construct a simple expression for a yield criteria that will capture the plastic collapse of the octet-truss lattice material under a variety of stress states to sufficient accuracy.

3.3 The elastic buckling strength

The octet-truss lattice material collapses by elastic buckling of the struts if the Euler buckling load of the struts as given by

$$P_E = \frac{n^2 \pi^3 E_s a^4}{4l^2} \tag{19}$$

is less than their plastic yielding load $P_Y = \pi a^2 \sigma_Y$. The factor n in (19) depends upon the rotational stiffness of the end nodes of the strut and is central to the problem of calculating P_E for a given network of struts. When a strut buckles, the rotation of its ends is opposed by the bending of the other struts: they exert a restoring moment and it is this that determines the factor n^2 in (19). Thus, n depends upon the buckling mode. The cells of the octet-truss lattice material may buckle in many different modes and the resulting problem is very complicated to analyse completely. We simplify the problem by assuming that the struts are pin-jointed. Thus, the rotational stiffness of the nodes is zero and $n = 1$ in (19). It is recalled that the buckling load of an axially loaded strut is strongly dependent on the end constraints, and so the calculations presented below should be viewed as lower bounds to the buckling strength.

The collapse stresses due to the elastic buckling of the struts are estimated by equating the external work to the internal work in buckling the struts for kinematically admissible collapse modes. In these analytical calculations we assume the struts are rigid up to the onset of buckling. The post buckling load-shortening relation for an inextensional pin-ended strut of length l is given by (Budiansky, 1974):

$$P \approx P_E \left(1 + \frac{\Delta}{2l}\right) \tag{20}$$

for small axial displacements Δ. Thus, a first order approximation of the work associated with a shortening Δ is $P_E\Delta$ and the total internal work is $\sum P_E\Delta$ over all the buckling struts. Note that in the analytical calculations we neglect the effects of elastic deformations prior to the onset of buckling. The accuracy of this assumption has been checked through finite deformation FE calculations.

In the FE calculations, the struts were assumed to be pin-jointed elastic beams comprising of Timoshenko beam elements (B32 of ABAQUS). The strut material was assumed to be elastic-plastic with the uniaxial stress versus strain law (7). Calculations were performed for two material yield strains $\epsilon_Y = 0.05$ and 0.1 with a strain hardening exponent $m = 80$ in both cases. As in the plastic calculations the octahedral cell was used in $(\sigma_{zz},\ \sigma_{xz})$ and $(\sigma_{xx},\ \sigma_{yy})$ collapse surface calculations while the tetrahedral unit cell was employed to calculate the $(\sigma_{33},\ \sigma_{13})$ collapse surface. An imperfection of shape given by the elastic buckling mode of pin-ended struts, and described by the initial transverse deflection,

$$w(x) = \zeta a \sin\left(\frac{\pi x}{l}\right) \tag{21}$$

was imposed on each strut. As in (8), ζ is the imperfection level and x is the axial co-ordinate along the strut measured from one end. For the calculations presented in this section, an imperfection level $\zeta = 0.01$ was added to all the struts. Note that the limit load for buckling is insensitive to the choice of ζ for the material and geometrical parameters considered here; see section 3.4 for details.

3.3.1 Buckling collapse surfaces

We now proceed to detail the collapse surfaces due to elastic buckling, as computed by analytical and FE methods for the combinations of macroscopic stressing considered earlier, $(\sigma_{zz},\ \sigma_{xz})$, $(\sigma_{xx},\ \sigma_{yy})$ and $(\sigma_{33},\ \sigma_{13})$.

Collapse surface in (σ_{zz}, σ_{xz}) space for elastic buckling

The sketches in Figure 7 show the possible buckling modes in side views of the octahedral cell, with the dashed lines representing the buckled struts. Since the struts only buckle in compression, a single collapse plane is associated with each buckled state and the equations of the collapse planes for the three collapse modes are given by

$$\text{Mode B-I}: \quad \frac{\sigma_{xz}}{\sigma_Y} = \frac{\sigma_{zz}}{2\sigma_Y} + \frac{\pi^3}{2\sqrt{2}\epsilon_Y}\left(\frac{a}{l}\right)^4, \tag{22a}$$

$$\text{Mode B-II}: \quad \frac{\sigma_{xz}}{\sigma_Y} = -\frac{\sigma_{zz}}{2\sigma_Y} - \frac{\pi^3}{2\sqrt{2}\epsilon_Y}\left(\frac{a}{l}\right)^4, \quad \text{and} \tag{22b}$$

$$\text{Mode B-III}: \quad \frac{\sigma_{zz}}{\sigma_Y} = \frac{\pi^3}{\sqrt{2}\epsilon_Y}\left(\frac{a}{l}\right)^4. \tag{22c}$$

The buckling collapse planes (22) are plotted in Figure 7 for $a/l = 0.1$ and solid material yield strains $\epsilon_Y = 0.05$ and 0.1. The appropriate plastic collapse planes are included in the figure. Good agreement is seen between the FE and analytical calculations in support of the infinitesimal deformation assumption made in the analytical calculations. On comparing the buckling collapse stresses (22) with the plastic collapse stresses we note that the entire collapse surface is governed by the elastic buckling of the struts when $\epsilon_Y > \frac{3\pi^2}{4}\left(\frac{a}{l}\right)^2$.

Collapse surface in (σ_{xx}, σ_{yy}) space for elastic buckling

The buckling collapse modes for the loading in (σ_{xx}, σ_{yy}) space are sketched in Figure 8. The buckled struts are represented by dashed lines in plan views of the octahedral cell. The equations of the collapse planes for the three collapse modes are

$$\text{Mode B-IV}: \quad \frac{\sigma_{yy}}{\sigma_Y} = \frac{\sigma_{xx}}{\sigma_Y} + \frac{\pi^3}{\sqrt{2}\epsilon_Y}\left(\frac{a}{l}\right)^4, \tag{23a}$$

$$\text{Mode B-V}: \quad \frac{\sigma_{yy}}{\sigma_Y} = -\frac{\sigma_{xx}}{\sigma_Y} - \frac{\pi^3}{\sqrt{2}\epsilon_Y}\left(\frac{a}{l}\right)^4, \quad \text{and} \tag{23b}$$

$$\text{Mode B-VI}: \quad \frac{\sigma_{yy}}{\sigma_Y} = \frac{\sigma_{xx}}{\sigma_Y} - \frac{\pi^3}{\sqrt{2}\epsilon_Y}\left(\frac{a}{l}\right)^4. \tag{23c}$$

FE and analytical predictions of the collapse surfaces in (σ_{xx}, σ_{yy}) space are shown in Figure 8 for $a/l = 0.1$ and $\epsilon_Y = 0.05$ and 0.1; the predictions of both methods are in good agreement. Elastic buckling collapse governs collapse for all stress states other than a biaxial tensile stress state: the three buckling modes B-IV to B-VI are activated in preference to plastic collapse if $\epsilon_Y > \frac{\pi^2}{4}\left(\frac{a}{l}\right)^2$. Under biaxial tension, the collapse mode is always by plastic yield irrespective of the value of ϵ_Y.

Collapse surface in (σ_{33}, σ_{13}) space for elastic buckling

The collapse modes in (σ_{33}, σ_{13}) space are sketched in top and side views of the tetrahedral cell in Figure 9. The equations of the four collapse modes are given by

$$\text{Mode B-VII}: \quad \frac{\sigma_{13}}{\sigma_Y} = \frac{\sigma_{33}}{\sqrt{2}\sigma_Y} + \frac{\pi^3}{2\epsilon_Y}\left(\frac{a}{l}\right)^4, \tag{24a}$$

$$\text{Mode B-VIII}: \quad \frac{\sigma_{13}}{\sigma_Y} = -\frac{\sigma_{33}}{2\sqrt{2}\sigma_Y} - \frac{\pi^3}{4\epsilon_Y}\left(\frac{a}{l}\right)^4, \tag{24b}$$

$$\text{Mode B-IX}: \quad \frac{\sigma_{13}}{\sigma_Y} = -\frac{\sigma_{33}}{2\sqrt{2}\sigma_Y} + \frac{3\pi^3}{4\epsilon_Y}\left(\frac{a}{l}\right)^4, \quad \text{and} \tag{24c}$$

$$\text{Mode B-X}: \quad \frac{\sigma_{13}}{\sigma_Y} = \frac{\sqrt{2}}{5}\frac{\sigma_{33}}{\sigma_Y} - \frac{3\pi^3}{5\epsilon_Y}\left(\frac{a}{l}\right)^4. \tag{24d}$$

On comparing these elastic buckling collapse stresses with the corresponding plastic collapse stresses (13) and (14), it follows that buckling modes B-VII and B-VIII are activated if $\epsilon_Y > \frac{\pi^2}{4}\left(\frac{a}{l}\right)^2$ while modes B-IX and B-X are triggered if ϵ_Y exceeds $\frac{3\pi^2}{4}\left(\frac{a}{l}\right)^2$ and $\frac{7\pi^2}{20}\left(\frac{a}{l}\right)^2$, respectively. Note that the entire collapse surface is governed by the elastic buckling of the struts when $\epsilon_Y > \frac{3\pi^2}{4}\left(\frac{a}{l}\right)^2$.

A comparison between the analytical and FE predictions of the collapse surface in (σ_{33}, σ_{13}) space is shown in Figure 9 for $a/l = 0.1$ and $\epsilon_Y = 0.05$ and 0.1. The small discrepancies between the analytical and FE predictions are due to finite deformation effects: as mentioned earlier the analytical calculations for the collapse loads were performed for infinitesimal deformations while the FE analysis was a finite deformation calculation.

3.4 Effect of geometric imperfections

In general, the elastic buckling and plastic collapse surfaces overestimate the collapse stresses of an elasto-plastic lattice material; interactions between the elastic buckling and plastic yielding of the struts substantially knock-down the collapse stresses. In this section we examine this interaction and use the finite element method to investigate the effect of imperfections in the form of strut waviness. For the sake of consistency with the elastic buckling calculations detailed in the previous section we assume that the struts are pin-jointed.

Here we consider imperfections of the same shape as the buckling mode and described by (21). The influence of the imperfection level ζ on the collapse loads of an axially loaded pin-ended strut is most marked when $\epsilon_Y \approx \left(\frac{\pi a}{2l}\right)^2$ (Hutchinson, 1974). For example, if $a/l = 0.1$ and $\epsilon_Y = 0.025$, the collapse loads are expected to be substantially reduced due to the influence of imperfections.

FE calculations of the collapse surface in $(\sigma_{zz}, \sigma_{xz})$ space for $a/l = 0.1$ and $\epsilon_Y = 0.025$ are shown in Figure 10 for two levels of imperfections, $\zeta = 0.01$ and 0.1. The collapse stresses for both levels of imperfections are substantially lower than those for the perfect structure. In fact, for $\zeta = 0.1$ the collapse load of the imperfect strut is about half that of the perfect strut which results in mode B-III becoming active and truncating the tensile side of the plastic collapse surface.

On the other hand, if ϵ_Y is either much greater than or much less than $\left(\frac{\pi a}{2l}\right)^2$ the collapse load of an axially loaded pin-ended strut is expected to be reasonably insensitive to the imperfection level. FE and analytical calculations of the collapse surfaces in $(\sigma_{zz}, \sigma_{xz})$ space for $a/l = 0.1$ are shown in Figure 11 for solid material yield strains $\epsilon_Y = 0.001$ and 0.1. As expected the collapse surface is reasonably insensitive to the imperfection level, with the collapse stresses decreasing by less than 10 % for $\zeta = 0.1$. We suggest here that the elasto-plastic collapse stresses of an imperfect octet-truss lattice material idealised as a pin-jointed structure can be estimated by re-calibrating the buckling collapse planes against the axial collapse load of an imperfect pin-ended strut.

4 Comparison between measured and predicted modulus and yield strength

We proceed by comparing the predictions detailed in the previous sections with the measured uniaxial compression strength of the octet-truss lattice material made from a casting aluminium alloy (LM25) of composition Al-Si 7-Mg 0.3 (wt %).

A brief description of the manufacturing route for this lattice material is given below. Triangulated layers with locating holes at the nodes, and tetrahedral cores with locating pins at the nodes, were injection moulded in polystyrene. The octet-truss microstructure was then constructed by adhering the triangulated layers in an "ABCABC..." arrangement with alternating layers of the tetrahedral core. This polystyrene lattice was used as the sacrificial pattern in a "lost-wax" investment casting process to produce the LM25 lattice material. The octet-truss lattice material employed in this study comprised solid cylindrical struts of radius $a = 1$ mm and length $l = 14$ mm, and the overall specimen dimension was 280 mm × 140 mm × 60 mm, with 5 tetrahedral core layers. A photograph of the lattice material made in LM25 is shown in Figure 12; the stacking of the 5 tetrahedral core layers separated by the triangulated layers is clearly seen in this picture.

Uniaxial compression tests in the 3-direction were performed using a standard screw driven test machine. The load was measured by the load cell of the test machine and used to define the nominal stress in the specimen. The average nominal strain between two triangulated layers was measured via a clip gauge. The measured uniaxial stress versus strain curve, σ_{33} versus ϵ_{33}, is plotted in Figure 13a for the nominal strain rate $\dot{\epsilon}_{33} = 10^{-3}$ s^{-1}. The stress versus strain curve exhibits a hardening response up to a strain of approximately 5 %. Beyond this strain, the response is softening corresponding to plastic buckling of the struts. Bedding-in effects during the early stages of deformation were detected as seen in Figure 13a. These bedding-in effects occur at the nodes in the lattice material: the pins of the tetrahedral core bed into the holes of the triangulated layers during the initial stages of deformation.

In order to compare the measured and predicted stiffness and strength of the lattice material we measured the uniaxial tensile response of the as-cast LM25 struts; the measured response is plotted in Figure 13b. It was found that the LM25 can be approximated by an elastic perfectly-plastic solid with a Young's modulus $E_s = 70$ GPa and a yield stress $\sigma_Y = 170$ MPa. While these values of E_s and σ_Y were used in the analytical predictions, the FE calculations were performed using the measured tensile stress versus strain response of the solid LM25, as given in Figure 13b. The analytical and FE predictions of the strength of the lattice material are shown in Figure 13a: they are in good agreement with the experimental data (note that $\left(\frac{\pi a}{2l}\right)^2 \frac{1}{\epsilon_Y} \approx 5$ and thus the collapse of this material is not expected to be imperfection sensitive). On the other hand, the calculations overestimate the stiffness of the lattice material. This is due to the bedding-in effects at nodes which were neither modelled in the analytical nor the FE calculations.

5 A comparison between the stiffness and strength of the octet-truss lattice material and other porous materials

5.1 Octet-truss lattice material vs. metallic foams

It is of practical interest to compare the mechanical properties of lattice materials with those of competing materials such as metallic foams. Here, the stiffness and strength of the octet-truss lattice material are compared in Figure 14 with those of metallic foams, for relative densities $\bar{\rho}$ in the range 0.01 to 0.1. The modulus E_{33} and strength σ_{33}^Y of the octet-truss lattice material are plotted in Figure 14, while the experimentally observed isotropic stiffness and strength values for metallic foams

$$\frac{E}{E_s} = \bar{\rho}^2, \quad \text{and} \tag{25a}$$

$$\frac{\sigma}{\sigma_Y} = 0.25\bar{\rho}^{1.5}. \tag{25b}$$

are employed; see for example Ashby et al. (1998). Figure 14 clearly shows that the stiffness and strength of the octet-truss lattice material exceed the corresponding values for metallic foams by a factor between 3 and 10.

5.2 Octet-truss lattice material vs. optimal microstructures

The design aim in the development of the octet-truss lattice material is to maximise the strength (or stiffness) to weight ratio of a nearly isotropic cellular material. To get an estimate of the performance of the lattice material with regards to achieving this goal we compare the properties of the octet-truss lattice material with the upper bounds on the stiffness and strength of isotropic voided materials. The H-S (Hashin and Shtrikman, 1963) upper bound on the Young's modulus (with $\nu_s = 1/3$) is shown in Figure 14. The figure also contains an upper bound on the uniaxial yield strength, obtained by transforming the linear H-S bound to the perfectly-plastic case, using the prescription of Suquet (1993). The stiffness and strength of the octet-truss lattice material are seen to be about half the theoretical upper bound values for $\bar{\rho}$ between 0.01 and 0.1.

A number of classes of two phase composites are known to attain the H-S bounds on the bulk and shear moduli. Readers are referred to Sigmund (1999) for details on these optimal microstructures. Here, we briefly review some of the microstructural features of those optimal composites. Norris (1985) and Milton (1986) proposed differential schemes for constructing composite structures with the extremal H-S bulk and shear moduli. While Milton (1986) used a laminate microstructure, Norris (1985) employed a coated sphere architecture. However, the procedures suggested by both these authors are incremental and require an infinite number of mixing processes. Moreover, the procedures do not specifically describe the underlying microstructure of the composite. On the other hand, Francfort and Murat (1986) suggested the so called "rank" laminates which attain both the bulk and shear H-S bounds with a finite number of layering directions. Rank laminates are obtained by a sequential process where at each stage the previous laminate is laminated again with a single lamina (always the same) in a new direction. Thus, a rank-n laminate is produced by n such successive laminations. Francfort and Murat (1986) showed that while in the 2D case, isotropic rank-3 laminates have the extremal bulk and shear moduli, in the 3D case rank-6 laminates are the optimal microstructures. Thus, there exist a variety of multi length-scale microstructures with extremal values of the bulk and shear moduli. However, no single length-scale microstructure that attains both the bulk and shear H-S bounds has been proposed to date.

The bulk and shear moduli of the octet-truss lattice material analysed in this paper are about half the H-S upper bound values. However, the octet-truss lattice with solid struts is a single length-scale microstructure that can be manufactured relatively easily and cheaply. Further, in contrast to the rank laminates, the octet-truss lattice material has additional potential by virtue of it's open structure for multi-functional applications. For example, a sandwich plate with solid skins and the octet-truss lattice core can serve as a heat transfer element while simultaneously carrying structural loads. Such applications of open-celled cellular materials are discussed by Evans et al. (1998). Thus, the octet-truss lattice material represents a relatively cheap and weight-efficient structural material with potential multi-functional applications.

6 Concluding remarks

The effective mechanical properties of the octet-truss lattice material have been investigated through analytical and FE calculations. Analytical expressions have been derived for the three independent moduli associated with the cubic symmetry of the octet-truss lattice material. Good agreement is observed between the analytical predictions and FE calculations, in support of the assumption that the contribution to the overall stiffness from the bending of the struts is small.

Analytical and FE calculations of the plastic collapse surfaces under three combinations of stressing are presented. Again, good agreement is seen between the analytical and FE calculations. An extension of Hill's anisotropic yield criterion fails to capture the form of the collapse surfaces accurately.

The collapse of the octet-truss lattice material by the elastic buckling of the struts has also been addressed through analytical and FE calculations. To simplify the buckling calculations, the struts are assumed to be pin-jointed. Thus, these calculations are expected to be underestimate the collapse stresses. The collapse surface calculations show that elastic buckling of the struts truncate the plastic collapse surfaces under all combinations of macroscopic stressing other than biaxial tension and hydrostatic tension. Further, the FE calculations confirmed that shape imperfections of the struts knock-down the collapse stresses only when the elastic buckling and plastic yielding loads of the struts are approximately equal.

An octet-truss lattice material manufactured in LM25 aluminium alloy was tested in uniaxial compression in the 3-direction. Good agreement is seen between the analytical and FE calculations of the strength and the experimental data. However, the experimentally observed stiffness was lower than the predicted value. This is attributed to the bedding-in of the struts into the nodes during the initial stages of deformation.

The stiffness and strength of the octet-truss lattice material compare favourably with the corresponding properties of metallic foams. In fact, the stiffness and strength values of the octet-truss material are about half the theoretical maximum values for isotropic voided materials: it's high strength to weight ratio, relative ease of manufacture and potential for multi-functional applications makes the octet-truss lattice material an attractive alternative to metallic foams.

Acknowledgements

The authors are grateful to DARPA/ONR for their financial support through MURI grant number N00014-1-96-1028 on the Ultralight Metal Structures project at Harvard University. The Maudslay research fellowship from Pembroke College, Cambridge provided funding for V. S. Deshpande.

References

Ashby, M. F., Evans, A. G. and and, J. W. H. (1998). Metal foams: A design guide, *Technical Report CUED/C-MICROMECH/TR. 3*, Cambridge University, Engineering Dept.

Brittain, S. T., Sugimura, Y., Schueller, J. A., Evans, A. G. and Whitesides, G. M. (2000). Fabrication of a mesoscale space-filling truss system using soft lithography and microelectrochemistry. Submitted to *Journal of Microelectromechanical Systems.*

Budiansky, B. (1974). Theory of buckling and post-buckling behaviour of elastic structures, *in* C.-S. Yih (ed.), *Advances in applied mechanics*, Vol. 14, Academic Press, pp. 2–65.

Deshpande, V. S., Ashby, M. F. and Fleck, N. A. (2000). Foam topology: bending versus stretching dominated architectures. Submitted to *European Journal of Mechanics, A: Solids.*

Evans, A. G., Hutchinson, J. W. and Ashby, M. F. (1998). Multifunctionality of cellular metal systems, *Progress in Materials Science* **43**(3): 171–221.

Francfort, G. and Murat, F. (1986). Homogenization and optimal bounds in linear elasticity, *Archive for Rational Mechanics and Analysis* **94**: 307–334.

Fuller, R. B. (1961). Octet truss, U.S. Patent. Serial No. 563,931.

Gibson, L. J. and Ashby, M. F. (1997). *Cellular solids: Structure and Properties*, 2nd edn, Cambridge University Press.

Hashin, Z. and Shtrikman, S. (1963). A variational approach to the theory of the elastic behaviour of multi-phase materials, *Journal of Mechanics and Physics of Solids* **11**: 127–140.

Hill, R. (1948). A theory of the yielding and plastic flow of anisotropic metals, *Proceedings of the Royal Society London A* **193**: 281–300.

HKS (1997). *ABAQUS/Standard users manual, Version 5.7*, Hibbit, Karlsson and Sorensen Inc., Providence, Rhode Island.

Hutchinson, J. W. (1974). Plastic buckling, *in* C.-S. Yih (ed.), *Advances in applied mechanics*, Vol. 14, Academic Press, pp. 67–144.

Milton, G. W. (1986). Modelling the properties of composites by laminates, *in* J. L. Ericksen, D. Kinderlehrer, R. Kohn and J.-L. Lions (eds), *Homogenization and effective moduli of materials and media*, Springer-Verlag, New York, pp. 150–174.

Norris, A. N. (1985). A differential scheme for the effective moduli of composites, *Mechanics of Materials* **4**: 1–16.

Sigmund, O. (1999). A new class of extremal composites, *Journal of Mechanics and Physics of Solids* **48**(2): 397–428.

Suquet, P. M. (1993). Overall potentials and extremal surfaces of power law or ideally plastic composites, *Journal of Mechanics and Physics of Solids* **41**(6): 981–1002.

Wallach, J. C. and Gibson, L. J. (2000). Mechanical behaviour of a three-dimensional truss material. Submitted to *International Journal of Solids and Structures*.

Wicks, N. and Hutchinson, J. W. (2000). Optimal truss plates, *Technical Report MECH 362*, Division of Engineering and Applied Sciences, Harvard University.

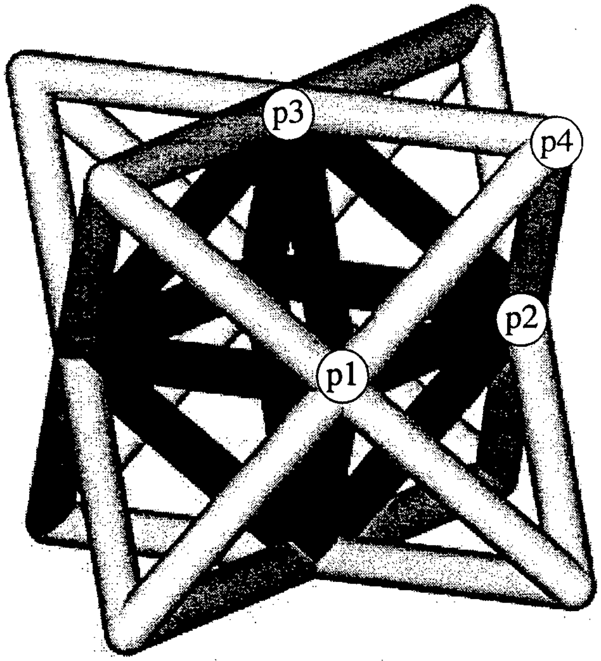

Figure 1: Structure of the octet-truss lattice material. The darkened struts represent a octahedral cell while the nodes labelled p1-p4 form a tetrahedral cell.

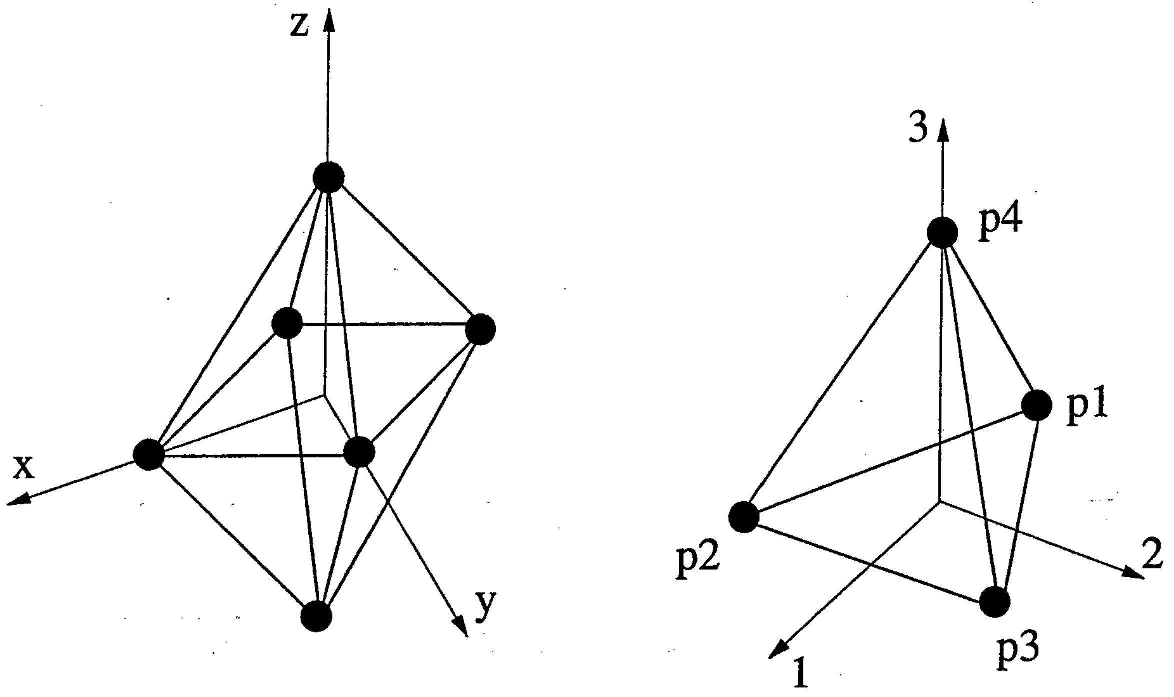

Octahedral cell

Tetrahedral cell

Figure 2: Isometric sketches of the octahedral and tetrahedral cells with the associated co-ordinate systems.

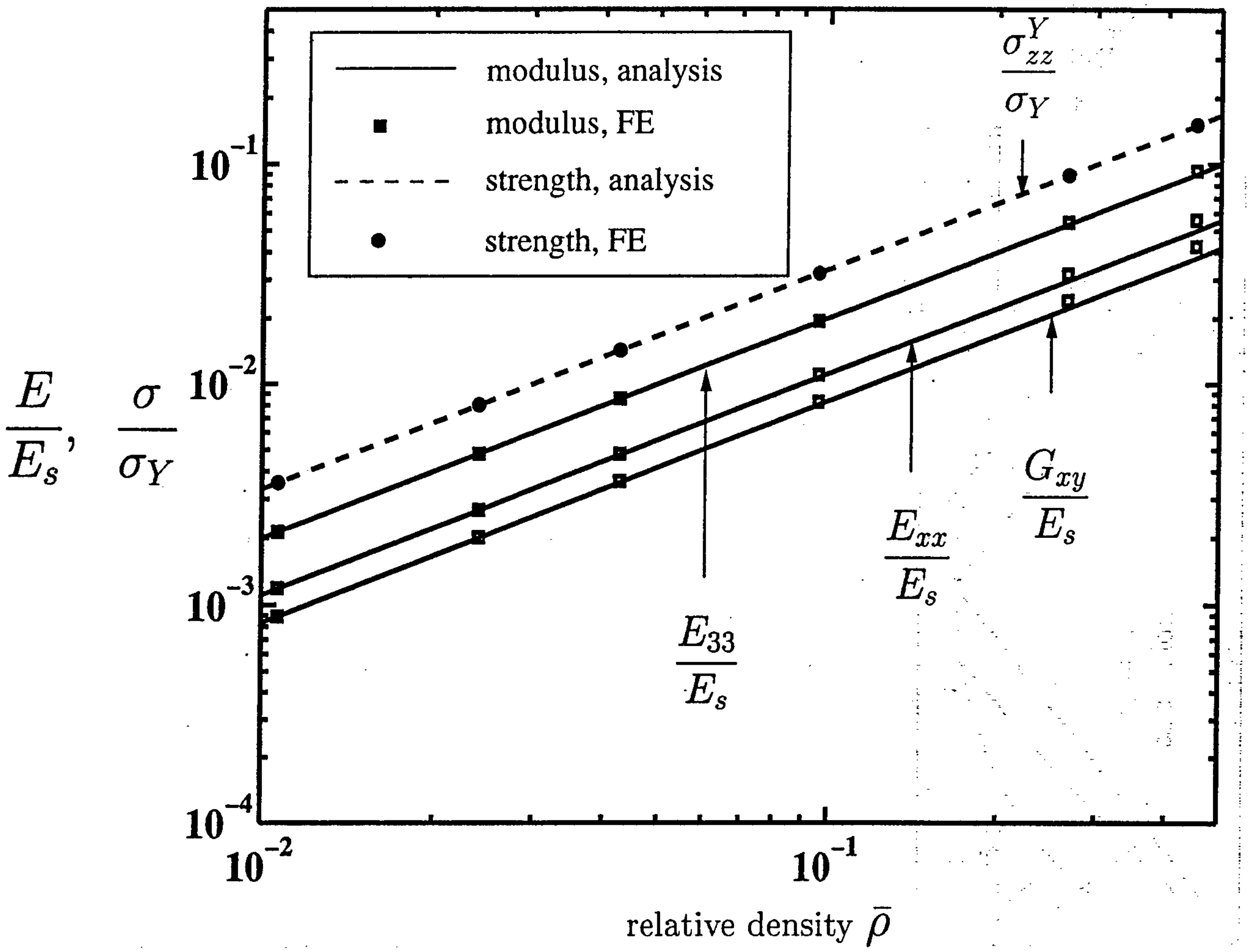

Figure 3: Comparison of the analytical and FE predictions of the elastic moduli and strength for the octet-truss lattice material.

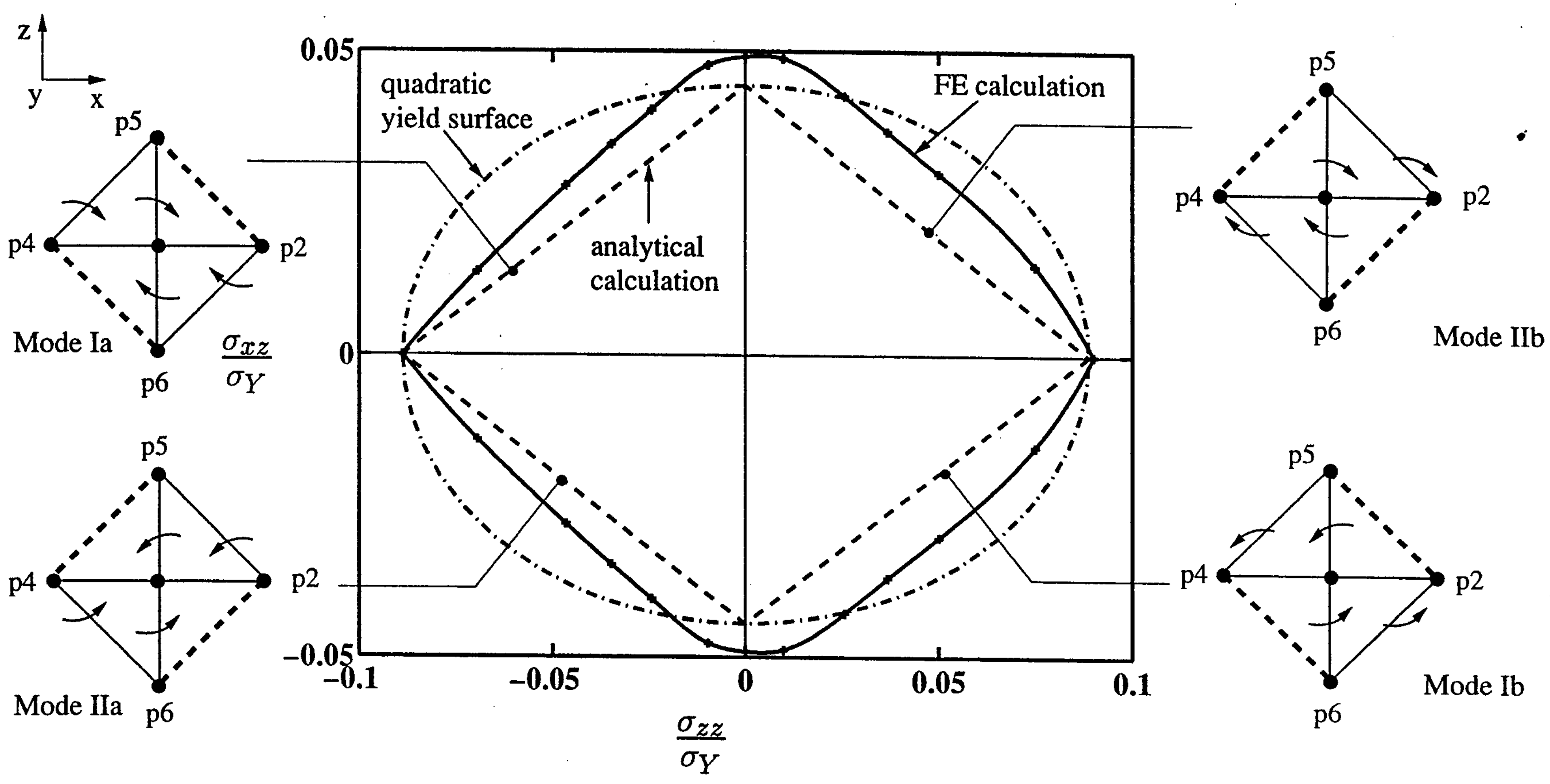

Figure 4: Comparison between the analytical, FE and proposed yield criterion predictions of the plastic collapse surface in $\sigma_{zz} - \sigma_{xz}$ space $(a/l = 0.1)$. In the sketches of the collapse modes, the dashed and solid lines represent struts at yield and in a rigid state, respectively.

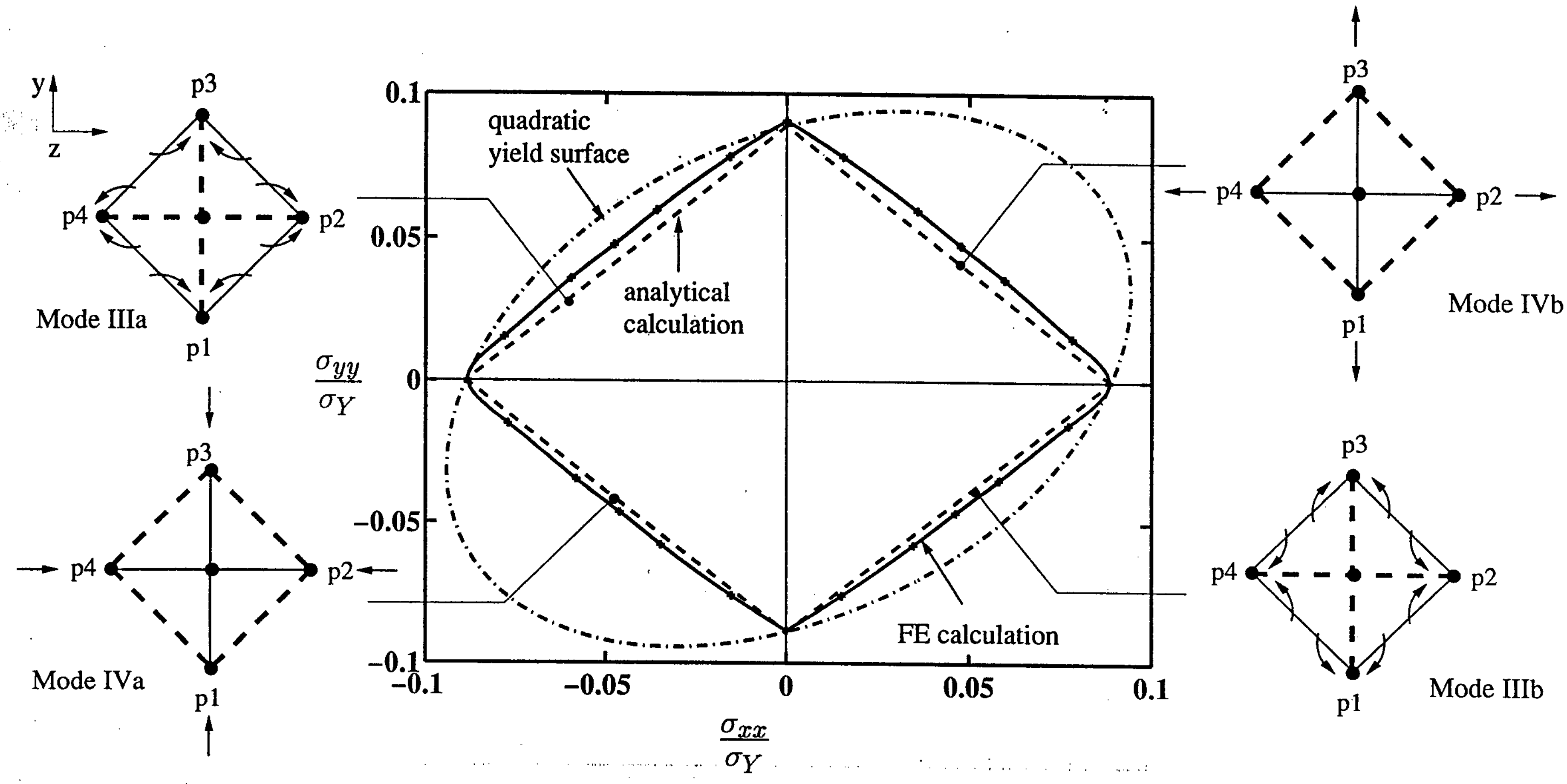

Figure 5: Comparison between the analytical, FE and proposed yield criterion predictions of the plastic collapse surface in $\sigma_{xx} - \sigma_{yy}$ space ($a/l = 0.1$). In the sketches of the collapse modes, the dashed and solid lines represent struts at yield and in a rigid state, respectively.

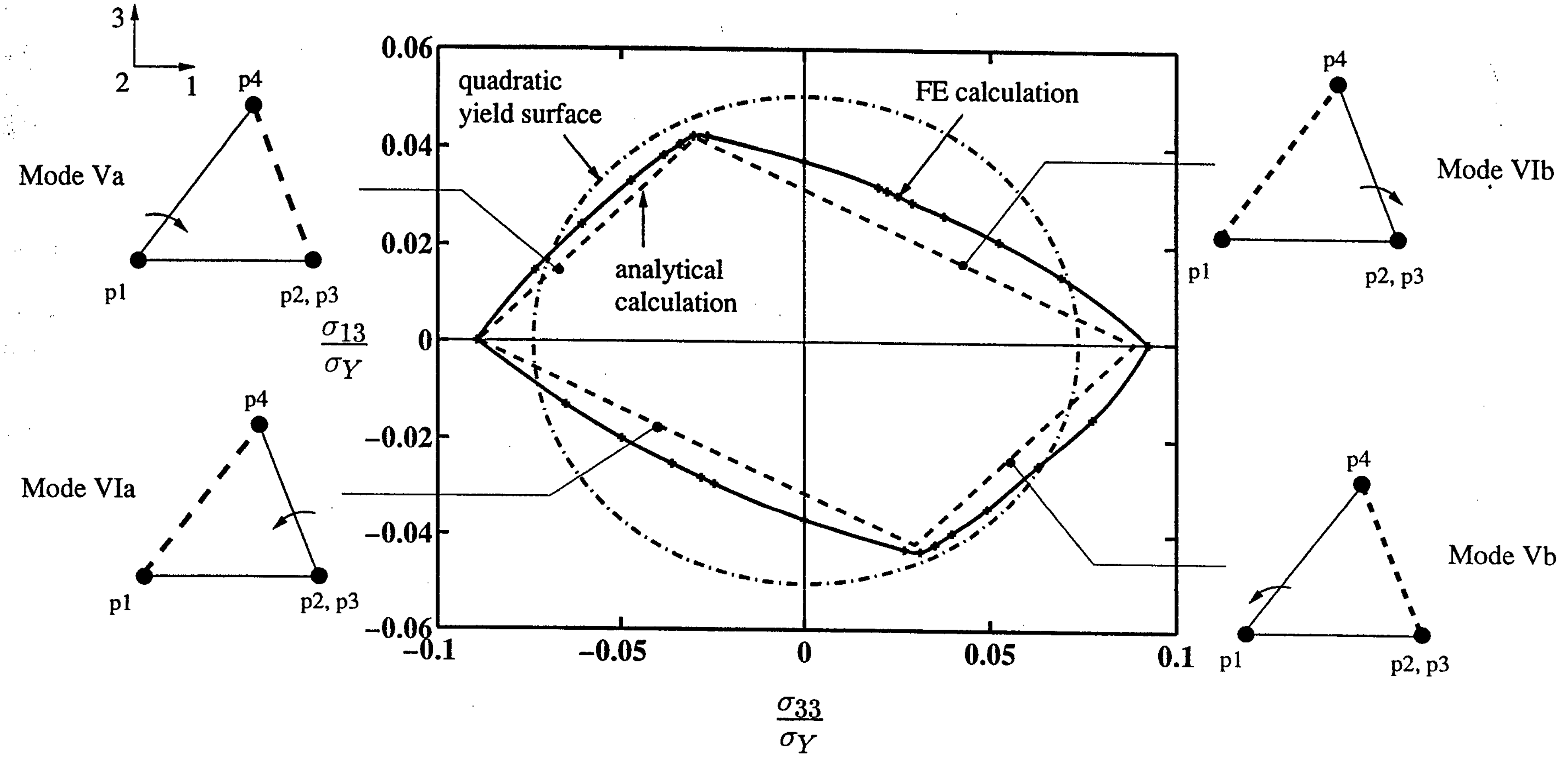

Figure 6: Comparison between the analytical, FE and proposed yield criterion predictions of the plastic collapse surface in $\sigma_{33} - \sigma_{13}$ space $(a/l = 0.1)$.In the sketches of the collapse modes, the dashed and solid lines represent struts at yield and in a rigid state, respectively.

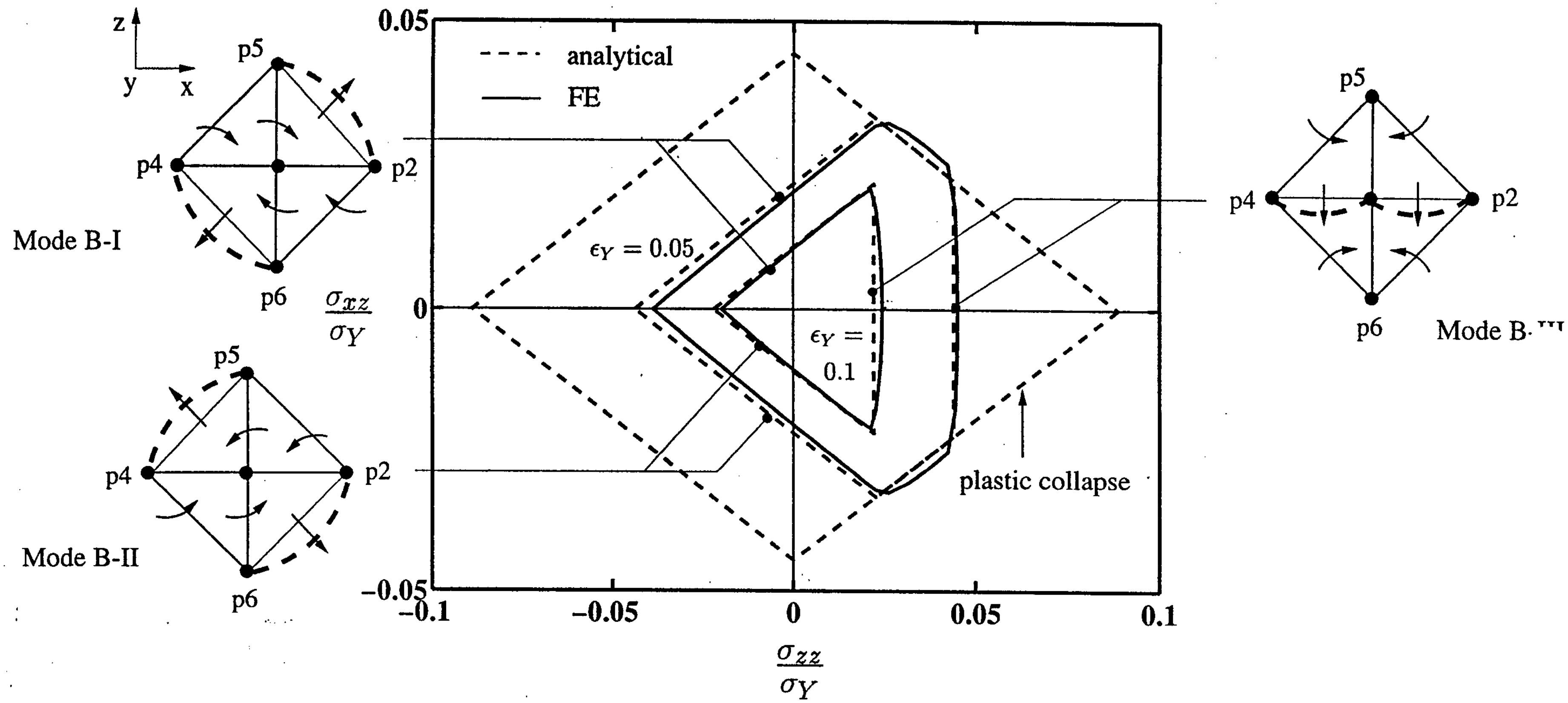

Figure 7: Comparison between the analytical and FE predictions of the buckling governed collapse surface in $\sigma_{zz} - \sigma_{xz}$ space, for $\epsilon_Y = 0.05$ and 0.1 ($a/l = 0.1$).

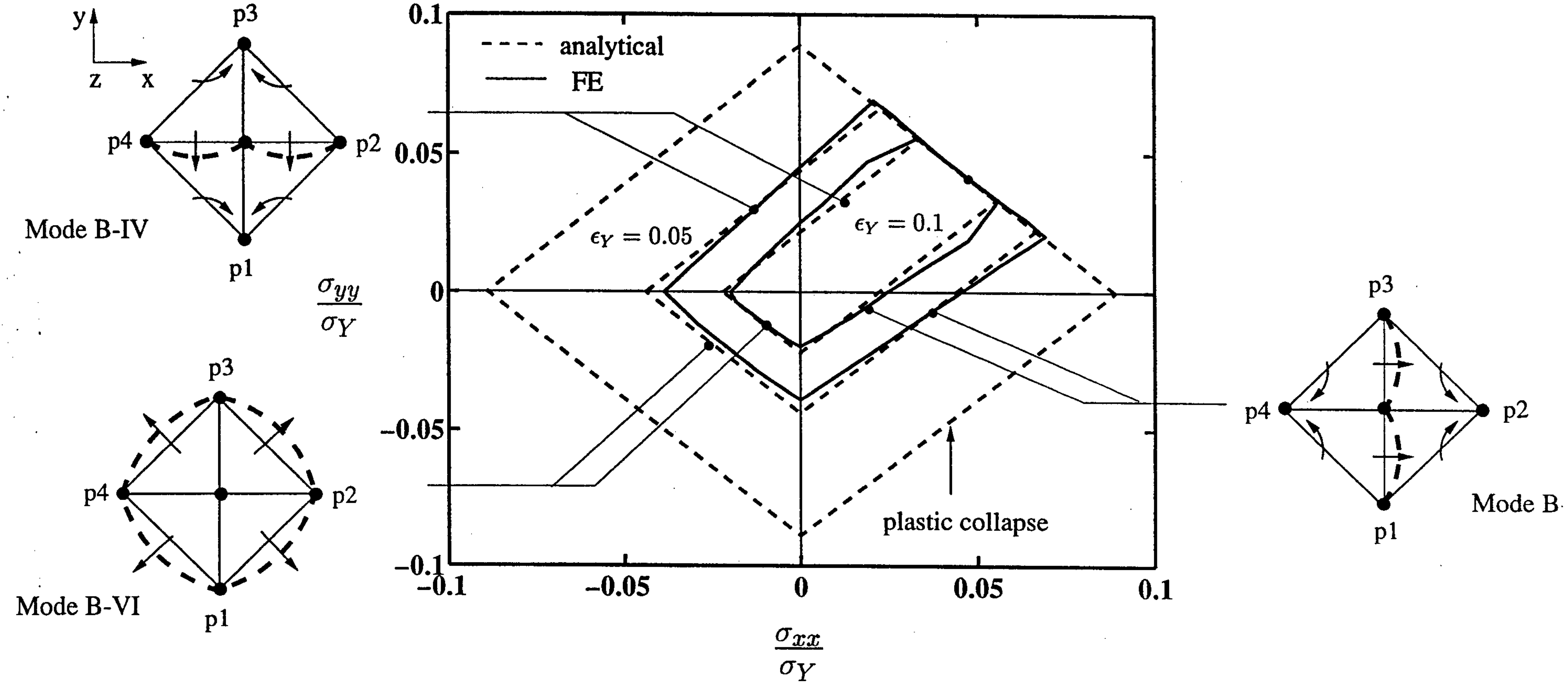

Figure 8: Comparison between the analytical and FE predictions of the buckling governed collapse surface in $\sigma_{xx} - \sigma_{yy}$ space, for $\epsilon_Y = 0.05$ and 0.1 ($a/l = 0.1$).

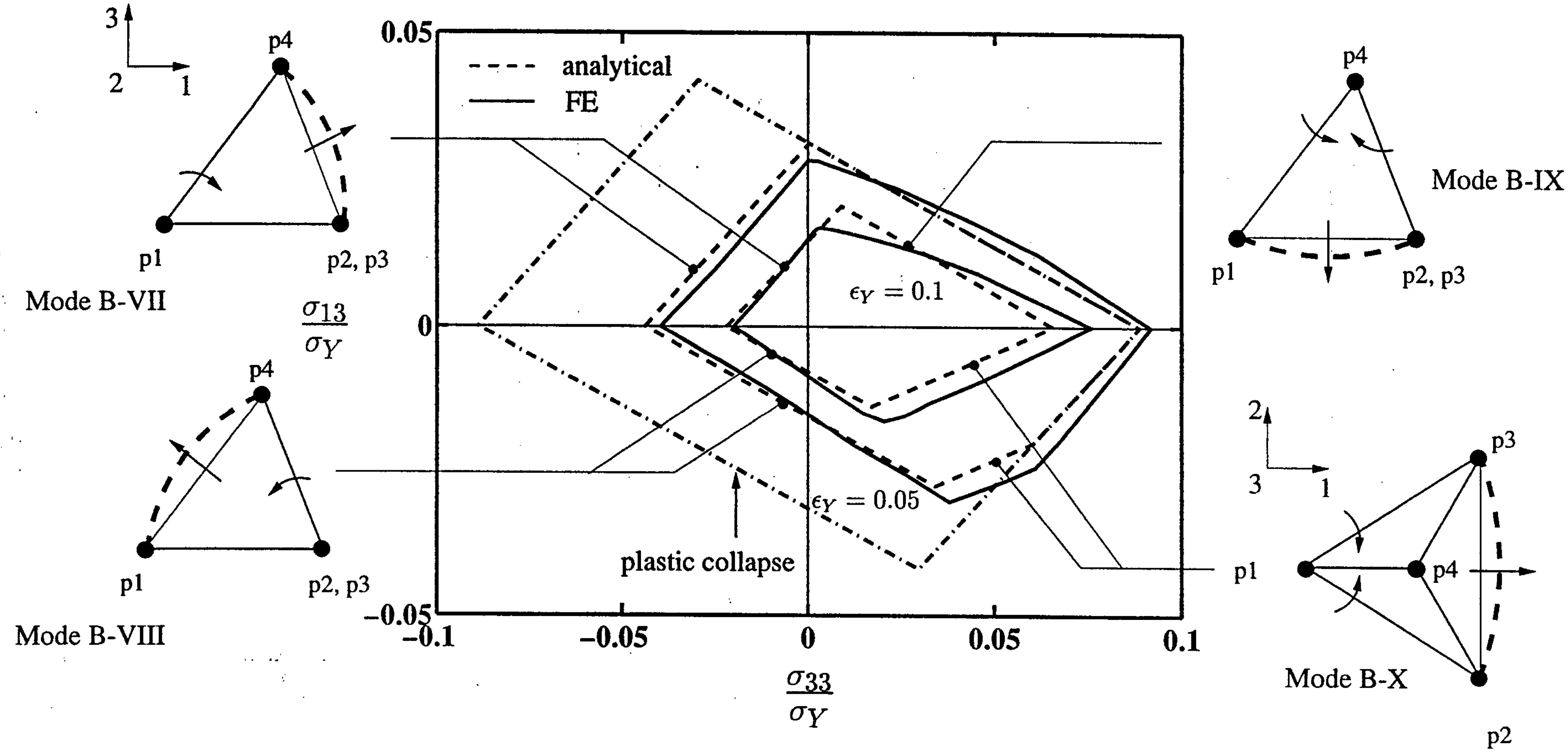

Figure 9: Comparison between the analytical and FE predictions of the buckling governed collapse surface in $\sigma_{33} - \sigma_{13}$ space, for $\epsilon_Y = 0.05$ and 0.1 $(a/l = 0.1)$.

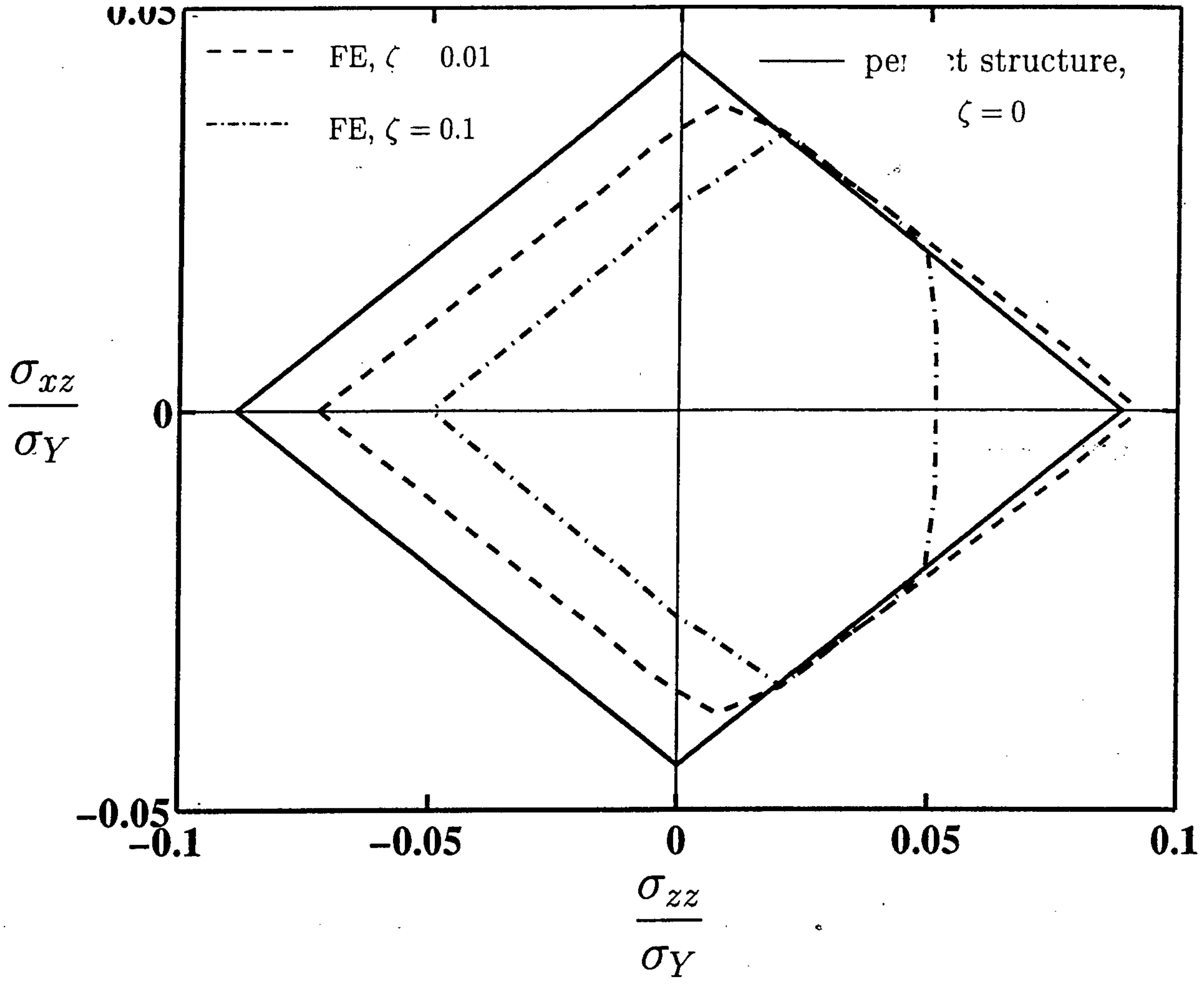

Figure 10: Effect of imperfections on the collapse surface in $\sigma_{zz} - \sigma_{xz}$ space, for $\epsilon_Y = 0.025$ and $a/l = 0.1$.

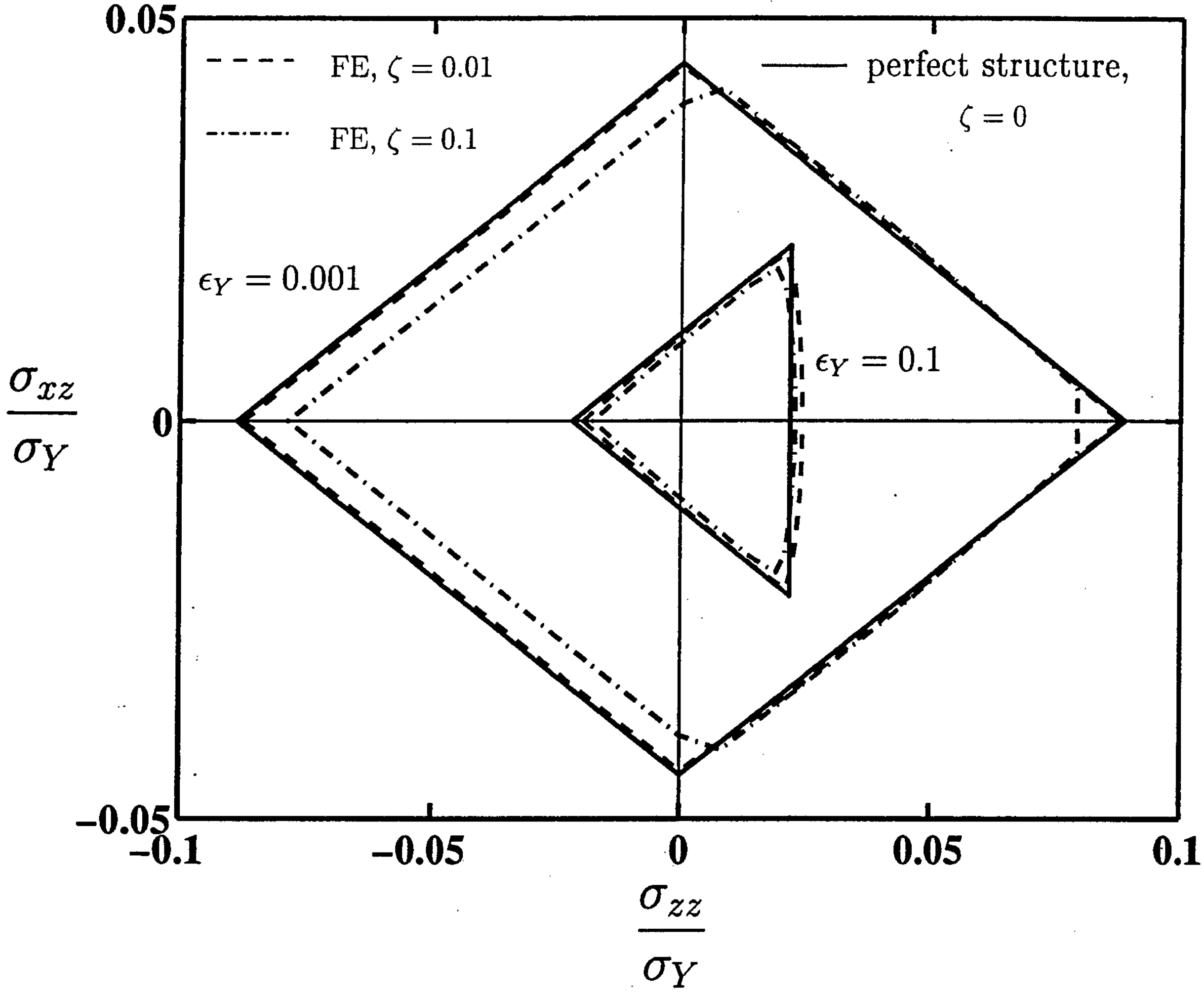

Figure 11: Effect of imperfections on the collapse surface in $\sigma_{zz} - \sigma_{xz}$ space, for $\epsilon_Y = 0.001$ and 0.1 ($a/l = 0.1$).

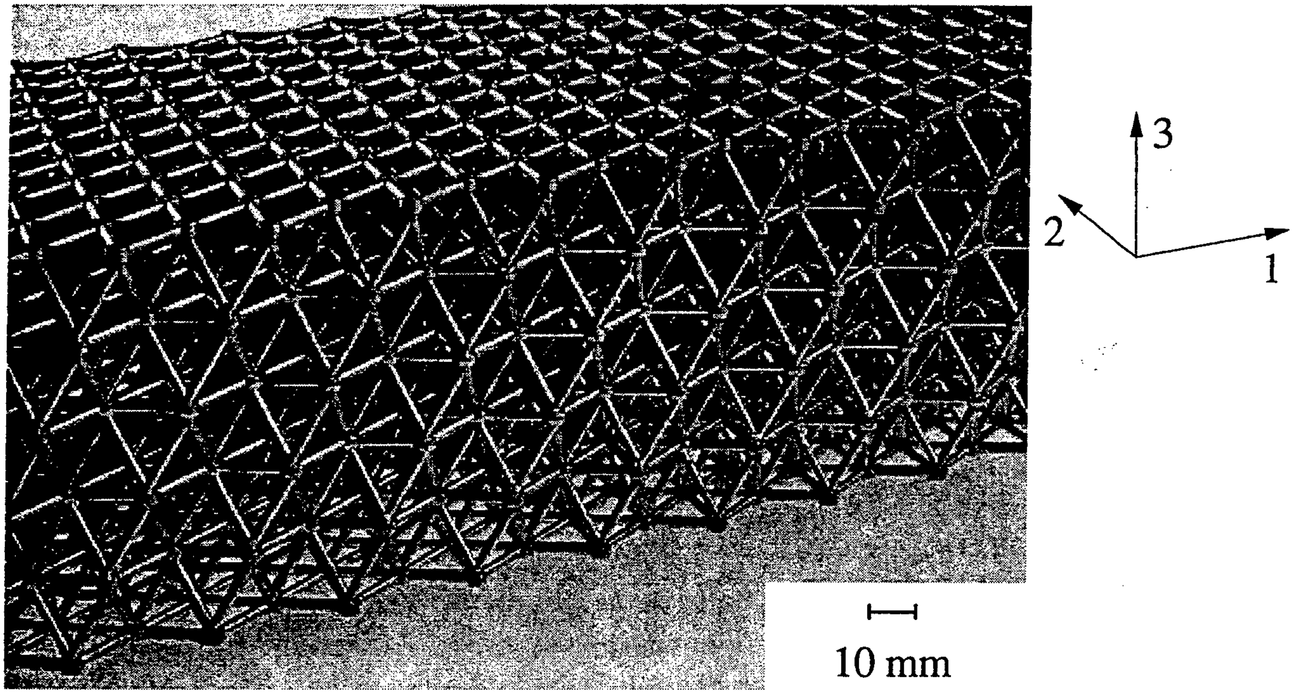

Figure 12: Photograph of the octet-truss lattice material made from a casting aluminium alloy, LM25.

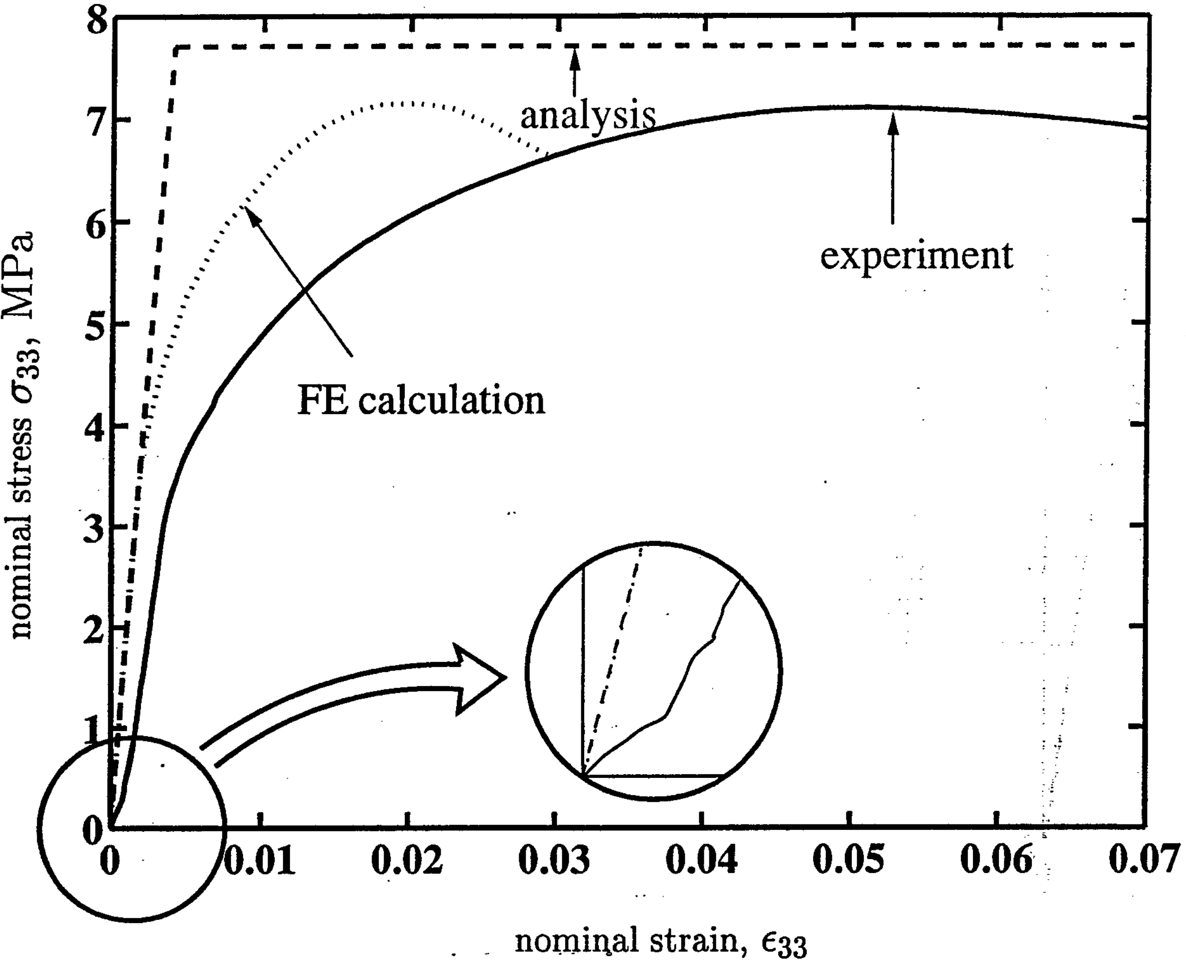

Figure 13: (a) Comparison between the experimental observations and predictions of the σ_{33} versus ϵ_{33} response of the LM25 lattice material.

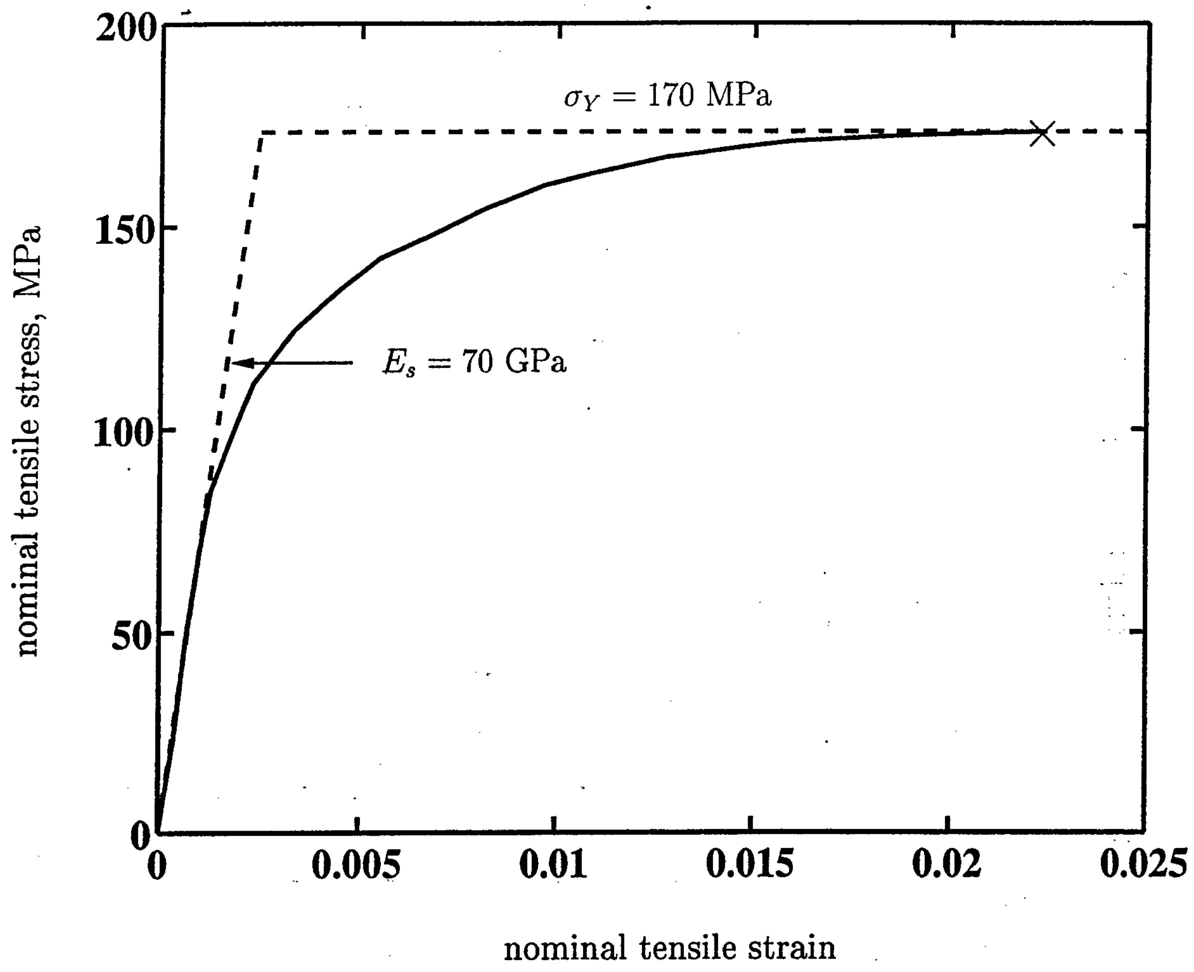

Figure 13: (b) Uniaxial tensile response of the as-cast LM25 aluminium alloy

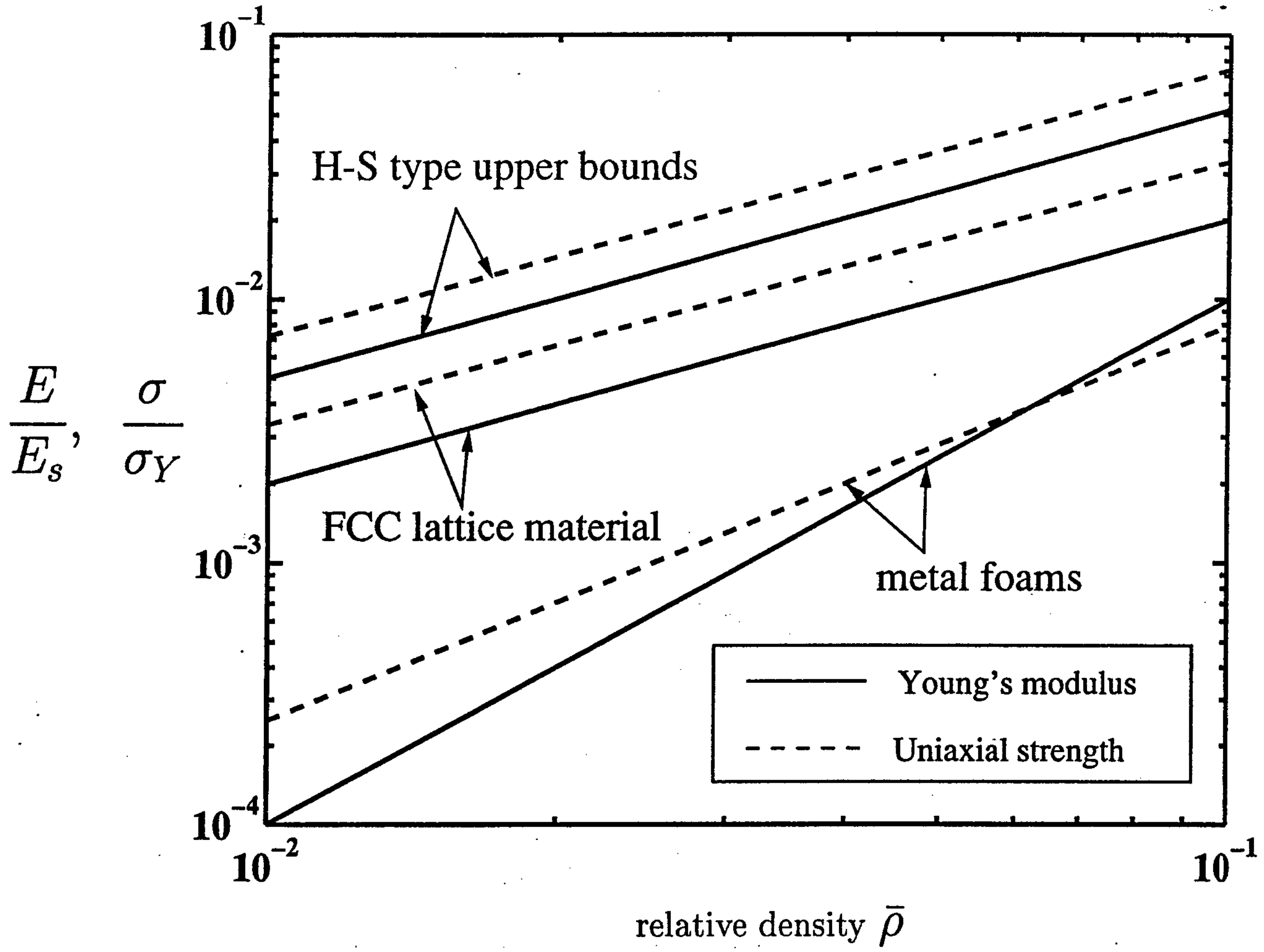

Figure 14: Comparison between the stiffness and strength of the octet-truss lattice material, metallic foams and the upper bounds for isotropic voided materials.

KAGOME PLATE STRUCTURES FOR ACTUATION

R. G. Hutchinson*, N. Wicks**, A. G. Evans***, N. A. Fleck*, and J. W. Hutchinson**
*Engineering Department, Cambridge University, Cambridge, UK
**Division of Engineering and Applied Sciences, Harvard University, Cambridge, MA
***Department of Materials Engineering, University of California, Santa Barbara, CA

Abstract

A class of planar, pin-jointed truss structures based on the ancient Kagome basket weave pattern with exceptional characteristics for actuation has been identified. Its in-plane stiffness is isotropic and has optimal weight among planar trusses for specified stiffness or strength. The version with welded joints resists plastic yielding and buckling, while storing minimal energy upon truss bending during actuation. Two plate structures are considered which employ the planar Kagome truss as the actuation plane. It is shown that these plates can be actuated with minimal internal resistance to achieve a wide range of shapes, while also sustaining large loads through their isotropic bending/stretching stiffness, and their excellent resistance to yielding/buckling.

1. Introduction

A class of actuating plate structures is introduced, based on a planar truss having the Kagome weave pattern (Fig. 1). The two planar manifestations to be explored both consist of faces connected by a tetrahedral truss core (Fig. 2) with the following distinctions:

(i) A Kagome plane and a solid skin,

(ii) Two Kagome faces.

The feature rendering the Kagome planar truss exceptional for actuation is that its members can be actuated (elongated or contacted) to achieve arbitrary in-plane nodal displacements with minimal internal resistance. This attribute arises because the infinite, pin-jointed version satisfies most of the requirements for static determinacy, permitting minimal elastic energy storage (in bending) even when the joints are welded. These benefits become apparent upon comparing with a highly redundant (isotropic) planar truss, exemplified by identical triangular units with equal length members. If such a truss replaces the Kagome in Fig. 2, axial deformation of the members would be required upon actuation, storing substantial energy. The Kagome truss is the only example known to us of an infinite planar truss amenable to assembly from repeat units having both isotropic stiffness and the properties desired for actuation.

This purpose of this paper is to introduce some important properties of the Kagome planar truss and to provide an overview of its role in actuating plate structures. More complete treatments will be given in subsequent papers. Several aspects of the performance of this configuration will be addressed.

(i) A discussion of determinacy for infinite pin-jointed trusses with repeating units reveals that no such configuration can be both statically and kinematically determinate.

(ii) The pin-jointed Kagome truss has kinematic mechanisms, but the weld-jointed version is resistant to premature failure by suppressing them and, moreover, inhibits premature failure by either plastic yielding or buckling.

(iii) In combination with superior in-plane stiffness (Hyun and Torquato, 2002), these features render the Kagome planar truss an ideal structural unit for two-dimensional actuation.

(iv) The actuation capability is revealed by analyzing the response of the plates in Fig. 2 at long wavelengths (relative to the truss member length).

2. Determinacy and the Kagome Planar Truss

The relevance of static determinacy to actuation of two and three-dimensional truss structures has been appreciated for some time in connection with the design of space antenna and mirrors (Miura, 1984a,b; Rhodes and Mikulas, 1985; Mikulas, Thorwald and Wada, 1993). Because the forces in the members of a pin-jointed, statically determinate truss are determined by equilibrium alone, any member can be elongated or shortened without inducing forces in other members, at least to lowest order in the nodal displacements. Accordingly, the structure offers no resistance to actuation, yet, simultaneously, it is capable of carrying applied loads. With a focus on large actuated structures, we consider infinite plates of the kind shown in Fig. 2 where the truss part of the structure is comprised of identical repeating units. The effects of finiteness are discussed elsewhere. The first step considers infinite planar trusses with pinned joints.

2.1 Static and kinematic determinacy of infinite planar trusses with repeating units

Maxwell's necessary condition for static determinacy of a pin-jointed truss requires that the number of member forces equal the number of joint equilibrium equations. For an infinite planar truss, this criterion requires an average of four members converging at each joint. Note that the Kagome truss (Fig. 1) satisfies this condition, whereas a triangulated truss with repeating equilateral triangles has an excess of two members at each joint.

Kinematic determinacy for a truss satisfying the above condition requires that joint positions are uniquely determined by member lengths (no mechanisms) such that member lengths can be varied independently without incurring deformation of any members.

Additional conditions must be imposed to ensure static or kinematic determinacy of an infinite, pin-jointed planar truss. These are discussed by Guest and Hutchinson (2002) and applied to periodic trusses such as the Kagome truss. These authors show that infinite trusses built up from repeating units (planar or three-dimensional) cannot satisfy all of the conditions for both static and kinematic determinacy. That is, any such infinite truss that is statically determinate will necessarily have kinematic mechanisms. Conversely, any infinite truss that is kinematically determinate will have states of self-stress.

2.2 The Kagome planar truss: stiffness and uniform actuation strains

The infinite pin-jointed Kagome truss is neither statically nor kinematically determinate (Wicks, 2002) and yet it is capable of bearing arbitrary overall loads. In contrast, for the case of a finite Kagome truss, it is possible to add additional members to the boundaries in order to make it both statically and kinematically determinate.

Consider the infinite Kagome truss and assume that each member is identical with length, L, cross-sectional area, A, and Young's modulus, E. Further, suppose the truss is loaded at infinity such that the normal and tangential stress resultants per unit length acting on an edge perpendicular to the x_1-direction are (N_{11}, N_{12}); similarly, the stress resultants on an edge perpendicular to the x_2-direction are (N_{21}, N_{22}), where $N_{21} = N_{12}$ and notation standard to plate theory is used. All bars with the same inclination carry identical loads. With three representative members denoted by A, B and C and for the truss orientation shown in Fig. 1, the forces are

$$F_A = (L/\sqrt{3})(3N_{11} - N_{22}),\ F_B = 2L\left(N_{22}/\sqrt{3} - N_{12}\right),\ F_C = 2L\left(N_{22}/\sqrt{3} + N_{12}\right) \qquad (1)$$

The overall stiffness of the Kagome planar truss is isotropic such that the relation between the average in-plane strains and the overall stress resultants are given by

$$\varepsilon_{11} = S^{-1}\left(N_{11} - \nu N_{22}\right),\ \varepsilon_{22} = S^{-1}\left(N_{22} - \nu N_{11}\right),\ \varepsilon_{12} = S^{-1}(1+\nu)N_{12} \qquad (2)$$

with $S = EA/(\sqrt{3}L)$ and $\nu = 1/3$. The inverted relation is (with $\nu = 1/3$)

$$N_{11} = \tfrac{9}{8}S(\varepsilon_{11} + \tfrac{1}{3}\varepsilon_{22}),\ N_{22} = \tfrac{9}{8}S(\varepsilon_{22} + \tfrac{1}{3}\varepsilon_{11}),\ N_{12} = \tfrac{3}{4}S\varepsilon_{12} \qquad (3)$$

Hyun and Torquato (2002) optimized the topology of infinite, planar isotropic truss-like structures in order to maximize stiffness for a given weight. They used an evolution algorithm coupled to a general plane stress analysis of the structure to arrive at an optimal geometry. The Kagome truss and the triangulated truss were found to be almost identical in stiffness per unit weight. When analyzed within the framework of pin-jointed trusses, the two geometries are precisely equally optimal, attaining the dilute limit of the Hashin-Shtrikman (1962) upper bounds.

It is an elementary exercise to relate the overall strains, $(\varepsilon_{11}, \varepsilon_{22}, \varepsilon_{12})$ to the actuation strains $(\varepsilon_A, \varepsilon_B, \varepsilon_C)$ of bars A, B and C, respectively. The overall strains can be achieved without inducing any stress in the members by actuating (i.e. elongating or contracting) the three sets of members according to

$$\varepsilon_A = \varepsilon_{11},\ \ \varepsilon_B = \tfrac{1}{4}\varepsilon_{11} + \tfrac{3}{4}\varepsilon_{22} - \tfrac{\sqrt{3}}{2}\varepsilon_{12},\ \ \varepsilon_C = \tfrac{1}{4}\varepsilon_{11} + \tfrac{3}{4}\varepsilon_{22} + \tfrac{\sqrt{3}}{2}\varepsilon_{12} \qquad (4)$$

or

$$\varepsilon_{11} = \varepsilon_A,\ \ \varepsilon_{22} = -\tfrac{1}{3}\varepsilon_A + \tfrac{2}{3}(\varepsilon_B + \varepsilon_C),\ \ \varepsilon_{12} = \tfrac{1}{\sqrt{3}}(\varepsilon_C - \varepsilon_B) \qquad (5)$$

When the joints are welded, bending in the members results in a small resistance to actuation. To estimate the magnitude, note that the strains induced by bending are of order, $(r/L)\varepsilon_A$, where ε_A is taken to be representative the actuation strain and $r=\sqrt{I/A}$ is the radius of gyration of the member, with I as the moment of inertia. Consequently, the elastic energy induced by actuation scales with $E(r\varepsilon_A/L)^2$ multiplied by the volume of truss deformed. The corresponding elastic energy-scaling factor for an actuated redundant truss is $E\varepsilon_A{}^2$. Thus, the energy stored in actuation of the Kagome truss is expected to be significantly lower than that in a redundant truss.

3. Mechanisms of the planar Kagome pin-jointed structure

It is instructive to determine the full set of possible collapse mechanisms for a pin-jointed planar Kagome structure of infinite extent. A systematic method has been developed to determine the competing collapse mechanisms for any pin-jointed periodic structure (Hutchinson and Fleck, 2002). The method builds upon the matrix methods of structural analysis pioneered by Pellegrino and Calladine (1986) and Pellegrino (1993), and the Bloch wave analysis for periodic continua by Triantafyllidis and Schnaidt (1993). An equivalent approach is to set up the governing set of finite difference equations for a periodic structure (e.g. Forman and Hutchinson (1970)). The main steps in the analysis are as follows.

(i) The kinematic matrix for the unit cell is derived; this relates the bar elongations to the nodal displacements for all nodes and bars of the unit cell.

(ii) For the given unit cell, the trial displacement field d_j^n of each node n at position $\boldsymbol{x}$ is written as

$$d_j^n = p_j^n \exp(i2\pi\boldsymbol{k}\cdot\boldsymbol{x}) \qquad j=1,2 \tag{6}$$

The harmonic function $\exp(i2\pi\boldsymbol{k}\cdot\boldsymbol{x})$, with wavevector $\boldsymbol{k}$, is modulated by an unknown periodic function p_j^n that repeats from one unit cell to the next. Substitution of the trial field (6) into the kinematic matrix for the unit cell leads to a reduced kinematic matrix for the unknown quantities p_j^n for the boundary and interior nodes.

(iii) The possible collapse mechanisms are obtained by taking the bar elongations of the unit cell to equal zero, and by examining the null space of the reduced kinematic matrix for any chosen values of $\boldsymbol{k}$. The dimension of the null space equals the number of mechanisms for the assumed wavevector ***k***. In general, the null space is complex, and the real and imaginary parts of the displacement field d_j^n constitute independent mechanisms.

3.1 Application of matrix analysis to the planar Kagome pin-jointed structure

The full set of mechanisms for the pin-jointed planar Kagome structure have been calculated using the above matrix analysis. The Kagome structure is represented by the primitive unit cell as outlined by dotted lines in Fig.1, with the local co-ordinates $(\hat{x}_1, \hat{x}_2)$ aligned with the sides of the unit cell, and oriented with respect to the Cartesian reference frame (x_1, x_2). Symmetry dictates the existence of 3 families of collapse mechanism, with one family characterised by the wavevector ***k*** along the $\hat{x}_1$- direction, one along the $\hat{x}_2$- direction and the third along the x_2- direction. It suffices to consider the canonical family of mechanisms associated with wavevectors along the x_2- direction; the other 2 families can be obtained simply by rotating the Kagome structure with its canonical family of mechanisms by a clockwise or counter-clockwise rotation through 60°.

The canonical mechanisms are associated with $|k|$ adopting the following values: $|k|=\sqrt{3}/4L$, $\sqrt{3}/6L$, $\sqrt{3}/8L$, $\sqrt{3}/10L$..., 0. For $|k|=0$, a single mechanism exists, and it can be characterized by the relative rotation of neighboring triangles, see Fig. 3a. This infinitesimal mechanism does not generate macroscopic strain, but the finite version of this mechanism does give rise to an equi-biaxial compressive strain. The mechanism for $|k|=\sqrt{3}/4L$ resembles twinning of alternating sign along the x_2- direction, as sketched in Fig. 3b. For intermediate values of $|k|$, such as $\sqrt{3}/6L$, two independent collapse mechanisms exist (given by the real and imaginary parts of d_j^n); each collapse mechanism comprises discrete bands of deformation that are periodic along the x_2- direction. For the sake of brevity, these additional collapse mechanisms are not shown, and the reader is referred to Hutchinson and Fleck (2002) for full details.

None of the infinitesimal collapse modes described above gives rise to macroscopic strain. This is consistent with the fact that the Kagome structure has a finite overall stiffness, as given by equation (3).

4. Strength of the planar Kagome structure with welded joints

When the joints of the Kagome planar truss are welded, the kinematic mechanisms identified above are suppressed. However, the issue remains as to whether the welded truss is susceptible to buckling in modes of similar shape to the mechanisms described above. This possibility is examined by performing a general bifurcation buckling analysis of the in-plane modes. As in the earlier sections, the length of each member is L, the modulus is E and the cross sectional area is A. The moment of inertia of the members governing in-plane bending is I. We first consider conditions for plastic yielding of the truss and continue with a complete analysis of the in-plane elastic buckling modes.

4.1 Yield

It is straightforward to obtain analytic expressions for the plastic collapse strength of the Kagome truss by assuming that each member behaves in rigid-ideally plastic manner, with a yield strength σ_Y, and by neglecting the small effect of bending. The effective yield locus is found by setting the bar tensions defined in (1) equal to the fully plastic axial yield load $\pm A\sigma_Y$ with the following results:

$$\begin{aligned} N_{11} - N_{22}/3 &= \pm A\sigma_Y/(\sqrt{3}L) \\ N_{22} - \sqrt{3}N_{12} &= \pm\sqrt{3}A\sigma_Y/(2L) \\ N_{22} + \sqrt{3}N_{12} &= \pm\sqrt{3}A\sigma_Y/(2L) \end{aligned} \tag{7}$$

Note the special case with $N_{12} = 0$ defines a four-sided convex yield locus in the (N_{11}, N_{22}) plane as shown in Fig. 4c. The relations (7) can be re-phrased in terms of the principal in-plane stresses (N_1, N_2) and the orientation of the principal directions with respect to the Kagome truss. Using this approach it can be shown that the Kagome truss is almost isotropic in its yield response (Hutchinson and Fleck, 2002).

4.2 Elastic buckling of the Kagome truss

Bloch wave theory can be used to obtain the elastic buckling strength of the welded Kagome truss subjected to arbitrary, macroscopic in-plane loading. Following Triantafyllidis and Schnaidt (1993), the first step is to determine the tangential stiffness matrix $\boldsymbol{K}$ for the primitive unit cell (Fig. 1) at a given macroscopic stress. Let $\boldsymbol{d}$ be the vector of virtual nodal displacements (two translations and one rotation per node), and f be the work-conjugate vector of generalised forces (two direct forces and one moment per node). Then, a non-trivial solution is sought for the homogeneous system of equations $\boldsymbol{Kd} = \boldsymbol{f}$ where $\boldsymbol{K}$ is the symmetric, tangential stiffness matrix of the primitive unit cell, in accordance with beam-column theory (see e.g. Livesley (1975)). One first forms the 15 X 15 matrix $\boldsymbol{K}$ for the Kagome unit cell of Fig. 1 (5 nodes each with 3 degrees of freedom, d.o.f.) with the axial bar forces determined by the macroscopic stress state using (1). Next, the generalised virtual displacement and force vectors $\boldsymbol{d}$ and $\boldsymbol{f}$ are given a Bloch wave representation similar to (6), and one thereby obtains a (9 X 9) reduced stiffness matrix $\boldsymbol{K_r}$. The governing equation for any buckling mode now reads $\boldsymbol{K_r}\, \boldsymbol{d_r} = \boldsymbol{0}$. Further reductions may be made if desired: e.g. one may "statically condense" internal d.o.f. such as those associated with joint 1 in Fig. 1. It is emphasized that the reduced stiffness matrix is a non-linear function of both the assumed pre-buckling stress state and the wavevector $\boldsymbol{k}$.

The buckling load of the welded Kagome truss is obtained by incrementing the macroscopic stress state (and thus the bar forces) along a given stress path, and by searching for a non-trivial solution of $\boldsymbol{K_r}\, \boldsymbol{d_r} = \boldsymbol{0}$ for all $\boldsymbol{k}$. This null space contains infinitesimal elastic buckling modes (in general, real and imaginary) analogous to the linear eigenvalue buckling analysis found in many commercial finite element codes (e.g. ABAQUS). At low loads the nullspace is trivial whereas at sufficiently high loads buckling is triggered and the nullspace is non-trivial.

The elastic buckling locus in the macroscopic (N_{11},N_{22}) plane is shown in Fig. 4 for various strut slenderness ratios. In this plot the stress resultants have been normalized by $A\sigma_Y / L$, and, thus, the elastic buckling locus depends upon the magnitude of the yield strain, $\varepsilon_Y = \sigma_Y / E$. Whether elastic buckling or plastic collapse controls the in-plane strength of the truss depends upon the ratio $r / \left(L\sqrt{\varepsilon_Y}\right)$, where $r \equiv \sqrt{I / A}$ is the radius of gyration of the cross-section. If $r / \left(L\sqrt{\varepsilon_Y}\right) > 0.45$, plastic yielding occurs prior to elastic bucking for all combinations of N_{11} and N_{22}. For example, if $\varepsilon_Y = 0.003$ then plastic yielding is operative if $r / L > 0.024$. In other words, only when its members are exceptionally slender will the weld-jointed Kagome truss be susceptible to elastic buckling.

In general, only two elastic buckling modes - modes A and B (Fig. 4) - are found to be of practical interest; all others occurred at higher loads. Mode A is associated with N_{22}-compression and the wavevector $|\boldsymbol{k}| = \sqrt{3} / 4L$ (note similarity to Fig. 3b) while Mode B is associated with N_{11}-compression and is equivalent to Mode A rotated by 60° analogous to the above "canonical pin-jointed mechanism" discussion.

5. Two Kagome Sandwich Plates

The two sandwich plates considered in this paper are shown in Fig. 2. Actuation of members of the Kagome planar trusses is envisioned. For the plate having just one truss face, it is assumed that face will be actuated to achieve desired shapes of the solid face sheet. The Gaussian curvature of the desired shape must be small, otherwise large actuation forces will be required to overcome stretching of the solid face. For the plate in Fig. 2b with two truss faces, each face will be actuated. This allows arbitrary shapes to be achieved with no restriction on the Gaussian curvature.

For the sandwich plate with a single truss plate, the core is comprised of tetragonal truss units connecting the nodes of the face to the solid face as shown in Fig. 2a. The spacing between the faces is H and the truss face sheet is characterized by (1)-(3). The solid face sheet has Young's modulus, E_f, Poisson's ratio, ν_f, thickness t_f, and stretching stiffness, $S_f = E_f t_f$. The sandwich plate has isotropic stretching and bending stiffnesses that can be readily derived. However, the expressions for these stiffnesses are algebraically lengthy. They simplify significantly if $\nu_f = \nu = 1/3$, in which case the plate stretching stiffness, $\overline{S}$, and bending stiffness, $\overline{B}$, under a single component of moment are given by

$$\overline{S} = S + S_f, \quad \overline{B} = \frac{H^2}{2} \frac{S^2 + S_f^{\,2}}{S + S_f} \tag{8}$$

The conventional plate bending stiffness, defined for curvature in only one direction, is $\overline{B}/(1-\nu^2)$.

Second, consider the sandwich plate with two Kagome truss faces; the core comprises tetragonal truss units symmetrically positioned with respect to the mid-plane and connected to the face nodes as shown in Fig. 2b. Equation (8) applies with S_f denoting the in-plane stiffness of the bottom face. If the two faces are identical, $\overline{S} = 2S$ and $\overline{B} = H^2 S/2$.

6. Long Wavelength Actuation of Kagome Plates

For the plate having one solid face, the Kagome back plane is actuated to achieve the desired shapes (figures 2 and 5). For this case, the Gaussian curvature of the goal shape must be small, otherwise large actuation forces will be required to overcome stretching. Conversely, for the plate with two truss faces, both can be actuated to realize arbitrary shapes with no restriction on the Gaussian curvature. The aim is to achieve specified non-planar shapes defined by the transverse displacement field, $w^0(x_1,x_2)$, of the lower face sheet as closely as possible (Fig. 5). When the desired shape has wavelengths that are long compared to the length of the truss members, the analysis is elementary. The results will be presented below. The corresponding analysis for shorter wavelengths will be presented in a subsequent paper.

6.1 Relation between member actuation and average in-plane displacements and strains for long wavelength modes in the 2D Kagome planar truss

Invoke a continuum description of the truss wherein the joints and members are imagined embedded within a planar membrane. Measure displacements and strains from the reference state of the undeformed membrane, and denote them in the usual way for a continuum by $u_\alpha(x_\mu)$ and $\varepsilon_{\alpha\beta}=(u_{\alpha,\beta}+u_{\beta,\alpha})/2$ where the Greek subscripts range from 1 to 2. The displacement of a truss node coincides with the displacement, u_α, of the membrane at that point, and the extensional strain, ε, of a member connecting neighboring nodes I and J is $\varepsilon=(u_\alpha(\vec{x}^I)-u_\alpha(\vec{x}^J))t_\alpha/L$ where t_α is the unit vector parallel to the member and directed from J to I. Equivalently, in the long wavelength limit the member strain can be expressed as $\varepsilon=\varepsilon_{\alpha\beta}t_\alpha t_\beta$ where the strain is evaluated at the member location. Denote the top Kagome face sheet by the superscript T. Then, an arbitrary in-plane displacement field, u_α^T, of the truss joints can be achieved by actuation of the members to undergo the extensional strain described above and derived from u_α^T, i.e. $\varepsilon^T=(u_\alpha^T(\vec{x}^I)-u_\alpha^T(\vec{x}^J))t_\alpha/L$. Thus, the Kagome planar truss can be actuated to achieve any long wavelength, in-plane strain field, $\varepsilon_{\alpha\beta}^T=(u_{\alpha,\beta}^T+u_{\beta,\alpha}^T)/2$. Relations (4) and (5) can be used to obtain the member actuation strains from $\varepsilon_{\alpha\beta}^T$. If the Kagome truss plate had true pin joints, arbitrary member actuation would leave the truss unstressed. The welded-joint Kagome truss is capable of arbitrary actuation without substantial resistance, while at the same time being stiff and strong in all directions.

6.2 Actuation of a Kagome-backed truss plate for long wavelength shapes

The combination of qualities noted above make the Kagome truss a unique two-dimensional element for actuating either of the plate structures shown in Fig. 2. The passive bending behavior of each of the plates is isotropic and substantial, as is the stretching stiffness. Moreover, the sandwich plate has a high resistance to local buckling. Under the restriction of long wavelength actuation modes, it will be shown that the Kagome planar truss comprising the top face of the plate can be actuated to achieve any normal deflection shape of the bottom face sheet, provided that the deflection slopes are sufficiently small. As already noted, larger deflections are limited to those shapes for which the Gaussian curvature of the solid face sheet is small. For the plate having a Kagome planar truss for both faces, this restriction can be removed if both faces are actuated, as will be discussed in Section 5.3.

Let $\varepsilon^0_{\alpha\beta}$ be the in-plane strains of the virtual middle surface of the sandwich. Let $w^0(x_1, x_2)$ be the normal deflection of that surface with $\kappa^0_{\alpha\beta}$ as its curvature tensor, where $\kappa^0_{\alpha\beta} = w^0_{,\alpha\beta}$. With $u^0_\alpha(x_\beta)$ as the in-plane displacements of the virtual middle surface, the in-plane strains are given by

$$\varepsilon^0_{\alpha\beta} = \frac{1}{2}\left(u^0_{\alpha,\beta} + u^0_{\beta,\alpha}\right) + \frac{1}{2} w^0_{,\alpha} w^0_{,\beta} \qquad (9)$$

The compatibility equation for the middle surface strains is

$$\varepsilon^0_{11,22} + \varepsilon^0_{22,11} - 2\varepsilon^0_{12,12} = \mathrm{G} \qquad (10)$$

where $\mathrm{G} = {\kappa^0_{12}}^2 - \kappa^0_{11}\kappa^0_{22}$ is the Gaussian curvature of the middle surface. The formulation is limited to the same restrictions as von Karman nonlinear plate theory: small strains and moderately large out-of-plane rotations such that $\left|u^0_{,\alpha}\right| << 1$ and $\left|w^0_{,\alpha}\right|^2 << 1$. For a core with ample shear stiffness, the strains in the top and bottom faces can be expressed in terms of the middle surface strain and curvature using the classical Euler-Bernoulli hypothesis. This hypothesis states that material points lying on a normal to the undeformed middle surface remain on the normal to the deformed middle surface. For the top Kagome face this implies

$$\varepsilon^T_{\alpha\beta} = \varepsilon^0_{\alpha\beta} - (H/2)\kappa^0_{\alpha\beta} \qquad (11)$$

while for the bottom face (Kagome or solid)

$$\varepsilon^B_{\alpha\beta} = \varepsilon^0_{\alpha\beta} + (H/2)\kappa^0_{\alpha\beta} \qquad (12)$$

Let $w^0(x_1,x_2)$ be the desired shape of the plate. (Under the present restrictions for which (11) and (12) apply, both the top and bottom face sheets have the same normal deflection as the virtual middle surface.) The objective is to activate the top Kagome truss sheet to achieve $w^0(x_1,x_2)$ such that there is no stretching strain in the bottom face sheet. This ensures that any resistance to actuation is due only to bending and, therefore, relatively small. Imposing $\varepsilon_{\alpha\beta}^B = 0$, requires $\varepsilon_{\alpha\beta}^0 = -(H/2)\kappa_{\alpha\beta}^0$. Then, by (11), it follows that the top Kagome truss sheet must be activated such that $\varepsilon_{\alpha\beta}^T = -H\kappa_{\alpha\beta}^0$. Compatibility of the middle surface strains, $\varepsilon_{\alpha\beta}^0$, requires that (10) be satisfied. Since $\varepsilon_{\alpha\beta}^0 = -(H/2)w_{,\alpha\beta}^0$ satisfies $\varepsilon_{11,22}^0 + \varepsilon_{22,11}^0 - 2\varepsilon_{12,12}^0 = 0$ identically, it follows from (10) that the choice of shape $w^0(x_1,x_2)$ must be restricted to have zero Gaussian curvature, that is $\mathrm{G} \equiv \kappa_{12}^{0\,2} - \kappa_{11}^0\kappa_{22}^0 = w_{,12}^{0\,2} - w_{,11}^0 w_{,22}^0 = 0$. (This condition can be relaxed for sufficiently small deflection slopes, as will be discussed later.)

Assuming $\mathrm{G} = 0$, the nodal displacements in the top Kagome truss needed to achieve the strains $\varepsilon_{\alpha\beta}^T = -H\kappa_{\alpha\beta}^0$ are $u_\alpha^T = -Hw_{,\alpha}^0$ and the elongation (or contraction), ΔL, of a member with orientation specified by the unit vector t_α is

$$\Delta L = -HL\kappa_{\alpha\beta}^0 t_\alpha t_\beta \tag{13}$$

As discussed above, this displacement field can always be achieved by actuating members of the Kagome truss plane. Moreover, upon actuating to produce any shape of zero Gaussian curvature there are no induced stresses except those caused by truss bending. Additional loads applied to the sandwich plate induce both bending and stretching. The members and solid face sheet must be designed to carry those loads. The work of actuation is that required to displace the applied loads, plus the small internal energy stored in bending.

The condition on w^0 that $\mathrm{G} = \kappa_{12}^{0\,2} - \kappa_{11}^0\kappa_{22}^0 = 0$ ensures that no stretch energy occurs in the face sheets. When the slopes of the desired shape, $w_{,\alpha}^0$, are restricted to be sufficiently small, the Gaussian curvature can be taken to vanish (since it is quadratic in $w^0{}_{,\alpha\beta}$), and the compatibility equation (10) can be linearized, with its right hand side vanishing identically. Then, *any* shape w^0 can be achieved by actuating the top Kagome truss, but some stretching energy will be induced if $G \neq 0$. The practical limits to the linear regime will depend on energy requirements for actuation and on buckling as well as plastic yielding constraints in the truss members and the solid face sheet.

6.3 Long wavelength actuation of both faces of a two-faced Kagome truss plate

If members of each face of the two-faced Kagome truss plate in Fig. 2 can be actuated, it is possible to achieve arbitrary shapes with no restriction on the Gaussian curvature of the desired shape. Given the desired shape, $w^0(x_1,x_2)$, take $u^0_\alpha = -\frac{1}{2}Hw^0_{,\alpha}$ such that, by (9), $\varepsilon^0_{\alpha\beta} = -\frac{1}{2}Hw^0_{,\alpha\beta} + \frac{1}{2}w^0_{,\alpha}w^0_{,\beta}$. (This choice necessarily satisfies (10).) Then, by (11) and (12), the strains that must be attained by actuation in the top and bottom faces are $\varepsilon^T_{\alpha\beta} = -H\kappa^0_{\alpha\beta} + \frac{1}{2}w^0_{,\alpha}w^0_{,\beta}$ and $\varepsilon^B_{\alpha\beta} = \frac{1}{2}w^0_{,\alpha}w^0_{,\beta}$, respectively. These strains are achieved by actuating length changes of the members according to $\Delta L = L\varepsilon_{\alpha\beta}t_\alpha t_\beta$, as already discussed.

It is worth noting that, as specified, the scheme is not unique. To prescribe unique actuation of the members, both the in-plane displacements and the normal deflection must be prescribed. If the virtual mid-plane undergoes displacements (u^0_α, w^0), $\varepsilon^0_{\alpha\beta}$ is given by (9). Then, by (11) and (12), the face sheets must be actuated to achieve (u^0_α, w^0) such that

$$\varepsilon^T_{\alpha\beta} = \tfrac{1}{2}(u^0_{\alpha,\beta} + u^0_{\beta,\alpha}) - \tfrac{1}{2}H\kappa^0_{\alpha\beta} + \tfrac{1}{2}w^0_{,\alpha}w^0_{,\beta} \text{ and } \varepsilon^B_{\alpha\beta} = \tfrac{1}{2}(u^0_{\alpha,\beta} + u^0_{\beta,\alpha}) + \tfrac{1}{2}H\kappa^0_{\alpha\beta} + \tfrac{1}{2}w^0_{,\alpha}w^0_{,\beta}.$$

The displacements in the bottom face are $(u^0_\alpha + \frac{1}{2}Hw^0_{,\alpha}, w^0)$. Thus, if the aim is to activate the top and bottom face sheets such that the bottom face sheet undergoes displacements (u^B_α, w^B), this can be achieved without incurring stretching energy by substituting $w^0 = w^B$ and $u^0_\alpha = u^B_\alpha - \dfrac{1}{2}Hw^0_{,\alpha}$ into the expressions just listed to obtain

$$\varepsilon^T_{\alpha\beta} = \tfrac{1}{2}(u^B_{\alpha,\beta} + u^B_{\beta,\alpha}) - H\kappa^B_{\alpha\beta} + \tfrac{1}{2}w^B_{,\alpha}w^B_{,\beta} \quad \text{and} \quad \varepsilon^B_{\alpha\beta} = \tfrac{1}{2}(u^B_{\alpha,\beta} + u^B_{\beta,\alpha}) + \tfrac{1}{2}w^B_{,\alpha}w^B_{,\beta} \qquad (14)$$

with $\kappa^B_{\alpha\beta} = w^B_{,\alpha\beta}$.

In summary, a plate having actuated Kagome planar trusses for each face can achieve any desired displacement of the nodes of one of the faces, in-plane and out-of-plane. The resistance to actuation is due only to truss bending effects. A prescription for shapes having wavelengths that are long compared to the plate thickness is presented. This prescription applies to shapes with moderately large slopes, $|w^0_{,\alpha}|^2 << 1$. It can be extended to shallow shells in a straightforward manner.

7. Concluding Remarks

The Kagome truss has been introduced as an actuating plane into a sandwich plate structure with the potential for achieving arbitrary non-planar shapes. The primary feature of the weld-jointed Kagome truss for actuation applications is its ability to deform as an effective medium with arbitrary in-plane strains against the minimal bending resistance of the joints. Other properties that make it especially effective for such applications are its isotropic stiffness, its substantial, near-isotropic in-plane yield strength, and its high local buckling strength. The sandwich plate with two Kagome truss faces can be actuated to achieve arbitrary displacements of the nodes of one face. The plate with only one face as a Kagome truss can be actuated to deform the solid skin to a desired shape. However, unless the Gaussian curvature of the desired shape is small, significant stretching forces will develop and the energy of actuation will be large.

When the actuation is limited to long wavelength modes surprisingly simple results pertain. Methods are being developed to cope with actuation into arbitrary shapes, including a detailed assessment of the stresses produced by both the actuation and by the applied loads to be displaced. Problems related to the potential for fatigue at welded joints will be addressed. More detailed results on the buckling strength will be published separately (Hutchinson and Fleck, 2002). Optimization of plates designed for specific actuation goals will also be performed in subsequent work.

Finally, we note that it has been possible to fabricate the panels described in figure 2 by using a procedure based on the CNC bending of perforated plates, followed by transient liquid phase bonding of the faces to the core. Tests on these structures are in progress to affirm the stiffness and strength, to ascertain the bending resistance of welded truss joints, and to establish limits on the realizable deformations imposed by fatigue.

Acknowledgements: This work was supported in part by the ONR Grant: Multifunctional Mechano-Electronic Materials and by Cambridge University, Harvard University and the University of California, Santa Barbara.

References

Forman, S. E., Hutchinson, J. W., 1970. Buckling of reticulated shell structures, Int. J. Solids. Structures 6, 909-932.

Guest, S. D., Hutchinson, J. W., 2002. On the determinancy of repetitive structures. To be published in J. Mech. Phys. Solids.

Hashin,Z., Strickman, S., 1962. On some variational principles in anisotropic and non-homogeneous elasticity. J. Mech. Phys. Solids 10, 335-342.

Hutchinson, R. G., Fleck, N. A., 2002. manuscript in preparation

Hyun, S., Torquato, S., 2002. Optimal and manufacturable two-dimensional Kagome-like cellular solid. J. Mater. Res. 17, no. 1, 137-144.

Livesley, R. K., 1975. Matrix methods in structural analysis. 2nd Edition, Pergamon Press.

Mikulas, M. M., Thorwald, G., Wada, B. K., 1993. Design considerations for doubly curved comformable trusses. Report JPL D-10528, Jet Propulsion Lab, Caltech, Pasadena, CA.

Miura, K., 1984a. Design and operation of a deployable truss structure. In Proc. 18th Aerospace Mechanisms Symposium, 2-4 May 1984, NASA Goddard Space Flight Center, Greenbelt, Maryland, NASA-CP-2311, 49-63.

Miura, K., 1984b. Variable geometry Truss and its application to deployable truss and space crane arm. In: Proc. 35th Congress of the Int. Astronautical Federation, 7-13 October 1984, Lausanne, Switzerland, IAF-84-394.

Pellegrino, S., 1993. Structural computations with the singular value decomposition of the equilibrium matrix. Int. J. Solids. Structures 30, 3025-3035.

Pellegrino, S., Calladine, C. R. 1986. Matrix analysis of statically and kinematically indeterminate frameworks. Int. J. Solids. Structures 22, 409-428.

Rhodes, M. D., Mikulas, M. M. 1985. Deployable controllable geometry truss beam. NASA Langley Research Center Report NASA TM-86366.

Triantafyllidis, N., Schnaidt, W. C., 1993. Comparison of microscopic and macroscopic instabilities in a class of two-dimensional periodic composites. J. Mech. Phys. Solids 41, 1533-1565.

Wicks, N., 2002. Optimization and actuation of truss structures. In preparation.

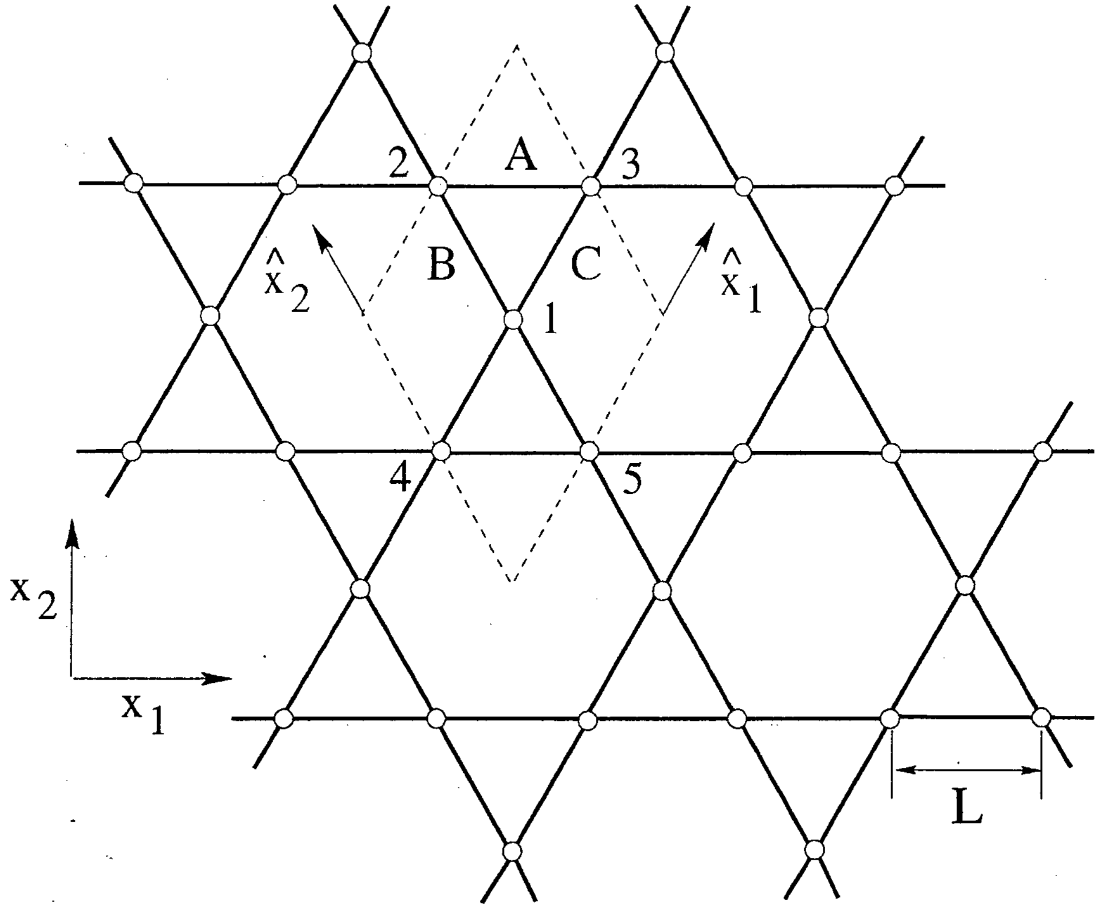

Figure 1. Sketch of pin-jointed, planar Kagome lattice with member length L, spatial coordinates x_1 and x_2 and primitive unit cell dash-outlined.

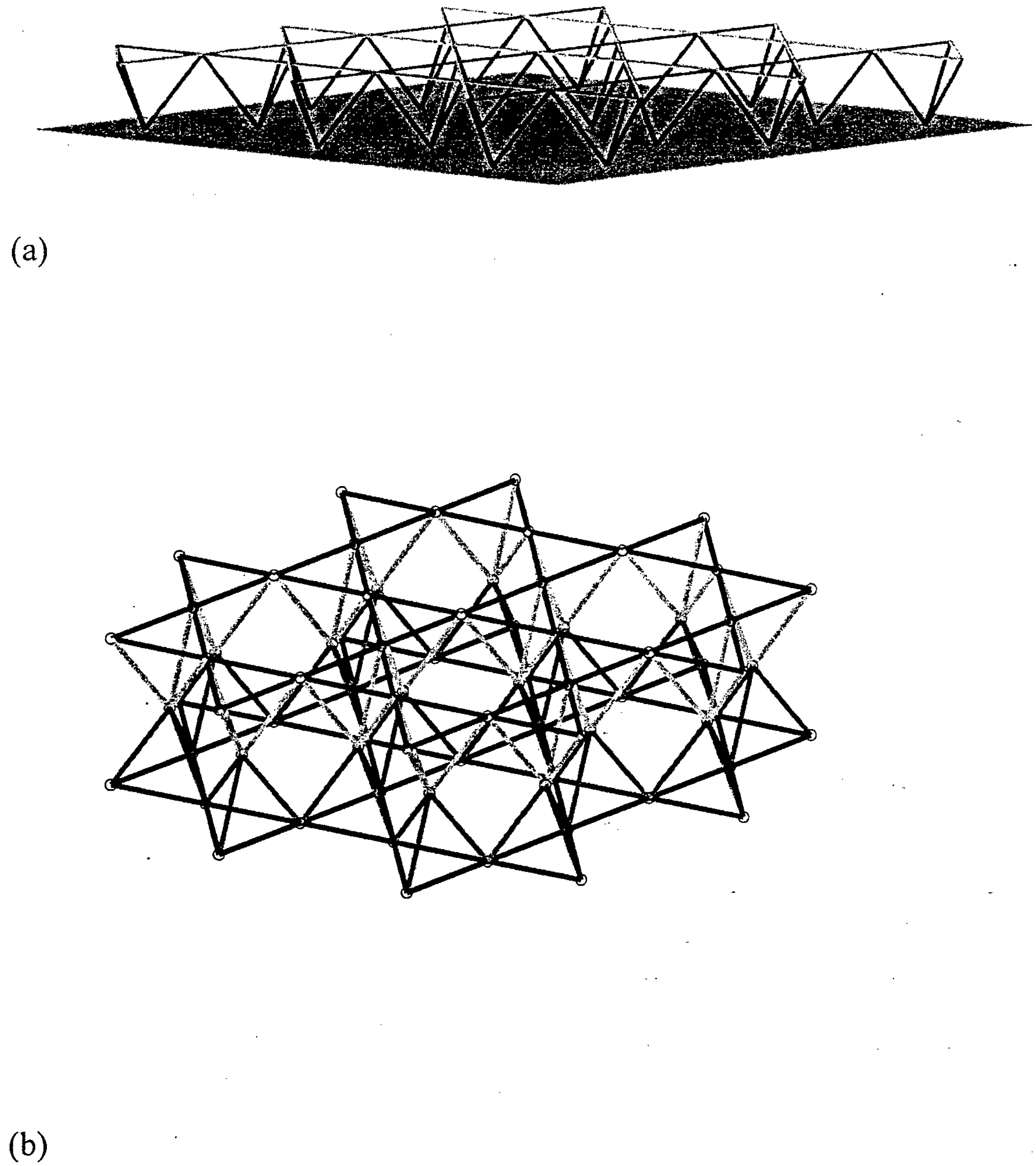

Fig. 2 Sandwich plates based on planar Kagome truss plates. (a) Sandwich with one Kagome truss face and a solid skin face. (b) Sandwich with two Kagome truss faces.

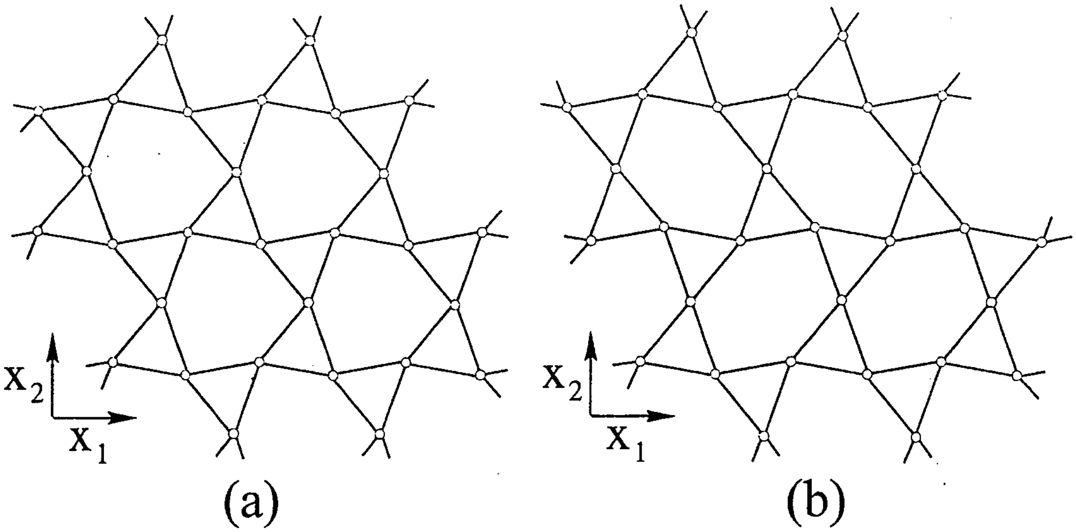

(a) (b)

Figure 3. Mechanisms of the planar Kagome truss. (a) $|\mathbf{k}| = 0$ and (b) $|\mathbf{k}| = \sqrt{3}/4L$.

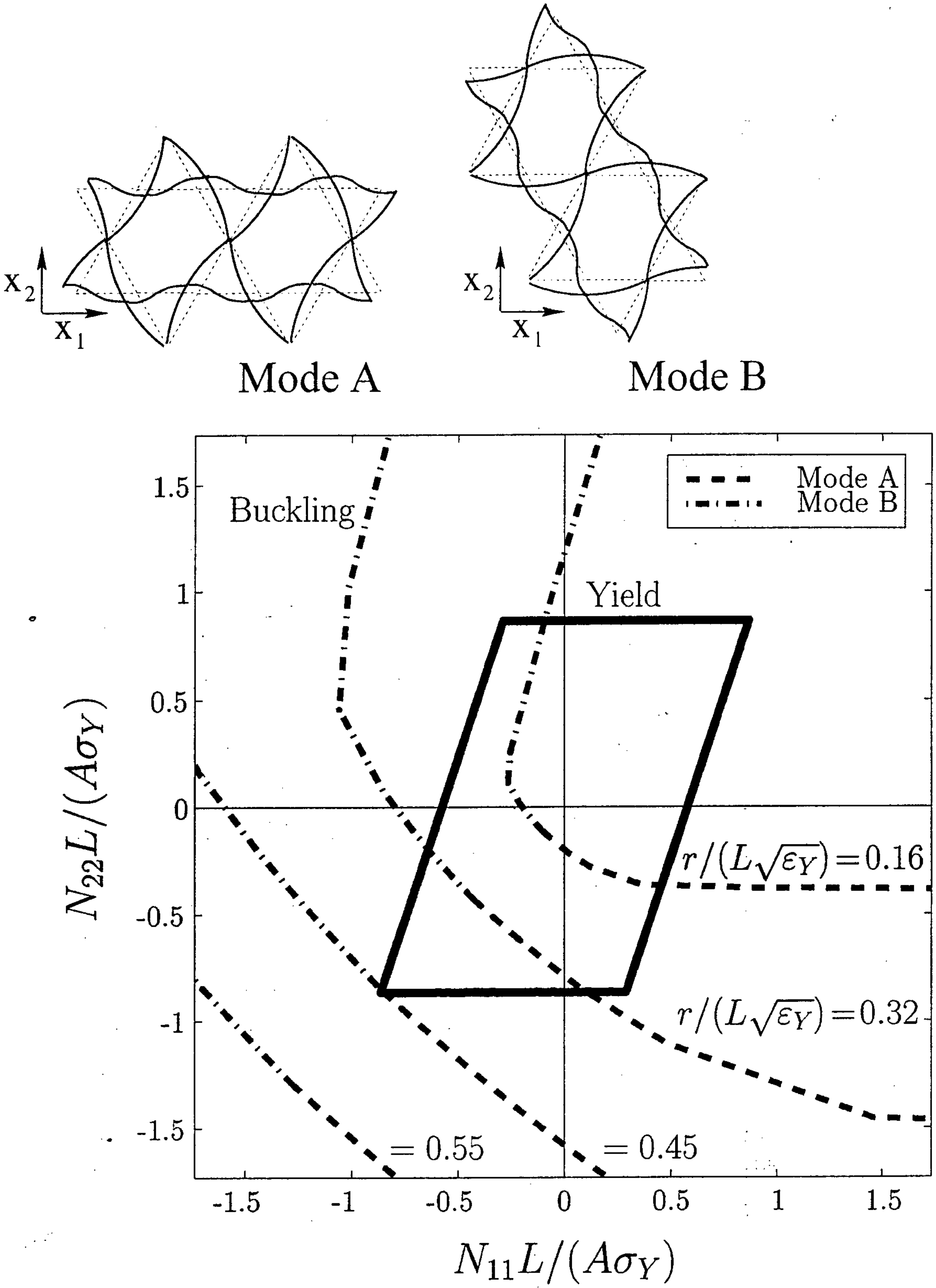

Fig. 4. The competition between elastic buckling and plastic collapse of the welded Kagome truss for selected values of slenderness ratio $r/\left(L\sqrt{\varepsilon_Y}\right)$.

Fig. 5 Desired shape to be achieved by actuation.

Figure Captions

Fig. 1. Sketch of pin-jointed, planar Kagome lattice with member length L. Dashed lines give the boundaries of the primitive unit cell.

Fig. 2 Sandwich plates based on planar Kagome truss plates. (a) Sandwich with one Kagome truss face and a solid skin face. (b) Sandwich with two Kagome truss faces.

Fig. 3. Mechanisms of the planar Kagome truss. (a) $|\mathbf{k}| = 0$ and (b) $|\mathbf{k}| = \sqrt{3}/4L$.

Fig. 4. The competition between elastic buckling and plastic collapse of the welded Kagome truss for selected values of slenderness ratio $r/\left(L\sqrt{\varepsilon_Y}\right)$.

Fig. 5 Desired shape to be achieved by actuation

MEASUREMENTS AND SIMULATIONS OF THE PERFORMANCE OF METALLIC SANDWICH STRUCTURES WITH A NEAR OPTIMAL TETRAHEDRAL TRUSS CORE

H.J. Rathbun, Z. Wei , M.Y.He, F.W. Zok, A.G. Evans,

Materials and Mechanical Engineering Departments
University of California, Santa Barbara, CA 93106

D.J. Sypeck
Aerospace Engineering Department
Embry-Riddle Aeronautical University

H.N.G. Wadley
Department of Materials Science and Engineering
University of Virginia, Charlottesville, VA

Abstract

Metallic sandwich panels with tetrahedral truss core panels have been fabricated and their structural performance evaluated. A novel fabrication technique involving deformation-shaping and transient liquid phase bonding has been used. The responses of the structure in core shear and panel bending have been measured. The results demonstrate robust behavior beyond the limit load, manifest as retained load bearing capacity and bending stiffness even after large plastic deformations. A model for the core shear response is presented as well as a finite element simulation. These duplicate the essential features found experimentally. When combined with the constitutive properties of the face sheet material, these shear characteristics can be used to predict the limit load for panels in bending.

1. Introduction

Hexagonal honeycomb core sandwich structures are the state-of-the-art choice for weight sensitive applications such as aircraft and satellite structures [1]. Panels with open truss cores offer an alternative [2-6]. They are more amenable to forming into complex shapes than honeycomb cores, and they allow fluids to readily pass through, rendering them less susceptible to internal corrosion. They are also attractive for multifunctional applications, such as combined cross flow heat exchange and load bearing [7]. For minimum weight, core topologies that deform by means of stretching or compressing (no bending) are required [3-6], exemplified by tetrahedral and pyramidal topologies [3]. In optimized flat panels, when optimized, such cores are predicted to be as light as honeycomb cores. For these cores, at loads relevant to aerospace applications, the minimum weight occurs at a core relative density in the range 2-3%, with thin faces (thickness to load span of order 3.10^{-3}). The failure mechanisms operating at the optimum depend on the yield strain of the alloy being used [3,7]. At the high yield strains pertinent to aerospace grade Al alloys, failure occurs by concurrent face yielding, face wrinkling and elastic buckling of the compressed truss core members. For the lower yield strains relevant to stainless steels, the failure modes are concurrent face yielding, face wrinkling and core member yielding [3].

Experimental assessments of these predictions have been made in near-optimal panels fabricated by an investment casting process [3], using materials having yield strains in the range where the core response is yield (rather than elastic buckling) dominated. These investigations had two primary limitations: (i) due to the constraints on aspect ratio imposed by investment casting, the faces were much thicker than the optimum so that only the core response could be probed, (ii) the casting introduced defects that limited the plastic strains deformations, inhibiting the ability to probe the performance envelope. Other limitations of investment casting include the relatively high manufacturing cost associated with investment casting, the limited alloy options for the casting of high aspect ratio shapes and the limited material property ranges that can be accessed (relative to a wrought material) and (particularly low ductility).

All of these issues are addressed in the present study by applying a manufacturing procedure for open cell tetrahedral truss core structures (figure 1) applicable to wrought metals [8]. The cores are made from wrought alloys using metal perforation and deformation-shaping processes. They are bonded to thin metal face-sheets using a transient liquid phase approach. The resulting structure has strong nodes and retained ductility. Other structurally attractive truss designs having pyramidal [6] and Kagomé [9] architectures can be fabricated in a similar way. In this article, the performance of tetrahedral truss core panels made in this manner, when subject to overall bending loads, is assessed and compared with predictions for near-optimized configurations [3]. Since regions within the core of panels loaded in this manner experience combinations of shear, compression and stretching, independent measurements of these properties become the basis for models that characterize the overall load supporting capacity.

2. Sandwich Panel Construction

Miniature truss cores can be fabricated from wrought metals by concertina-bending starting with perforated metal sheets and concertina-bending along diagonal lines of nodes [8]. To illustrate the fabrication, a commercially available 304 stainless steel (Fe-18Cr-8Ni) sheet with hexagonal perforations was obtained from Woven Metal Products, Inc. (Alvin, TX). fabricated. The truss members had width w =1.26 mm and thickness, h =0.59 mm. After bending (figure 2a), the core height was, c=1.0cm, such that the relative density was, $\bar{\rho} \equiv \rho_c / \rho_s$ = 1.7%, (where ρ_c is the density of the core and ρ_s is the density of the solid material).

A transient liquid phase approach was used for attaching the face-sheets to the cores. The cores were lightly sprayed with a powder comprising a mix of a polymer (Nicrobraz® 520) and 140 mesh Ni-25Cr-10P alloy (Nicrobraz® 51) both supplied by Wal Colmonoy Corp. (Madison Heights, MI). The solidus and liquidus of this alloy are 880°C and 950°C, respectively: whereas the solidus of 304 stainless steel is approximately 1400°C. The coated cores were placed between solid 304 stainless steel face-sheets and a small compressive pressure was applied. The panel assemblies were heated in a vacuum ($<10^{-2}$ torr) to 550°C for 1h to volatilize the polymer. (Note that the alloy powder remains adhered to the structure after volatilization). The system was evacuated to $<10^{-3}$ torr, the temperature increased to 1100°C and held for 1 h. At temperature, the alloy melts and is drawn into the core/face-sheet contacts by capillarity. Transient liquid phase bonding then occurs as inter-diffusion changes the local composition, causing it to solidify. Robust joints with desirable nodes ensue (Figure 2b). Upon bonding, the core height diminishes slightly, increasing the core density to $\bar{\rho}$ = 1.8%.

For the panel bending assessment, a face thickness, d =0.75 mm, was chosen. This thickness exceeds that for the optimum structure [6], assuring that the bending response is core dominated (not limited by face yielding). Thicker-than-optimum faces also have the practical attribute that they are less susceptible to penetration by sharp objects (albeit subject to the penalty that the overall weight is increased). For the core shear tests, much thicker faces were used (d=3mm) to prevent distortions from occurring during the measurements.

3. Test Design

After furnace cooling to ambient, the panels were machined for testing. The flexure panels had a span length, l = 24.7cm, width b = 6.6cm, and a mass of 219g. They were tested in three-point loading by using a procedure similar to that described elsewhere [5,10]. Flat-faced loading platens 16 mm wide were adhesively-bonded to the faces of the panels. The loads were applied through lubricated rollers inset into the platens that allowed the specimen to rotate upon bending, with minimal friction. Strain gages were bonded to the tensile face at two locations. One set was attached to the face immediately opposite the inner platen. Strains were monitored in both 0° and 90° orientations. A second set was attached to the same face mid-way between the inner and outer platens. The test was performed in a servo-electric test frame. The load, load-point displacements and strains were measured simultaneously.

The shear test assembly comprised two L-shaped platens that rigidly held the panel. The assembly was placed between flat loading surfaces connected to the load cell and actuator of a servo-hydraulic load frame. Imposing a compressive load to the assembly created a condition of nearly pure shear at the truss core. The tests were performed at a load point displacement rate of 0.10mm/min. Displacements were measured by a laser extensometer. Tests were performed in the negative and positive orientations [3,5,9].

A high resolution digital camera was connected to the testing frame in order to capture side-view images of the core. These images were subsequently used to identify the failure mechanisms.

4. Measurements and Observations

The constitutive properties of the 304 stainless steel used in the face sheets was measured after exposure to a simulated bonding cycle. Flat dog bone-shaped tensile specimens tested at a strain-rate of 10^{-4} s^{-1} gave the stress/strain results plotted on figure 3. The material exhibits almost linear hardening beyond yield with a 0.2% offset yield strength, $\sigma_y = 217$MPa. The hardening rate beyond yield can be characterized approximately by a hardening modulus, $H \equiv d\sigma / d\varepsilon = 2.5GPa$.

The shear stress/strain responses measured in the positive and negative orientations (Figure 4) demonstrate the asymmetry of the tetrahedral truss core. In the negative orientation, the limit load is appreciably lower than in the positive orientation because the most heavily stressed trusses are in compression and susceptible to plastic buckling. The maximum shear stress in this orientation is, $\tau_{\max} = 1.04\,MPa$, occurring at a shear strain of 1.4%, observed to be coincident with plastic buckling of the compressed members. In the positive orientation, the corresponding maximum was $\tau_{\max} = 1.70\,MPa$, occurring at a shear strain of 13.3 %. In this orientation, the most highly stressed trusses are tension. They stretch plastically and transfer load onto the compressed trusses, eventually causing them to buckle plastically. Periodic unloading and reloading was conducted for tests performed in the positive orientation in order to evaluate the unloading value of the shear modulus, *G*. This modulus has a magnitude, $G \approx 135\,MPa$, which remained essentially unchanged for strains up to about 5%.

A load/displacement curve measured in bending is summarized on Figure 5. A steady-state load, $P_{ss} = 1470$N is attained at displacements between, 2mm < δ_{ss} < 5mm, followed by gradual softening beyond 5mm. In the steady-state range, the unloading stiffness remains essentially invariant at, P/δ = 2.5MN/m. *This response is remarkably robust relative to that for the equivalent cast panel* [5], which softens immediately after reaching the limit load, with rapidly diminishing load capacity. This same advantage also exists relative to minimum weight panels with honeycomb cores [3]. The robustness of the present system is attributed to the ductility of the wrought alloy and to the yield (rather than buckling) controlled failure of the core. An image obtained at the limit load (figure 6) indicates that the response is asymmetric and that the panel fails by core shear (preferentially on the left of the figure), with the compressed truss members exhibiting plastic buckling. This response occurs because, in three-point bending, the truss assemblies on the left experience negative shear [3,5]. The consequent plastic buckling of the compressed members induces large strains that cause plastic hinges at both the central and outer load platens. The right side experiences positive shear, whereupon the trusses stretch with relatively small ensuing strain levels, inhibiting hinging at the outer platen. After unloading, all of the core/face-sheet bonds were intact with no visible cracking.

5. Evaluation of the Shear Strength

5.1 Analytical Model

Initially, a simple analytical model for the core deformation is used to estimate the core shear strength, embellishing a result previously derived by Deshpande and Fleck [6]. A modification to their model is needed since the truss members in the present tests are rectangular, rather than circular. Consider a pure shear force, F_s, applied to the top node of a single truss assembly. All members support only uniaxial compression or tension [3]. The member stresses σ_A and σ_B are:

$$\sigma_A = F_s / \sqrt{3} A_m \qquad (1)$$

$$\sigma_B = 2 F_s / \sqrt{3} A_m$$

where A_m is the cross sectional area. Strains are determined from the stresses through the constitutive data (figure 3). The associated shear displacement is obtained from the strains using:

$$\Delta = \frac{L}{\sqrt{3}} \left[(1+\varepsilon_A)^2 - (1-\varepsilon_B)^2 \right] \qquad (2)$$

For the tetrahedral configuration wherein all members have the same length and the base is an equilateral triangle, the maximum shear stress in the negative orientation is related to the plastic buckling stress, σ_{pb}, by [6]:

$$\frac{\tau_{\max}^{neg}}{\sigma_{pb}} = \frac{\sqrt{2}}{6} \bar{\rho} \qquad (3)$$

In turn, the plastic buckling stress for a material with a bilinear stress/strain response is [11]:

$$\sigma_{pb} = \frac{k^2 \pi^2 H I}{A_m L^2} \qquad (4)$$

where I is the moment of area for the rectangular cross section and L is the member length (for pinned joints, k = 1, and for built-in ends, k = 2). For the hardening rate, H, pertinent to the present material (figure 3), (4) reveals that for either end condition, plastic buckling is coincident with yielding, such that, $\sigma_{pb} \equiv \sigma_Y = 217MPa$. More refined results are presented below using a finite element approach. In the positive orientation, the corresponding shear stress maximum, $\tau_{\max}^{pos}$ (being governed by plastic buckling of the members originally in tension) is twice that for the negative orientation.

Based on the measured relative density (1.8%), these solutions provide estimates of the shear stress/strain response in the positive orientation and the peak stresses in both orientations. When superposed on the measured stress/strain curves (figure 4), the peak stress determined for the negative orientation, $\tau_{\max}^{\text{neg}} = 0.92$MPa, is somewhat smaller than the measured maximum ($1.04MPa$), while that for the positive orientation, $\tau_{\max}^{pos}=1.84$MPa, is somewhat larger. The implication is that this simple approach may thus be used with some assurance to estimate the core shear strength.

Note that the model indicates a shear stiffness ($G = 388MPa$) much larger than the measured value by almost a factor 3 [6]. This discrepancy is related to displacements occurring at the nodes, which are not incorporated in the boundary conditions used for the analysis. Further assessments are needed to resolve this discrepancy.

5.2 Finite Element Simulation

The shear stress/strain response has also been explored using a finite element simulation, similar to atthe described by Hyun et al [9]. In this case, the exact rectangular geometry of the truss members has been used, as well as the measured stress/strain curve for the faces (figure 3). The truss assembly and the finite element mesh are shown ion figure 7. The finite element code ABAQUS has been used. For the calculations, the base of the truss assembly is fixed. The top, where the assembly is bonded to the upper face, is displaced parallel to the face and the induced forces are calculated. The top plane of the assembly is allowed to displace in the vertical plane, without rotation, to represent a stiff face. The deformations of the core that occur in the negative and positive orientations at large displacements are shown on figure 7. The similarities with the core responses observed on the two sides of the panel in bending (figure 6) is evident: that is, the plastic buckling of the compressed member in the negative orientation and the stretching of the tensile member in the positive orientation.

The calculated stress/strain curves in the two orientations are plotted on figure 8. To achieve explicit comparison with the measurements in the plastic range (given the discrepancy in the shear modulus noted above), the experimental measurements are superposed on the simulations by shifting the elastic response to match the simulations. The similarity between the curves in both orientations affirms the self-consistency of the present measurement and simulation protocols. There are two minor discrepancies. The simulations generally underestimate the flow strength by a few percent. Since the simulations use the stiffest possible boundary conditions (where the truss assembly attaches to the faces), this difference implies that the material comprising the truss members has a somewhat higher strain hardening than that measured for the faces. It is possible this is result of compositional differences arising from the transient liquid phase bonding process. The second discrepancy relates to the onset of plastic buckling in the negative orientation. The simulation overestimates the stress at which this occurs by about 10%. The presumption is that surfacethe imperfections present in the actual truss structure lead to a small diminution in the buckling load.

6. The Bending Response

The beam theory solution for the collapse load of a sandwich panel in three-point bending with small overhang, h, is given by [7]:

$$F_A = \frac{2bd^2}{l}\sigma_y + 2bc\tau_{\max}\left(1+\frac{2h}{l}\right) \qquad (5a)$$

The corresponding result for panels with large overhang is [7]:

$$F_B = \frac{4bd^2}{l}\sigma_y + 2bc\tau_{\max} \qquad (5b)$$

In these formulae, c is the core thickness, d the face thickness, b the panel width and l the span, while σ_y is the yield strength of the faces. In practice, the lower of the two loads F_A, F_B should govern the measured limit load.

To compare these predicted results with the measurements, the number of truss elements within the panel supporting the loads must be ascertained. Based on this assessment, the relevant dimensions panel dimensions are: width b = 6.6cm, core height c = 9.8 mm, face sheet thickness d= 0.75 mm, span l = 20.2cm, and overhang h = 2.25cm. Assume that the load capacity is limited by the shear response in the softer, negative orientation. Then, upon incorporating the measured shear strength, $\tau_{\max} = 1.04\text{MPa}$, as well as the measured face sheet yield strength, $\sigma_Y = 217\text{MPa}$, the peak loads are predicted by (5) as, F_A = 1725N and F_B = 1505N. The lower value compares well with the measured collapse load, $F_{\max}$=1470N. The small discrepancy is attributed both to the strain hardening of the faces, which would serve to elevate the effective σ_y at the limit load, and to the extra load support provided by that portion of the core (on the right side) subject to positive shear. Nevertheless, the quality of the agreement suggests that simple beam theory models of the type given in (5) are able to adequately account for measured limit loads, provided that independent information about the core shear strength is available.

7. Summary

Metallic sandwich panels with tetrahedral truss core panels have been fabricated using a novel method involving deformation-shaping and transient liquid phase bonding. The responses in core shear and panel bending have been measured. The results demonstrate retained load bearing capacity and bending stiffness despite large plastic deformations. This robustness is attributed to the wrought nature of the material fabricated in this manner, as well as the high strain hardening characteristics of the alloy, plus the ductility of the nodes produced by TLP. A model for the core shear response is presented as well as a finite element simulation. These results duplicate the essential features found experimentally. A small (few percent) discrepancy is attributed to incomplete understanding of the stress/strain characteristics of the material state in the truss members.

When combined with the constitutive properties of the face sheet material, the core shear characteristics have been used to predict the limit load for panels in bending by means of simple beam theory solutions. The closeness of the agreement between indicates that simple models are capable of adequately predicting limit loads, given independent information about the core shear strength.

Acknowledgement

We are grateful to DARPA/ONR for the support of this work through research grants; N00014-96-1-1028 (program manager, S. Fishman) and N00014-01-1-0517 (program managers, L. Christodoulou and S. Fishman).

References

1. HexWebTM Honeycomb Attributes and Properties, Publication No. TSB 120, Hexcel Composites, Pleasanton 1999.

2. Fuller, R.B., U.S. Patent No. 2,986,241, 30 May 1961.

3. N. Wicks and J.W. Hutchinson, Int. J. Solids and Structures 2001, 38, 5165.

4. A.G. Evans, J.W. Hutchinson, N.A. Fleck, M.F. Ashby and H.N.G. Wadley, Prog. Mater. Sci. 2001, 46, 309.

5. S. Chiras, D.R. Mumm, A.G. Evans, N. Wicks, J.W. Hutchinson, K. Dharmasena, H.N.G. Wadley and S. Fichter, International Journal of Solids and Structures, 39, 4093-4115 (2002).

6. V.S. Deshpande and N.A. Fleck, Int. J. Solids and Structures 2001, 38, 6275.

7. M.F. Ashby, A.G. Evans, N.A. Fleck, L.J. Gibson, J.W. Hutchinson and H.N.G. Wadley, Metal Foams: A Design Guide, Butterworth-Heinemann, Boston 2000.

8. D.J. Sypeck, H.N.G. Wadley, Advanced Engineering Materials, 2002, 4, (No.10) 759-764.

9. S. Hyun, A.G. Evans, A.M. Karlsson, S. Torquato and A.G. Evans, Int. J. Solids and Structures 2002, in press.

10. H. Bart-Smith, J.W. Hutchinson and A.G. Evans, Int. J. Mechanical Sciences 2001, 43, 1945.

11. J.W. Hutchinson, Advances in Applied Mechanics, ed. C.S. Yih, 1974, 14, 67-144.

Figures

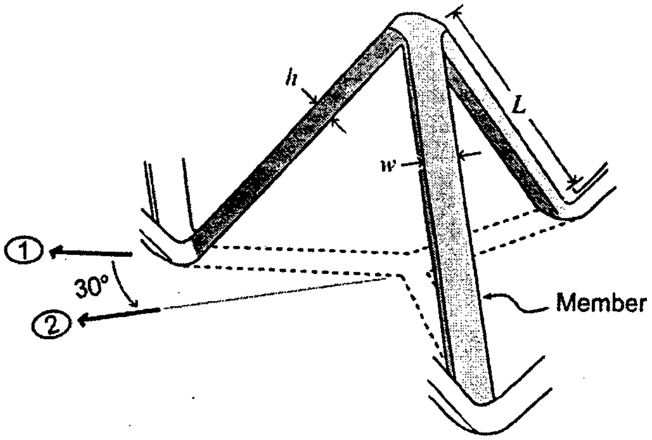

Figure 1. Tetrahedral unit with ligaments having rectangular cross-section.

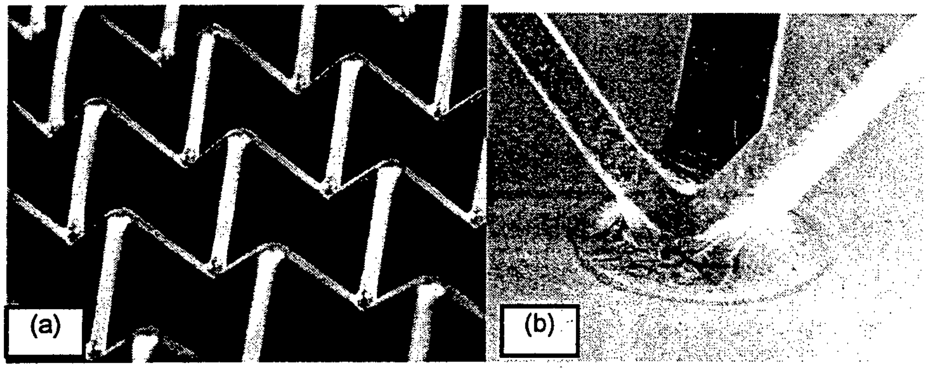

Figure 2. (a) Tetrahedral truss core after shaping. (b) Typical core/face-sheet bond.

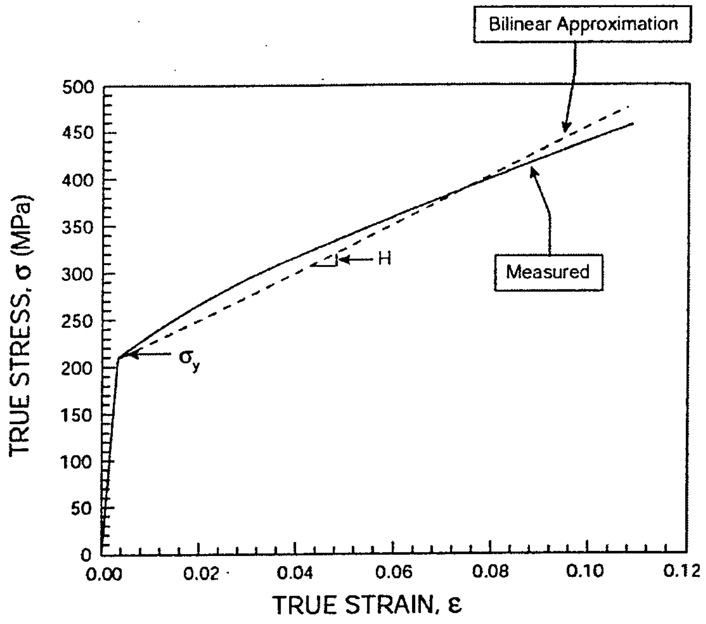

Figure 3. True stress – strain for 304 stainless steel following annealing at 1100 C for 1 hour.

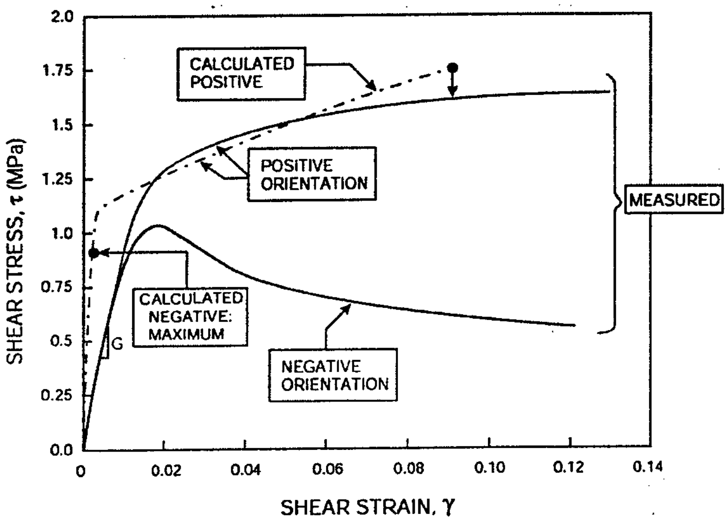

Figure 4. Shear stress/strain response of tetrahedral truss core panels in the negative and positive orientations. Calculated results are shown for comparison.

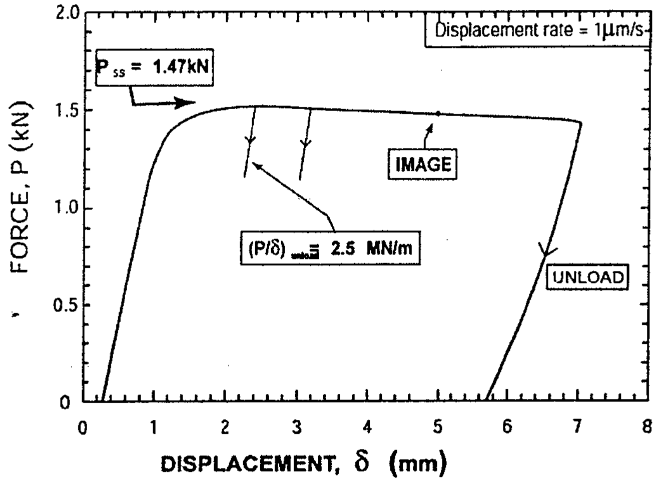

Figure 5. Load-deflection response during panel bending

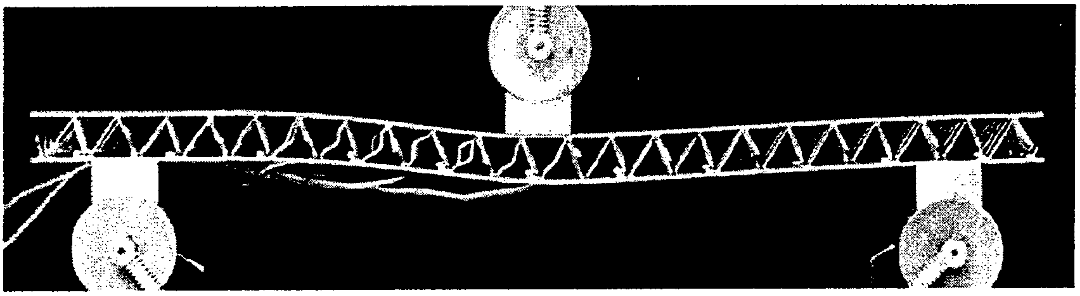

Figure 6. Image of the panel obtained at the displacement indicated on Figure 5. Note the plastic buckling of the compressed truss core members on the left side and the plastic hinge. The span was l = 202 mm and the flat steel indenters were 16.0 mm wide and the overall thickness, H = 22.5mm.

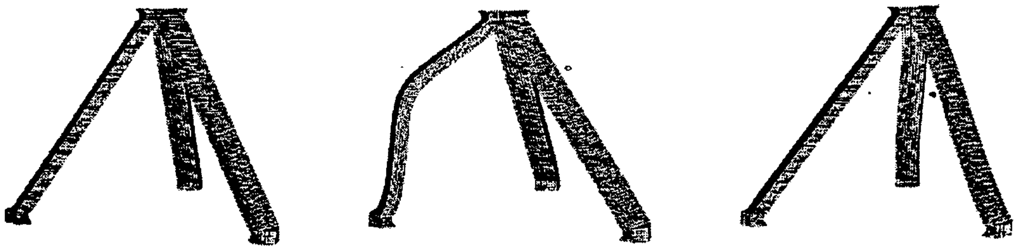

(a) (b) (c)

Figure 7. The finite element model of the truss assembly showing (a) the finite element mesh and the geometry, (b) the deformation after shearing in the negative orientation and (c) the deformation after shearing in the positive orientation.

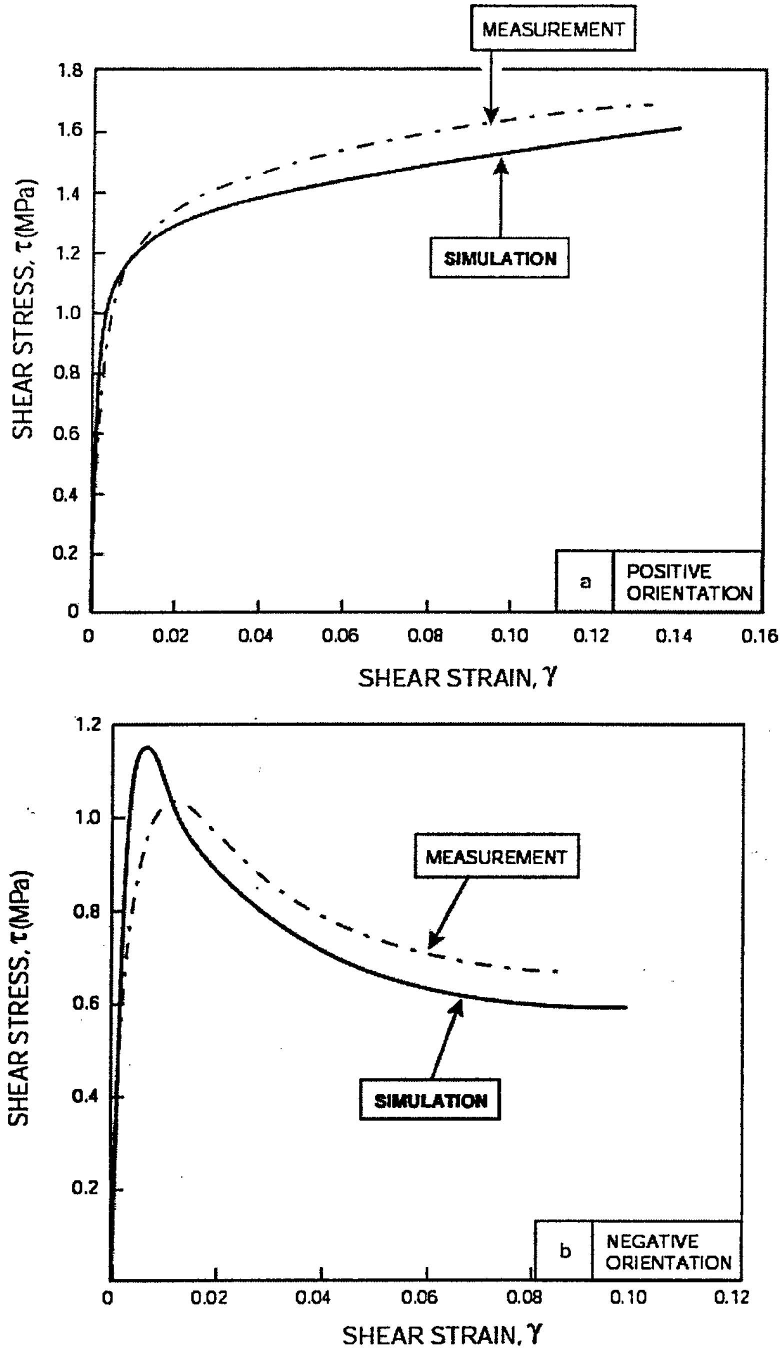

Figure 8. Simulations of the shear stress/strain curves in (a) the negative orientation and (b) the positive orientation. The measurements have been superposed by shifting the elastic strains to match those determined in the simulations.

MINIMUM WEIGHT DESIGN OF A HIGH AUTHORITY FLEXURAL ACTUATOR BASED ON ELECTROELASTOMERS

L.H. Han[*], T. J. Lu[*]
[*]Department of Engineering, University of Cambridge
Trumpington Street, Cambridge CB2 1PZ, UK

A.G. Evans[**]
[**]Materials Department, University of California
Santa Barbara, CA, USA, 93106

NOMENCLATURE

B	Cantilever width
C_0	Permittivity of free space
C_r	Dielectric constant of elastomer film
d	Diameter of spring wire
d_s	Diameter of SMA wire
D	Mean coil diameter of spring
D_0	Outside diameter of spring
E_A	Young's modulus of SMA in austenite phase
E_c	Young's modulus of core material
E_e	Young's modulus of elastomer film
E_f	Young's modulus of facesheet material
E_M	Young's modulus of SMA in martensite phase
F_{cr}	Euler buckling load
f_n	Natural frequency of spring
G	Shear modulus
H	Core thickness
K	Spring constant
K_e	Effective length factor
L	Cantilever length
L_{act}	Length of actuation element
L_{free}	Free length of spring
L_s	Solid length of spring
L_0	Initial length of elastomer film in x direction
ΔL	Actuated length
N	Design Load
N^*	Number of inactive coils
N_a	Number of active coils
$N_{\min}$	Minimum number of active coils
n_{film}	Number of film layers
P	Electric field
$\overline{p}$	Coil pitch
p_e	Effective pressure in the thickness direction
p_e'	Effective pressure in the thickness direction when the film is subject to an external force
S_{es}	Endurance strength of spring wire
S_{ew}	Torsional fatigue strength of spring wire
S_{us}	Ultimate shear strength of spring wire
S_{ut}	Ultimate tensile strength of spring wire
t_c	Thickness of core member
t_e	Thickness of film layers
t_f	Thickness of facesheet
V	Applied voltage

W_{spring}	Weight of spring
W_{core}	Core weight
W_{face}	Facesheet weight
W_{film}	Film weight
z_0	Initial thickness of elastomer film
z	Final thickness of elastomer film
α	Cross sectional area of film layers
β	Corrugation angle
θ	Helix angle of spring
δ_0	Design requirement for tip deflection of cantilever
$\Delta_{\max}$	Maximum compression of spring
$\Delta_{\min}$	Minimum compression of spring
ε_{r0}	Initial remaining strain
ε_T	Actuation strain
ε_{x0}	Pre-strain of film in the x direction
ε_{y0}	Pre-strain of film in the y direction
κ_s	Transverse shear factor
λ	Half-length of corrugation pitch
ϖ	Natural frequency of cantilever
ρ_c	Core density
ρ_f	Facesheet density
ρ_{SMA}	SMA density
ρ_s	Spring wire density
σ_Y^A	Yielding strength of SMA in austenite phase
σ_Y^M	Yielding strength of SMA in martensite phase
τ	Shear stress

Subscript

c	Core
f	Facesheet
e	Elastomer film
y	Yielding strength

ABSTRACT

A flexural actuator based on the operating principles of electro-elastomers has been designed and analyzed. The actuating element comprises multilayers of the electro-elastomer and a helical spring. The variables are the geometrical dimensions and the failure modes. A design that integrates this basic unit into a high authority flexural system has been analyzed. An optimization procedure has been devised and used to determine preferred designs. The analysis establishes the authority (product of end displacement and load to be lifted), at specified electric field by determining the minimum weight as a function of the actuation strain and the number of electro-elastomer layers, n_{film}. The dimensions of the constituents at the minimum weight emerge from the analysis. A comparison with a flexural actuator made using a one-way shape memory alloy reveals the performance advantages of the electro-elastomer system. An assessment of the variation in minimum weight with n_{film} has provided a basis for a future weight/cost trade-off analysis.

Keywords: Optimal design; Actuator; Electroelastomer; Shape Memory Alloy; Minimum weight

1. INTRODUCTION

Recent articles have described high authority flexural actuators designed using structural concepts based on sandwich panels with corrugated cores (Wood et al., 1998; Pelrine et al., 2000; Lu et al., 2001, 2002). The concepts combine the mechanical duality of static determinancy with high bending stiffness. This combination facilitates systems capable of displacing large forces at low overall weight. However, the actuating mechanisms impose performance limitations. Actuators based on shape memory alloys (SMA) and electrostrictive polymers (ESP) have the following limitations.

(i) The SMA actuated system only operates at low frequency and requires large amounts of power (Lu et al., 2001)

(ii) The ESP system has excellent operating characteristics, but there are challenges in manufacturing the requisite number of polymer/electrode multi-layers (Lu et al., 2002).

The present article explores another actuation method, based on electro-elastomers, embodied within the same structural system. Such materials have large specific energy output and strain response, as well as high frequency and energy efficiency. For instance, acrylics (such as VHB^{TM} 3910 from the 3M corp.) have demonstrated an actuation strain over 200%, with actuation stresses up to 7MPa and energy densities exceeding 3kJ/kg (Pelrine et al., 2000). For this material to realize high authority, it must be combined with a mechanical spring, to form an actuation element (Section 2).

In this article, the minimum weight flexural actuator capable of actuation by an electro-elastomer is designed, subject to all failure modes and prototypical constraints on geometry and voltage (Fig. 1). To illustrate the design, one end of the cantilever is clamped while the other is free. More complex bending and hinging modes can be envisaged and will be assessed in a subsequent study. The cantilever of length L is required to flex over a displacement δ_0 while sustaining a load N, which may vary with displacement and frequency. To realize low weight, the passive upper face and core are made from a high strength Al alloy. Multiple actuation elements are distributed between the nodes in the lower surface (Fig. 1). When a voltage is applied, the actuator extends and the tip deflects to the required displacement. When the voltage is cut off, the actuator contracts and the structure recovers its original configuration. The system cycles at a frequency to be determined in the analysis.

The design objective is to minimize the overall weight of the actuation system. To realize this objective, the operations of the actuator must be characterized and the structural responses identified. Aspects of the latter are summarized in the Appendix. Note that the design places the actuator in compression when the load N is imposed (Fig. 1).

2. ELECTROELASTOMER ACTUATORS

The actuation element consists of a pre-compressed helical spring embedded within a concentric multi-layer of pre-stretched electro-elastomer with flexible electrodes (Fig. 2). When a voltage is applied, the actuator expands along its axis. The pre-compression in the spring allows the actuator to elongate while delivering appreciable force. The design embodies the choice of spring (material, diameter and so on) and the number of electro-elastomer layers, subject to voltage constraints. Ultimately, the design is performed in conjunction with that of an actuating system, as discussed in section 3.

For comparison, a one-way SMA actuator with helical springs acting as the pull-back mechanism is also evaluated (Fig. 3). Results of the minimum weight design for both actuators will be discussed in section 4.

2.1 Operating Principle

When a voltage, V, is applied to the electrodes within any segment of the electro-elastomer (Fig. 3), the electrostatic forces cause the film to compress in thickness (z-direction) and expand in area (Pelrine et al., 1998; 2001). The effective pressure, p_e, exerted by the electrodes is:

$$p_e = C_0 C_r P^2 = C_0 C_r \left(\frac{V}{z} \right)^2 \tag{1}$$

where C_r is the dielectric constant of the elastomer; $C_0 = 8.85 \times 10^{-12} F/m$ is the permittivity of free space; P is the electric field; and z is the film thickness. In practice, the film is plastically pre-stretched to enhance the actuator performance and the electrical breakdown strength (Pelrine et al., 2000). If such a film with initial thickness z_0 is pre-strained ε_{x0} in the x direction and ε_{y0} in the y direction, its final thickness will be $z = z_0 / \left[(1+\varepsilon_{x0})(1+\varepsilon_{y0})\right]$. Since the elastomer is incompressible (Poisson's ratio 0.5), the effective longitudinal force is, $F_e = -0.5 p_e \alpha$, where α is the cross sectional area of the film layers. This force causes the actuation element to change its length by ΔL. If there is no external force, the spring is released from point A_0 to B_0 on Fig. 4. The blocking force when a voltage V is applied and the actuator is rigidly constrained is represented by C_0C. The horizontal distance between A_0 and B_0 represents the stroke. If an external force F_N is applied, the work line A_0B_0 displaces to AB.

The equilibrium state of the actuation element without the external force is given by,

$$E_e(\Delta L / L_0)\alpha + F_s = p_e \alpha / 2 \tag{2}$$

where L_0 is the initial length of the film, $F_s(= K\Delta L)$ is the spring force, with K the spring constant. The stroke of the actuation element is,

$$\Delta L = L_{act}\varepsilon_T \tag{3}$$

Here ε_T is the stress-free strain of the actuation element, while $L_{act} = (1+\varepsilon_{x0})L_0$ is the length of the element after the pre-stretch ε_{x0} caused by the spring. From Eq. (2) the actuation strain induced by an electric field P can be described by:

$$\begin{aligned} \varepsilon_T &= \frac{1}{2}\frac{p_e \alpha}{\left(E_e \alpha / L_0 + K\right) L_{act}} \\ &= \frac{1}{2}\frac{C_r C_0}{\left(E_e + K L_0 / \alpha\right)\left(1+\varepsilon_{x0}\right)} P \\ &= \frac{1}{2}\frac{C_r C_0}{\left(E_e + K L_0 / \alpha\right)\left(1+\varepsilon_{x0}\right)}\left(\frac{V}{z}\right)^2 \end{aligned} \tag{4}$$

Note that the cross-sectional area of the layers $\alpha \approx \pi D_0 t_e$, with D_0 the outside diameter of the spring and $t_e = n_{film} z$ the total thickness of the n_{film} layers. The thickness z of an elastomer film upon deformation $\varepsilon_x, \varepsilon_y$ in its planar area is

$$z = \frac{z_0}{(1+\varepsilon_x)(1+\varepsilon_y)} \tag{5}$$

When an external force F_N is applied, the strain ε_x is determined from the equilibrium state of the actuation element ($B'B_0$ in Fig. 4) as:

$$\varepsilon_x = \varepsilon_{x0} - \frac{F_N}{KL_0 + E_e\alpha} \tag{6}$$

Because the film is constrained in the y direction, ε_y is constant, ε_{y0}. To avoid buckling, the spring load must assure that the film is always in tension: $\varepsilon_x \geq 0$.

2.2 Spring Design (Juvinall et al., 1999)

The weight of the spring is given by:

$$W_{Spring} = \left[\frac{\pi^2}{4}\right]\rho_s d^2 D\left[\frac{N_a}{\cos\theta} + N^*\right] \tag{7}$$

where ρ_s is the density of the spring wire, D is the mean diameter of the spring, d is the coil diameter, and θ is the helix angle (the angle between the coils and the base of the spring). Here N_a and N^* are the number of active and inactive coils, respectively. The helix angle θ is related to the coil-pitch $\overline{p}$ (see Fig. 5) by: $\theta = \tan^{-1}(\overline{p}/\pi D)$. A closed-coil requires a small helix angle ($\theta \leq 15^o$), therefore $\cos\theta \approx 1$. For plates in contact with the end of the spring, $N^* = 2$. The number of active springs, N_a, is governed by the spring constant as: $N_a = Gd^4/8D^3K$, with G the shear modulus of the wire, such that, from (7):

$$W_{Spring} \approx \left(\frac{\pi^2}{4}\right)\rho_s d^2 D\left[\frac{Gd^4}{8D^3K} + 2\right] \tag{8}$$

When the actuation strain ε_T is specified, the spring constant K can be determined by Eq. (4): whereupon, D, and d become the variables in the optimization problem.

2.3 Material Selection

High strength steel wires are the preferred material for lightweight springs (Ashby, 1992). Common steel wires have diameters 0.1-6.5mm. The *tensile strength* S_{ut} is a function of wire diameter d:

$$S_{ut} \cong A(d)^b \tag{9a}$$

with $A = 2.2$ GPa and $b = -0.163$ when d is measured in *mm*. The *shear strength* S_{us} is related to the ultimate tensile strength by:

$$S_{us} \cong 0.67 S_{ut} \tag{9b}$$

2.4 Maximum and Minimum Compression

The *maximum* compression of the spring occurs at the clamped end of the actuator. It is given by the sum of initial displacement $\Delta_{init} = L_{free} - L_{act}$ and the compression Δ_a induced by force F_N (due to external load N; point A in Fig. 4):

$$\Delta_{\max} = \Delta_a + \Delta_{init} = L_{free} - L_A \tag{10a}$$

$$\begin{aligned} \Delta_a &= \frac{F_N}{E_e\alpha + KL_0} L_0 \\ &= \frac{NL}{H\left(E_e\alpha + KL_0\right)} L_0 \end{aligned} \tag{10b}$$

$$F_N = \frac{NL}{H} \tag{10c}$$

$$L_{free} = \frac{E_e\alpha\varepsilon_{x0}}{K} + L_{act} \tag{10d}$$

$$L_A = L_{free} - \Delta_{\max} \tag{10e}$$

When an external force is applied, the corresponding *minimum* (point B in Fig.4) is:

$$\Delta_{\min} = L_{free} - L_B \tag{11a}$$

$$\begin{aligned} L_B &= L_A + 0.5\frac{p'_e\alpha}{K + \dfrac{E_e\alpha}{L_0}} \\ &= L_A + 0.5\frac{C_0C_r}{\dfrac{KL_0}{\alpha} + E_e}\left(\frac{V}{z'}\right)^2 L_0 \end{aligned} \tag{11b}$$

$$z' = \frac{z_0}{(1+\varepsilon_{xA})(1+\varepsilon_{yA})} \tag{11c}$$

$$\varepsilon_{xA} = \frac{L_A}{L_0} - 1 \text{ and } \varepsilon_{yA} = \varepsilon_{y0} \tag{11d}$$

The realizable displacements are limited by *spring consolidation.* The usual recommendation is to provide a clash allowance of approximately 10% of the total spring deflection $\Delta_{\max}$ at maximum working load, $\Delta_{solid} - \Delta_{\max} \geq 0.1\Delta_{\max}$, or in non-dimensional form:

$$\frac{\Delta_{\max}}{L} \leq 0.9\left[\frac{L_{free}}{L} - \frac{L_s}{L}\right] \tag{12}$$

where $L_s = d(N_a + 3)$ for closed coil springs.

2.5 Failure Criteria

The limitation imposed by *yielding* of the spring can be expressed in non-dimensional form, as:

$$\frac{\tau_{\max}}{E_f} = 8\kappa_s\left[\frac{K}{\pi E_f L}\right]\frac{\Delta_{\max}}{L}\left(\frac{D}{L}\right)\left(\frac{L}{d}\right)^3 \tag{13}$$

where the transverse shear factor (Wahl, 1963), $\kappa_s = 1 + 0.5d/D$.

Buckling occurs if the ratio of spring displacement to free spring length L_{free} exceeds a critical value Δ_{crit}/L_{free} (Wahl, 1963):

$$c_1\frac{\Delta_{crit}}{L_{free}} = 1 - \sqrt{1-\left(c_2\frac{D}{L_{free}}\xi\right)^2} \tag{14}$$

where, for steel, the constants are $c_1 = (1+2\nu)/(1+\nu) = 1.23$ and $c_2 = \pi\sqrt{(1+2\nu)/(2+\nu)} = 2.62$. The parameter ξ reflects the method of support. If both ends are guided axially, but free to rotate (like a hinged column), then $\xi = 1$. If both ends are guided, and prevented from rotating, then $\xi = 0.5$. Based on the maximum compression $\Delta_{\max}$ (Eq. (10)), the critical free length L_{crit} becomes:

$$L_{free} \le L_{crit} = 0.5c_1\Delta_{\max}\left[1+\left(\frac{c_2 D}{c_1\lambda\Delta_{\max}}\right)^2\right] \tag{15}$$

Accordingly, when both ends of the spring are prevented from rotation, spring buckling will be avoided if

$$L_{free} \le 0.615\Delta_{\max}\left[1+\left(4.5\frac{D}{\Delta_{\max}}\right)^2\right] \tag{16}$$

Torsional fatigue is dictated by the fully reversed endurance limit:

$$S_{es} = 0.5\left[\frac{S_{ew}S_{us}}{S_{us} - 0.5S_{ew}}\right] \tag{17}$$

where S_{ew} is the torsional fatigue strength, and S_{us} is the ultimate shear strength.

Surging must be avoided in high-speed cyclic applications. For this purpose, the natural frequency of the spring should be greater than about 12 times that of the applied forcing frequency f_{an}:

$$f_n \geq 12 f_{an} \tag{18}$$

The fundamental natural frequency is,

$$f_n = \frac{2}{\pi N_a}\left(\frac{d}{D^2}\right)\sqrt{\frac{Gg}{32\rho}} \tag{19}$$

where ρ is the density of the spring material.

A lower limit on the *number of coils* must be imposed in order to obtain accuracy and control in manufacturing. A value of 3 is normally used as an absolute minimum, but a larger value can be selected to assure a small helix angle:

$$N_a = \frac{Gd^4}{8D^3K} \geq N_{\min} > 3 \tag{20}$$

3. DESIGN OF THE ACTUATING SYSTEM

The objective is to design an actuating system capable of realizing a specified performance (authority) at lowest possible overall weight, given by:

$$W = \rho_f LBt_f + \rho_c\left[\frac{L}{\cos\beta}\right]Bt_c + N_m\left(W_{film} + W_{spring}\right) \tag{21}$$

where $W_{film} + W_{spring}$ is the weight of the actuation element (above) and $N_m = (L-\lambda)/2\lambda$ is the total number of elements. The face thickness t_f/L, core member thickness t_c/L, core thickness H/L, number of layers n_{film}, actuation strain ε_T, mean coil diameter D/L and spring wire diameter d/L are the design variables. Failure mechanisms, spring behavior, and geometry constraints are considered.

The objective function in non-dimensional form is:

$$\Psi = \frac{W}{\rho_f BL^2} = w_{face} + w_{core} + w_{film} + w_{spring} \tag{22}$$

where

$$w_{face} = \frac{t_f}{L} \tag{22a}$$

$$w_{core} = \frac{1}{\cos\beta}\frac{\rho_c}{\rho_f}\frac{t_c}{L} \tag{22b}$$

$$w_{film} = 0.5\left(\frac{L}{H}\tan\beta - 1\right)\frac{\rho_e}{\rho_f}\left(\frac{L_{act}}{L}\right)\frac{L}{B}\left\{\pi\left(\frac{D}{L}+\frac{d}{L}\right)\frac{t_e}{L}+\pi\left(\frac{t_e}{L}\right)^2\right\} \tag{22c}$$

$$w_{spring} = 0.5\left(\frac{L}{H}\tan\beta - 1\right)\frac{\pi^2}{4}\frac{\rho_s}{\rho_f}\left(\frac{d}{L}\right)^2\left(\frac{D}{L}\right)\frac{L}{B}\left(\frac{N_a}{\cos\theta}+2\right) \tag{22d}$$

The weight minimization is subject to the following constraints:

Minimum deflection

$$\begin{aligned}1-\left(\frac{1}{2}+\frac{1}{\varepsilon_T}\right)\frac{H}{L}\left(1-\cos\varepsilon_T\frac{L}{H}\right)\frac{\delta_0}{L}+\frac{1}{3}\left[\frac{N}{E_fBL}\right]\frac{B}{L}\left(\frac{E_fL^4}{D_{eq}}\right)\frac{\delta_0}{L}+\\ \frac{\delta_0}{L}\left[\frac{N}{E_fBL}\right]\frac{E_fL^2}{D_q}\leq 0\end{aligned} \tag{23a}$$

Face yielding

$$\frac{B}{L}\left(\frac{L}{t_f}\right)\left(\frac{L}{H}\right)\left[\frac{N}{E_fBL}\right]\frac{E_f}{\sigma_Y^f}-1\leq 0 \tag{23b}$$

Core yielding

$$\frac{1}{\sin\beta}\left[\frac{N}{E_fBL}\right]\frac{E_f}{\sigma_Y^c}\left(\frac{L}{t_c}\right)-1\leq 0 \tag{23c}$$

Core buckling

$$\frac{12}{\pi^2\sin^3\beta}\left[\frac{N}{E_fBL}\right]\frac{E_f}{E_c}\left(\frac{L}{t_c}\right)^3\left(\frac{H}{L}\right)^2\left(\frac{(\pi^2C_A+2)(\pi^2C_B+2)}{(\pi^2C_A+4)(\pi^2C_B+4)}\right)-1\leq 0 \tag{23d}$$

There are multiple constraints for the actuating element:

Minimum number of coils

$$1-\frac{1}{48(1+\nu)}\left[\frac{E_fL}{K}\right]\left(\frac{L}{D}\right)^3\left(\frac{d}{L}\right)^4\frac{E_S}{E_f}\leq 0 \tag{23e}$$

Limits on spring index

$$(D/L)(L/d)/20-1\leq 0 \qquad \text{(Upper)} \tag{23f}$$

$$1-(D/l)(L/d)/4\leq 0 \qquad \text{(Lower)} \tag{23g}$$

Clash allowance

$$\frac{\Delta_{\max}}{L}\leq 0.91\left[\frac{L_{free}}{L}-\frac{d}{L}(N_a+3)\right] \tag{23h}$$

Surging

$$1-\frac{1}{6\pi N_a f_{an}}\frac{d}{D^2}\sqrt{\frac{Gg}{32\rho}}\leq 0 \qquad (23i)$$

Spring compression

$$1-\frac{L_{free}}{(1+\varepsilon_T)L_{act}}\leq 0 \qquad (23j)$$

Structural integrity

$$1-\frac{S_{es}(S_{us}-\tau_i)}{S_{es}(\tau_m-\tau_i)+S_{us}\tau_a}\leq 0 \qquad \text{(fatigue)} \qquad (23k)$$

$$8K_s\left[\frac{K}{\pi E_f L}\right]\left(\frac{\Delta_{\max}}{L}\right)\frac{D}{L}\left(\frac{L}{d}\right)^3\frac{E_f}{S_{ys}}-1\leq 0 \qquad \text{(yielding)} \qquad (23l)$$

$$\left[1+\left[4.26\frac{D}{\Delta_{\max}}\left(\frac{D}{L}\right)\right]^2\right]^{-1}\frac{L_{free}}{L}\left(\frac{L}{\Delta_{\max}}\right)-0.615\leq 0 \qquad \text{(spring buckling)} \qquad (23m)$$

$$1-\frac{L_A}{L}\frac{L}{L_0}\leq 0 \qquad \text{(film buckling)} \qquad (23n)$$

A MatLab program using the method of sequential quadratic programming (SQP) (Matlab, 1998) was implemented to find optimal solutions. Since the objective function has many local optima, an algorithm (Aird and Rice, 1977) based on systematic placement of points was implemented to generate starting points. Owing to manufacturing limitations on size and shape, the design parameters are often restricted to only integer (or discrete) values. For instance, design variables such as the wire diameter, corrugation angle, coil number and layer number are not continuous functions but discrete values. Therefore, finding the optimal design involves discrete programming. The SQP approach remains valid in such situations. Initially, it solves the problem by assuming continuous design variables. Then the discrete/integer values closest to the continuous optimum solutions are assigned and the design checked for feasibility using the backtrack programming method (Farkas, 1984). Through trial and error, the most feasible design closest to the continuous optimum is obtained.

4. OPTIMAL RESULTS

4.1 Optimization Procedure

Actuators made with a high strength aluminum alloy are chosen for the design examples. The material properties used are summarized in Table 1. The design parameters are listed in Table 2. The graphical method for optimization illustrates the design process (Fig. 6). The two examples use the face thickness, t_f / L, and core thickness, H / L, as co-ordinates. All of the parameters governing the actuation element have been fixed [$D / L, d / L$, $n_{film} = 5$, ε_T, $\varepsilon_{x0} = 500\%$ and $\varepsilon_{y0} = 600\%$]. The maps have been constructed for a required end displacement, $\delta_0 / L = 0.05$, and a specified load index, $\Pi = N / \left(E_f BL\right) = 1.33 \times 10^{-7}$. Two different values of the core member thickness have been used. For these cases, core yielding does not occur (it is a function of the external force and core thickness, independent of the two variables H / L and t_f / L used in Fig. 6). All of the parameters related to the actuation element depend only on the core thickness (independent of t_f / L), as indicated by the arrows along the abscissa. For the avoidance of spring yielding, film buckling and clash, the requirement is that the core thickness should *exceed* the indicated values. For these examples, the most stringent among these constraints is that due to clash, which imposes a minimum on H/L. Conversely, for the avoidance of spring buckling the core thickness must *be less than* the indicated value: whereupon, clash and spring buckling place bounds on the allowable core thickness.

Face yielding, deflection and core buckling must also be considered. It is apparent from the figures that the face yield requirement is confined to the lower left and is not a limitation. Limits are posed by the deflection constraint and by buckling of the core members. The curves representing the deflection constraint dictate the lowest allowable face thickness, as indicated on the figures. Core buckling imposes another upper limit on the core thickness. In case (a) involving the thinner core members, this limit supercedes that due to spring buckling, causing the allowable core thickness to be bound by core buckling and clash, as indicated by the permissible (shaded) domain on the figure. For case (b), with the thicker core members, the core buckling constraint displaces to larger levels of core thickness and spring buckling establishes the upper bound on the permissible domain.

It remains to ascertain which part of the permissible domain dictates the design point. This is achieved by superposing contours of constant weight. The most lightweight solution that resides within the permissible domain governs the design point, indicated by A in the figures. The optimum solutions are weight $w = 8.6\,g$, face thickness $t_f = 1.5\ mm$ and core thickness $H = 31.5\ mm$ for Fig. 6a, and weight $w = 8.6\,g$, face thickness $t_f = 1.4\ mm$ and core thickness $H = 25.6\ mm$ for Fig. 6b.

4.2 Design Examples

With Fig. 6 used to illustrate the issues that enter the optimization, a few examples are given to highlight the key considerations affecting the weight, fabrication and operating conditions. There are many different ways of posing the design problem. Here, we start by requiring that the end displacement be fixed at, $\delta_0 / L = 0.05$, and that compact transformers capable of operating at 5kV are available (Emco High Voltage, model Q50). The passive structure is made from a high strength Al alloy (Table 1).

To investigate the effect of actuation strain on the optimum design, three different values, 5%, 10% and 15%, are assigned to the design variable ε_T. The trends in the lowest weight and in the number of film layers n_{film} are plotted on Figs. 7a, b. The dimensions of the passive components, determined at the lowest weight designs are plotted as functions of the force to be lifted on Fig. 8. At actuation strains ε_T>10%, when the loads to be lifted are large, the core thickness remains unchanged (Fig. 8c), because the corrugation angle, $\beta = 54.7^o$, must be maintained. Corresponding results for the spring are summarized on Fig. 9. While the coil diameter is relatively invariant with ε_T, especially at large forces (Fig. 9a), the spring diameter must be increased systematically as ε_T is increased (Fig. 9b). There are associated implications for the spring constant (Fig. 9c). It is emphasized that, for each load to be lifted, there is an explicit design solution (Figs. 7, 8, 9). Accordingly, if the design dictates a range of different loads, the design should be based on the largest and would be sub-optimal for all lower loads. In practical design, it remains to ascertain whether the dimensions satisfy minimum gauge or other fabrication limitations.

Note that increasing the actuation strain causes the face-sheet thickness to decrease (Fig. 8a) and the coil and wire diameters to increase (Figs. 9a,b), resulting in increased spring and decreased face-sheet weight. Consequently, at a fixed end load, there is an optimum actuation strain for the lowest weight. Repeating the analysis with the actuation strain as a design variable (Fig. 10) reveals that $(\varepsilon_{\mathrm{T}})_{\mathrm{optimal}} \approx 10\%$, regardless of the load to be lifted.

The attainable operational frequency (Fig. 11) increases as the load index is increased. Note that an actuator with the optimum actuation strain of about 10% can operate at a higher frequency than the actuator with a larger (15%) actuation strain, because of its lower weight and thicker face-sheet, which together provide a higher bending stiffness (Figs. 7a and 8a).

A major interplay to be addressed in a final optimization is that between weight and cost. The former is governed by the overall weight, described above, and the latter by aspects of the manufacturing related to the number of elastomer layers, n_{film}, needed to realize the weight objective. To assess some aspects of this interplay, the lowest weight is plotted as a function of the number of layers for a fixed end load of $10N$ and actuation strain, $\varepsilon_{\mathrm{T}} = 10\%$ (Fig. 12). For this example, the weight has a minimum when $n_{film} = 5$. This curve, combined with independent information about cost, could be used to elaborate this interplay.

There may be other limits imposed by breakdown, not specifically introduced in this optimization. All such information should be included in further optimization studies.

5. COMPARISON WITH SHAPE MEMORY ALLOY (SMA) ACTUATOR

A comparison is made with a bias spring one-way SMA actuator with similar geometrical configuration (Liang and Roger, 1992; Lu et al., 2001) (Fig. 3). The design of the passive structure remains the same. The SMA wire is resistively heated. When assembled with a helical spring, the recovery force generated by the shape memory alloy compresses the spring. Then, when the wire is cooled, the stress induced in the SMA by the spring is designed to be large enough to enact the reverse transformation, causing the SMA wire to revert back to its initial length.

The design variables are the face-sheet thickness t_f / L, the thickness of the core members t_c / L, the SMA wire diameter d_s / L, the core thickness H / L, the mean coil diameter of spring D / L, the spring wire diameter d / L, the actuation strain ε_T and the remnant strain ε_{r0}. The design parameters are listed in Table 3. Other parameters are the same as those used for the elastomer actuator. The minimum weight as a function of the authority is plotted for both systems subject to the same design requirement, $\delta_o / L = 5\%$ (Fig. 13). Given the similarity in the achievable levels of authority, the choice between these two systems would be based on other considerations, especially power, frequency and cost.

6. CONCLUSION

A flexural actuation system based on the operating principles of electro-elastomers has been analyzed. An actuating element has been emphasized in which the primary variables are the geometrical dimensions and the failure modes. A design that integrates this basic unit into a high authority flexural actuation system has been explored. An optimization procedure has been devised and used to determine preferred designs.

The analysis establishes the authority (product of end displacement and load to be lifted), at specified electric field (5kV), by determining the minimum weight as functions of the actuation strain and the number of electro-elastomer layers. The dimensions of the constituents at the minimum weight emerge from the analysis.

A comparison with a one-way shape memory alloy system reveals that, for the same weight, full advantage can be taken of the power and frequency attributes of the electro-elastomer.

An assessment of the minimum weight against the number of electro-elastomer layers n_{film} provides a basis for a future weight/cost trade-off analysis.

APPENDIX

1. Failure Modes

Three failure modes may occur: face yielding, core yielding, and core buckling. *Face yielding* occurs when tensile stress in the face equals yield strength. To avoid face yielding at the clamped end:

$$\left[\frac{N}{E_f BL}\right]\frac{E_f}{\sigma_Y^f}\left(\frac{B}{L}\right)\frac{L}{t_f}-1\leq 0 \qquad \text{(A1)}$$

where E_f is the Young's modulus. To avoid *core yielding*:

$$\frac{1}{\sin\beta}\left[\frac{N}{E_f BL}\right]\frac{E_f}{\sigma_Y^c}\left(\frac{L}{t_c}\right)-1\leq 0 \qquad \text{(A2)}$$

Beam theory is adopted to study the *buckling of the core* (Weiernicki et al., 1991). The Euler buckling load F_{cr} for the core is:

$$F_{cr}=\frac{\pi^2 E_c I_c}{(k_e L_c)^2} \qquad \text{(A3)}$$

where $E_c I_c$ is the bending stiffness, and k_e is the effective length factor for column buckling, determined from structural steel design practice (Tall, 1974; Weiernicki et al., 1991) as:

$$k_e=\left[\frac{(\pi^2 C_A+2)(\pi^2 C_B+2)}{(\pi^2 C_A+4)(\pi^2 C_B+4)}\right]^{1/2} \qquad \text{(A4)}$$

Here,

$$C_A=\frac{\sin\beta}{12H}\left\{\frac{E_c B t_c^3}{\frac{3(EI)_{act}}{H}\tan\beta+\frac{E_c B t_c^3}{4H}\sin\beta}\right\}=\left\{\frac{3}{\cos\beta}\frac{(EI)_{act}}{E_f L^4}\frac{E_f}{E_c}\frac{L}{B}\left(\frac{L}{t_c}\right)^3+3\right\}^{-1}$$

$$C_B=\left(\frac{E_c I_c}{L_c}\right)\left(\frac{1}{R_B}\right)=\frac{E_c B t_c^3\sin\beta}{12H}\left\{\frac{E_f B t_f^3}{4H}\tan\beta+\frac{E_c B t_c^3}{4H}\sin\beta\right\}^{-1}=\left\{\frac{36}{\cos\beta}\frac{E_f}{E_c}\left(\frac{t_f}{L}\right)^3\left(\frac{L}{t_c}\right)^3+3\right\}^{-1}$$

with

$$R_A = \sum \frac{3E_l I_l}{p_l} = 3\left(\frac{2(EI)_{base}}{2\lambda} + \frac{E_c B t_c^3}{12L_c}\right) = \frac{3(EI)_{act}}{H}\tan\beta + \frac{\sin\beta E_c B t_c^3}{4H}$$

$$R_B = \sum \frac{3E_l I_l}{p_l} = 3\left(\frac{2E_f B t_f^3}{12(2\lambda)} + \frac{E_c B t_c^3}{12L_c}\right) = \frac{E_f B t_f^3}{4H}\tan\beta + \frac{E_c B t_c^3}{4H}\sin\beta$$

In the above expressions, the equivalent stiffness of the actuation element consists of the stiffness of the spring (Wahl, 1963) and the electro-elastomer multi-layer, which can be described as:

$$(EI)_{act} = \frac{\pi E_e}{64}\left[(D+d+2t_e)^4 - (D+d)^4\right] + \frac{L_{free} E_s G d^4}{16N_a D(2G+E_s)} \qquad \text{(A5)}$$

Failure can be avoided if the member stress σ_c arising from the applied force N is less than the critical stress F_{cr}/Bt_c:

$$\frac{12}{\pi^2 \sin^3\beta}\left[\frac{N}{E_f BL}\right]\frac{E_f}{E_c}\left(\frac{L}{t_c}\right)^3\left(\frac{H}{L}\right)^2 k_e^2 - 1 \le 0 \qquad \text{(A6)}$$

To determine the *tip deflection*, the small constraining effect from the core is ignored. The stiffness of the electrodes is also neglected. The length change upon actuation, $\Delta L = \varepsilon_T L$, causes the beam to bend upwards, with a tip deflection δ_1 given by:

$$\frac{\delta_1}{L} = \left(\frac{1}{2} + \frac{1}{\varepsilon_T}\right)\frac{H}{L}\left(1 - \cos\varepsilon_T \frac{L}{H}\right) \qquad \text{(A7)}$$

The tip deflection δ_2 due to external force N applied at the free end is (Allen, 1969)

$$\frac{\delta_2}{L} = \frac{1}{3}\left[\frac{N}{E_f BL}\right]\frac{B}{L}\left[\frac{E_f L^4}{D_{eq}}\right] + \left[\frac{N}{E_f BL}\right]\frac{E_f L^2}{D_q} \qquad \text{(A8)}$$

where D_{eq} and D_q are the equivalent flexural and transverse shear stiffness of the actuator, respectively: D_{eq} can be derived from simple beam theory (Zenkert, 1995):

$$D_{eq} = \left(E_e \alpha(1+\varepsilon_0) + KL_{act}\right)\left(\frac{H}{2} + e\right)^2 + \frac{1}{3}E_f B\left\{\left(\frac{H}{2} - e + t_f\right)^3 - \left(\frac{H}{2} - e\right)^3\right\}$$

where

$$e = \frac{1}{2}\frac{E_f B t_f (H + t_f) - (E_e \alpha(1+\varepsilon_0) + KL_{act})H}{E_e \alpha(1+\varepsilon_0) + KL_{act} + E_f B t_f}$$

is the distance between the neutral axis of the actuation element and the center of core, D_q can be described as (Lu et al., 2001):

$$D_q = E_c B d_c \sin^2\beta\cos\beta$$

Based on the overall deflection $\delta = \delta_1 - \delta_2$, the deflection constraint for the actuator is given by

$$\delta_f = \delta_1 - \delta_2 \geq \delta_0 \tag{A9}$$

where δ_0 represents the minimum deflection that the actuator must attain to satisfy design objectives.

2. ***Natural Frequency***

For a cantilever fixed at one end, the resonance frequency in bending is (Young, 1989):

$$\varpi = \frac{k^2}{2\pi L^2}\left(\frac{D_{eq}}{m}\right)^2 \tag{A10}$$

where $k = 1.875$ for the first mode and 4.69 for the second mode, D_{eq} is the equivalent bending stiffness of the cantilever, and $m = W / L$ is the mass per unit length.

Acknowledgements

This work is supported by the DARPA MURI project on multifunctional materials.

References

Aird T.J., and J.R. Rice, 1977. Systematic search in high dimensional sets, SIAM Journal on Numerical Analysis, 14, 296-312.

Allen H.G., 1969. Analysis and Design of Structural Sandwich Panels. Pergamon Press, Oxford.

Ashby M.F., 1992. Materials Selection in Mechanical Design. Pergamon Press, Oxford.

Farkas J., 1984. Optimum Design of Metal Structures. Ellis Horwood Ltd., Chichester

Juvinall R.C. and Marshek K.M., 1999. Fundamentals of Machine Component Design. Wiley, New York.

Lu T.J., Hutchinson J.W. and Evans A.G., 2001. Optimal design of a flexural actuator, J. Mech. Phys. Soilds, 49, 2071-2093.

Lu T.J. and Evans, A.G., 2002. Design of a high authority flexural actuator using an electrostrictive polymer, Sensors and Actuators, A 99, 290-296.

Liang C. and Rogers C.A, 1992. Design of shape memory alloy actuators, J. Mechanical Design, 114, 223-230.

Matlab 5. 1998, Mathworks Inc.

Pelrine R.E., Kornbluh R. and Joseph J.P., 1998. Electrostriction of polymer dielectrics with compliant electrodes as a means of actuation, Sensors and Actuators, A 64, 77-85.

Pelrine R., Kornbluh R., Pei Q. and Joseph J., 2000. High-speed electrically actuated elastomers with strain greater than 100%, Science, 287, 836-839.

Pelrine R., Sommer-Larsen P., Kornbluh R., Heydt R., Kofod G., Pei Q and Gravesen P., 2001. Applications of dielectric elastomer actuators, In: Smart Structures and Materials 2001: Electroactive Polymers and Devices, Proceedings of SPIE 4329, 335-349.

Tall L., 1974. Structural Steel Design (2nd Ed.). The Ronald Press Co., New York.

Wahl A.W., 1963. Mechanical Springs (2nd Ed.). McGraw-Hill Inc, New York.

Weiernicki C.J., Liem P.E., Woods G.D. and Furio A.J., 1991. Structural analysis methods for lightweight metallic corrugated core sandwich panels subjected to blast loads, Naval Engineering J. 103, 192-203.

Wood D., Burdess J.S. and Harris A.J., 1998. Actuators and their mechanisms in microengineering, IEEE Engineering Science and Education Journal 7(1), 19-27.

Young W.C., 1989. Roarks Formulas for Stress and Strain. McGraw -Hill, New York.

Zenkert D., 1995. An Introduction to Sandwich Construction. Warley, West Midlands.

Table1 Material parameters used in the example study

Material	Young's Modulus $E(GPa)$	Yield Strength $\sigma_Y(MPa)$	Density $\rho(Kg/m^3)$
Aluminum Alloy 2014-T6	75	400	2790
VHB4910 Tape	3.10^{-3}	----	960
Polymer	2	40	1300
Music wire A228	210	-----	7800

Table 2 Design parameters used in the example study

Width B (m)	0.01
Length L (m)	0.1
Corrugation angle (β)	$\tan^{-1}\sqrt{2}=54.7^{\circ}$
Minimum size of music wire (mm)	0.1
Minimum deflection δ_0 / L	5%
Pre-strain in x direction ε_{x0}	500%
Pre-strain in y direction ε_{y0}	600%
Applied voltage (kV)	5
Initial thickness of 3M VHB4910 tape (z_0) (mm)	1

Table 3 Design parameters of the SMA actuator

$E_A = 90\text{GPa}$	$E_M = 30\text{GPa}$
$\sigma_Y^A = 300MPa$	$\sigma_Y^M = 100MPa$
$\rho_{SMA} = 6500 kg/m^3$	$\varepsilon_{\max} = 6.7\%$

LIST OF FIGURES

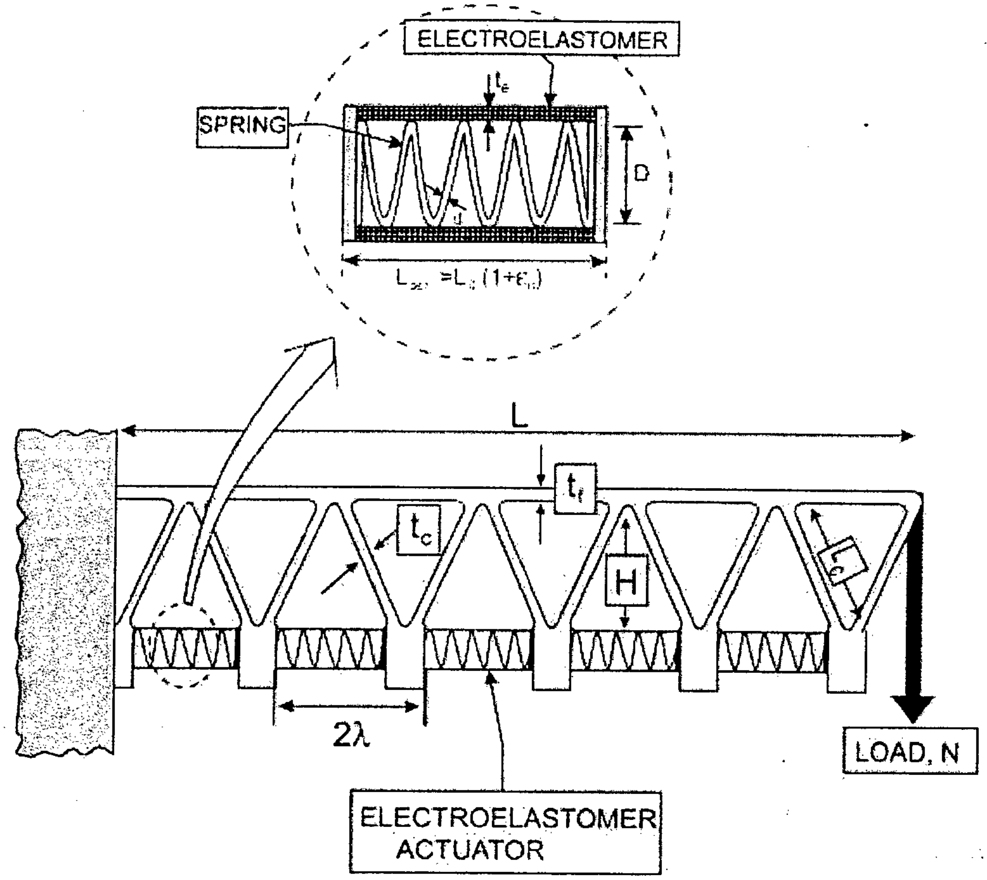
ELECTROELASTOMER
t_e
SPRING
D
d
$L = L (1+\epsilon)$
L
t_f
t_c
H
L_c
2λ
LOAD, N
ELECTROELASTOMER ACTUATOR

Figure 1

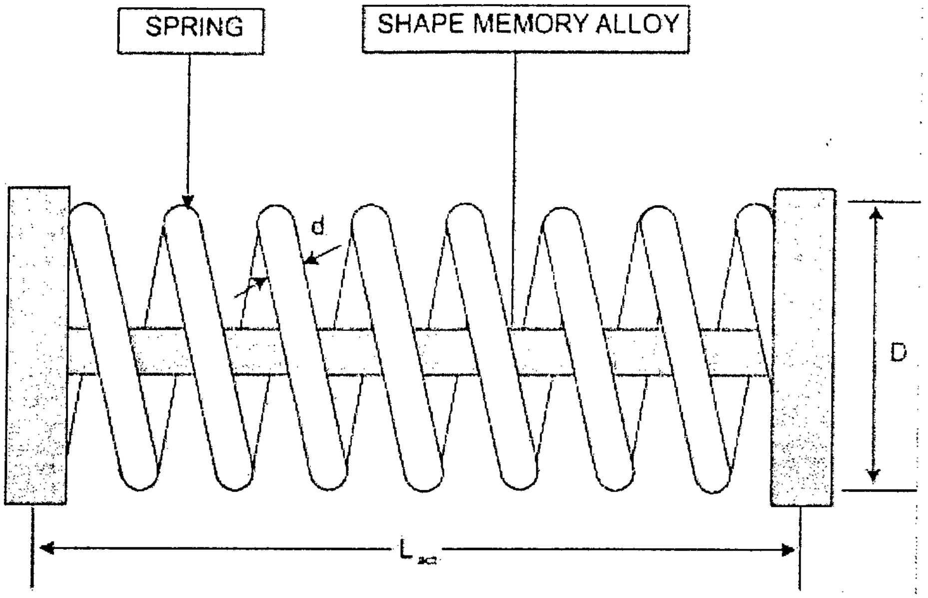

Figure 2

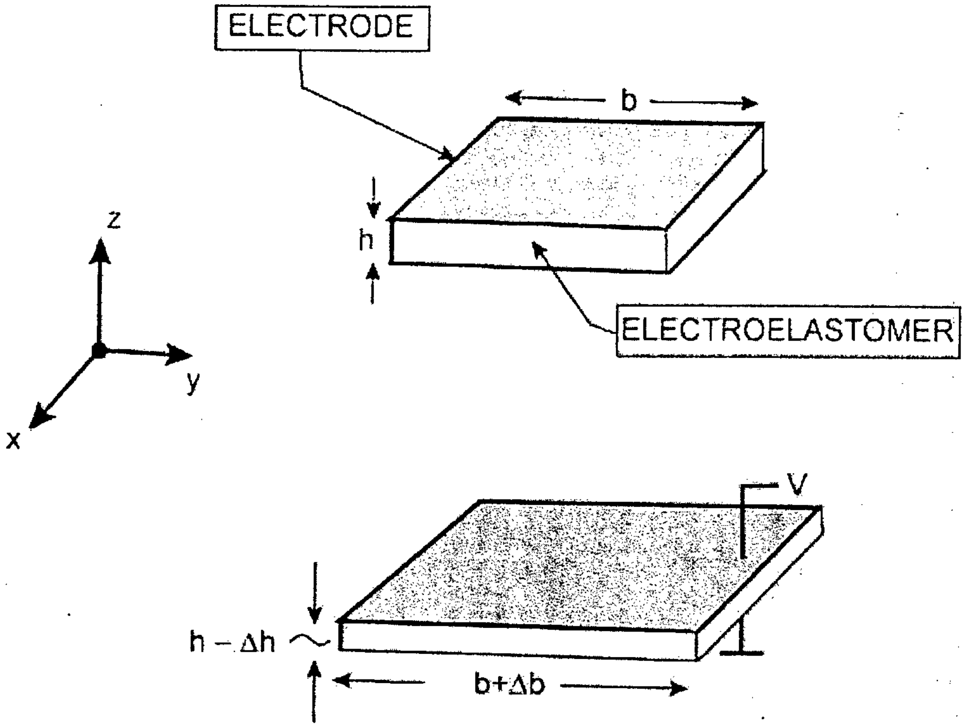

$$\boxed{\varepsilon_{zz} = -\Delta h/h, \ \varepsilon_{xx} = \varepsilon_{yy} = \Delta b/b = \varepsilon_{zz}/2}$$

Figure 3

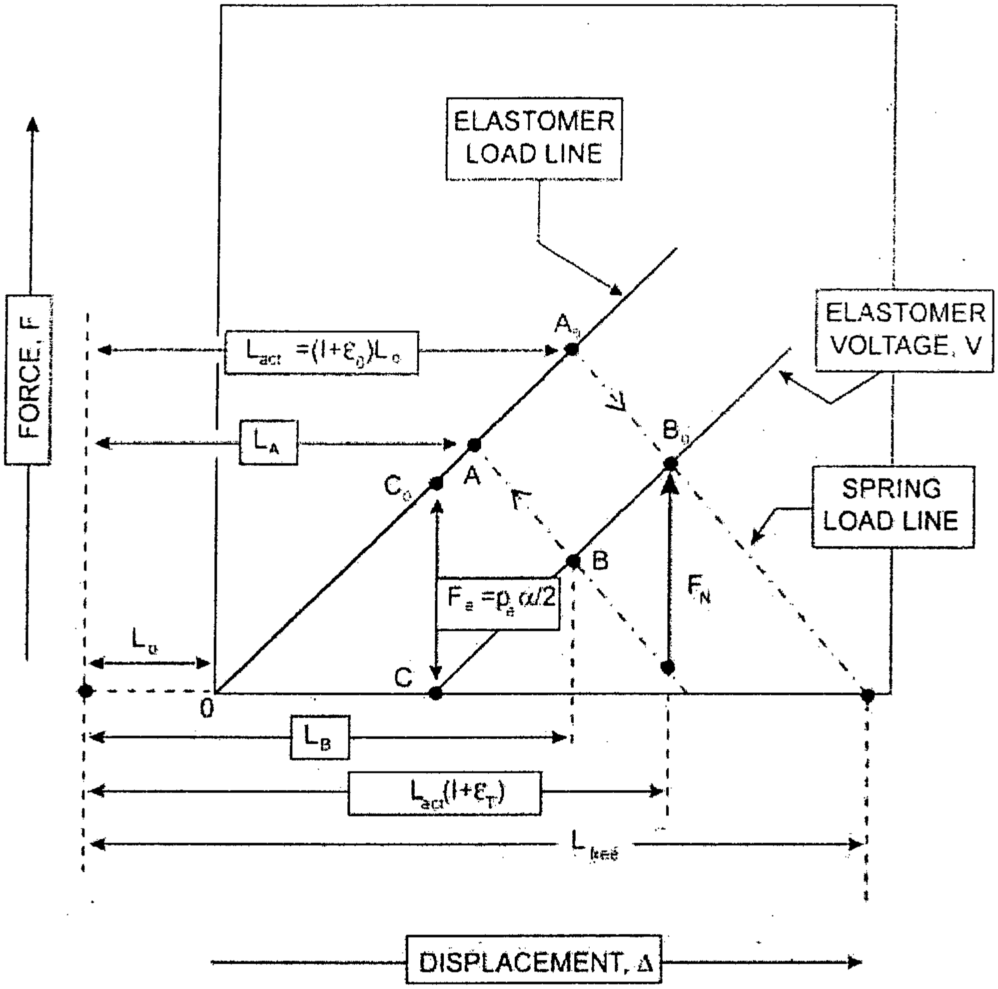

ELASTOMER LOAD LINE
ELASTOMER VOLTAGE, V
SPRING LOAD LINE
FORCE, F
$L_{act} = (1+\varepsilon_0)L_o$
L_A
A_0
A
B_0
B
C_0
C
$F_a = p_a\alpha/2$
F_N
L_o
0
L_B
$L_{act}(1+\varepsilon_T)$
L_{free}
DISPLACEMENT, Δ

Figure 4

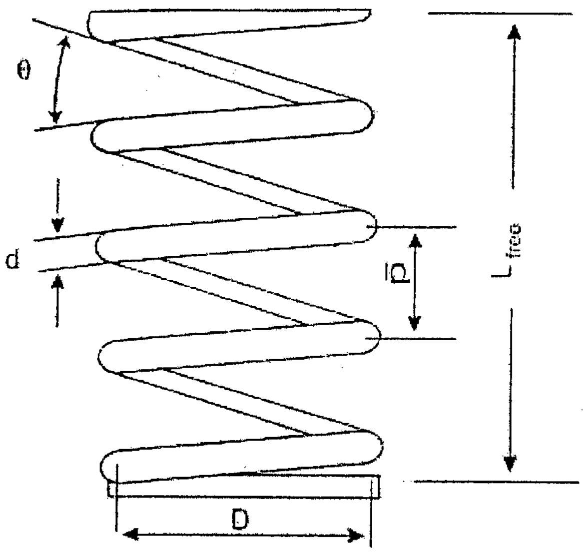

Figure 5

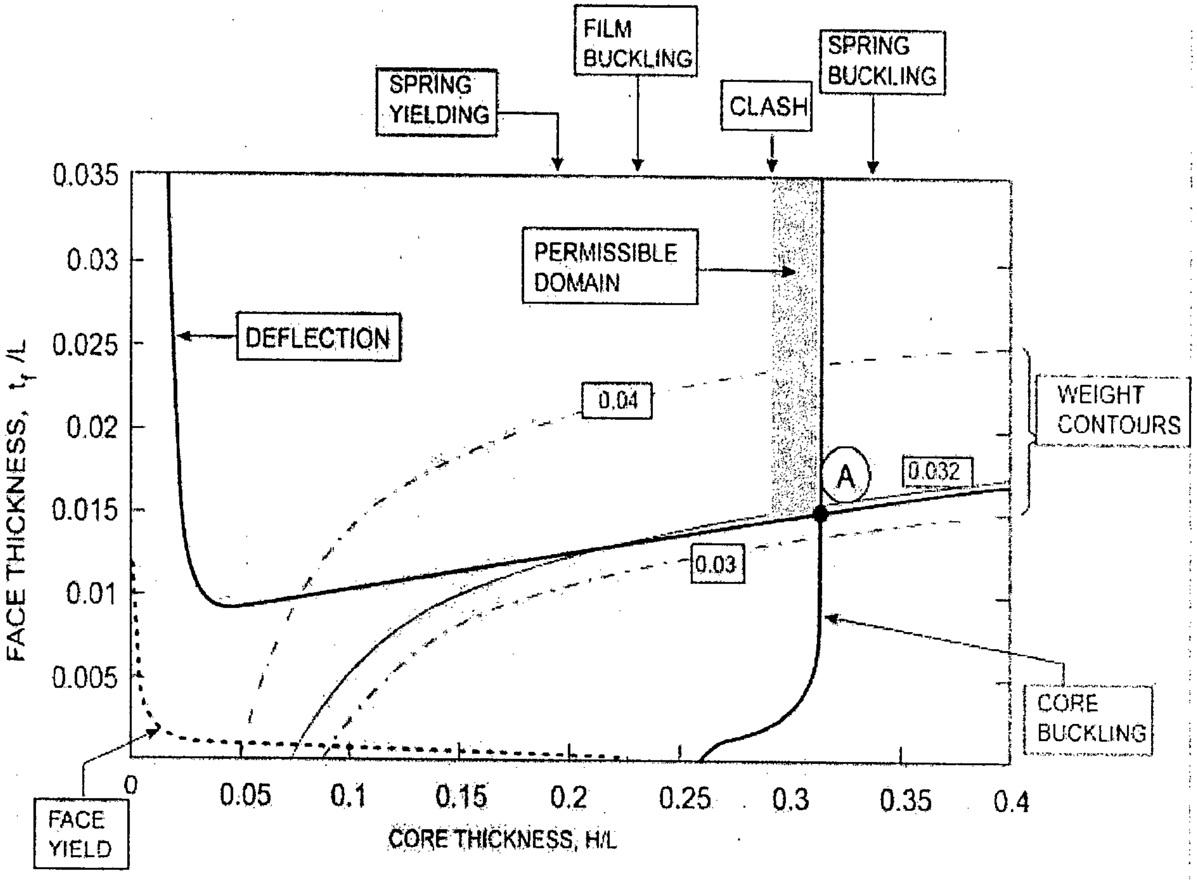

SPRING YIELDING
FILM BUCKLING
CLASH
SPRING BUCKLING
PERMISSIBLE DOMAIN
DEFLECTION
0.04
WEIGHT CONTOURS
A
0.032
0.03
CORE BUCKLING
FACE YIELD
FACE THICKNESS, t_f /L
0.035
0.03
0.025
0.02
0.015
0.01
0.005
0
0.05
0.1
0.15
0.2
0.25
0.3
0.35
0.4
CORE THICKNESS, H/L

Figure 6a

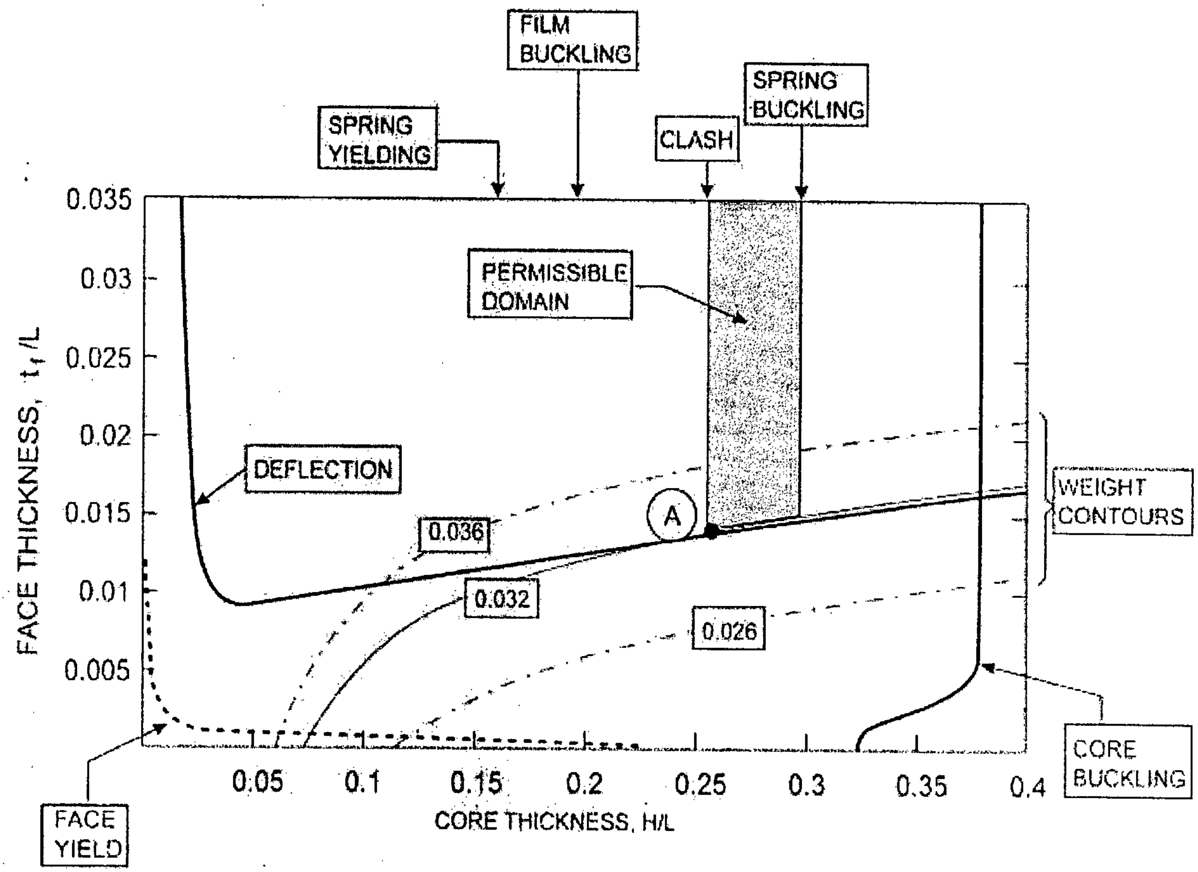
FILM BUCKLING
SPRING YIELDING
CLASH
SPRING BUCKLING
PERMISSIBLE DOMAIN
DEFLECTION
0.036
0.032
0.026
A
WEIGHT CONTOURS
CORE BUCKLING
FACE YIELD
FACE THICKNESS, t_f/L
0.035
0.03
0.025
0.02
0.015
0.01
0.005
0.05
0.1
0.15
0.2
0.25
0.3
0.35
0.4
CORE THICKNESS, H/L

Figure 6b

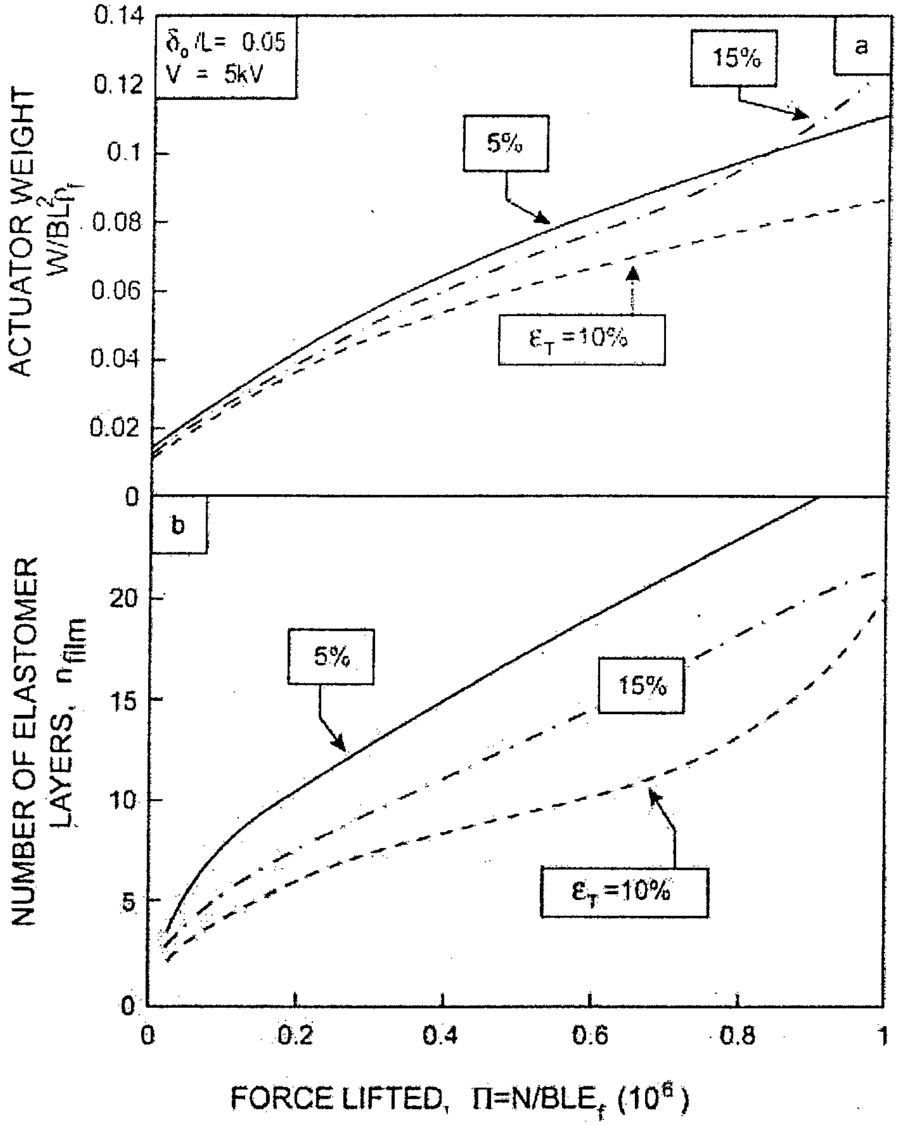

a
b
δo /L= 0.05
V = 5kV
ACTUATOR WEIGHT
W/BL²ρf
0.14
0.12
0.1
0.08
0.06
0.04
0.02
0
5%
15%
εT =10%
NUMBER OF ELASTOMER LAYERS, nfilm
20
15
10
5
0
0.2
0.4
0.6
0.8
1
FORCE LIFTED, Π=N/BLEf (10⁶)

Figure 7

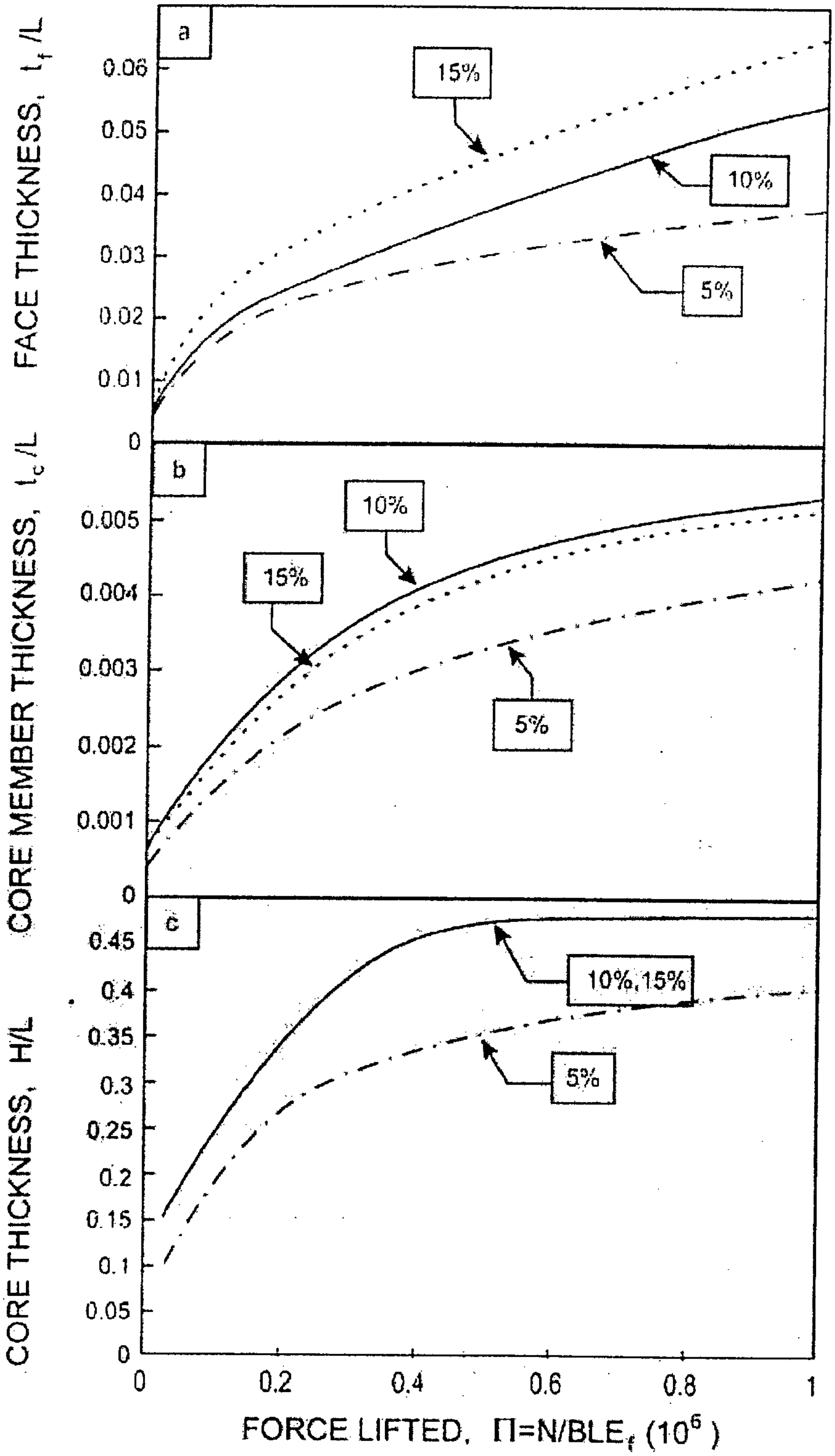
FACE THICKNESS, t_f /L
a
15%
10%
5%
0.06
0.05
0.04
0.03
0.02
0.01
0
CORE MEMBER THICKNESS, t_c /L
b
10%
15%
5%
0.005
0.004
0.003
0.002
0.001
0
CORE THICKNESS, H/L
c
10%,15%
5%
0.45
0.4
0.35
0.3
0.25
0.2
0.15
0.1
0.05
0
0
0.2
0.4
0.6
0.8
1
FORCE LIFTED, $\Pi = N/BLE_f\ (10^6)$

Figure 8

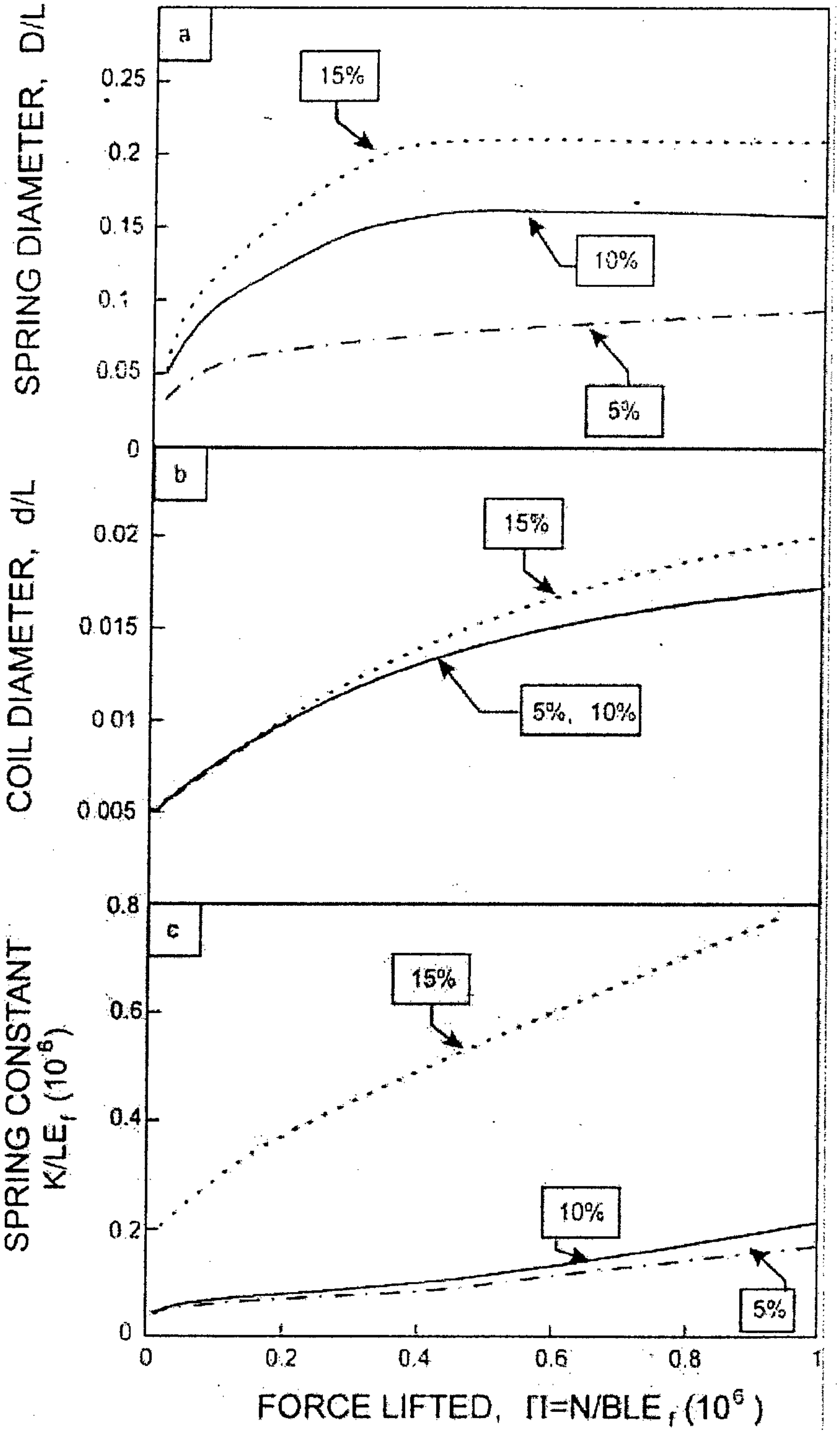

a
SPRING DIAMETER, D/L
0.25
0.2
0.15
0.1
0.05
0
15%
10%
5%
b
COIL DIAMETER, d/L
0.02
0.015
0.01
0.005
15%
5%, 10%
c
SPRING CONSTANT
K/LE$_f$ (10^{-6})
0.8
0.6
0.4
0.2
0
15%
10%
5%
0
0.2
0.4
0.6
0.8
1
FORCE LIFTED, Π=N/BLE$_f$ (10^6)

Figure 9

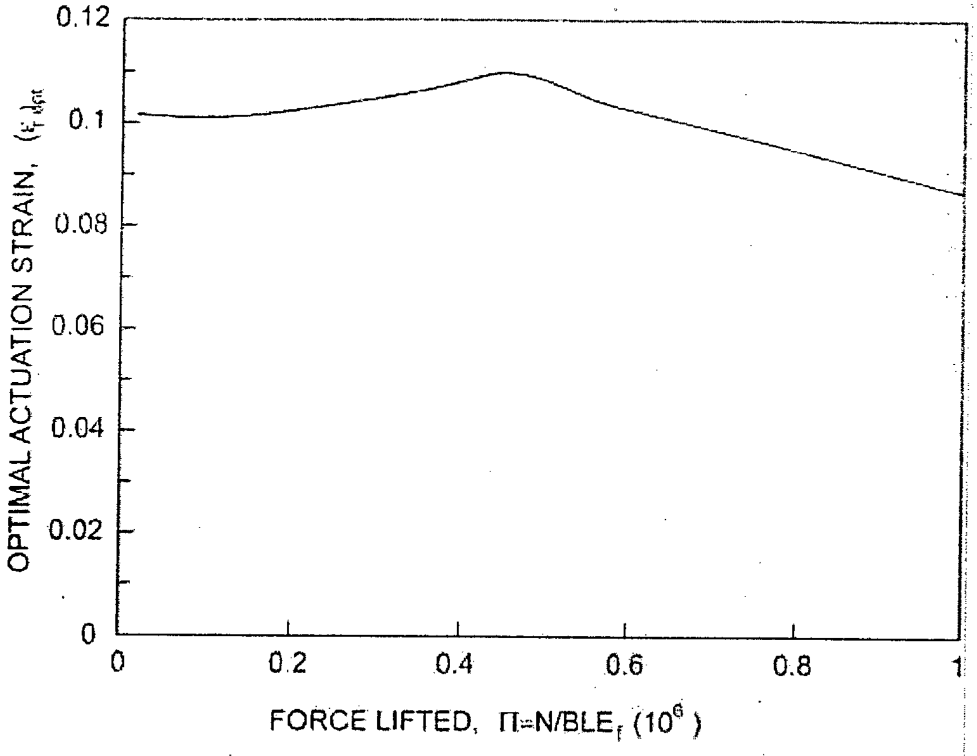
0.12
0.1
0.08
0.06
0.04
0.02
0
0
0.2
0.4
0.6
0.8
1
OPTIMAL ACTUATION STRAIN, $(\varepsilon_f)_{opt}$
FORCE LIFTED, $\Pi = N/BLE_f$ (10^6)

Figure 10

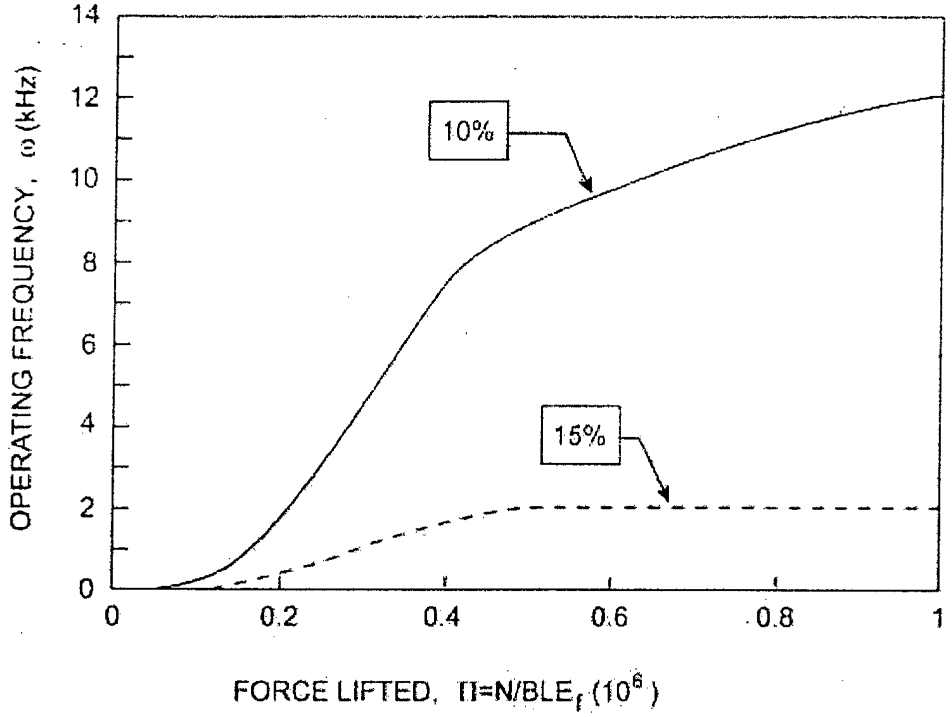

14
12
10
8
6
4
2
0
0
0.2
0.4
0.6
0.8
1
OPERATING FREQUENCY, ω (kHz)
FORCE LIFTED, Π=N/BLE$_f$ (10^6)
10%
15%

Figure 11

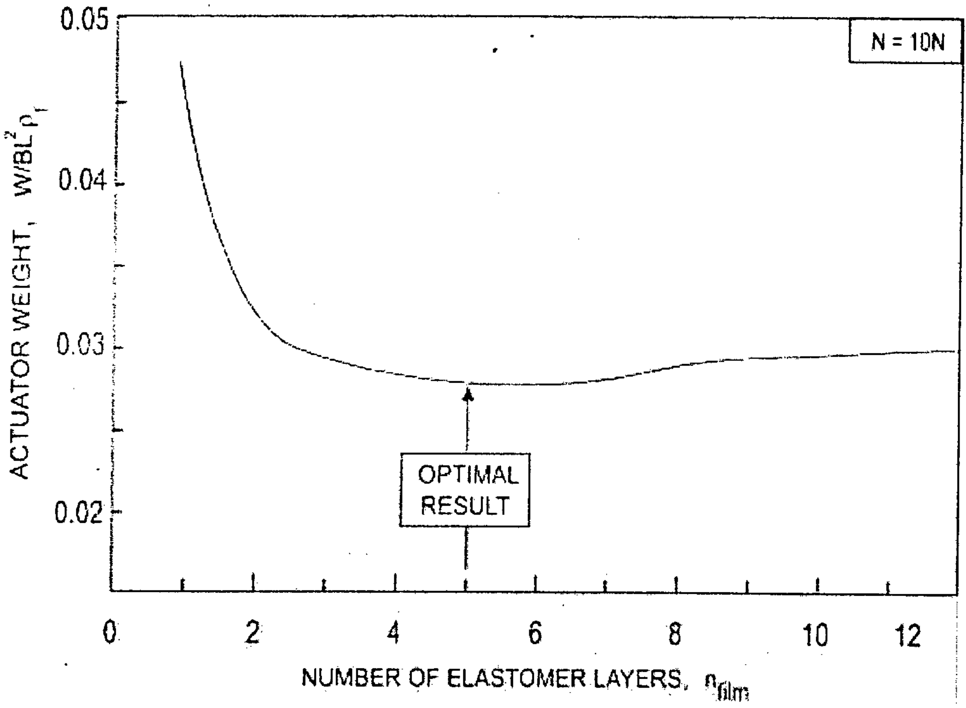
0.05
0.04
0.03
0.02
ACTUATOR WEIGHT, $W/BL^2\rho_f$
N = 10N
OPTIMAL RESULT
0
2
4
6
8
10
12
NUMBER OF ELASTOMER LAYERS, n_{film}

Figure 12

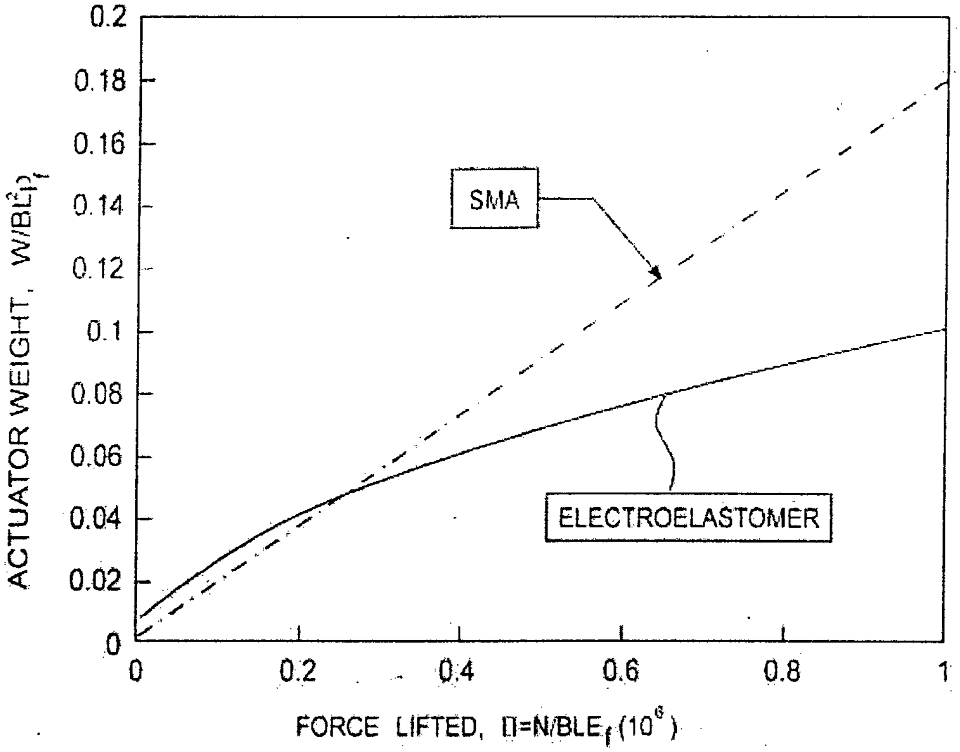

0.2
0.18
0.16
0.14
0.12
0.1
0.08
0.06
0.04
0.02
0
ACTUATOR WEIGHT, $W/BL^2\rho_f$
SMA
ELECTROELASTOMER
0
0.2
0.4
0.6
0.8
1
FORCE LIFTED, $\Pi = N/BLE_f\,(10^6)$

Figure 13

PERGAMON

International Journal of Solids and Structures 38 (2001) 5165–5183

INTERNATIONAL JOURNAL OF SOLIDS and STRUCTURES

www.elsevier.com/locate/ijsolstr

Optimal truss plates

Nathan Wicks, John W. Hutchinson *

Division of Engineering and Applied Sciences, 315, Pierce Hall, Harvard University, 29 Oxford Street, Cambridge, MA 02138, USA

Received 23 March 2000; in revised form 3 August 2000

Abstract

Sandwich plates comprised of truss cores faced with either planar trusses or solid sheets are optimally designed for minimum weight subject to prescribed combinations of bending and transverse shear loads. Motivated by recent advances in manufacturing possibilities, attention is focussed on plates with truss elements and faces made from a single material. The optimized plates are compared with similarly optimized honeycomb core sandwich plates fashioned from the same material. Sandwich plates with solid sheet faces and truss cores are highly efficient from a weight standpoint. These are also studied for their performance as compression panels. Optimized compression panels of this construction compare favorably with the most efficient stringer stiffened plates. © 2001 Elsevier Science Ltd. All rights reserved.

Keywords: Truss plates; Octet truss; Optimal design

---

1. Introduction

Recent developments in the manufacturing of truss structures appear to greatly extend their application possibilities. New efficient casting-based procedures have been devised which permit entire truss structure components to be produced at scales ranging from millimeters to tens of centimeters. Two examples are shown in Fig. 1. Electro-deposition has been used to form truss structures at an even smaller scales with elements whose diameters can be as small as fifty microns (Brittain et al., 2000). Efforts are underway to determine the stiffness of truss structures and to assess their strength, both experimentally and theoretically (Wallach and Gibson, 2000).

Well designed structures using truss elements can be highly efficient from a weight standpoint, as will be established for plates in this paper. They have additional potential by virtue of their open structure for multi-functional applications. For example, sandwich plates with solid skins and truss cores can serve as a heat transfer elements simultaneously carrying loads. The cavity between the skins could be used for storage of a liquid or pressurized gas in other applications. Honeycomb core sandwiches or conventional stringer stiffened construction does not facilitate either of these dual purposes.

---

[*] Corresponding author. Tel.: +1-617-495-2848; fax: +1-617-495-9837.
E-mail address: hutchinson@husm.harvard.edu (J.W. Hutchinson).

PII: S0020-7683(00)00315-2

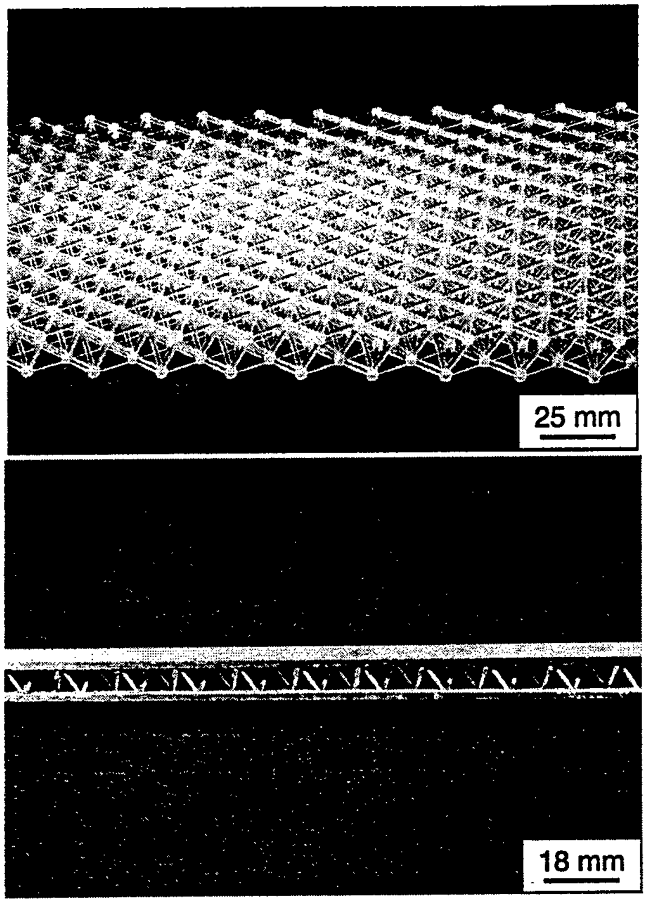

Fig. 1. Sandwich plates. Octet truss plate whose members are identical (top) and sandwich plate with truss core (bottom).

The two types of plate structures considered in this paper are shown in Fig. 2. One has triangulated planar truss faces, while the other has solid sheet faces. Each has a truss core with 120° in-plane symmetry. The plates are uniform (untapered). The length of the members in the core is L_c and the core thickness is H_c. The angle between the core members and the faces is $\varphi_c = \sin^{-1}(H_c/L_c)$. In the present study, only solid circular members will be considered, and the core member radius is R_c. For the plates with truss faces (Fig. 2a), the length and radius of the solid circular face members are denoted by L_f and R_f where,

$$L_f = \sqrt{3(L_c^2 - H_c^2)}. \tag{1}$$

The thickness of the solid isotropic sheets comprising the faces of the sandwich plates in Fig. 2b is denoted by t_f. The 120° symmetry of the plates ensures that their bending and in-plane stretching stiffnesses are isotropic.

While more efficient designs might make use of distinct materials for the core and faces, here we will limit the possibilities by taking a common material for all truss members and face sheets. The Young's modulus, Poisson's ratio, uniaxial yield strength and weight density of the material are denoted by E, ν, σ_Y and ρ, respectively. The designs will account for buckling and plastic yielding of the faces and core members. Optimal designs will be sought, wherein the weight is minimized subject to the failure constraints for

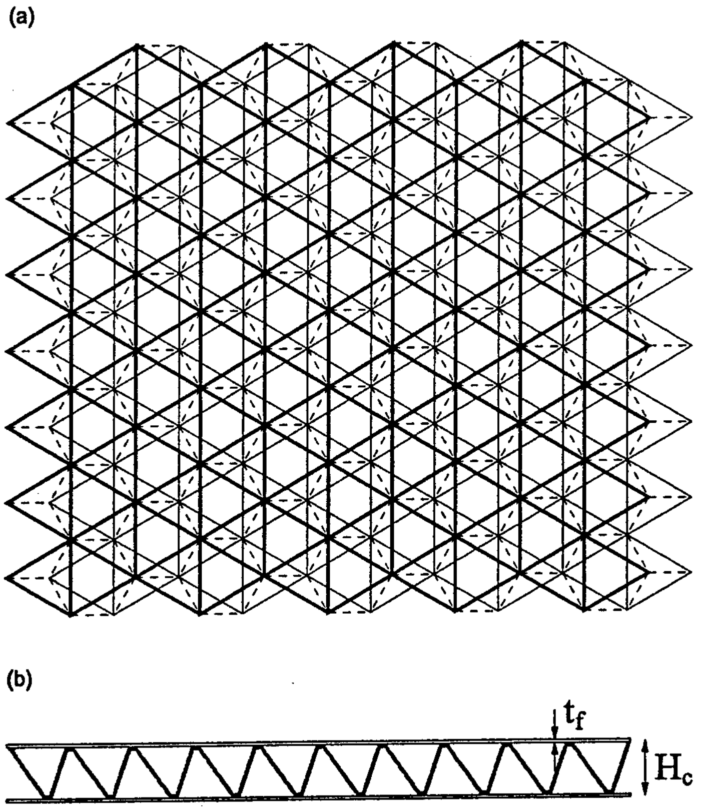

Fig. 2. Plate structures with truss cores. (a) Plates with planar truss faces. The darker members are top face members, the lighter solid members the bottom face members, and the dashed members the core members. (b) Plates with solid sheet faces.

specified combinations of bending moment and transverse shear force. In addition, optimal design of the plates as compression panels will be considered. The weight per unit area of the plate with truss faces is

$$W = 2\sqrt{3}\pi\rho\left[2\frac{R_f^2}{L_f} + \frac{L_c R_c^2}{L_f^2}\right], \tag{2}$$

and that of the plate with solid sheet faces is

$$W = 2\rho\left[t_f + \frac{\pi}{\sqrt{3}}\frac{L_c R_c^2}{L_c^2 - H_c^2}\right]. \tag{3}$$

2. Plates with truss cores and truss faces subject to bending and transverse shear

The general situation envisioned for the design problem is that the uniform, infinitely wide plate must carry a maximum moment per unit length M and a maximum transverse shear force per unit length V. Bending occurs only about the direction parallel to the loading line. A wide plate under three-point loading, with force per unit length, $2P$, at the center is a prototypical example. Each half of the plate carries a uniform transverse shear load per length, $V = P$, and a maximum moment per length, $M = P\ell$, at the center, where ℓ is the half-length of the plate. In this example, the maximum moment and the maximum shear transverse force are attained at the same point, but that is not essential nor to be expected. In the general situation, the ratio of the maximum moment to the maximum transverse force (both per unit length),

$$\ell \equiv \frac{M}{V}, \tag{4}$$

defines a quantity with dimensions of length which will be central in the analysis. The study is limited to relatively thin plates in the sense that the thickness, H_c, is assumed to be small compared to ℓ. Thus, L_c/ℓ and L_f/ℓ will also be small.

An essential step in the optimization process is the determination of the maximum member forces in terms of maximum moment and maximum shear force. To facilitate the analysis, the truss joints are idealized as pin joints offering no rotational resistance from member to member or to the faces. The member forces are expected to be given fairly accurately by this idealization, which is widely used in truss analysis. However, the buckling resistance of the truss will be underestimated, thereby overestimating the weight of the optimal structure. Implications of the assumption of pinned joints will be discussed later in the paper.

The truss plate of Fig. 2(a) is not statically determinant: for each repeating unit of the structure there are three more unknown member forces than joint equilibrium equations. Nevertheless, simple expressions for member forces can be obtained from equilibrium considerations alone for certain load orientations. For the load orientation parallel to A–A' in Fig. 3, the deformation involves bending about a single direction (A–A'), assuming appropriate constraint at infinity in the transverse direction. The members in the faces parallel to the load line undergo no straining and their forces are zero. The remaining member forces can be obtained

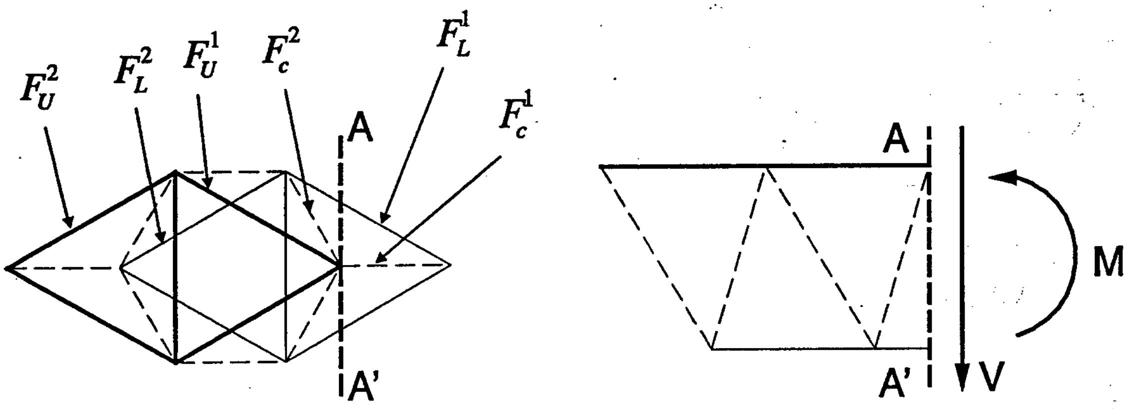

$$F_c^1 = -VL_f\left(\frac{L_c}{H_c}\right) \qquad F_c^2 = \frac{VL_f}{2}\left(\frac{L_c}{H_c}\right)$$

$$F_U^1 = \frac{ML_f}{\sqrt{3}}\left(\frac{1+\left(\frac{L_f}{l}\right)\frac{1}{2\sqrt{3}}}{H_c}\right) \qquad F_U^2 = \frac{ML_f}{\sqrt{3}}\left(\frac{1+\left(\frac{L_f}{l}\right)\frac{2}{\sqrt{3}}}{H_c}\right)$$

$$F_L^1 = -\frac{ML_f}{\sqrt{3}H_c} \qquad F_L^2 = -\frac{ML_f}{\sqrt{3}}\left(\frac{1+\left(\frac{L_f}{l}\right)\frac{\sqrt{3}}{2}}{H_c}\right)$$

Fig. 3. Nonzero member forces in the truss plate at section A–A'. The load line is parallel to A–A', and the members which are parallel to A–A' carry zero force.

from the method of sections. Consider a typical section A–A' shown in Fig. 3, where the moment per unit length and transverse force per unit length carried by the plate at that section are M and V. The members with nonzero forces are labeled in Fig. 3. The method of sections gives the member forces neighboring A–A', as detailed in Fig. 3. The forces in the core members are

$$F_c^1 = -VL_f\left(\frac{L_c}{H_c}\right), \qquad F_c^2 = \frac{VL_f}{2}\left(\frac{L_c}{H_c}\right). \tag{5}$$

If terms of relative order L_f/ℓ are neglected in the expression for the force in the face members, the members inclined to the load line experience

$$F_f = \frac{M}{\sqrt{3}}\left(\frac{L_f}{H_c}\right) \tag{6}$$

with due account for the sign difference between the top and bottom members. Forces in all the other members can be derived from these formulas by accounting for the shift of M and V from section to section.

The magnitude of the maximum force in a core member is thus related to the *maximum* shear force per unit length, V, by

$$F_c = VL_f\left(\frac{L_c}{H_c}\right). \tag{7}$$

This force is compressive if V acts downward in Fig. 3, which will be assumed in the following. (Note, for example, that the truss in a three-point bend configuration experiences a sign of V on one side of the center and the opposite sign on the other. In this case, therefore, the maximum compressive load in a core member is always Eq. (7)). Let the *maximum* moment per unit length be M, it follows that the magnitude of the maximum force in a face sheet member is

$$F_f = \frac{M}{\sqrt{3}}\left(\frac{L_f}{H_c}\right), \tag{8}$$

acting as compression in one of the faces and tension in the other, depending on the sense of M.

The four constraints on the maximum member forces are

$$\frac{M}{\sqrt{3}}\left(\frac{L_f}{H_c}\right) \leqslant \sigma_Y \pi R_f^2, \quad \text{(face member yielding)}, \tag{9a}$$

$$\frac{M}{\sqrt{3}}\left(\frac{L_f}{H_c}\right) \leqslant \frac{\pi^3 E R_f^4}{4L_f^2}, \quad \text{(face member buckling)}, \tag{9b}$$

$$VL_f\left(\frac{L_c}{H_c}\right) \leqslant \sigma_Y \pi R_c^2, \quad \text{(core member yielding)}, \tag{9c}$$

$$VL_f\left(\frac{L_c}{H_c}\right) \leqslant \frac{\pi^3 E R_c^4}{4L_c^2}, \quad \text{(core member buckling)}. \tag{9d}$$

The two conditions on buckling take the beam members to be simply-supported at their ends, consistent with the pinned joint idealization. In each case, this approximation provides a lower bound to the actual member forces which can be sustained. Later in the paper, we will provide some indication of the extent to which the underestimate of the critical buckling loads affects the optimization outcome. Improvement of the present analysis will require more accurate formulas for the buckling constraints (9b) and (9d).

2.1. The optimization problem

The maximum load quantities, M and V, are assumed to be specified and ℓ is given by Eq. (4). The material properties are also specified. Define four dimensionless geometric design variables as

$$\vec{x} \equiv (x_1, x_2, x_3, x_4) = (R_f/\ell, L_f/\ell, R_c/\ell, H_c/\ell), \tag{10}$$

where $L_c/\ell = \sqrt{x_4^2 + x_2^2/3}$. The dimensionless weight per unit area of the truss plate from Eq. (2) is

$$\frac{W}{\rho\ell} = 2\sqrt{3}\pi\left[2x_1^2x_2^{-1} + x_3^2x_2^{-2}\sqrt{x_4^2 + x_2^2/3}\right]. \tag{11}$$

The optimization problem requires the minimization of $W/\rho\ell$ with respect to $\vec{x}$ subject to the four constraints in Eq. (9), which in dimensionless form become

$$\frac{1}{\sqrt{3}\pi}\left(\frac{V^2}{EM}\right)\left(\frac{E}{\sigma_Y}\right)x_1^{-2}x_2x_4^{-1} \leqslant 1, \text{ (face member yielding)}, \tag{12a}$$

$$\frac{4}{\sqrt{3}\pi^3}\left(\frac{V^2}{EM}\right)x_1^{-4}x_2^3x_4^{-1} \leqslant 1, \text{ (face member buckling)}, \tag{12b}$$

$$\frac{1}{\pi}\left(\frac{V^2}{EM}\right)\left(\frac{E}{\sigma_Y}\right)x_2x_3^{-2}x_4^{-1}\sqrt{x_4^2 + x_2^2/3} \leqslant 1, \text{ (core member yielding)}, \tag{12c}$$

$$\frac{4}{\pi^3}\left(\frac{V^2}{EM}\right)x_2x_3^{-4}x_4^{-1}\left(x_4^2 + x_2^2/3\right)^{3/2} \leqslant 1, \text{ (core member buckling)}. \tag{12d}$$

There is one dimensionless material parameter in the problem, σ_Y/E, and only one dimensionless load parameter, $V^2/(EM)$.

2.2. The optimal plate truss

The optimization problem has been solved using a sequential quadratic programming algorithm which is included in the IMSL Library. The material is assumed to be representative of a relatively high strength aluminum with $\sigma_Y/E = 0.007$. The optimization is carried out for specified values of $V^2/(EM)$. An effective parameter tracking method uses the solution at one value of $V^2/(EM)$ as the initial guess in the iteration for the solution at a smaller $V^2/(EM)$, because this guess necessarily satisfies all the inequalities in Eq. (12). The solution is presented in Figs. 4 and 5. Both the dimensionless weight parameter and the member geometry parameters are plotted against $V/\sqrt{EM}$, rather than $V^2/(EM)$, because the variations are nearly linear in $V/\sqrt{EM}$. The plots are terminated at $V/\sqrt{EM} \cong 0.002$. Larger values of $V/\sqrt{EM}$ would generate plates that would not be considered as thin. Over the entire range of $V/\sqrt{EM}$ plotted, three of the constraints in Eq. (12) are active: face member buckling and yielding, and core member buckling.

2.3. Optimal plate truss with identical face and core members

Consider a subset of truss plates, known as octet trusses (Fuller, 1983), comprised of identical members, i.e.,

$$R_f = R_c \equiv R, \quad L_f = L_c \equiv L, \quad \text{and} \quad H_c = \sqrt{2/3}L \tag{13a}$$

with

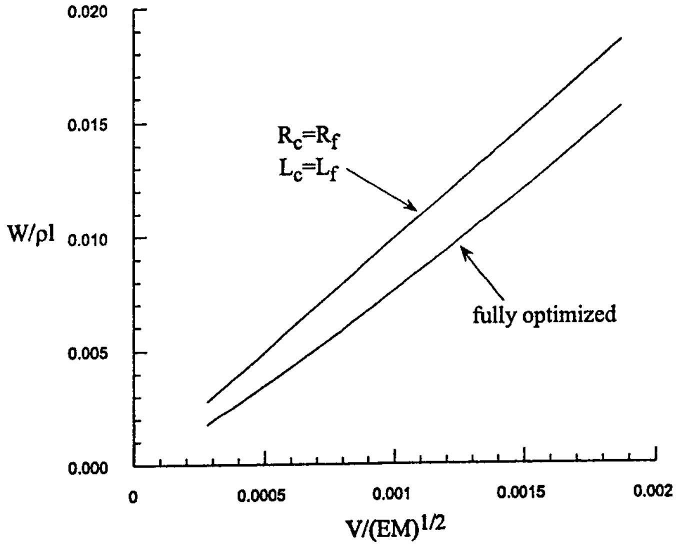

Fig. 4. Normalized weight per unit area of optimized truss plates as a function of the dimensionless load parameter ($\sigma_Y/E = 0.007$). The upper curve applies to an octet truss plate whose members are all the same. The lower curve is for a fully optimized truss plate with distinct face and core members.

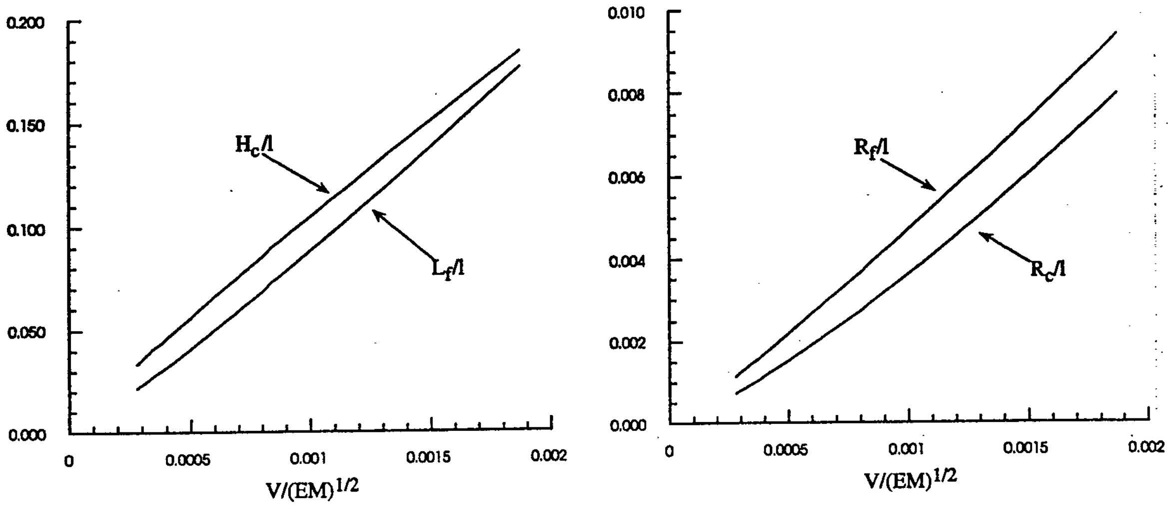

Fig. 5. Member sizes for the fully optimized truss plate, where $\ell = M/V$ ($\sigma_Y/E = 0.007$).

$$x_1 = R/\ell, \quad \text{and} \quad x_2 = L/\ell. \tag{13b}$$

This subset is interesting from the vantage point of its geometric aesthetics, and plate trusses in this class (Fig. 1) have been constructed in both plastic and metal. Eqs. (11) and (12) become

$$\frac{W}{\rho\ell} = 6\sqrt{3}\pi x_1^2 x_2^{-1}, \tag{14}$$

and

$$\frac{1}{\sqrt{2}\pi}\left(\frac{V^2}{EM}\right)\left(\frac{E}{\sigma_Y}\right)x_1^{-2} \leqslant 1, \text{ (face member yielding)}, \tag{15a}$$

$$\frac{2\sqrt{2}}{\pi^3}\left(\frac{V^2}{EM}\right)x_1^{-4}x_2^2 \leqslant 1, \text{ (face member buckling)}, \tag{15b}$$

$$\frac{\sqrt{3}}{\sqrt{2}\pi}\left(\frac{V^2}{EM}\right)\left(\frac{E}{\sigma_Y}\right)x_1^{-2}x_2 \leqslant 1, \text{ (core member yielding)}, \tag{15c}$$

$$\frac{2\sqrt{6}}{\pi^3}\left(\frac{V^2}{EM}\right)x_1^{-4}x_2^3 \leqslant 1, \text{ (core member buckling)}. \tag{15d}$$

Comparison of Eqs. (15a) and (15c) reveals that the core members will never yield before the face members if $\sqrt{3}x_2 < 1$, which will always pertain to slender plate trusses. Similarly, $\sqrt{3}x_2 < 1$ ensures that face member buckling will always precede core member buckling. Thus, only face member yielding and buckling need to be considered. Anticipate that face member buckling governs, i.e., from Eqs. (15a) and (15b):

$$x_1 \equiv \frac{R}{\ell} > \frac{1}{\sqrt{\sqrt{2}\pi}}\left(\frac{V}{\sqrt{EM}}\right)\sqrt{\frac{E}{\sigma_Y}}, \tag{16}$$

and

$$x_1^2x_2^{-1} = \frac{2}{\sqrt{\sqrt{2}\pi^3}}\left(\frac{V}{\sqrt{EM}}\right). \tag{17}$$

Then one notes immediately from Eqs. (17) and (14) that the normalized minimum weight per unit area depends precisely linearly on $V/\sqrt{EM}$ according to

$$\frac{W}{\rho\ell} = \frac{12\sqrt{3}}{\sqrt{\sqrt{2}\pi}}\frac{V}{\sqrt{EM}} = 9.861\frac{V}{\sqrt{EM}}. \tag{18}$$

The minimum is attained for any *combination* of x_1 and x_2 satisfying Eq. (17) and $\sqrt{3}x_2 < 1$. Note also that if the equality in Eq. (16) is met together with Eq. (17), corresponding to simultaneous buckling and yielding of the face members, the minimum is still given by Eq. (18). Further inspection of the constraints reveals that if yield holds but buckling does not, then the normalized weight exceeds Eq. (18). It follows, for all $V/\sqrt{EM}$, the minimum weight is given by Eq. (18), since x_1 and x_2 can always be chosen to meet Eqs. (16) and (17). The minimum weight relation (18) for truss plates with identical members is included in Fig. 4, and it can be seen to lie between 20% and 30% above the minimum weight for the truss plates, whose core and face members are not constrained to be the same.

Minimum weight octet trusses with identical members are not unique. A *family of trusses* exists, specified by Eq. (17) and limited by Eq. (16), for which each truss is at minimum weight. A curious outcome of this nonuniqueness is that any plate truss whose members are identical is a minimum weight truss for some particular loading. More precisely, given a geometry specified by x_1 and x_2, determine $V/\sqrt{EM}$ from Eq. (17). If Eq. (16) is met, it follows that the truss is minimum weight at $V/\sqrt{EM}$.

With reference to the dimensional Eqs. (9a) and (9b), it can be seen that V plays no role in the optimization of the truss plate with identical members. The design of this restricted class of plates is, in effect, designed under a pure moment M. This is revealed by rewriting Eq. (18), with the aid of Eq. (4), as

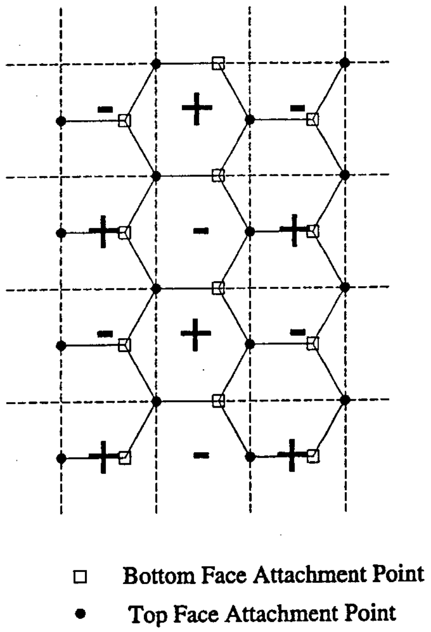

Fig. 6. Nodal lines of the face sheet buckling mode for sandwich plates with truss core. Compression is in the horizontal direction. A "+" within nodal lines represents an upward deflection, while a "−" denotes a downward deflection.

member buckling. The choice $k = 1$ corresponds to simply-supported conditions at the member ends. This choice, which will be used in most of the computations, neglects the rotational constraint provided by the other members and the face sheet at each end. This choice will certainly underestimate the maximum allowable shear force associated with core member buckling. The other extreme choice is $k = 4$, corresponding to fully clamped conditions at each end. This choice is expected to significantly overestimate the maximum shear force at buckling. Predictions based on the two limiting choices, $k = 1$ and 4, will be contrasted to assess the sensitivity to this constraint of the optimal design.

The weight per unit area (3) and the constraints (21) are written in dimensionless form using $\ell = M/V$ and the four design variables

$$\vec{x} = (t_f/\ell, R_c/\ell, H_c/\ell, d/\ell). \tag{22}$$

The normalized weight per unit area, $W/\rho\ell$, and the four dimensionless constraints involve only σ_Y/E (and v, which is taken to be 1/3 in the calculations) and $V^2/(EM)$, as well as $\vec{x}$. For a given σ_Y/E, the relation of $W/\rho\ell$ to $V^2/(EM)$ is universal for the optimally designed sandwich plate. That relation is plotted in Fig. 7 over the range for which the plates can be considered slender or "thin" for $\sigma_Y/E = 0.007$ with $k = 1$. The associated values of the design variables are plotted in Fig. 8. The active constraints over the entire range plotted are face sheet yielding and buckling, and core member buckling. If the geometry of the core truss is constrained in the same manner as was considered of the octet trusses in Section 2, i.e., such that and $d = L_c/\sqrt{3}$, then there are only three independent design variables, t_f/ℓ, R_c/ℓ and H_c/ℓ. The optimal sandwich plate in this sub-class is also included in Fig. 7, where it can be seen to be only slightly heavier than the fully optimized structure. The important implication is that this special core geometry appears to be almost as promising as the fully optimized core. The same three constraints noted above are active.

As remarked above, the assumption of simply supported truss member ends ($k = 1$) is conservative, leading to an overestimate of $W/\rho\ell$. The effect of taking the end conditions to be fully clamped ($k = 4$) is

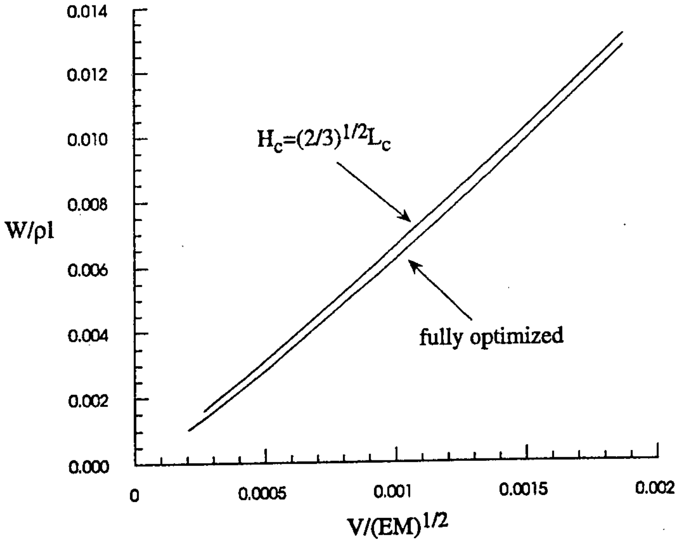

Fig. 7. Normalized weight per unit area as a function of the dimensionless load parameter for optimally designed sandwich plates with truss cores ($\sigma_Y/E = 0.007$, $\nu = 1/3$ and $k = 1$). The geometry of the plate for the upper curve is constrained such that $H_c = \sqrt{2/3}L_c$. The lower curve is for the fully optimized plate.

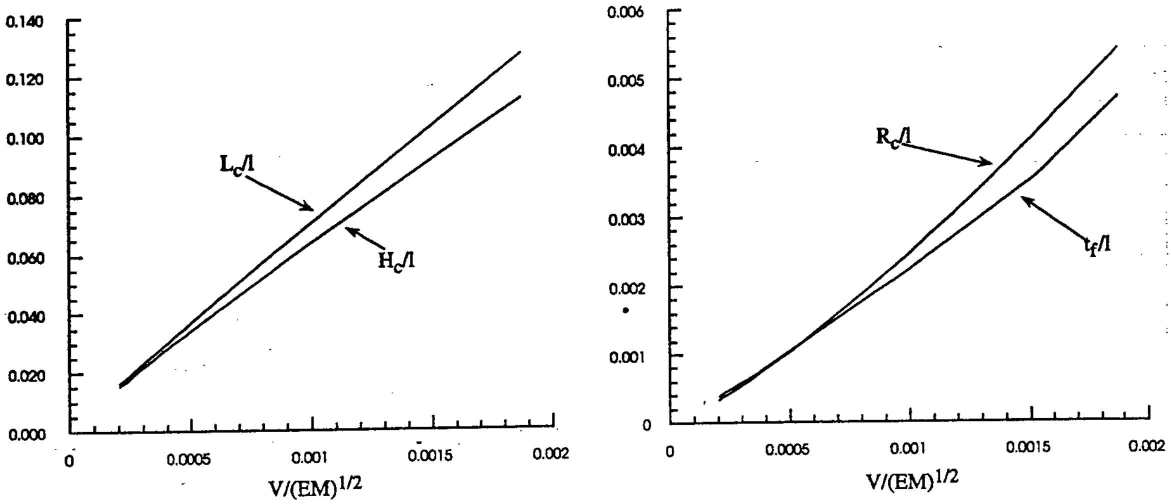

Fig. 8. Face sheet thickness and core member size for the fully optimized sandwich plate ($\sigma_Y/E = 0.007$, $\nu = 1/3$, $k = 1$).

seen in Fig. 9, where both curves have been computed for the unconstrained core geometry. Full clamping is unconservative such that the predicted trend for $W/\rho\ell$ is expected to underestimate the optimal weight of sandwich plates with truss cores. The fact that the spread between the two estimates in Fig. 9 is relatively narrow in spite of the significant difference between the two modeling assumptions suggests that the pinned jointed idealization used in this paper may not give rise to significant error. To the left of the vertical line in Fig. 9, the clamped case has the same three active constraints noted for the case $k = 1$. To the right of the line, all four constraints are active.

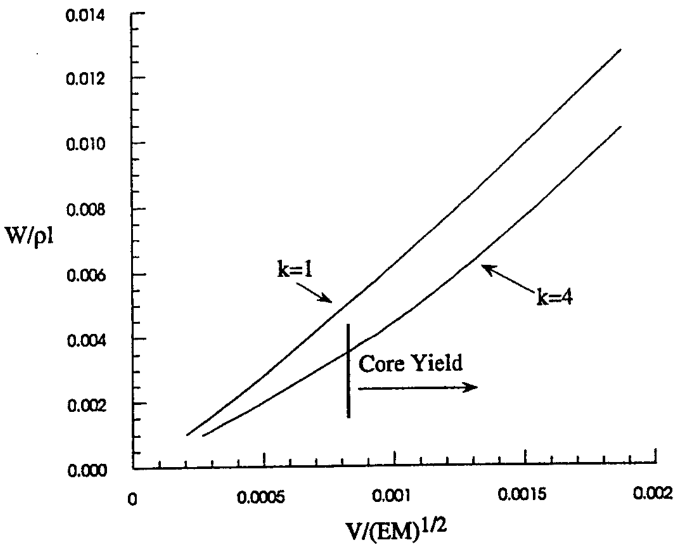

Fig. 9. Comparison of optimal weights of fully optimized sandwich plates with truss cores for two choices of core member end conditions: $k = 1$ (simply-supported) and $k = 4$ (clamped).

4. Weight comparison: truss plates, sandwich plates with truss cores, and honeycomb sandwich plates

Fig. 10 compares the weight per unit area of the fully optimized truss plate of Section 2 and that of the fully optimized sandwich plate with the truss core (with $k = 1$) from Section 3. Included in this plot are the corresponding results for optimized honeycomb sandwich plates, where both the face sheets and the

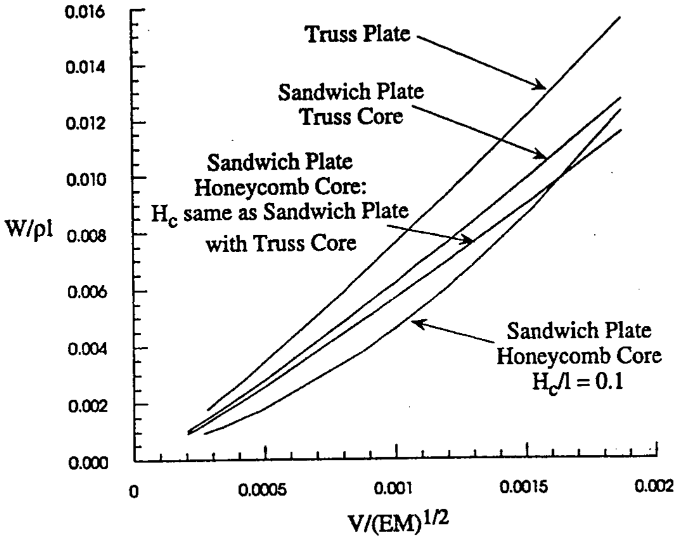

Fig. 10. Comparison of optimal weights of truss plates, sandwich plates with truss cores ($k = 1$), and sandwich plates with honeycomb cores, all with $\sigma_Y/E = 0.007$ and $\nu = 1/3$. The two plates with truss cores are fully optimized. Two cases of the honeycomb plates have been considered: the core thickness fixed at $H_c/\ell = 0.1$; and the core thickness taken equal to that of the sandwich plate with truss core at the same value of $V/\sqrt{EM}$.

honeycomb core are made from the same material as the other two plate structures ($\sigma_Y/E = 0.007$ and $\nu = 1/3$). As in the case of the other two plate structures, the sole dimensionless loading parameter in the optimization of the honeycomb sandwich is $V^2/(EM)$. The optimization analysis of the honeycomb sandwich is outlined in Appendix A. Four competing failure modes have been considered: face sheet buckling and yielding, and core web buckling and yielding under shear. The four design variables are face sheet thickness, core thickness, web thickness, and the size of the honeycomb hexagon. The fully optimized honeycomb sandwich has a much larger core thickness than either of the two other plate structures analyzed here. So thick, in fact, that the honeycomb sandwich could hardly be considered to be thin and would be unlikely to be a realistic contender. To make a meaningful comparison, two restricted optimization calculations have been performed for the honeycomb sandwich plates. In one, the thickness of the honeycomb sandwich, H_c, was set equal to the thickness of the truss core sandwich plate at the corresponding value of $V^2/(EM)$ (Fig. 8a). In the other calculation, the thickness of the honeycomb plate was set to be $H_c/\ell = 0.1$ over the whole range of $V^2/(EM)$. In each set of calculations, the optimization was then performed with respect to the other three design variables. The outcomes of these restricted optimizations for the honeycomb sandwich are plotted in Fig. 10.

It is striking that the weights of the optimized sandwich plates with truss and honeycomb cores are so similar. Sandwiches with honeycomb cores are generally regarded as the lightest weight plate structures. The comparison of Fig. 10 suggests that truss cores may be equally effective for sandwich plates. Opportunities associated with an open core and possible advantages in face/core bonding may augur well for employment of truss cores.

The optimal weight estimates in Fig. 10 have been determined under approximations to the buckling strengths of each of the three types of plates (e.g. pinned joints and simple supports at joints, where the webs or beam members merge with the faces). All the approximations tend to underestimate the buckling capacity, and thus it is expected that the optimal weight estimates in Fig. 10 are all overestimates. Further work will be required to refine these estimates and to fully certify the relative weight advantages of the three types of plate structures. It seems to us, that of the three types, the design weight of the truss plate is likely to be reduced the most by more accurate buckling analysis. This assertion arises from our expectation that the major error following from the idealization of pinned joints is in the critical load for buckling of the truss faces.

5. Plates with truss cores and solid sheet faces designed as compression panels

The competitive performance under transverse loads of the sandwich plates comprised of solid sheet faces with a truss core motivates their consideration as candidates for compression panels. Here, attention is focused on simply supported wide plates of length, ℓ, designed to carry a prescribed compressive load per unit length, P. (Note that ℓ in this section is defined differently from the previous sections.) In the spirit of a study by Budiansky (1999), the optimal design will be compared with optimally designed stringer stiffened construction, which is among the most efficient for applications requiring light weight. As in the earlier parts of the present study, attention is limited to sandwich plates made from a single material. The structure is the same as that in Section 3, and the notation of that section continues to apply. Specifically, the task in this section is to minimize the weight per unit area (3) of the plate subject to the failure constraints, which now include overall buckling of the plate in the wide column mode. As before, only the loading regime leading to relatively thin plates will be investigated.

Under axial compression P, the face sheets of the unbuckled plate carry all the load such that the forces in the truss members are zero. Yielding or buckling of the individual truss members are no longer limitations on the design. However, the transverse shear stiffness of the core enters into the overall buckling strength of the plate. The elastic buckling load for a simply supported wide plate of length ℓ having bending stiffness D and transverse shear stiffness S is (Allen, 1969)

$$P_{\mathrm{crit}} = \frac{\pi^2 D}{\ell^2}\left[1 + \frac{\pi^2 D}{\ell^2 S}\right]^{-1}. \tag{23}$$

Only the face sheets contribute to the bending stiffness:

$$D = \frac{1}{2}Et_{\mathrm{f}}(H_{\mathrm{c}} + t_{\mathrm{f}})^2 \cong \frac{1}{2}Et_{\mathrm{f}}H_{\mathrm{c}}^2, \tag{24}$$

where, as in Section 3, it is anticipated that $t_{\mathrm{f}}/H_{\mathrm{c}} \ll 1$, such that the approximation given above can be used. The transverse shear stiffness (which is isotropic) depends on the truss core members according to

$$S = \frac{\pi E R_{\mathrm{c}}^2 H_{\mathrm{c}}^2}{\sqrt{3}L_{\mathrm{c}}^3}. \tag{25}$$

Thus, the overall buckling constraint is

$$P \leqslant P_{\mathrm{crit}}. \tag{26a}$$

There are three other potential failure modes which potentially constrain the design, the first two of which were employed in Section 3. Avoidance of face sheet yielding requires

$$P \leqslant 2\sigma_Y t_{\mathrm{f}}, \tag{26b}$$

while the condition for localized face sheet buckling requires

$$P \leqslant \frac{49}{216}\frac{\pi^2}{(1-\nu^2)}\frac{Et_{\mathrm{f}}^3}{(L_{\mathrm{c}}^2 - H_{\mathrm{c}}^2)}. \tag{26c}$$

The remaining failure mode which must be considered is a compressive kinking mode, which can occur if the transverse shear stiffness is very low. This is a localized mode of buckling, in the order of the thickness of the plate, in which the core shears cause a kink in the centerline of the plate (Allen, 1969). The constraint against kinking is $P \leqslant S$, or, by Eq. (25),

$$P \leqslant \frac{\pi E R_{\mathrm{c}}^2 H_{\mathrm{c}}^2}{\sqrt{3}L_{\mathrm{c}}^3}. \tag{26d}$$

The optimal design problem is the minimization of W in Eq. (3) with respect to t_{f}, L_{c}, R_{c} and H_{c}, subject to the four constraints (26). Again, let $d = \sqrt{L_{\mathrm{c}}^2 - H_{\mathrm{c}}^2}$, and take the vector of dimensionless unknowns to be as defined in Eq. (22). Then, the problem becomes the minimization of the dimensionless weight per area

$$W/(\rho\ell) = 2\left[x_1 + \pi x_2^2\sqrt{x_3^2 + x_4^2}/(\sqrt{3}x_4^2)\right], \tag{27}$$

subject to the four constraints:

$$\left(\frac{P}{E\ell}\right)\frac{2}{\pi^2}x_1^{-1}x_3^{-2}\left[1 + \frac{\sqrt{3}\pi}{2}x_1\left(x_3^2 + x_4^2\right)^{3/2}/x_2^2\right]^{-1} \leqslant 1, \text{ (overall buckling)}, \tag{28a}$$

$$\frac{1}{2}\left(\frac{P}{E\ell}\right)\left(\frac{E}{\sigma_Y}\right)x_1^{-1} \leqslant 1, \text{ (face sheet yielding)}, \tag{28b}$$

$$\left(\frac{P}{E\ell}\right)\frac{216(1-\nu^2)}{49\pi^2}x_1^{-3}x_4^2 \leqslant 1, \text{ (face sheet buckling)}, \tag{28c}$$

$$\left(\frac{P}{E\ell}\right)\frac{\sqrt{3}}{\pi}x_2^{-2}x_3^{-2}\left(x_3^2+x_4^2\right)^{3/2} \leqslant 1, \text{ (localized kinking)}. \tag{28d}$$

The prescribed dimensionless load parameter is $P/(E\ell)$, and the two material parameters are σ_Y/E and ν.

The outcome of the optimization analysis is shown in Figs. 11 and 12 for $\sigma_Y/E = 0.007$ and $\nu = 1/3$. Both the full optimization with respect to the four variables and the geometrically constrained optimization are included with $H_c = \sqrt{2/3}L_c$, corresponding to the same tetrahedral core geometry considered in Sections 2 and 3. The range of the load parameter has been chosen to be consistent with the stated condition

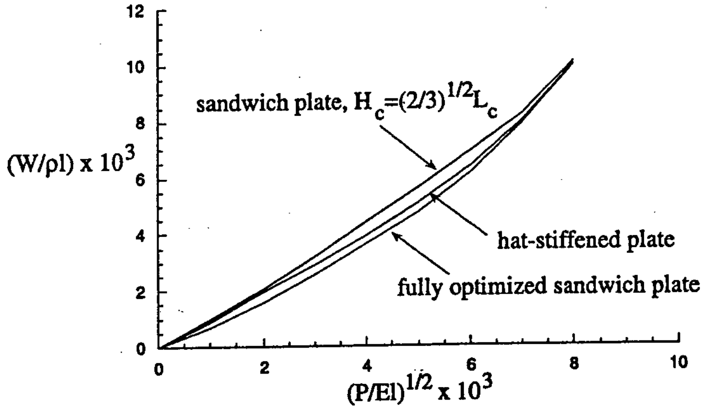

Fig. 11. Normalized weight per unit area as a function of the dimensionless load parameter for optimally designed simply-supported wide panels under axial compression ($\sigma_Y/E = 0.007$ and $\nu = 1/3$). The upper and lower curves are for the sandwich plates with a truss core, constrained with $H_c = \sqrt{2/3}L_c$ and unconstrained, respectively. The middle curve is an optimized hat-stiffened single layer plate, which is regarded as one of the most efficient structures for this application.

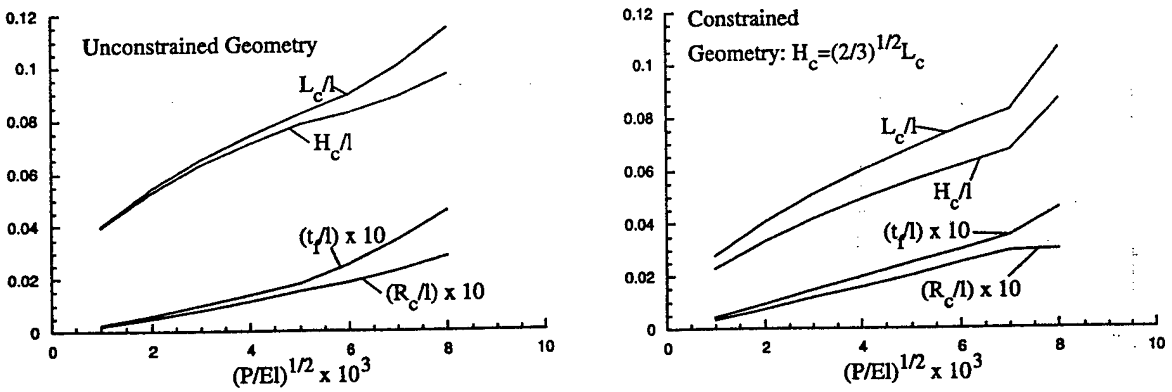

Fig. 12. Normalized variables specifying the optimal truss core sandwich plates in Fig. 11: (a) unconstrained case and (b) constrained case ($H_c = \sqrt{2/3}L_c$).

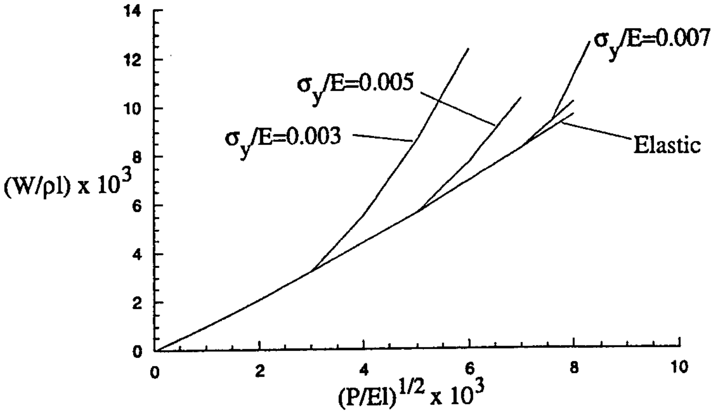

Fig. 13. Normalized weight per unit area for truss core sandwich plates with constrained geometry ($H_c = \sqrt{2/3}L_c$) for strictly elastic designs and for three values of σ_Y/E, all with $\nu = 1/3$.

that the plate be relatively thin. Plots of the design variables for the optimum plates are displayed in Fig. 12 revealing that H_c/ℓ approaches 1/10 at the upper end of the range of the load parameter plotted. The kinking mode is never active over the entire range of the load parameter considered. The more heavily loaded compression panels have three of the constraints active in the optimal design: overall and face sheet buckling and face sheet yielding. More lightly loaded panels (below the jump in the slope of the curves) buckle at the design load simultaneously in the overall and localized face sheet modes, but are stressed below yield.

Included in Fig. 11 as a standard for evaluating the performance of the optimal truss core sandwich plates is the weight for an optimal hat-stiffened plate (Budiansky, 1999), also with $\sigma_Y/E = 0.007$ and $\nu = 1/3$. Hat-stiffened plates are generally regarded to be one of the most efficient light weight constructions for compression panels. The unconstrained truss core sandwich plates are lighter than the hat-stiffened plates, while the constrained design is only slightly heavier.

The results for the more lightly loaded optimal panels buckle below yield and therefore depend only on the elastic moduli. However, the upper limit of $P/(E\ell)$ for strictly elastic design depends on σ_Y/E. Fig. 13 presents the weight per unit area as a function of the load parameter for three values of σ_Y/E for optimized compression sandwich plates with truss cores. These results are for plates with cores subject to the geometric constraint $H_c = \sqrt{2/3}L_c$, but results for the fully optimized panels follow the same trend. The weight of the more heavily loaded panels increases sharply with decrease in yield strength material.

Acknowledgements

This work was supported in part by grants ONR-N00014-1-96-1028 and NSF-DMR-98-09363 and in part by the Division of Applied Sciences, Harvard University. Nathan Wicks acknowledges the fellowship support of the National Defense Science and Engineering Graduate Fellowship Program.

Appendix A. Optimized honeycomb sandwich plates

Sandwich plates with honeycomb cores are used in Fig. 10 to gauge the performance of the truss plates and the sandwich plates with truss cores. The faces and the honeycomb core are assumed to be made of the

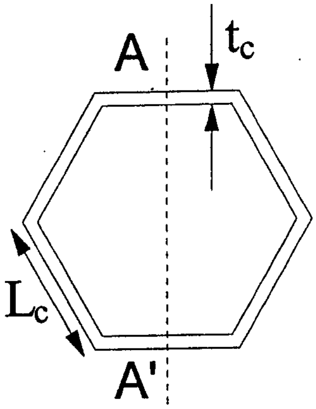

Fig. 14. Conventions for honeycomb core analysis.

same material, as was the case of the other two structures. The face sheet thickness is t_f, the core thickness is H_c, the thickness of the honeycomb web is t_c, and the length of each side of the honeycomb hexagon is L_c. The weight per unit area is

$$W = \rho\left(\frac{2H_c t_c}{\sqrt{3}L_c} + 2t_f\right). \tag{A.1}$$

The analysis follows that of the truss core sandwich fairly closely, with similar approximations. The maximum moment per unit length and transverse shear force per unit length are again denoted by M and V and oriented parallel to the section A–A' in Fig. 14. The transverse shear force is assumed to be carried entirely by the honeycomb core. Under these assumptions, the stress in the face sheet is

$$\sigma_f = \frac{M}{t_f H_c}, \tag{A.2}$$

while the average shear stress in the core web oriented perpendicular to the load line is

$$\tau_c = \frac{\sqrt{3}VL_c}{t_c H_c}. \tag{A.3}$$

The weight per unit area is minimized subject to the following four strength constraints:

$$\frac{M}{t_f H_c} \leqslant \sigma_Y, \ \text{(face sheet yielding)}, \tag{A.4}$$

$$\frac{M}{t_f H_c} \leqslant \frac{379\pi^2 E t_f^2}{1728(1-\nu^2)L_c^2}, \ \text{(face sheet buckling)}, \tag{A.5}$$

$$\frac{\sqrt{3}VL_c}{t_c H_c} \leqslant \tau_Y, \ \text{(core web yielding)}, \tag{A.6}$$

$$\begin{aligned} \frac{\sqrt{3}VL_c}{t_c H_c} &\leqslant \frac{\pi^2 E}{12(1-\nu^2)}\left[5.35\frac{t_c^2}{H_c^2} + 4\frac{t_c^2}{L_c^2}\right], \quad \text{if } L_c > H_c \\ &\leqslant \frac{\pi^2 E}{12(1-\nu^2)}\left[5.35\frac{t_c^2}{L_c^2} + 4\frac{t_c^2}{H_c^2}\right], \quad \text{if } H_c > L_c, \end{aligned} \quad \text{(core web buckling)}, \tag{A.7}$$

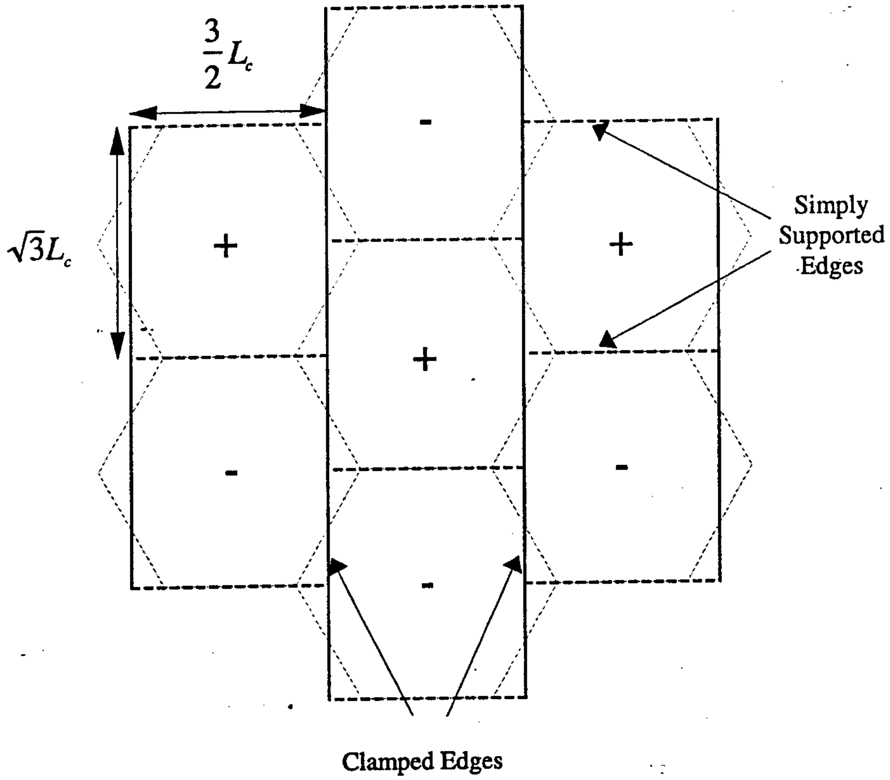

Fig. 15. Nodal lines for face sheet buckling mode for sandwich plates with honeycomb core. The compression direction is horizontal. To comply with the constraint of the core geometry, simple support conditions are taken along the horizontal nodal lines, and clamped conditions are assumed along the vertical nodal lines.

where $\tau_Y = \sigma_Y/\sqrt{3}$. The face sheet buckling mode is approximated by a rectangular pattern with dimensions $3L_c/2$ by $\sqrt{3}L_c$ and clamped on the edges parallel to the load line and simply supported on the edges perpendicular to the load line. This choice was made to model the constraint of the honeycomb core on the sheet buckling mode, as indicated in Fig. 15. The average shear stress in the core is equated to the yield stress in shear to determine (A.6). Core buckling is assumed to be associated with a plate subject to uniform shear τ_c of dimension L_c by H_c and simply supported on all its edges (Timoshenko and Gere, 1961). The simple support conditions underestimate the rotational constraint of the adjoining webs and the face sheets.

When cast into dimensionless variables in the manner of the previous sections, the only load parameter is $V/\sqrt{EM}$ and the material parameters are σ_Y/E and ν. Computations minimizing the weight subject to the four constraints have been carried out for $\sigma_Y/E = 0.007$ and $\nu = 1/3$. Over the entire range of the loading parameter considered in this paper, the value H_c/ℓ of associated with the optimum was greater than 0.15. This is not a thin plate and it is highly unlikely that such a plate would be considered in an application. To make a meaningful comparison between the honeycomb core sandwich and the other plate structures, two different constraints on H_c were considered: (i) H_c/ℓ was fixed at 0.1 for all values of $V/\sqrt{EM}$ and (ii) H_c/ℓ was taken to be same as H_c/ℓ for the fully optimized truss core sandwich plate at each value of $V/\sqrt{EM}$. In each of these two cases, the honeycomb core sandwich was then optimized with respect to the remaining three variables. The results are shown in Fig. 10. Over the entire range of the load parameter plotted, the optimal honeycomb core sandwich exhibits simultaneous face sheet yielding, face sheet buckling and core buckling.

References

Allen, H.G., 1969. Analysis and Design of Structural Sandwich Panels. Pergamon Press, Oxford.

Brittain, S.T., Sugimura, Y., Schueller, J.A., Evans, A.G., Whitesides, G.M., 2000. Fabrication of a mesoscale, space-filling truss system using soft lithography and microelectrochemistry, submitted for publication.

Budiansky, B., 1999. On the minimum weights of compression panels. Int. J. Solids Struct. 36, 3677–3708.

Fuller, R.B., 1983. Octet truss (1961) in inventions, St. Martins Press, New York, pp. 167–177.

Timoshenko, S.P., Gere, J.M., 1961. Theory of elastic stability. McGraw-Hill, New York.

Wallach, J.C., Gibson, L.G., 2000. Mechanical behaviour of a three-dimensional truss material. Int. J. Solids Struct. submitted for publication.

ON THE PERFORMANCE OF LIGHT WEIGHT METALLIC PANELS FABRICATED USING TEXTILE TECHNOLOGY

D. R. Mumm*, S. Chiras, A. G. Evans

Princeton Materials Institute, Princeton University
70 Prospect Avenue, Princeton, NJ 08540-5211, USA

J. W. Hutchinson

Division of Engineering and Applied Science, Harvard University
29 Oxford Street, Cambridge, MA 02138, USA

D. J. Sypeck and H. N. G. Wadley

Department of Materials Science and Engineering, University of Virginia
Thornton Hall, Charlottesville, VA 22903-2442, USA

August, 2001

---

* Corresponding author: Tel.: +1-609-258-5823, Fax.: +1-609-258-5877.
E-mail address: mumm@princeton.edu (D.R. Mumm).

ABSTRACT

The performance of sandwich panels with plain weave, metallic, textile cores manufactured using a transient liquid phase bonding process has been characterized. The response of the cores has been measured and analyzed in shear and compression: that for the panels measured in bending. The characterization has been performed for weaves configured in both square and diamond orientations (relative to the face sheets). Dramatic differences in performance exhibited by the two orientations highlight the fundamental influence of core topology on load capacity and weight. The superior performance demonstrated for panels with the diamond cores is explicitly related to the avoidance of bending moments on truss members. The measurements of the core properties, as well as the panel performance in bending, have been correlated with beam theory models. The correlations have allowed a preliminary optimization that demonstrates performance benefits relative to competing concepts.

Keywords: sandwich panels, cellular metals, lightweight structures, textiles, optimal design

1. INTRODUCTION

Progress toward the design and implementation of robust, ultra-light materials and systems has directed attention toward cellular-metal-based concepts. Panels with topologically configured cores and dense face layers have been demonstrated to have attractive performance characteristics [1–5]. An example for flat panels in bending is presented on Fig. 1a. The key features are as follows. (a) Panels having cores with a stochastic cellular topology are not weight efficient, but have the benefits of relatively low cost [6] and excellent robustness [7,8]. (b) Periodic structures, such as truss core panels having tetragonal and pyramidal topology, exhibit superior thermostructural characteristics [2–4]. They are at least as weight efficient as the best competing concepts and, moreover, have multi-functionality advantages [9]. (c) The benefits to be realized by using configured cores increases for curved, relative to flat, panels because of the biaxial nature of the strain (Fig. 1b).

Approaches for creating cellular metallic panels based on textile technology have the potential for improving the performance/cost ratio [10,11]. The method uses a commercial plain weave metal fabric as the basic unit and adopts a transient liquid phase (TLP) bonding strategy for creating robust nodes at wire crossovers and for attaching the core to the faces (Fig. 2) [11]. This study examines the performance of stainless steel panels fabricated using this technology.

2. TEXTILE-BASED CORES

2.1 Concepts

The literature on the performance of panels in bending and compression has highlighted the salient failure modes, as well as providing test protocols for evaluating performance [2, 4–8,12]. The most important modes for metal structures consist of core shear, core compression and face yielding. Face wrinkling and debonding are rarely encountered. Core designs and test methods that address and probe the core failure modes are most relevant.

Plain weaves provide two basic core design options: (a) "squares" with trusses parallel and perpendicular to the faces and (b) "diamonds" with both sets of trusses oriented at 45° to the panel faces. These two orientations highlight the key role of topology (section 2.2). The square topology is expected to have inferior in-plane shear strength and stiffness, because the trusses experience bending upon shear loading of the panel. The diamond topology should exhibit excellent shear characteristics, because the trusses are in either tension or compression, with minimal bending. In either design, the curvature introduced into the individual struts as a result of the weaving process is likely to diminish the performance. The measurements described in section 4 establish weaving factors applicable to the design of minimum weight structures.

2.2 Core Properties

Diamond Weave

The response of the core in shear and compression is assessed using beam theory, neglecting the weaving-induced strut curvature present in the (1,3) plane (see Fig. 3). When the diamond core is subject to in-plane shear stress, τ, as depicted on Fig. 3, the trusses are alternately in either tension or compression, with minimal bending. Equilibrium requires that each be subject to axial stress, $\sigma_a = \pm\tau$. When failure occurs by *yielding*, equating this stress to the tensile/compressive yield strength for the constituent alloy, σ_Y, the shear yield strength of the core, τ_Y^c, becomes:

$$(\pi/4)\sigma_Y D^2 = \tau_Y^c W_1 W_2 \tag{1}$$

where W_1 and W_2 are the cell dimensions depicted on Fig. 3 and D is the truss diameter. Noting that $W_1 = 2D$, the relative density is related to the dimensions by:

$$\begin{aligned}\bar{\rho} &\equiv (\pi/2)D^2/W_1 W_2 \\ &\equiv (\pi/8)W_1/W_2\end{aligned} \tag{2}$$

and inserting (2) into (1) gives:

$$\tau_Y^c/\sigma_Y = \bar{\rho}/2 \tag{3a}$$

This strength is large relative to other truss designs [3], because this topology maximizes the shear resistance in the (1,2) plane. It is twice that for plates with either the tetragonal or pyramidal truss cores [2–4,10]. In practice, the strength is expected to be lower than (3a), because of the imperfections around the nodes caused by the weaving. This degradation is expressed through a knock-down factor, $\alpha\,(<1)$, such that:

$$\tau_Y^c/\sigma_Y = \alpha\bar{\rho}/2 \tag{3b}$$

The shear strength in the other (1,3) plane has yet to be ascertained, but is expected to be lower.

When failure occurs by *elastic buckling*, the compression on the truss is:

$$\begin{aligned}\sigma_b &\equiv \frac{k^2\pi^2}{(\pi/4)D^2}\left[\frac{EI}{W_2^2}\right] = \frac{\pi^2 k^2 E(D/W_2)^2}{16} \\ &= \frac{k^2\pi\bar{\rho}EW_1}{8W_2}\end{aligned} \tag{4}$$

where I is the moment of area and k is a measure of the rotational constraint at the junctions ($k=1$ when there is no constraint and $k=2$ when clamped). The core shear strength when buckling dominates is thus:

$$\tau_b^c \equiv \bar{\rho}\,\sigma_b/2 = \frac{k^2\pi\bar{\rho}^2 EW_1}{16W_2} \tag{5}$$

Comparing (5) with (3), core yielding should occur in preference to elastic buckling when:

$$\bar{\rho} \geq \frac{8\sigma_Y W_2}{k^2 \pi E W_1} \tag{6}$$

It will be shown below that the inequality (6) is satisfied for most cores of practical interest.

The diamond topology would have performance limitations imposed by core crushing were it not for the constraint provided by the faces. Absent constraint, the core would expand laterally, as it compresses, and a bending moment, M, would be induced in the trusses:

$$M = \sigma_Y D^3 / 6. \tag{7a}$$

With M related to the compressive stress, σ_C, by:

$$M = \sigma_C W_1 W_2^2 / 8, \tag{7b}$$

the compressive strength would become:

$$\frac{\sigma_C}{\sigma_Y} = \frac{2(2/\pi)^{3/2}}{3} \sqrt{\frac{W_1}{W_2}} \bar{\rho}^{3/2} \tag{8}$$

In practice, the faces limit the transverse expansion to:

$$u_x = \frac{\nu \sigma_C W_2}{\sqrt{2} E} \tag{9}$$

with ν the Poisson ratio. This displacement allows the development of a moment:

$$M = \frac{3 u_x E D^4}{32\sqrt{2} W_2^2} \tag{10}$$

The stress associated with this moment is small, relative to the axial stress in the trusses. That is, the constraint negates the degradation due to bending. The final result for the compressive strength is:

$$\frac{\sigma_C}{\sigma_Y} = \frac{\alpha \bar{\rho} / 2}{1 + (9/64) \nu \bar{\rho}^2 W_2 / W_1} \approx \frac{\alpha \bar{\rho}}{2} \tag{11}$$

Accordingly, the yield surface for the core is that depicted on Fig. 3b.

Square Weave

The compressive strength is obtained trivially as:

$$\frac{\sigma_C}{\sigma_Y} = \alpha \frac{\bar{\rho}}{2} \tag{12}$$

Moreover, equilibrium requires that the shear strength of the squares be half the unconstrained compressive strength of the diamonds, as evident from the bending moments on the wires (see (7) and (8)). It is given by:

$$\frac{\tau_Y^c}{\sigma_Y} = \frac{(2/\pi)^{3/2}}{3} \sqrt{\frac{W_1}{W_2}} \bar{\rho}^{3/2} \tag{13}$$

Note that in comparing topological architectures, the relative core shear strengths for the diamond and square weave topologies is:

$$\frac{(\tau_Y^c)_{diamond}}{(\tau_Y^c)_{square}} = \frac{3(\pi)^{3/2}}{4\sqrt{2}} \sqrt{\frac{W_2}{W_1}} \bar{\rho}^{-1/2} \tag{14}$$

3. MEASUREMENT PROTOCOL

Textile-core sandwich panels were made from stainless steel, using procedures elaborated in [11]. They were evaluated using a flat platen bend test methodology [7] [Fig. 4]. The tests were designed to promote core shear failure, by choosing relatively thick faces and a thin core (Appendix, Table 1), after making certain assumptions about the core shear strength. The platen fixtures were ground from high strength steel and attached to the sample using a high strength adhesive. Displacements were applied using a servo-electric test frame. The induced loads were measured continuously, as well as the displacements at the center-point and the underside of the sample, directly beneath the center platen. Optical images of the structure were recorded during testing to characterize the deformation mechanisms and failure modes. Images were captured using a high-resolution digital camera equipped with a long focal-length lens.

The shear and compressive properties of the cores were measured independently on sections cut from larger panels. The test approaches, elaborated elsewhere [2], are depicted on Fig. 5. For shear testing, the faces had thickness three times that for the flexure panels, in order to avert premature failure by either face yielding or plastic buckling. The faces were attached rigidly to the loading plates to minimize rotation. Based on previous analysis [2], the influence of the small normal stress induced by using this method is expected to be small. The loading and imaging systems are the same as those used for the panel bending measurements.

The yield characteristics of the face sheets were independently evaluated by tensile testing of sections extracted from sandwich panels. This approach assures that changes in alloy properties during panel fabrication are captured. A gage attached to the reduced section measured the strain.

4. MEASUREMENTS AND ANALYSIS

4.1 Core Characterization

The plain weave core has been manufactured from type 304 stainless steel with a truss radius, $R_c = 356\,\mu m$, and cell size, $W_2 = 3.18\,mm$, with nodes rigidized by transient liquid phase bonding (Figs. 2; 3a). The separation between adjacent layers in the structure is, $W_1 = 1.42\,mm$. The relative density has been determined by standard weight measurement methods as: $\bar{\rho} = 0.22$. Based purely on the wire geometry (and accounting for the bending of the wires induced in the weaving process), the density should be $\bar{\rho} \approx 0.21$. The slight difference lies in the addition of the TLP bonding agent.

4.2 Face Sheet Properties

A representative tensile stress/strain, $\sigma(\varepsilon)$, curve measured on a section prepared from one of the faces after bonding is presented in Fig. 6a. Unload/reload lines obtained at several plastic strain levels establish the Young's modulus. The side view of the sample after testing (Fig. 7a) shows remnants of the core structure after extraction from the panels. These remnants affect the relation between the load/displacement response and the stress-strain behavior, as evident from the local thinning (Fig. 7b). To calibrate the configuration, the unload-reload compliance is matched to the known modulus of the 304SS material, $E = 193\,GPa$.

Thereafter, the loading response is fit to a Ramberg-Osgood representation:

$$\varepsilon = \sigma / E + \beta (\sigma_Y^R / E)(\sigma / \sigma_Y^R)^N \tag{15}$$

where σ_Y^R is the yield strength, N the strain hardening exponent and β a stress coefficient. The fit to the stress/strain measurements (Fig. 6b) indicates that: $\beta = 3/7$, $N = 10.3$, $\sigma_Y = 158\ MPa$ and $\varepsilon_Y \equiv \sigma_Y / E = 8.2 \times 10^{-4}$. This fit is used in the subsequent analysis to interpret the panel bending, shear and compression tests. Since the core is made from the same alloy and has been subject to the same thermochemical treatment, it is assumed to have the identical stress/strain response.

4.3 Core Compression

Compression tests were conducted on sections cut from the as-manufactured panels. The sections had cross-sectional dimensions of $b = 21.3\ mm$, $w = 31.8\ mm$ for the square configuration and $b = 21.3\ mm$, $w = 23.6\ mm$ for the diamond configuration, such that $(A^c)_{square} = 6.8 \times 10^{-4}\ m^2$ and $(A^c)_{diamond} = 5.0 \times 10^{-4}\ m^2$. The load/displacement responses were recorded and optical images of the section captured on the digital imaging system. The images [Figs. 8, 9] indicate that some of the exterior trusses are non-load bearing, especially in the diamond orientation. Accordingly, there is some ambiguity in converting the applied load to stress. In the following plots, the trusses at the extremities are fully discounted.

The stress/strain curve for the *diamond orientation*, ascertained in this manner, is presented on Fig. 10a. The onset of non-linearity occurs at about $10\ MPa$. There is subsequent strain hardening up to a peak stress, $(\sigma_{max}^c)_{diamond} = 17\ MPa$. Beyond the peak, rapid softening occurs. The optical images and their correlation with the imposed stresses [Figs. 8, 10a] indicate that the stress maximum is associated with plastic buckling. The compressive load capacity can thus be addressed in terms of buckling expressions, coupled with the above beam theory results.

For a Ramberg-Osgood material (15), the plastic buckling strength, σ_{pb}, is given by the implicit formula [5]:

$$\left(\frac{k\pi R_c}{2W_2}\right)^2 \varepsilon_Y^{-1} = \left(\frac{\sigma_{pb}}{\sigma_Y^R}\right) + \beta N \left(\frac{\sigma_{pb}}{\sigma_Y^R}\right)^N \tag{16}$$

Inserting the cell dimensions and the Ramberg-Osgood coefficients into (16) indicates that, for rigid nodes ($k = 2$) the stress on the trusses at buckling becomes: $\sigma_{pb} = 222\ MPa$. With the premise that the face-constrained result (11) provides the appropriate representation, the peak compressive strength becomes:

$$\sigma^c_{max} / \sigma_{pb} = \alpha \bar{\rho} / 2 \qquad (17)$$

Inserting the relative density and the measured peak strength, as well as the plastic buckling stress determined from (16), *the knockdown factor for the diamond structure in compression is found to be:* $\alpha \approx 0.70$.

The corresponding results for the *square orientation* [Fig. 10b] indicate that the stress maximum is $(\sigma^c_{max})_{square} = 18\ MPa$, again dictated by plastic buckling. Inserting the measured stress maximum and the plastic buckling stress into (17) indicates essentially the same knockdown factor, $\alpha \approx 0.74$.

The small knockdown effect is surprising given the presence of imperfections, such as the wire curvature caused by weaving and the non-uniform chemistry/structure at the nodes due to the TLP bonding. This finding remains to be explained. The slightly larger degradation for the diamond orientation suggests that the face constraint is less effective than implied by the analysis in section 3. Nevertheless, the crush resistance substantially exceeds the unconstrained strength.

4.4 Core Shear

The loads imposed in shear are converted into shear stresses, τ, by using the load-bearing cross-section described above. The overall shear strains, γ, are determined from the displacements and core thickness. The plastic shear strains induced in the core, γ_{pl}, are obtained by measuring the change in the weave angle from the optical images. The stress/strain results obtained in this manner are summarized on Fig. 11. Images taken during the tests are presented on Fig. 12.

The results for the diamond core specimen indicate that yielding commences at about $(\tau^c_Y)_{diamond} \approx 17\ MPa$. It then strain hardens and reaches a peak at stress, $(\tau^c_{max})_{diamond} \approx 37\ MPa$. Over this range, the images reveal that the trusses in compression exhibit plastic buckling, while those in tension stretch. The peak load is coincident with tensile rupture of some of the stretched trusses. Comparing the measured *yield strength* with (3b) indicates that there is essentially *no* *knockdown* ($\alpha \approx 1$). The extra load capacity beyond yield is assumed to be associated with strain hardening of trusses subject to tension.

The corresponding results for the square core indicate that yielding commences at about $(\tau_Y^c)_{square} \approx 1.8\,MPa$. Again, significant strain hardening occurs. The test is halted at a displacement equivalent to that imposed on the diamond core sample.

It is evident from Fig. 11 that the shear resistance of the two core topologies is very different. The ratio of the shear yield strength for the two core topologies is predicted from (14) as: $(\tau_Y^c)_{diamond} / (\tau_Y^c)_{square} = 9.4$. A ratio of 9.2 is measured experimentally.

4.5 Panel Bending

The load/deflection responses for the panels in bending are presented on Fig. 13. Note that the stiffness and the yield load are appreciably larger for the panel with the diamond orientation. The yield load for the diamonds is $(P_Y)_{diamond} \approx 1.4\,kN$, and only $(P_Y)_{square} \approx 0.9\,kN$ for the squares. Beyond yield, with both core configurations, the load capacity systematically increases as additional displacement is imposed until reaching a plateau (at which point the tests were discontinued). The maximum loads are similar, though somewhat larger for the diamond orientation than for the square. This small difference is not representative of the performance advantages of the diamond weave, because both panels are far from optimum (see section 5) such that the failure mechanisms differ, as discussed below. When optimized, the diamond cores sustain loads at much lower weight than square cores.

Images taken during the tests reveal the most important consequences of the topology (Fig. 14). In the *square orientation*, the response is dominated by *shear yielding of the core*: apparent from the shear distortion of the cells in the region between the load platens, as well as the plastic hinges in the faces at the inner and outer platens. These core characteristics are attributed to truss bending (section 3). The beam theory expression governing the limit load is that for core shear with plastic hinging of the faces (Appendix, A3):

$$P_{CS} = \frac{4bh^2}{L}\sigma_Y + 2bc\,\tau_Y^c$$

Inserting the independently determined values of the face yield strength and the core shear yield strength, the predicted limit load can be calculated. The limit load equations (see Appendix), utilized here are based upon elastic-perfectly plastic yielding of the constituent alloy. Therefore, as indicated in Fig. 6b, the face yield strength is taken to be $\sigma_Y^P = 215\ MPa$ for this and subsequent calculations. The limit load determined for core shear (with plastic hinging) is calculated as: $P_{CS} = 1.31\ kN$. Superposing on the measured load/displacement curve indicates that the measured load significantly exceeds that predicted by the beam theory formula based on the yield strength.

In the *diamond orientation*, the response is quite different. Now the cells in the shear region between the load platens retain their shape, indicating that they resist plastic shear: for the reasons discussed in section 3. Moreover, there is no crushing beneath the central platen, consistent with constrained compression. Instead, failure occurs by *plastic stretching of the face* at the center. Accordingly, the limit load is within the face yield domain, given by (Appendix, A4):

$$P_{FY} = \frac{4bh^2\,[1 + c/h]\,\sigma_Y}{L} + bc\left(\frac{c}{L}\right)\sigma_Y^c$$

Inserting the measured values of the elastic-plastic face yield strength, σ_Y^P, and the core yield strength, the limit load is predicted to be, $P_{FY} = 3.46\ kN$. Again, this is appreciably lower than the measured value.

For both configurations, the calculated limit loads are much smaller than the measured load maxima. A related discrepancy has been found in earlier studies [7], particularly when the response is controlled by face yield. That discrepancy was resolved by implementing a full numerical simulation [7]. Three factors are involved in the discrepancy. (i) The strain hardening of the faces beyond yield enhances the load capacity and could elevate the limit load by as much as 50%. (ii) The use of finite width platens diminishes the bending moment (relative to that assumed in beam theory), resulting in a load elevation of order 10 - 20%. (iii) The rotation of the outer supports during the testing (see Fig. 14) also diminishes the bending moment and, based on the observations, could account for another 10 - 20% load elevation. The sum of these three contributions is expected to account for most of the discrepancy. Numerical simulations are needed to provide a final resolution.

5. PRELIMINARY PERFORMANCE COMPARISON

The performance of the diamond core panels may be compared in a preliminary manner with other design concepts. For the present weave geometry, at typical yield strains, $\varepsilon_Y \approx 10^{-3}$, elastic buckling only becomes important (6) when $\bar{\rho} \le 0.0012$ and can be discounted. Moreover, because of the high shear strength of the diamond core, the failure loads are assumed to be limited by face yielding. With this premise, the moment per unit width, M^*, at failure is obtained from (A4) as:

$$M^* \equiv \frac{PL}{4b} = hC\sigma_Y \tag{18}$$

where $C = c + h \approx c$ for thin faces. The weight per unit area is given by [6]:

$$W^* = \rho_s(2h + c\bar{\rho}) \tag{19}$$

where ρ_s is the solid material density. Eliminating h and assuming thin faces, gives:

$$W^* / \rho_s = 2M^* / c\sigma_Y + c\bar{\rho} \tag{20}$$

Differentiation and setting $dW^* / dc = 0$ to obtain the minimum, gives an explicit core thickness:

$$c_{opt} = \sqrt{2M^* / \sigma_Y \bar{\rho}} \tag{21}$$

Inserting back into (20) gives the non-dimensional minimum weight:

$$\Psi \equiv W^*_{min} / \rho_s L = 2\sqrt{2\bar{\rho} / \varepsilon_Y}\,\frac{V}{\sqrt{EM^*}} \tag{22}$$

The shear force, $V = M^* / L$, has been used since the associated load index, $V / \sqrt{EM^*}$, allows direct comparison with minimum weight designs previously derived for tetragonal and hexagonal honeycomb cores [1,3] (Figs. 1 and 15). To allow a meaningful comparison, a yield strain, $\varepsilon_Y = 0.007$, pertinent to structural Al alloys, has been used [1,3]. Then, at the lowest applicable core density $(\bar{\rho} = 0.01)$, the weight from (22) becomes, $\Psi = 3.4\,V / \sqrt{EM^*}$ (Fig. 15a): *indicative of structures lighter than both honeycomb and tetrahedral truss core* *panels over most of the load range*. For a larger relative density $(\bar{\rho}=0.05)$, the weights are larger (Fig. 15b), but still competitive given the other attributes of the textile system.

The applicability of (21) is checked by determining the core shear response, upon inserting (20) into (A3). This assessment reveals that face yield only occurs in preference to core shear when:

$$\frac{V}{\sqrt{E\,M^*}} \leq \sqrt{\frac{\bar{\rho}\,\varepsilon_Y}{2}} \tag{22}$$

For core densities in the range, $\bar{\rho} \geq 0.01$, and for typical yield strains, $\varepsilon_Y \approx 10^{-3}$, this inequality signifies that face yielding should dominate provided that the load index satisfies:

$$V/\sqrt{E\,M^*} \leq 0.002$$

This is the range having practical relevance [13,3] (Figures 1 and 15).

A reservation pertinent to (22) is that the actual core thickness implied by (20) may become unacceptably large [3]. If a limiting thickness, $c^*/L = 0.1$, is imposed, the weight increases to:

$$\Psi = \frac{2}{(c^*/L)\,\varepsilon_Y}\left[\frac{V^2}{E\,M^*}\right] + \bar{\rho}\,(c^*/L) \equiv 3.0\times10^3\left[\frac{V^2}{E\,M^*}\right] + 0.001 \tag{23}$$

When superposed on Fig. 15b, this weight is seen to be slightly less than that for honeycomb core panels having the same thickness. This comparison affirms the potential for lightweight panels made with diamond weave cores when in-plane bending loads are relevant. Recall, however, that the woven core is anisotropic and that the weights will be larger when out-of-plane loads are involved.

6. IMPLICATIONS AND CONCLUSIONS

Truss core panels with plain weave cores have been fabricated and tested in bending. The observations provide a vivid demonstration of the role of topology. The panels with square weaves have core members susceptible to bending. They fail by core shear with inferior load capacity. Panels with the same weave in the diamond orientation have a much lower susceptibility to truss bending. Accordingly, they have a high resistance to core shear and fail by face yielding with superior load capacity.

The response of the diamond core has been analyzed using beam theory and the expectations correlated with measurements. The knock down factor associated with weaving imperfections has been ascertained. It is relatively small, $\alpha \approx 0.7$. With two basic assumptions, the overall performance of diamond core flat panels subject to axial bending has been evaluated. Namely, as the core density is reduced, (a) the same failure mechanisms apply and (b) the knockdown factor is unchanged. The analysis indicates that this design is competitive with panels made with hexagonal honeycomb cores, subject to several caveats and restrictions.

(i) The core is anisotropic and the properties in the (1,3) plane remain to be determined. For biaxial bending, the unknown out-of-plane properties are expected to be performance limiting.

(ii) Upon reducing the relative density to realize weight benefits, larger knockdown factors from weaving imperfections are likely, diminishing the benefits of the design. Performance measurements conducted with much lower density cores are needed.

(iii) Concepts based on hollow wires [11] woven in the diamond topology are thought to be an attractive approach for reducing the relative density, while retaining minimal degradation from weaving imperfections. However, higher costs may be prohibitive, and weaving processes problematic due to the limited flexibility of such hollow wires.

ACKNOWLEDGEMENTS

This work was supported in part by the DARPA/ONR MURI program on Ultralight Metallic Structures, Contract No. N00014-1-96-1028.

APPENDIX

Notation

D	Truss diameter
L	Span length of bend specimen
W_1	Ply spacing
W_2	Cell size
R_c	Truss radius
R	Platen width for platen 3-Point bend testing
b	Depth of load-bearing cross-section
w	Width of load-bearing cross-section
k	Nodal response parameter for elastic or plastic buckling $(1 \rightarrow 2)$
A^c	Area of load-bearing cross-section
ρ_s	Density of the solid constituent material
$\overline{\rho}$	Relative density
c	Core thickness
c_{opt}	Optimum core thickness
c^*	Limiting core thickness
h	Face sheet thickness
C	Effective panel thickness
B	Overhang length for bend specimen
P	Applied load
P_c	Crush load of core structure
P_{CS}	Limit load for panel bending (failure controlled by core shear with full plastic hinging)
P_{FY}	Limit load for panel bending (failure controlled by face yielding)
P_Y	Yield load recorded during panel bending
P_{max}	Peak load measured during panel bending
σ	Applied stress
σ_a	Axial stress exerted on truss members
σ_Y	Yield strength of constituent alloy
σ_Y^c	Yield strength of core structure
σ_b	Compressive stress on trusses for failure occurring by elastic buckling
σ_C	Core compressive strength
σ^c_{max}	Peak stress measured during compression testing
σ_{pb}	Compressive strength for panel failure controlled by plastic buckling of truss members
σ_Y^R	Yield strength determined through Ramberg-Osgood analysis
σ_Y^P	Yield strength determined for elastic – perfectly plastic behavior
ε	Strain
ε_Y	Yield strain
E	Elastic (Young's) modulus

N	Strain hardening exponent
β	Strain hardening behavior stress coefficient
α	Knockdown factor
I	Moment of inertia
M	Bending moment
M^*	Bending moment per unit width
v	Poisson ratio
u_x	Expansion of core in plane of ply
τ	Applied shear stress
τ_Y^c	Core shear yield strength
τ_b^c	Core shear strength when buckling dominates
τ_{max}^c	Peak shear stress sustained by the core structure
γ	Shear strain
γ_{pl}	Plastic shear strain
V	Shear Force
W^*	Weight per unit area
W_{min}^*	Weight per unit area of minimum-weight structure
Ψ	Non-dimensional minimum weight index
Π_{CS}^{I}	Non-dimensional limit load for type I core shear conditions
Π_{CS}^{II}	Non-dimensional limit load for type II core shear conditions
Π_{FY}	Non-dimensional limit load for face yield conditions
Π_C	Non-dimensional limit load for core compression (indentation)

Panel Bending Formulae [6]

Results for the limit loads exhibited by panels in bending, needed for the analyses conducted in the text, are summarized here for convenience. In the *core shear* domain, the load depends on the response in the overhang, length B. Shear in the overhang occurs when,

$$B/c \le (1/2)(h/c)^2(\sigma_Y/\tau_Y^c) \qquad \text{(A1)}$$

When (A1) is satisfied, the limit load is [6,10]:

$$\Pi_{CS}^{\mathrm{I}} \equiv P_{CS}/bL\sigma_Y = 2(h/L)^2 + 2(c/L)\left(1+2B/L\right)(\tau_Y^c/\sigma_Y) \qquad \text{(A2)}$$

where σ_Y is the flow strength at the strain level induced in the face sheet. Absent shearing in the overhang, plastic hinges form at the outer platens and the limit load becomes:

$$\Pi_{CS}^{II} \equiv P_{CS} / bL\sigma_Y = 4(h/L)^2 + 2(c/L)(\tau_Y^c / \sigma_Y) \tag{A3a}$$

which for the diamond core (3b) is:

$$(\Pi_{CS}^{II})_{diamond} = 4(h/L)^2 + \alpha\bar{\rho}(c/L) \tag{A3b}$$

When *face yielding* predominates, the corresponding limit load is:

$$\begin{aligned} \Pi_{FY} \equiv P_{FY} / bL\sigma_Y &= \frac{4h^2[1+c/h]}{L^2} + \left(\frac{c}{L}\right)^2 (\sigma_Y^c / \sigma_Y) \\ &\approx \frac{4h^2[1+c/h]}{L^2} \end{aligned} \tag{A4}$$

Normally, the second (core compression) term can be ignored.

Crushing of the core occurs when the load reaches [6]:

$$P_C = 2bh\sqrt{\sigma_Y^c \sigma_Y} + Rbc\sigma_Y^c \tag{A5}$$

with R being the width of the platen. Using the result for the compressive strength of the core from section 3 gives:

$$\Pi_C \equiv P_C / bL\sigma_Y = (h/L)\left[2\sqrt{\frac{\alpha\bar{\rho}}{2}} + \frac{\alpha\bar{\rho}R}{2h}\right] \tag{A6}$$

Comparison with (A3) indicates that, except for localized zones of pressure, $R/h \leq 5$, crushing will not occur in preference to core shear.

REFERENCES

1. Evans, A.G., Hutchinson, J.W., Fleck, N.A., Ashby, M.F. and Wadley, H.N.G., 2001. The Topological Design of Multifunctional Cellular Metals. Progress in Materials Science, 46, 309-327.
2. Chiras, S., Mumm, D.R., Evans, A.G., Wicks, N., Hutchinson, J.W., Dharmasena, K., Wadley, H.N.G. and Fichter, S., 2001. The Structural Performance of Near-Optimized Truss-Core Panels. International Journal of Solids and Structures, in press.
3. Wicks, N. and Hutchinson, J.W., 2001. Optimal Truss Plates. International Journal of Solids and Structures, 38, 5165-5183.
4. Deshpande, V.S., Fleck, N.A. and Ashby, M.F., 2001. Effective Properties of the Octet-Truss Lattice Material. Journal of the Mechanics and Physics of Solids, 49, 1747-1769.
5. Deshpande, V.S. and Fleck, N.A., 2001. Collapse of Truss Core Sandwich Beams in 3-Point Bending. International Journal of Solids and Structures, 38, 6275-6305.
6. Ashby, M.F., Evans, A.G., Fleck, N.A., Gibson, L.J., Hutchinson, J.W. and Wadley, H.N.G., 2000. Metal Foams: A Design Guide. Butterworth-Heinemann. Boston, MA.
7. Bart-Smith, H., Hutchinson, J.W. and Evans, A.G., 2001. Measurement and Analysis of the Structural Performance of Cellular Metal Sandwich Construction. International Journal of Mechanical Sciences, 43, 1945-1963.
8. Chen, C., Harte, A.-M. and Fleck, N.A., 2001. The Plastic Collapse of Sandwich Beams with a Metallic Foam Core. International Journal of Mechanical Sciences, 43, 1483-1506.
9. Evans, A.G., Hutchinson, J.W. and Ashby, M.F., 1999. Multifunctionality of Cellular Metal Systems. Progress in Materials Science, 43, 171-221.
10. Evans, A.G., 2001. Lightweight Materials and Structures. MRS Bulletin, in press.
11. Sypeck, D.J. and Wadley, H.N.G., 2001. Multifunctional Microtruss Laminates: Textile Synthesis and Properties. Journal of Materials Research, 16 (3), 890-897.
12. McCormack, T.M., Miller, R., Kesler, O. and Gibson, L.J., 2001. Failure of Sandwich beams with Metallic Foam Cores. International Journal of Solids and Structures, 38, 4901-4920.
13. Budiansky, B., 1999. On the Minimum Weights of Compression Structures. International Journal of Solids and Structures, 36, 3677-3708.

FIGURE CAPTIONS

Figure 1. The minimum wieght of a structure as a function of a given collapse load, for panels subject to imposed bending moments, comparing competing concepts for sandwich panel configurations.

Figure 2. The minimum weights of curved panels in compression, as a function of collapse load, illustrating performance benefits associated with truss-core sandwich panel constructions relative to competing concepts.

Figure 3. Schematic showing the stresses experienced by individual struts in the diamond-configuration sandwich panel core, along with the resultant yield surface for such a topologically-configured structure.

Figure 4. Schematic of the platen three-point bend configuration developed for, and used to, experimentally probe core-dependent sandwich panel failure mechanisms [7].

Figure 5. Illustrations of the test configurations used to measure the (a) shear and (b) compressive stress/strain behavior for the core configurations.

Figure 6. The tensile stress/strain response for a segment of the face sheet structure extracted from a sandwich panel construct. In (a) the unload/reload segments are fit to evaluate the modulus of the structure, while in (b) the stress/strain response is fit to a Ramberg-Osgood relation to determine yield and strain hardening characteristics.

Figure 7. Optical images of the (a) edge and (b) face of a segment of the face sheet after tensile straining, showing the remnant core structure and its effect on the overall development of plastic deformation.

Figure 8. Images of the diamond-configuration core structure loaded in compression, illustrating that peak load is correlated with plastic buckling of core struts.

Figure 9. Images of the square-configuration core structure loaded in compression, again illustrating that peak load is correlated with plastic buckling.

Figure 10. Stress/strain curves for the (a) square-configuration and (b) diamond-configuration core structures loaded in compression. The load points corresponding to the images captured during testing (Figs. 8 and 9) are indicated.

Figure 11. Shear stress/strain curves for the (a) diamond and (b) square configuration cores. Note the substantially larger peak stress measured for the diamond configuration.

Figure 12. Images detailing the mode of failure for the (a) diamond and (b) square configuration core structures loaded in shear.

Figure 13. Load-displacement responses for the square and diamond topology panels tested in 3-point bending. (a) Overall load-displacement behavior, illustrating the peak load measured with each structure and comparison with analytical limit loads based on beam theory. (b) The behavior at small displacements, showing a significant difference in both the initial yield points and stiffnesses of the two core configurations.

Figure 14. Optical images captured during bend testing of panels with (a) square and (b) diamond configuration cores. Note that the square core configuration leads to failure by core shear, with full plastic hinging at the outer loading points. For the diamond core configuration, failure initiates with face sheet yielding under the center load point, with no evidence of core shear between the center and outer load points.

Figure 15. Comparison of the minimum-weight performance characteristics of competing, topologically-designed core structures, affirming the potential for lightweight panels with diamond-configuration textile core structures. Compared are cores having: (a) the lowest applicable core density $(\bar{\rho} = 0.01)$, and (b) higher density cores $(\bar{\rho} = 0.05)$.

TABLES

Table 1: Specimen Design

Face Sheet	Core Material	h/L	c/L	h	c (mm)	L (mm)	R/L	B
304 SS	304 SS	0.0149	0.0620	2.09	8.67	140.0	0.114	40.0

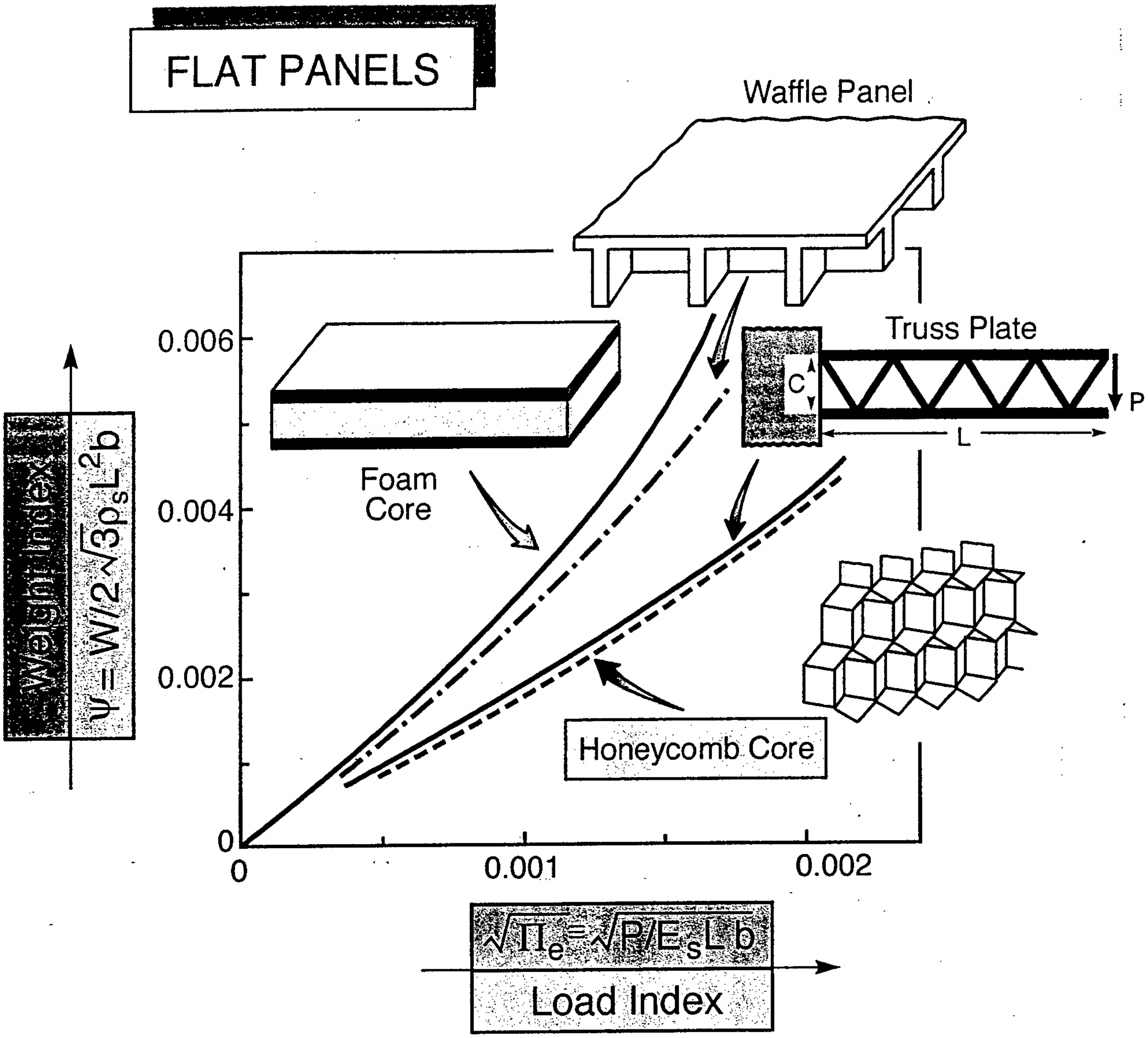
FLAT PANELS
Waffle Panel
Truss Plate
C
P
L
Foam Core
Honeycomb Core
0.006
0.004
0.002
0
0
0.001
0.002
Weight Index
$\Psi = W/2\sqrt{3}\rho_s L^2 b$
$\sqrt{\Pi_e} = \sqrt{P/E_s L b}$
Load Index

Figure 1a

CURVED PANELS

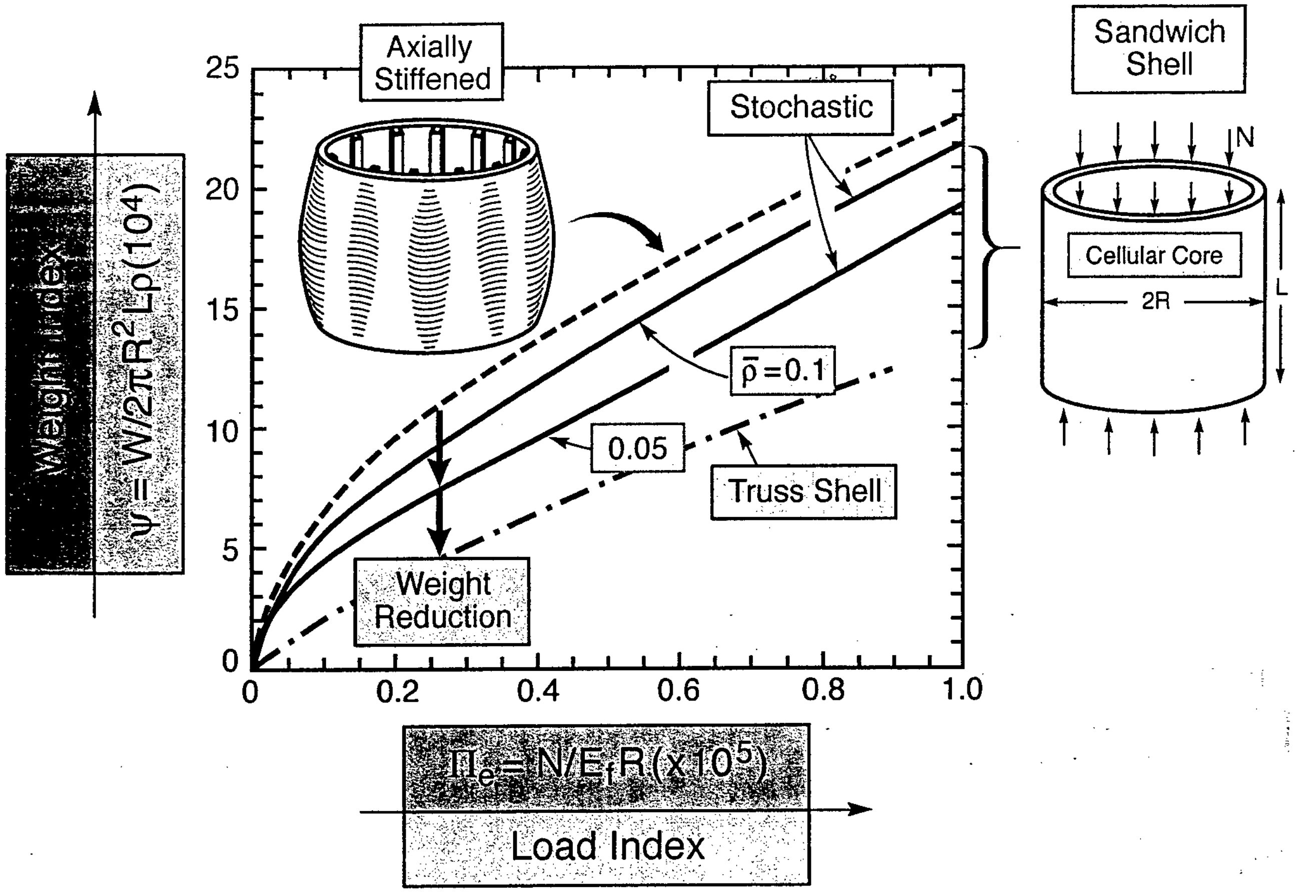

Figure 1b

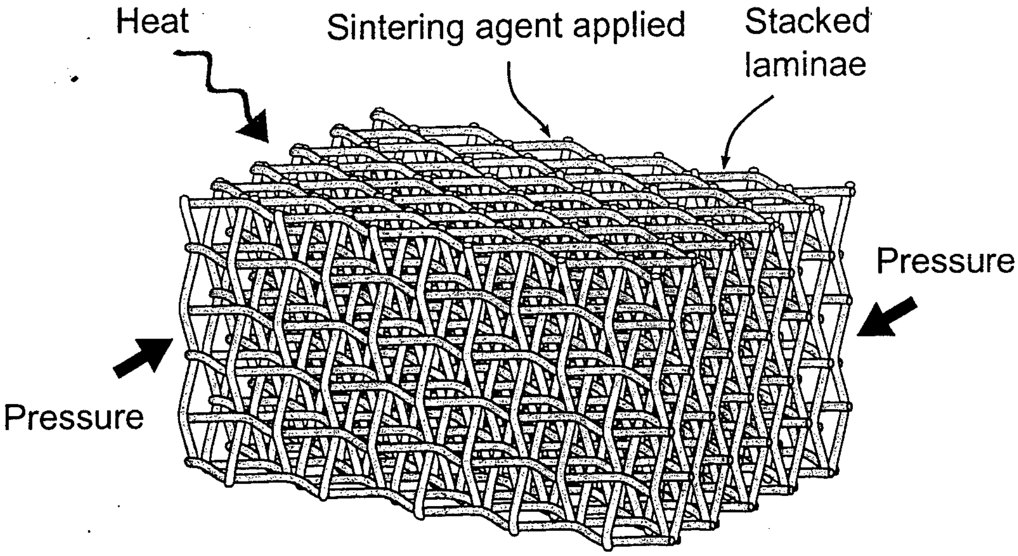

a Core Lamination

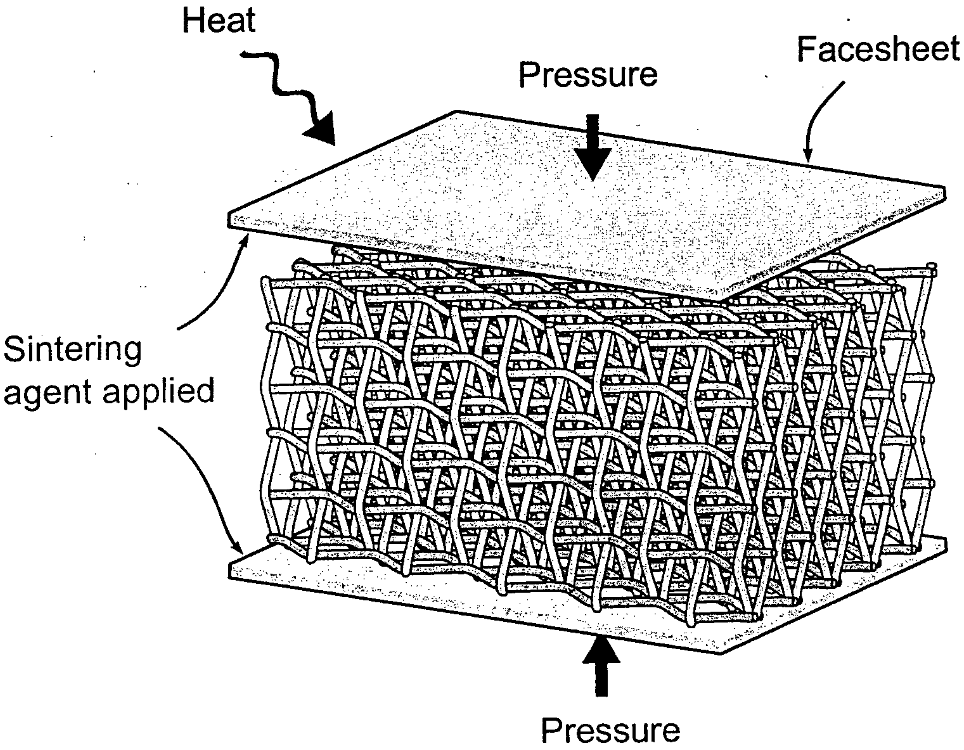

b Face Sheet Addition

Figure 2

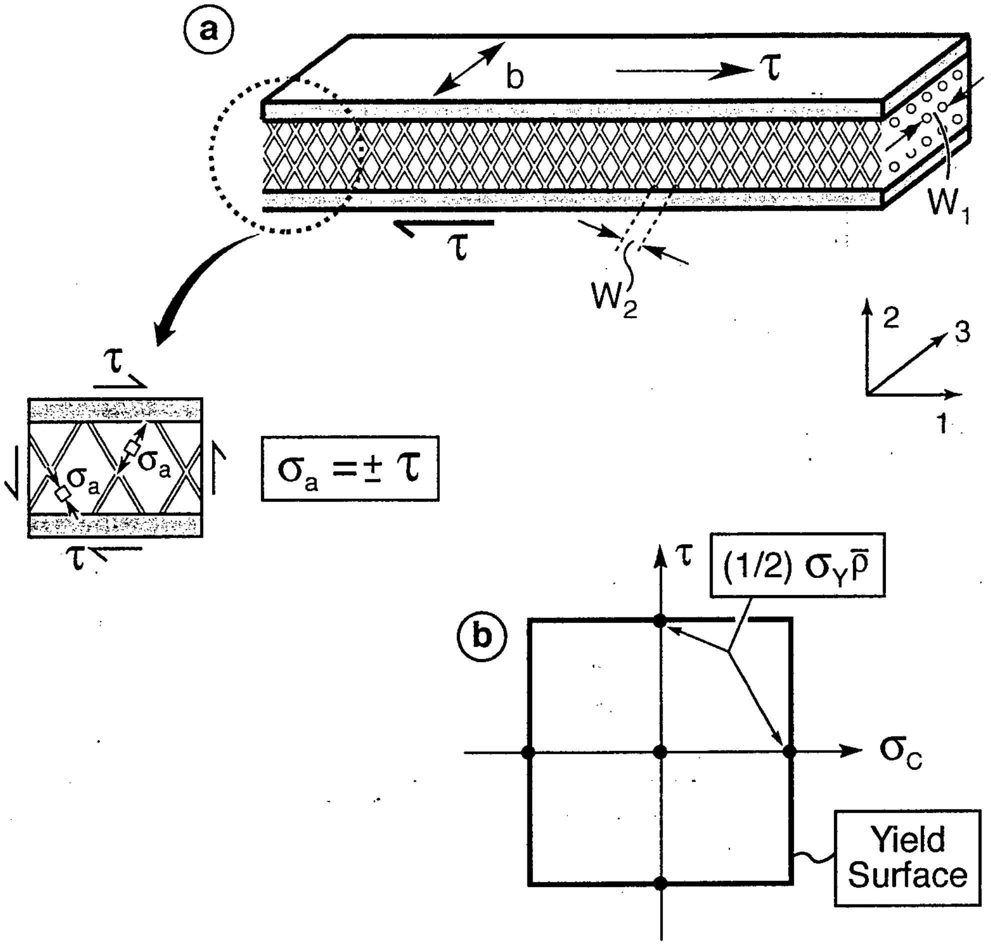

Figure 3

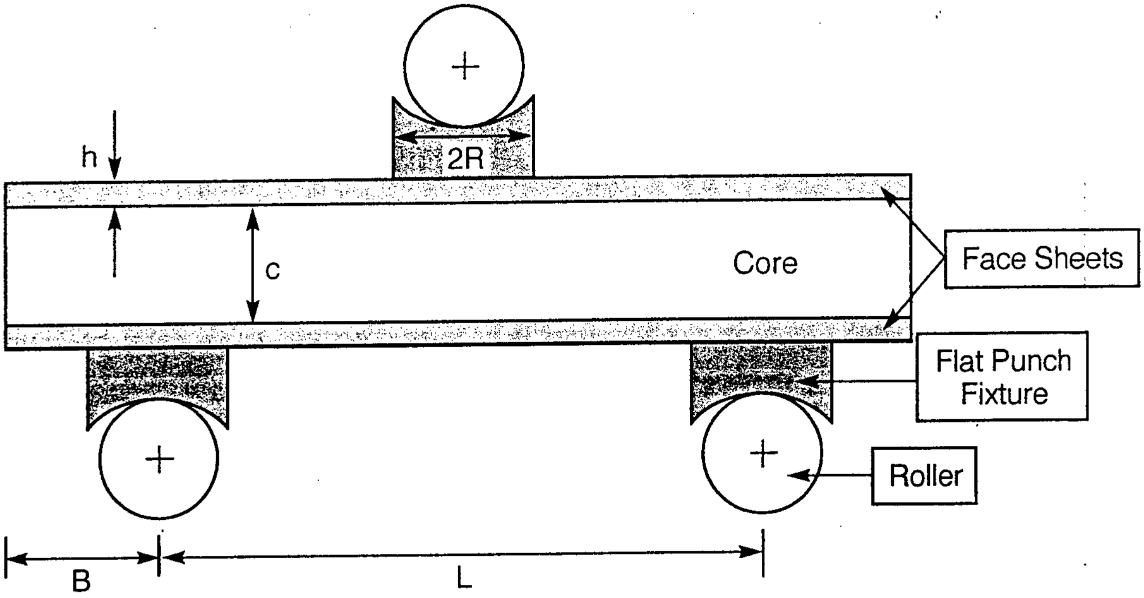

Figure 4

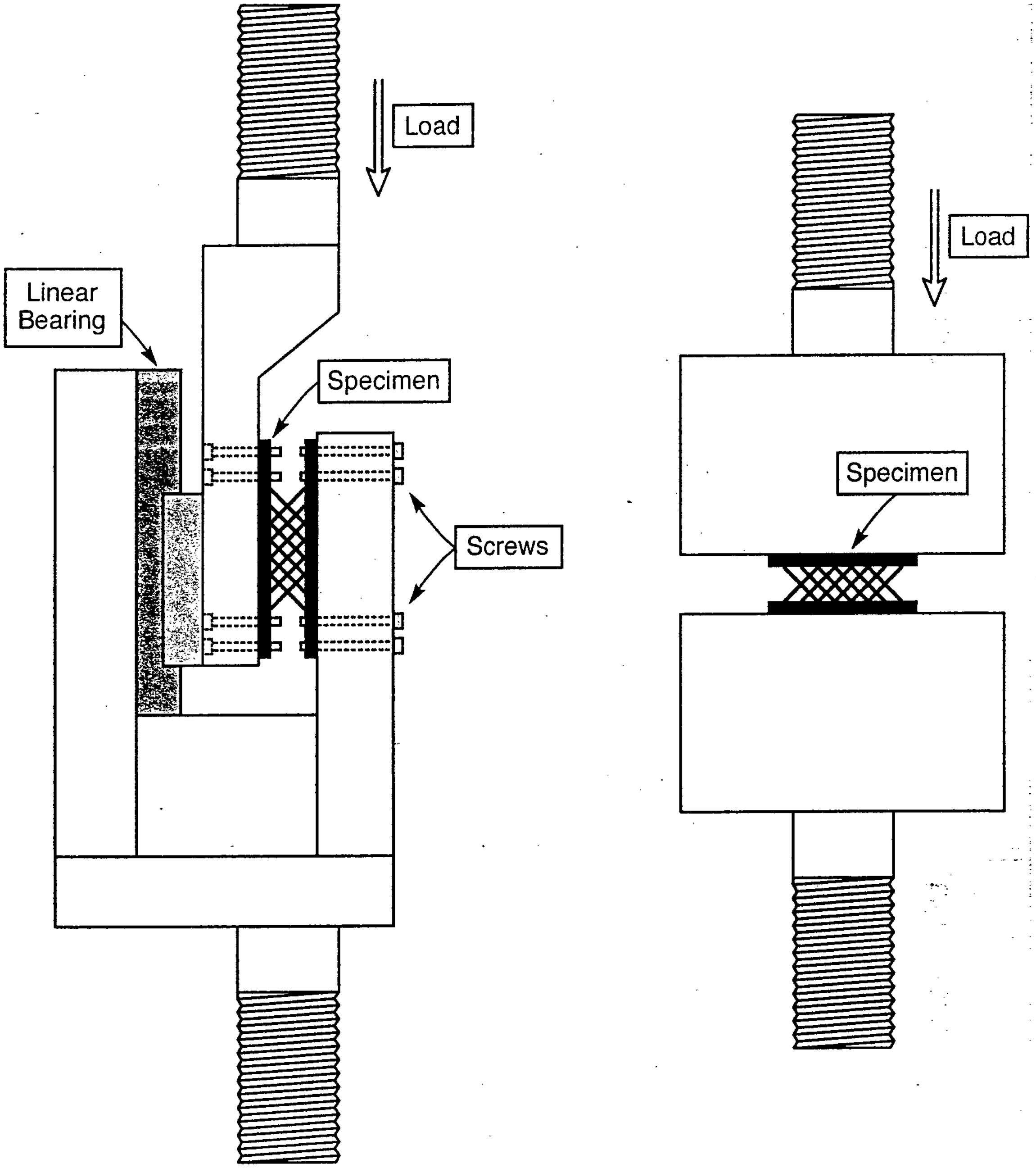

(a)

(b)

Figure 5

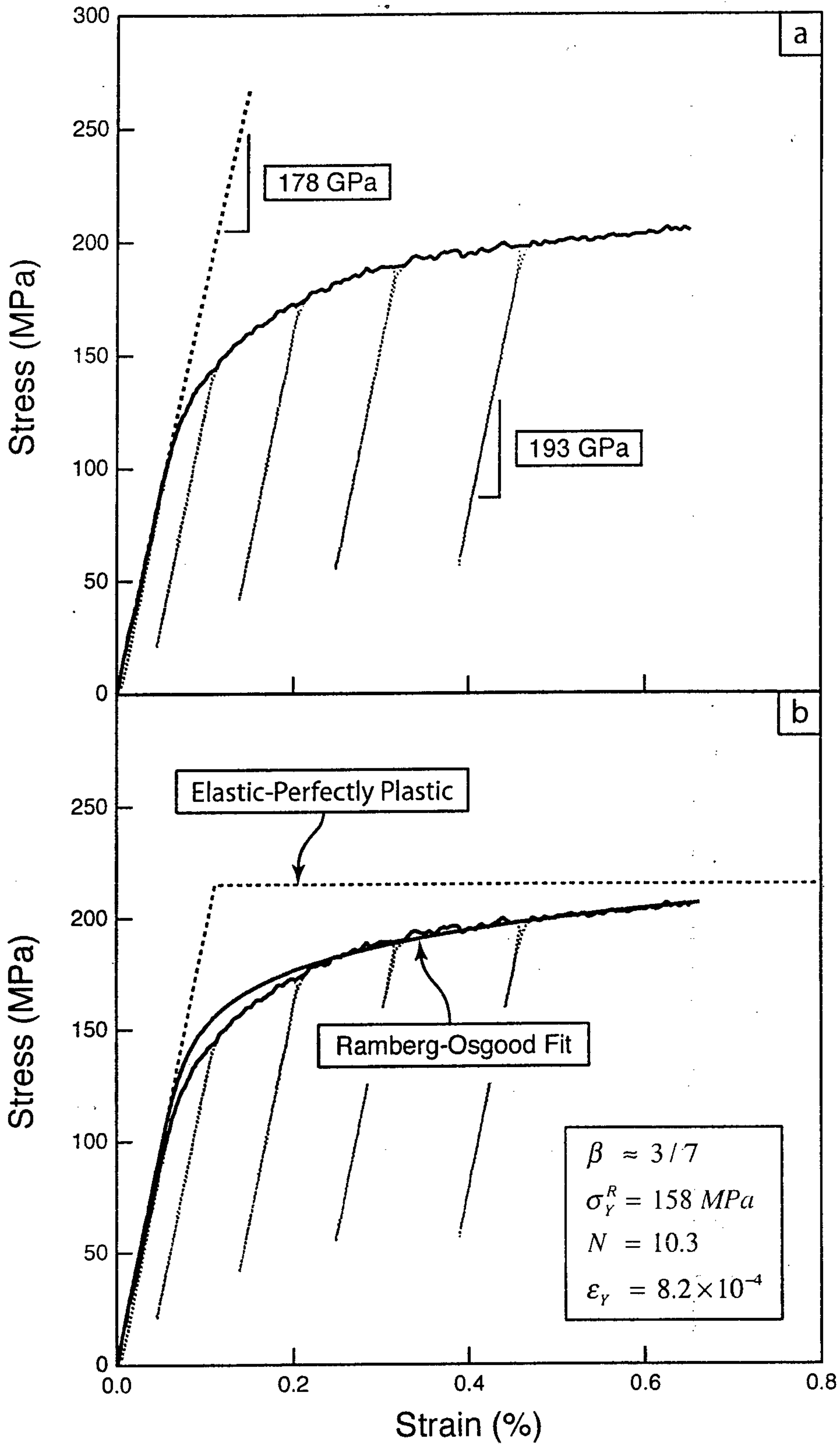
a
b
Stress (MPa)
Strain (%)
0
50
100
150
200
250
300
0.0
0.2
0.4
0.6
0.8
178 GPa
193 GPa
Elastic-Perfectly Plastic
Ramberg-Osgood Fit
$\beta \approx 3/7$
$\sigma_Y^R = 158\ MPa$
$N = 10.3$
$\varepsilon_Y = 8.2\times10^{-4}$

Figure 6

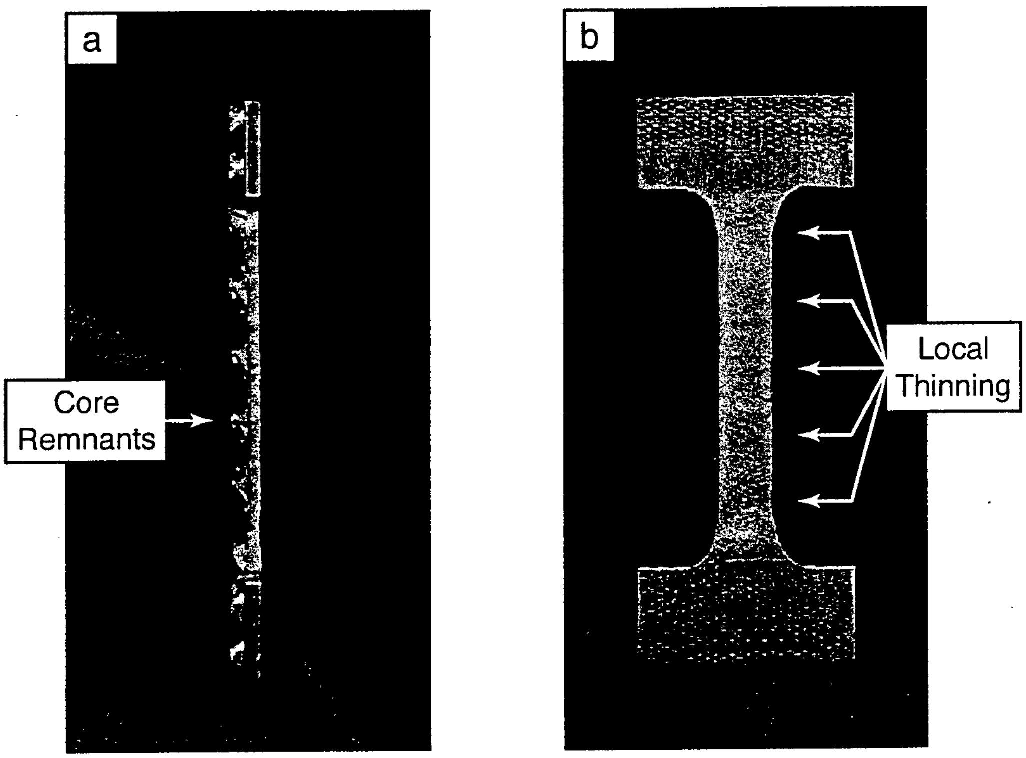

Figure 7

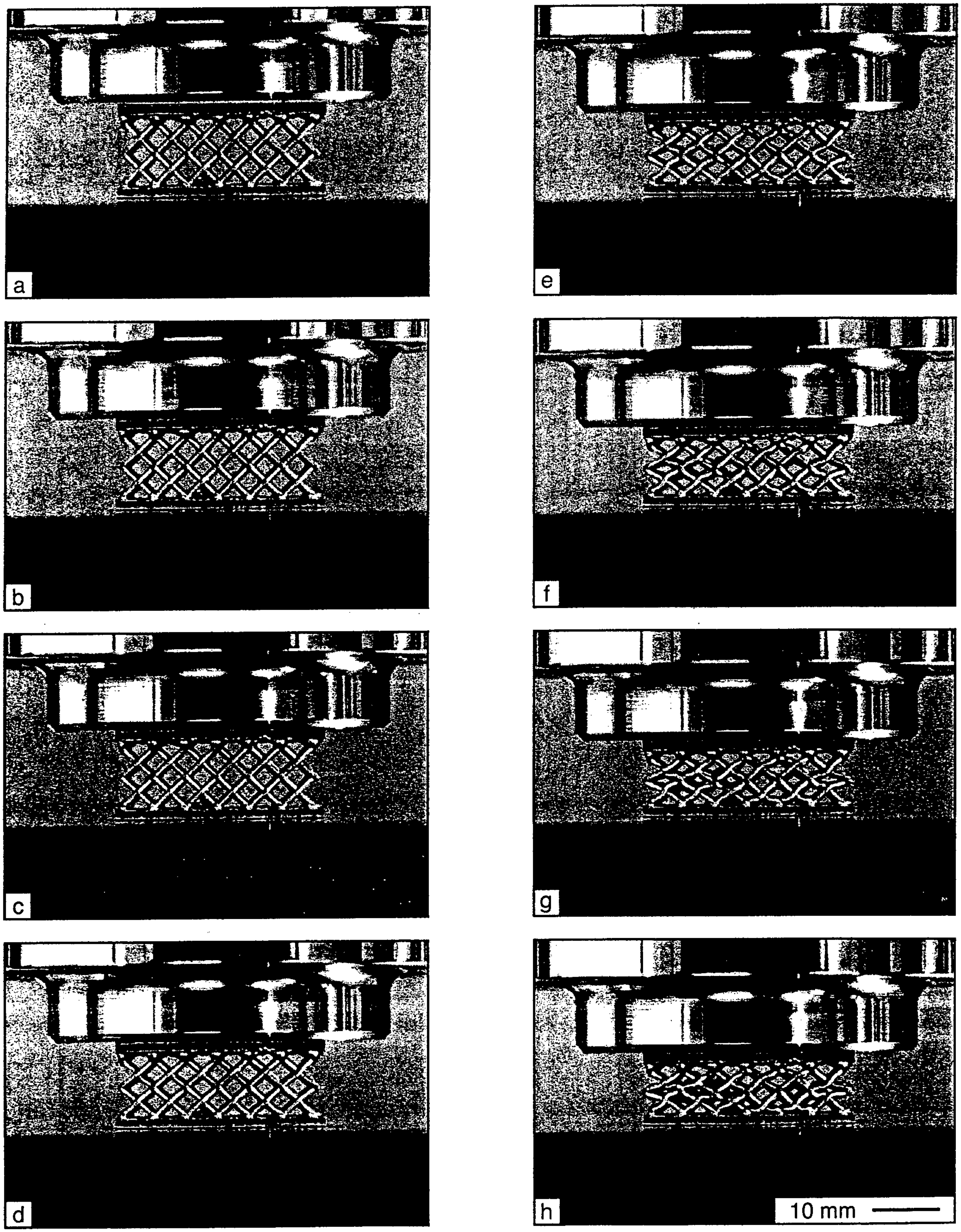

Figure 8

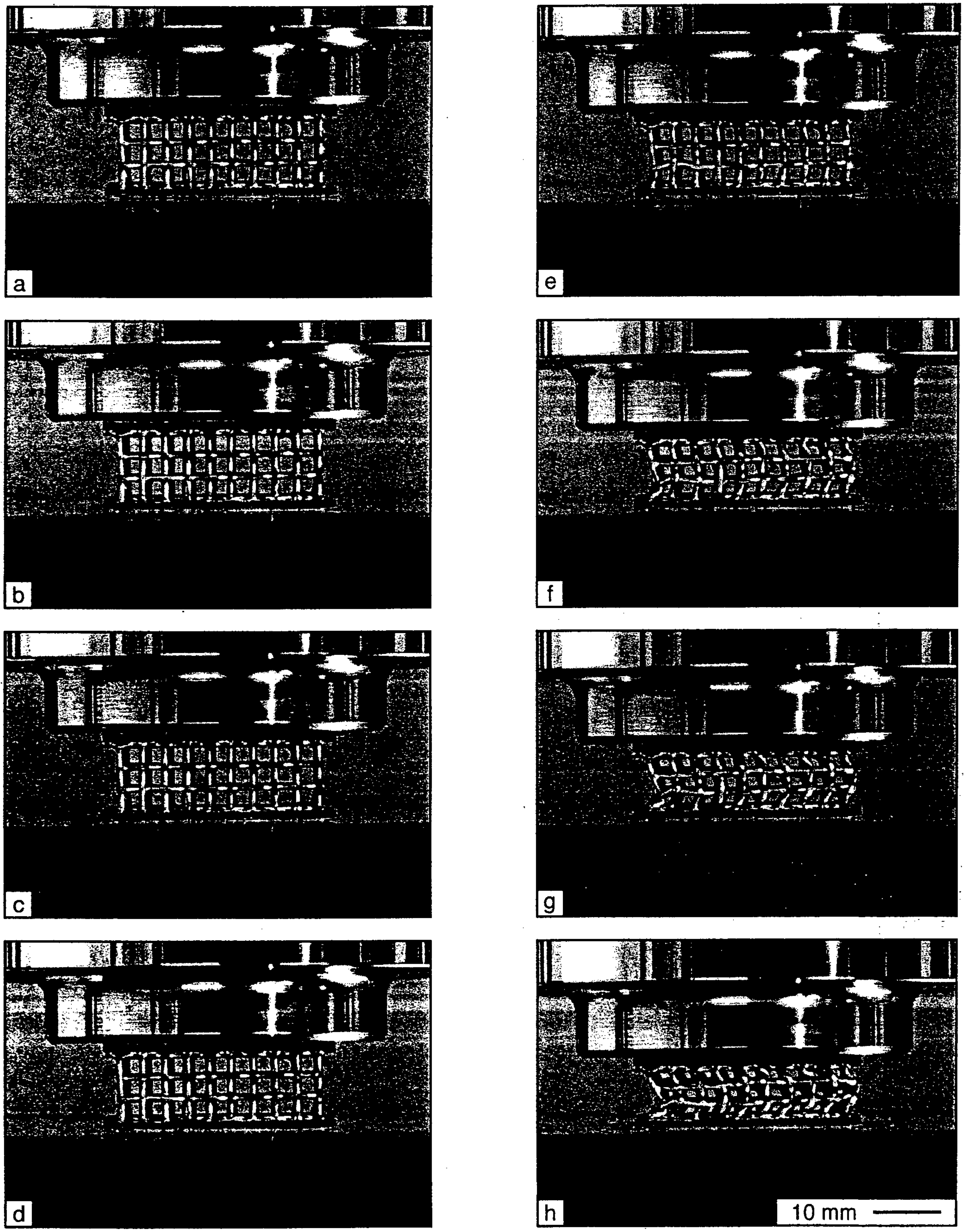

Figure 9

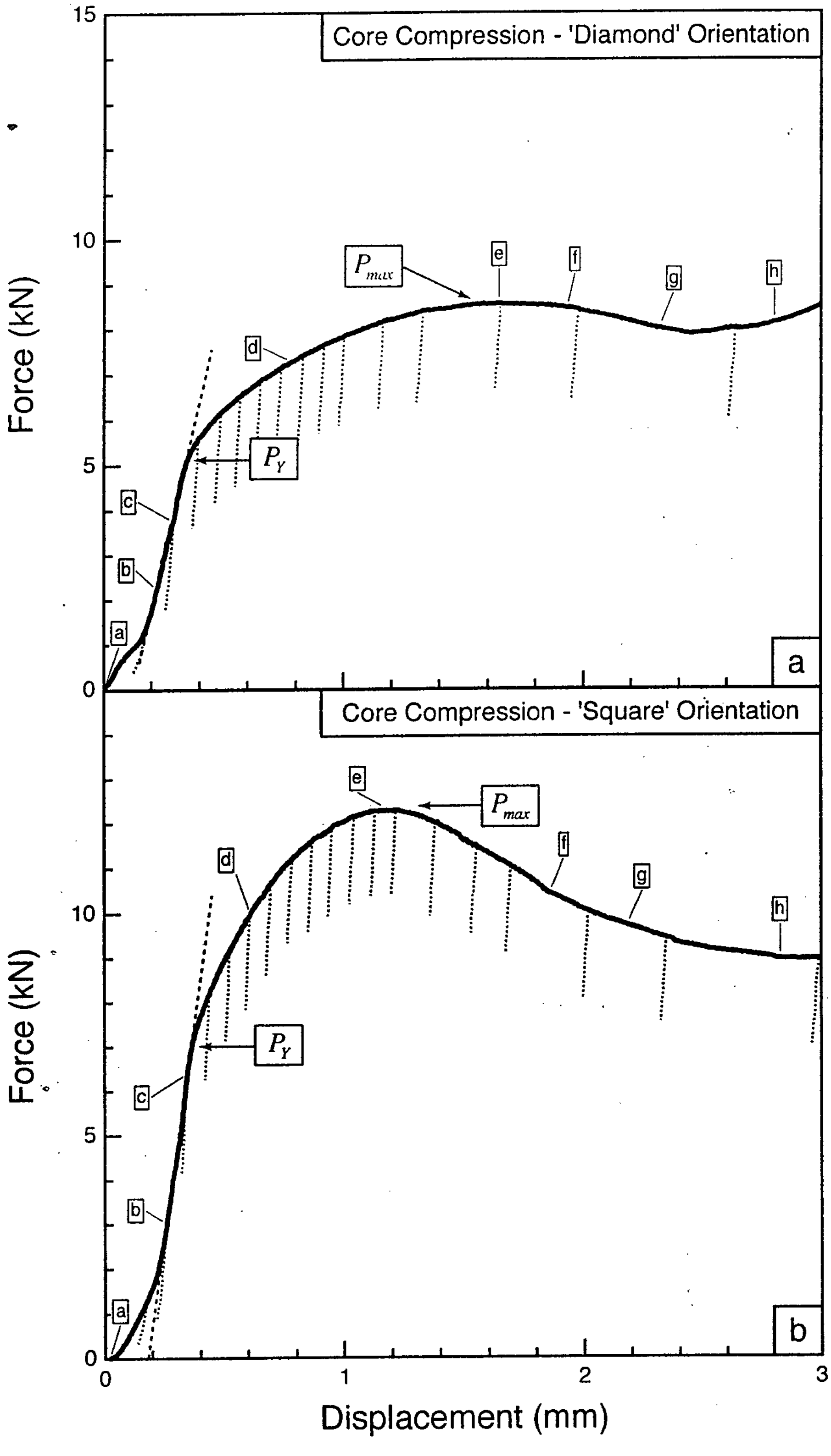
Core Compression - 'Diamond' Orientation
Core Compression - 'Square' Orientation
a
b
P_{max}
P_Y
e
f
g
h
d
c
b
a
Force (kN)
Displacement (mm)
0
5
10
15
0
1
2
3

Figure 10

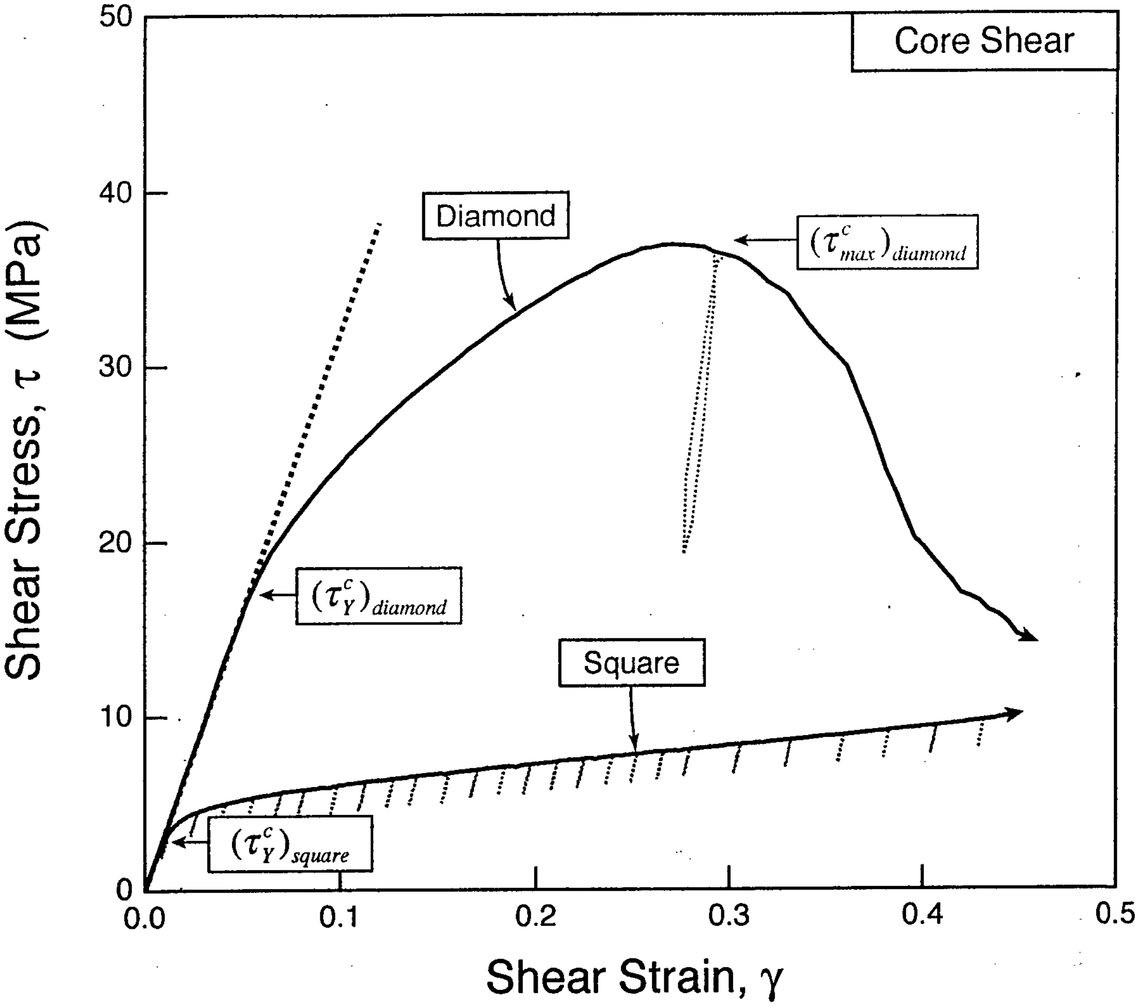Core Shear
Diamond
Square
$(\tau^c_{max})_{diamond}$
$(\tau^c_Y)_{diamond}$
$(\tau^c_Y)_{square}$
Shear Stress, τ (MPa)
Shear Strain, γ
0
10
20
30
40
50
0.0
0.1
0.2
0.3
0.4
0.5

Figure 11

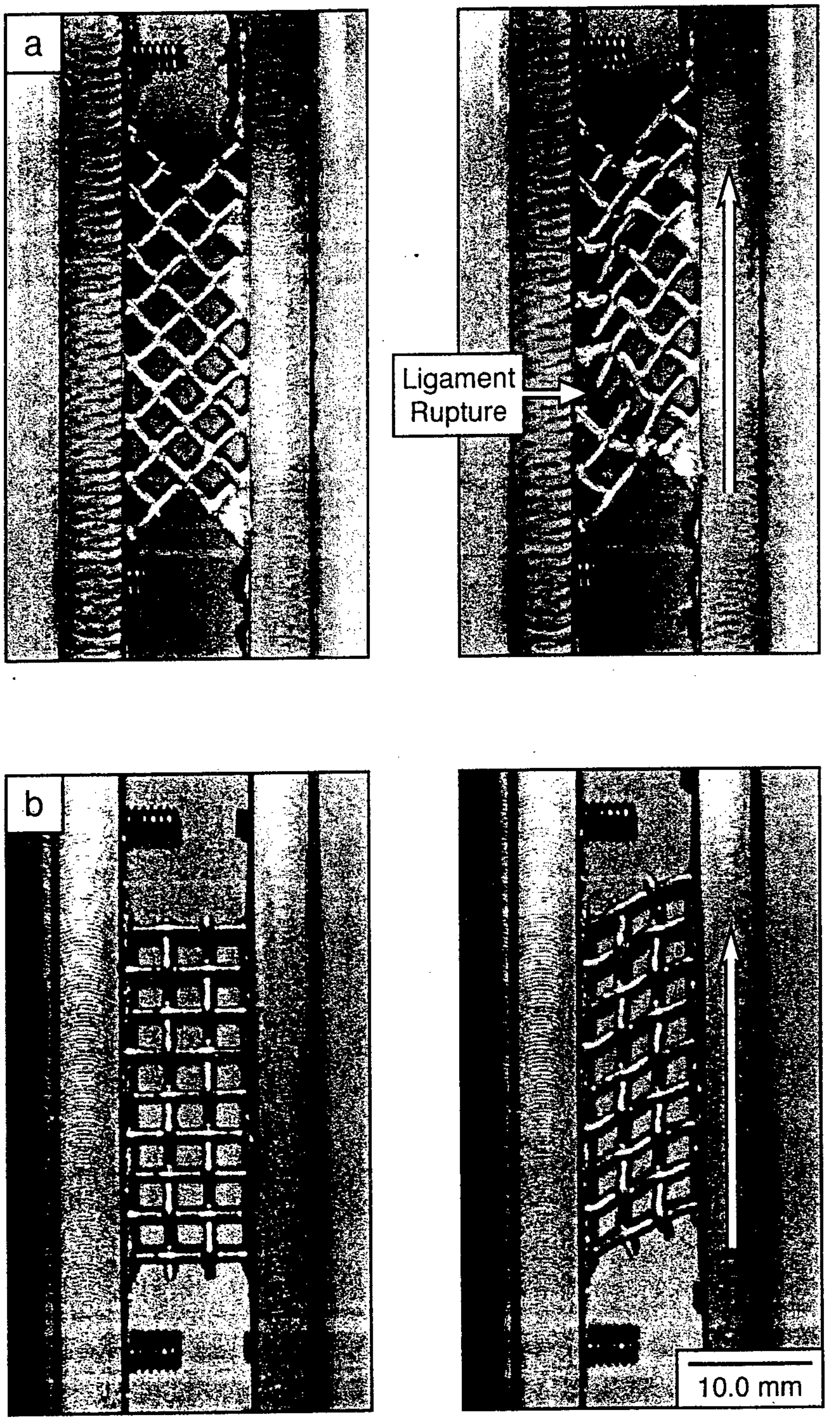

Figure 12

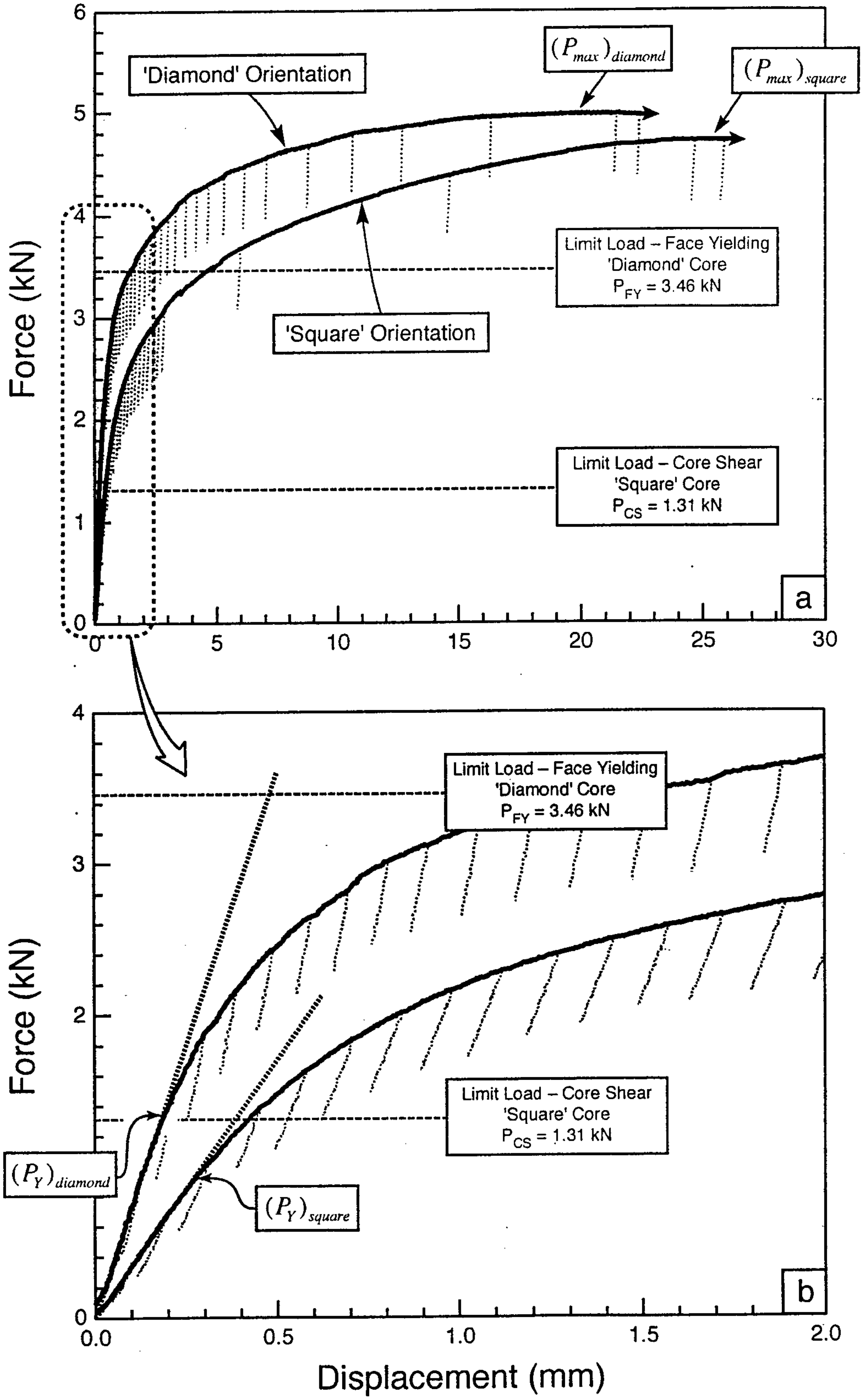
'Diamond' Orientation
$(P_{max})_{diamond}$
$(P_{max})_{square}$
Limit Load – Face Yielding
'Diamond' Core
P_{FY} = 3.46 kN
'Square' Orientation
Limit Load – Core Shear
'Square' Core
P_{CS} = 1.31 kN
a
Force (kN)
0
1
2
3
4
5
6
0
5
10
15
20
25
30
Limit Load – Face Yielding
'Diamond' Core
P_{FY} = 3.46 kN
Limit Load – Core Shear
'Square' Core
P_{CS} = 1.31 kN
$(P_Y)_{diamond}$
$(P_Y)_{square}$
b
Force (kN)
0
2
3
4
0.0
0.5
1.0
1.5
2.0
Displacement (mm)

Figure 13

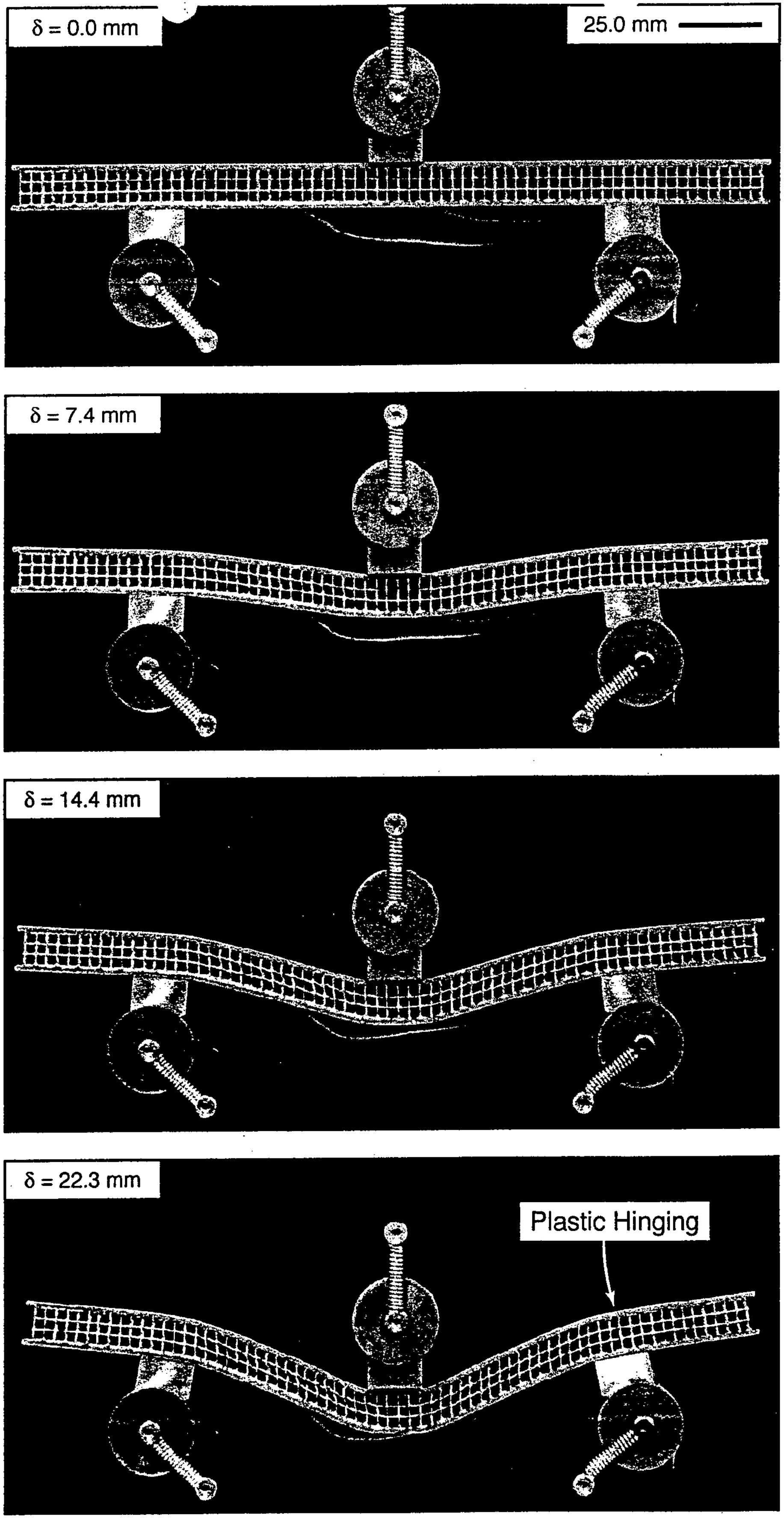

Figure 14a

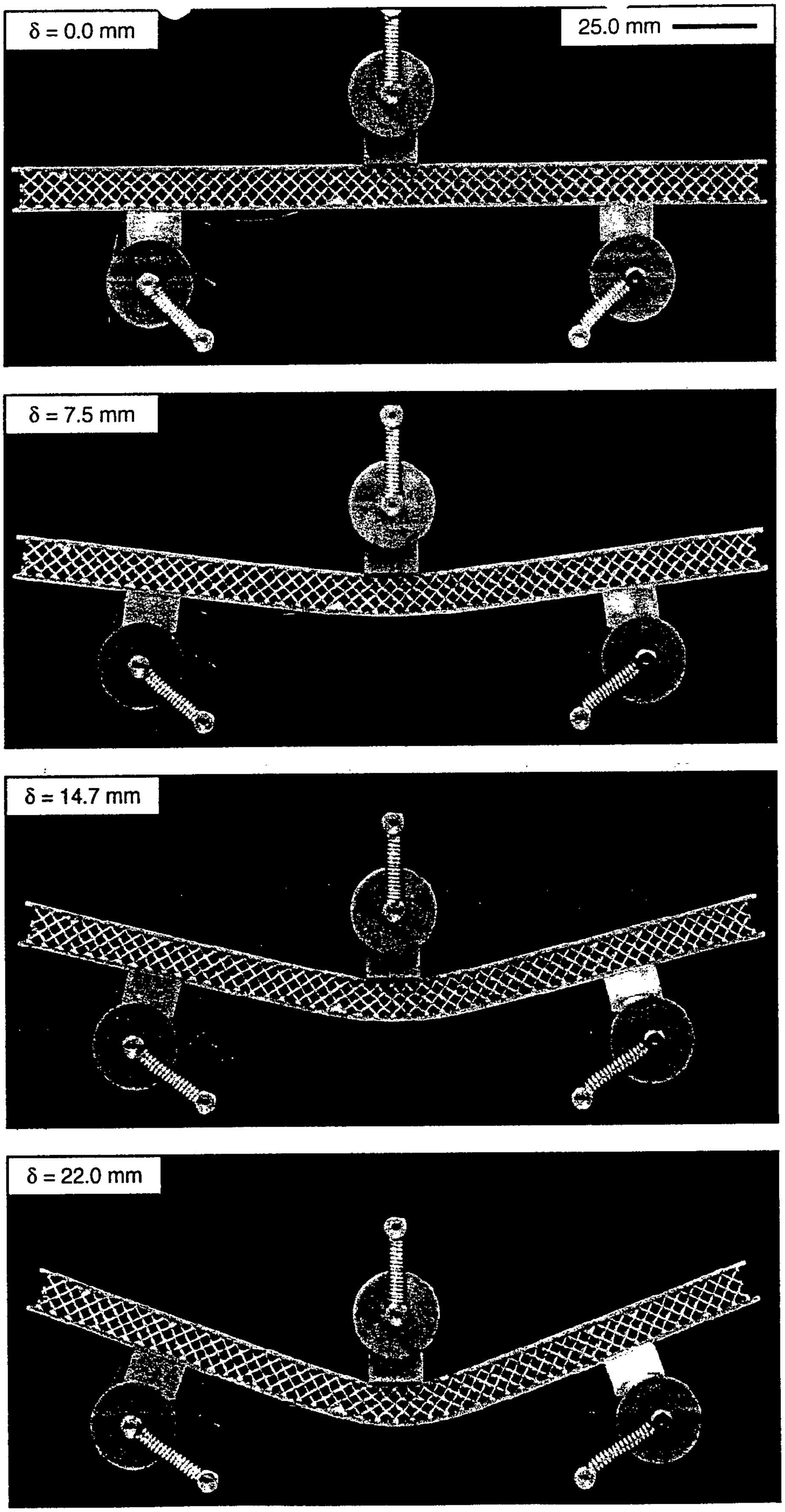

Figure 14b

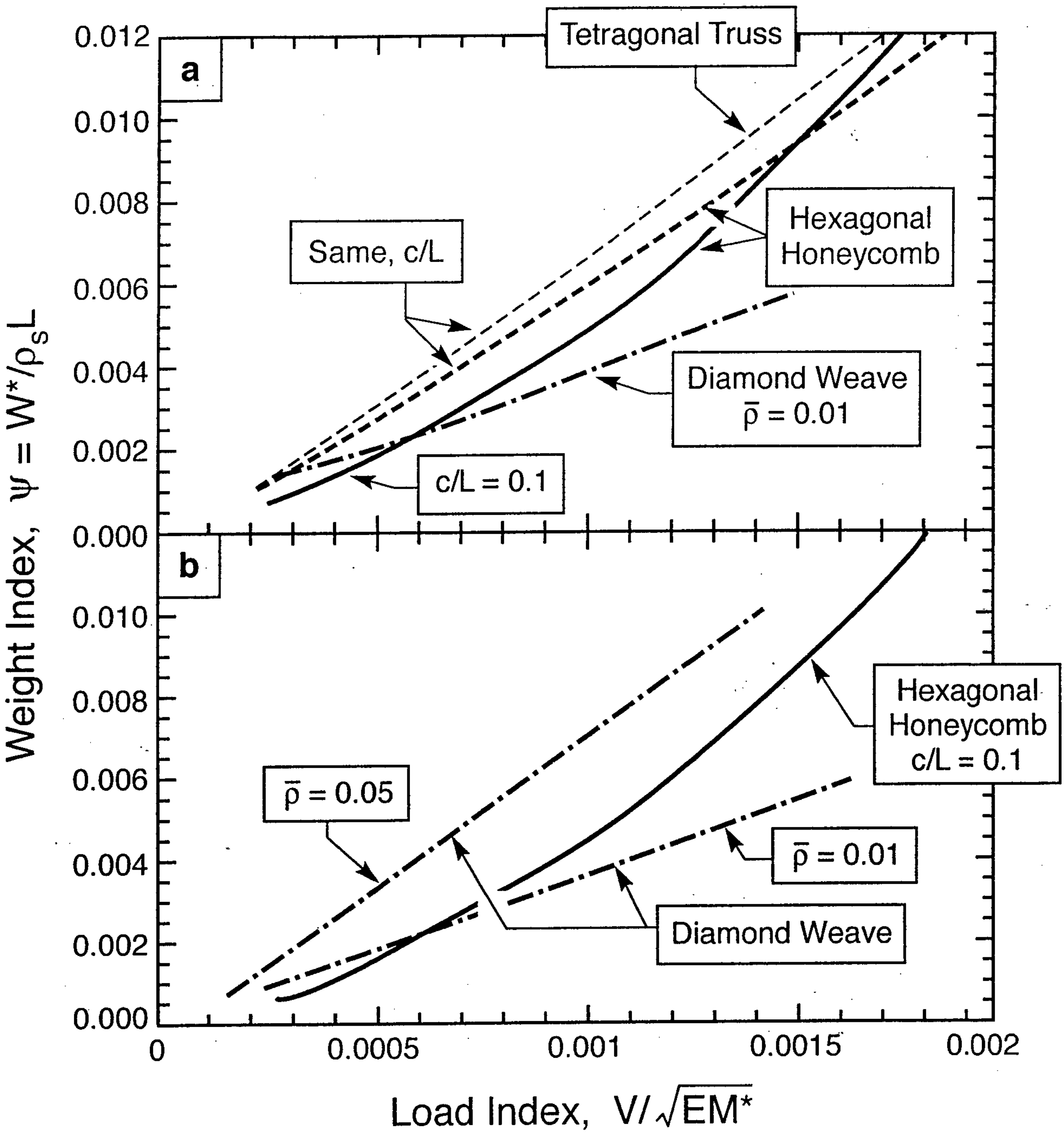
a
b
Tetragonal Truss
Same, c/L
Hexagonal Honeycomb
Diamond Weave
$\bar{\rho} = 0.01$
c/L = 0.1
Hexagonal Honeycomb
c/L = 0.1
$\bar{\rho} = 0.05$
$\bar{\rho} = 0.01$
Diamond Weave
Weight Index, $\psi = W^*/\rho_s L$
Load Index, $V/\sqrt{EM^*}$
0.000
0.002
0.004
0.006
0.008
0.010
0.012
0
0.0005
0.001
0.0015
0.002

Figure 15

PERFORMANCE OF SANDWICH PLATES WITH TRUSS CORES

Nathan Wicks and John W. Hutchinson

Division of Engineering and Applied Sciences
Harvard University
Cambridge, MA 02138

Abstract

Sandwich plates with truss cores fashioned from straight struts have distinct advantages relative to other constructions, including those with honeycomb cores. In addition to opportunities afforded by their open architecture, the truss core sandwich plates meet or exceed the load carrying capacity of other competitive constructions. The weight of truss core sandwich plates subject to a crushing stress and arbitrary combinations of bending and transverse shear are optimized subject to buckling and plastic yielding constraints and then compared with the weight performance of other types of optimized plates. Several issues central to the optimization process are addressed by a fundamental model study. These include the relation of designs based on a pure moment loading to those based on combined moment and transverse shear and the accuracy needed to model the various modes of buckling that must be taken into account in the design process.

Keywords: Sandwich plates; Truss cores; Optimal design; Buckling; Plastic yielding

1. Introduction

New focus on sandwich plates with truss cores has been motivated by potential multifunctional applications that exploit their open architecture as well as their apparent superior strength and stiffness (Evans et al., 2001). Moreover, new methods have been devised which permit "micro" plates with truss cores to be manufactured (Brittain et el., 2001). In the present context the terminology "truss core" refers to a core constructed from beam elements but not folded plates, as is sometimes implied. A preliminary study (Wicks and Hutchinson, 2001) has revealed that the performance of optimized sandwich plates with truss cores is competitive with more widely used constructions, including sandwich plates with honeycomb cores and stringer stiffened plates. A more extensive study of the performance of optimized truss core sandwich plates is undertaken in the present paper. We begin by investigating the optimal design of a model two-dimensional truss structure subject to pure bending (see Fig. 1). The various buckling modes of this structure can be analyzed exactly, providing insights into the validity of the approximations that are usually invoked in the optimal design of more complicated structures such as truss core sandwich plates. The model problem also reveals the connection between an optimal configuration designed to carry a pure moment and its counterpart designed to carry a combination of moment and transverse shear force. The second part of the paper specifically addresses the optimization of sandwich plates with truss cores subject to a crushing stress, bending, and transverse shear. The optimal configurations are compared to optimized plates with honeycomb cores.

2. A two-dimensional truss under pure moment

The infinite truss shown in Fig. 1 carries a moment $M = PH_c$. Each member is taken to have a solid circular cross section, with radius R_f for the horizontal members and radius R_c for the inclined core members. All members are made from the same material whose Young's modulus is E and yield stress in tension is σ_Y. All members have length L such that each triangular group is equilateral and $H_c = \sqrt{3}L/2$. Individual truss members are assumed to be slender (i.e. $R/L \ll 1$) and they are regarded as beam-columns. At the joints, the members are assumed rigidly connected to one another such that ends of each member meeting at a joint undergo the same displacements and rotation. Only in-plane deformations are considered.

2.1 Bifurcation buckling analysis: exact formulation

The analysis reveals all possible bifurcation buckling modes of the truss and the associated critical moments. Two distinct modes of importance emerge: a mode with half-wavelength equal to the member length wherein compressed members buckle between their joints and a longer wavelength mode.

As is customary in investigations of this kind, the pre-buckling load is approximated as being carried entirely by the horizontal members. This is an excellent approximation since the axial forces in the core members are zero and the elastic energy induced by bending in the pre-buckling response is extremely small. The bifurcation buckling analysis is given in the Appendix. Each member is represented as a beam-column, and its deformation is expressed in terms of the displacement components and rotation at its ends where it connects to adjoining members. The eigenvalue problem for the bifurcation mode is formulated exactly as an infinite set of finite difference equations involving the joint displacements and rotations. The equations admit sinusoidal solutions with a wavelength λ. With $M_c(\lambda)$ denoting the minimum eigenvalue at a given λ, the critical moment governing bifurcation is the lowest value of $M_c(\lambda)$ over the entire spectrum of λ. The full spectrum of eigenvalues is spanned for the range of wavelengths, $1 \le \lambda/(2L) < \infty$, as discussed in the Appendix.

Examples of the eigenvalue spectrum are plotted in Fig. 2. In the example with the larger ratio, R_c/R_f, the lowest eigenvalue is associated with the short wave mode ($\lambda = 2L$), corresponding to buckling of the compressed horizontal members between their joints, as depicted. The other eigenvalue spectrum shown is for very slender core members relative to the horizontal members. In this example, the lowest eigenvalue is associated with a longer wave mode ($\lambda \approx 3.6L$). This longer wave mode appears when the ratio, R_c/R_f, is very small, as will be quantified in the next section. The result from the approximate formula for the short wave eigenvalue that is presented in the next sub-section very accurately predicts the value plotted at $\lambda = 2L$ for both of the R_c/R_f values shown in Fig. 2.

2.2 Approximate results for short and longer wavelength buckling modes

The model problem is sufficiently simple such that it is possible to use results from the exact analysis to carry out an optimal design of the truss, and this will be done. The primary aim in conducting the model study, however, is to make use of the exact solution to assess the validity of using approximate formulas for the two buckling modes highlighted above. Optimal design of more complex structures under more general loads will generally employ approximate formulas of the type that will be introduced below. Thus, the present model problem affords an opportunity to quantitatively evaluate the accuracy of optimal configurations obtained using approximate buckling formulas.

The scheme for estimating the constraining effect of the lower portion of the structure on the bucking of the horizontal members in the *short wavelength mode* is depicted in Fig. 3a. The top compression member is constrained to have zero deflection at each joint and its rotation is constrained by a torsional spring. The spring constant is determined from the problem depicted in Fig. 3b where a moments of equal magnitude but alternating sign act on the remaining part of the truss. If the effect of the tensile load P on the bottom horizontal member is neglected, the torsional spring constant can be determined exactly as

$$K = M/\theta = \frac{8EI_c}{L}\left\{1+\frac{16}{3}q^2+\frac{8}{3}\frac{I_c}{I_f}\left(\frac{3}{4}-q\right)^2\right\}^{-1}, \quad q=\frac{3I_c}{8I_f+4I_c} \qquad (1)$$

where $I_f = \pi R_f^4/4$ and $I_c = \pi R_c^4/4$. If the horizontal members are much thicker than the core members such that $q \cong 0$, then $K = 8EI_c/L$, and this is identical to case where the core members are attached to a rigid foundation. The eigenvalue equation for the critical load P for an infinite beam having zero deflection and constrained by the above torsional spring at equally spaced distances L is

$$\sqrt{\frac{P}{EI_f}}\frac{L}{2}\cot\left(\sqrt{\frac{P}{EI_f}}\frac{L}{2}\right) = -\frac{KL}{4EI_f} \qquad (2)$$

By expanding (2) in a Taylor series about $\sqrt{P/EI_f}L=\pi$ (appropriate for sufficiently small KL/EI_f) and retaining up to and including terms of second order, one obtains the explicit approximation for the short wavelength buckling load

$$\sqrt{\frac{P}{EI_f}}\frac{L}{2} = \frac{\pi}{4}+\sqrt{\left(\frac{\pi}{4}\right)^2+\frac{KL}{4EI_f}} \qquad (3)$$

Results for the critical buckling moment from the exact analysis are compared in Fig. 3c with results from (3) for the full expression (1) for K, and the two sets are in good agreement for values of R_c/R_f up to about 0.5. In this figure, M_c^o denotes the critical moment with $K=0$ corresponding to simple support of a beam of length L. An even better approximation is seen to pertain for the case where the base horizontal members are taken to be rigid, i.e. $K = 8EI_c/L$.

The lowest eigenvalue is associated with a "long" wavelength mode only when R_c/R_f becomes smaller than a transitional value. Fig. 3d is a plot of the transition value of R_c/R_f as a function of R_f/L at which the long wavelength mode has the same eigenvalue (buckling moment) as the short wavelength mode ($\lambda = 2L$). The condition that ensures that the short wavelength mode is critical is well approximated by

$$\frac{R_c}{R_f} \geq -0.00313 + 2.62\frac{R_f}{L} \tag{4}$$

An approximate approach to estimating the critical load associated with the "long" wavelength mode has the compressed beam resting on an elastic foundation where the spring constant for normal displacement is obtained for triangular core elements rigidly supported at the bottom beam. The critical load from such an analysis is $P = 2\sqrt{EI_f S}$, where the spring constant is $S = 2H^2R_c^2\pi E / L^4$. Equating this critical load with the short wavelength critical load based on simple support at the nodes gives the approximation to the transition as $R_c/R_f = \pi^2 R_f / 2\sqrt{6}L = 2.01R_f/L$. The error in this result compared to the transition (4) is due to the fact that the so-called long wavelength mode, in fact, is not really long compared to the member length.

In the optimization described below for a pure moment loading, condition (4) will be invoked as a constraint on the design. It is conceivable that a lighter weight design might be attained if R_c/R_f were allowed to become even smaller. However, as we shall see, the inclusion of any realistic level transverse shear in the design process ensures that R_c/R_f is well above the transition ensuring that short wavelength buckling is critical.

2.3 Optimization of the two dimensional truss subject to pure moment

The dimensions of the truss members, R_c, R_f and L, are now identified that give the lightest weight given that the truss must support a prescribed moment M such that the force carried by the horizontal members is $P = 2M / \sqrt{3}L$. With w as the weight per unit volume of the material comprising the members, the weight per unit length of the truss is $W = 2\pi w\left(R_c^{\,2} + R_f^{\,2}\right)$. The horizontal members must not exceed yield requiring, $\sqrt{3}\pi\sigma_Y R_f^{\,2}L/2 \geq M$, while the short wavelength (3) and long wavelength (4) buckling conditions provide the respective constraints

$$\frac{\sqrt{3}}{2}\pi\left(\frac{\pi}{4} + \sqrt{\left(\frac{\pi}{4}\right)^2 + \frac{KL}{4EI_f}}\right)^2 \frac{ER_f^{\,4}}{L} \geq M \text{ and } \frac{R_c}{R_f} \geq -0.00313 + 2.62\frac{R_f}{L}$$

Plastic buckling of the horizontal members is not explicitly considered since it is excluded by the constraint on plastic yielding. The yielding constraint could be replaced by a constraint on plastic buckling, but this would have relatively little influence on the optimal design. Except for materials with very high strain hardening, the plastic buckling load is only slightly higher than the load at plastic yield and for this reason the constraint on plastic yielding is only slightly conservative.

The only length quantity other than unknown member dimensions is $(M/E)^{1/3}$. To put the optimization problem in non-dimensional form, introduce dimensionless member variables as $\vec{x} \equiv (x_1, x_2, x_3) = (R_f, R_c, L)/(M/E)^{1/3}$. The dimensionless optimization problem requires that the dimensionless weight, $W/[w(M/E)^{2/3}] = 2\pi(x_1^2 + x_2^2)$, be minimized with respect to $\vec{x}$ subject to the three constraints noted above, i.e.

$$\begin{aligned} &\frac{\sqrt{3}\pi}{2}\varepsilon_Y x_1^2 x_3 \geq 1 \\ &\frac{\sqrt{3}\pi^3}{8}\left(\frac{1}{2}+\sqrt{\frac{1}{4}+k}\right)^2 x_1^4 x_3^{-1} \geq 1 \qquad (5) \\ &\frac{x_2}{x_1} \geq -0.00313 + 2.62\frac{x_1}{x_3} \end{aligned}$$

Here, $\varepsilon_Y = \sigma_Y / E$ is the yield strain and k is

$$k = \frac{KL}{\pi^2 EI_f} = \frac{4}{\pi^2}(x_2/x_1)^4 \frac{(x_2/x_1)^4 + 2}{2(x_2/x_1)^4 + 1}$$

The yield strain is the only parameter in the dimensionless optimization problem. For a numerical example, take $\varepsilon_Y = 0.007$ corresponding to a high strength aluminum considered in the earlier study (Wicks and Hutchinson, 2001). The solution to the optimization problem is

$$x_1 = 1.4088 \quad x_2 = 0.19249 \quad x_3 = 26.457 \quad W/[w(M/E)^{2/3}] = 12.703 \qquad (6)$$

All three constraints in (5) are active for the solution.

3. The optimal two-dimensional truss subject to both moment and transverse shear force

Now suppose the same truss at its most severely loaded section carries a moment M and a shear force V. Let $\ell = M/V$ and assume that $\ell >> L$, which necessarily holds if the truss contains multiple sections. (A cantilever beam of length ℓ loaded with a force V at its free end experiences the moment $M = V\ell$ at its supported end.) The most heavily loaded core members are subject to forces $\pm 2V/\sqrt{3}$, depending on their inclination and the direction of the shear force, while the most heavily loaded horizontal members are subject to $2M/(\sqrt{3}L)$.

With M and V prescribed, the truss weight is to be minimized by selecting R_c, R_f and L subject to the three constraints imposed in the previous sub-section (long and short wavelength buckling and yield of the horizontal members) plus an additional two constraints: buckling and yield of the core members. The prior discussion of plastic buckling being excluded by the constraint on plastic yielding applies here as well. Now, the long and short wavelength buckling conditions for the compressed horizontal members are clearly approximate because the moment and, therefore the axial load, vary from member to member. As is customary in optimization studies, the conditions are nevertheless assumed to apply "locally". This approach is appropriate for a slender structure with $\ell >> L$ for which the axial forces will change by a small amount from member to member. Since the design is based on the maximum moment carried by the structure, this approach will underestimate the buckling loads and lead to a conservative design. A set of dimensionless variables different from that employed above is used: $\vec{x} \equiv (x_1, x_2, x_3) = (R_f, R_c, L)/\ell$. With this choice, $W/(w\ell^2) = 2\pi(x_1^2 + x_2^2)$ must be minimized with respect to $\vec{x}$ subject to the five constraints

$$\begin{aligned}
&\frac{\sqrt{3}\pi^3}{8}\left(\frac{1}{2}+\sqrt{\frac{1}{4}+k}\right)^2 x_1^4 x_3^{-1} \geq \Omega,\ \textit{short wavelength buckling}\\
&\frac{x_2}{x_1} \geq -0.00313 + 2.62\frac{x_1}{x_3},\ \textit{long wavelength buckling}\\
&\frac{\sqrt{3}\pi}{2}\varepsilon_Y x_1^2 x_3 \geq \Omega,\ \textit{yield of faces}\\
&\frac{\sqrt{3}\pi^3}{2} x_2^4 x_3^{-2} \geq \Omega,\ \textit{buckling of core}\\
&\frac{\sqrt{3}\pi}{2}\varepsilon_Y x_2^2 \geq \Omega,\ \textit{yielding of core}
\end{aligned} \tag{7}$$

Now there are two dimensionless parameters in the problem, ε_Y and the dimensionless load combination, $\Omega = V^3/(EM^2)$. The core members are taken as clamped at the ends in evaluating their elastic buckling loads, consistent with the optimal outcome wherein the truss has face members which are more than twice as thick as the core members.

The solution to the optimization problem can be determined with a nonlinear optimization routine such as that available in the IMSL Library for numerical analysis. For ε_Y=0.007, the dimensionless weight of the optimal truss is plotted against $V/(EM^2)^{1/3}$ in Fig. 4a, while the member dimensions for the optimal truss are shown in Figs. 4b, 4c, and 4d. This plot spans the entire range of loading for which the truss can be regarded as being a relatively slender beam. Note that at the largest value of $V/(EM^2)^{1/3}$ shown, L/ℓ is 0.20. The constraints active over the entire range plotted are short wavelength buckling, yield of faces, and elastic buckling of the core members. The aspect ratio of the core members is such that the long wavelength buckling mode is not at issue (i.e. the left hand side of second constraint in (7) greatly exceeds the right hand side).

The dimensionless results for the pure moment problem in (6) can be re-expressed in terms of the non-dimensional variables used in (7) and in Fig. 4 as

$$\frac{W}{w\ell^2}=\Omega^{2/3}\frac{W}{w(M/E)^{2/3}},\ (R_f,R_c,L)/\ell=\Omega^{1/3}(R_f,R_c,L)/(M/E)^{1/3} \qquad (8)$$

In this form, V is an inessential parameter that appears in the normalization on both sides of the equations in the same manner. Thus, the results for the truss optimized under a pure moment can be directly compared with the optimal truss designed to carry both moment and transverse shear force, and that comparison is included in the several parts of Fig. 4. Even when the shear force is very small, the pure moment design always underestimates the weight of a truss designed to carry both moment and shear force, although the error in weight is not very large. More significantly, the member dimensions of the truss designed to carry only a pure moment are very different from those based on the combined load design. While the optimal dimensions for L/ℓ and R_f/ℓ are comparable for the two cases, the pure moment analysis underestimates R_c/ℓ by as much as 400% compared to the combined load analysis over the load range plotted.

The optimal values of R_c/R_f for the combined moment and transverse shear case are all well within the range where the short wave buckling mode is the lowest buckling eigenvalue, as already emphasized. A lower weight design under pure moment optimization might exist if the constraint requiring the short wavelength mode to be critical were relaxed. This would hardly be worth pursuing given that essentially any transverse load applied to the structure excludes the possibility of the long wavelength mode. Sizing the core members to carry the transverse shear ensures that they are sufficiently substantial such that the long wavelength mode does not occur. For the two-dimensional truss beam, at least, a optimal design based on a pure moment appears to lead to a structure which is inadequate even when very small transverse shear loads are applied.

4. Optimization of Sandwich Plates with Truss and Honeycomb Cores

Optimizations of sandwich plates with truss cores and with honeycomb cores have been performed previously (Wicks and Hutchinson, 2001). In this section we optimize sandwich plates with truss cores subject to bending, transverse shear, and a crushing stress, as shown in Fig. 5. A more accurate approximation for the critical buckling stress of the face sheets than that employed earlier is introduced in this paper. A similar optimization is also performed for a honeycomb core sandwich plate to provide a weight performance comparison.

As in the examples discussed above, the design focuses on uniform plates even though for specific load distributions a tapered plate might be more weight efficient. The objective in this paper is to uncover the relative performance of truss core sandwich plates relative to honeycomb construction. More efficient designs might also make use of distinct materials for the core and faces. Here, to limit the possibilities, we restrict attention to a common material with weight density w for all core members and face sheets. The tetragonal truss core is comprised of tripods whose members all have length L_c and a solid circular cross-section of radius R_c. The weight per unit area of a plate with truss core and solid face sheets is

$$W = 2w\left[t_f + \frac{\pi}{\sqrt{3}}\frac{L_c R_c^2}{L_c^2 - H_c^2}\right] \tag{9}$$

with t_f as the face sheet thickness and H_c as the core thickness. Conventions for the tetragonal core structure are shown in Fig. 6a and 6b. The honeycomb core is a regular hexagon with height H_c (the core thickness), web thickness t_c, and web length L_c. The weight per unit area of sandwich plate with the honeycomb core is

$$W = 2w\left[t_f + \frac{H_c t_c}{\sqrt{3}L_c}\right] \tag{10}$$

where t_f is the thickness of each face sheet. The conventions for the honeycomb cores are shown in Fig. 6c.

The performance of tetragonal and honeycomb cores under shear and compression are of particular interest in sandwich plate design. Key design properties of the two cores are the elastic shear modulus, the crushing strength (both yield and elastic buckling), and shear strength (again, both yield and elastic buckling). These properties are tabulated in Fig. 7a, expressed in terms of the relative density (ρ_c) of the core defined as the volume of core material per volume of core. The properties in Fig. 7a are for a regular tetragonal core ($H_c/L_c = \sqrt{2/3}$). Of particular relevance is the scaling of the elastic buckling properties of these cores. For the tetragonal core, the buckling strength scales with the core relative density squared. For the honeycomb core, the buckling strength scales with the core relative density cubed. To illustrate the importance of this factor, the crushing strength properties of both cores as a function of core relative density have been plotted for a representative yield strain of 0.007 in Fig. 7b. For low density cores, typical of those used in sandwich plates, the tetragonal core is significantly stronger. This observation points to the potential advantage of tetragonal core structures for use in sandwich panels.

4.1 Sandwich Plate with Truss or Honeycomb Core

The general situation envisioned is again that of a uniform, infinitely wide plate subject to a maximum moment per unit length M and a maximum transverse shear force per unit length V. Bending occurs only about the direction parallel to the loading line. A wide plate under three-point loading with force per unit length $2P$ at the center is a prototypical example. Each half of the plate carries a uniform transverse shear load per length, $V = P$, and a maximum moment per length, $M = P\ell$, at the center, where ℓ is the half-length of the plate. In this example, the maximum moment and the maximum shear transverse force are attained at the same point, but that is not essential nor to be expected. In the general situation, the ratio of the maximum moment to the maximum transverse force (both per unit length),

$$\ell \equiv \frac{M}{V}$$

defines a quantity with dimensions of length which is central in the analysis. The study is limited to relatively thin plates in the sense that the thickness, H_c, is assumed to be small compared to ℓ. Thus, L_c, the core member length, will also be small compared to ℓ.

The four constraints in the optimization under moment and transverse shear are face sheet yielding, face sheet buckling/wrinkling, core member yield, and core member buckling. In this study, a constraint on crushing strength is also included because sandwich plates optimized without this constraint tend to be susceptible to crushing. This is especially true for honeycomb core plates. Consider a plate subject to a uniform crushing stress σ_c, as shown in Fig. 5. The tetragonal core member forces due to this crushing stress are $\sqrt{3}\sigma_c L_c d^2/2H_c$ where $d=\sqrt{L_c^2-H_c^2}$.

This crushing stress adds two more strength constraints to the optimization – core member yielding and buckling under crushing stress. The six constraints are thus

$$\frac{M}{t_f H_c} \le \sigma_Y \quad \text{(face sheet yielding)}$$

$$\frac{M}{t_f H_c} \le \frac{4E}{27(1-\nu^2)}\left(\frac{t_f}{d}\right)^2\left(\frac{\pi}{4}+\sqrt{\left(\frac{\pi}{4}\right)^2+\frac{9(1-\nu^2)d}{4Et_f^3}\kappa}\right)^2 \quad \text{(face sheet buckling)}$$

$$\text{where } \kappa=\frac{\pi E R_c^4}{4\sqrt{3}L_c d}\left(12-\frac{6d^2}{L_c^2}\right)+\frac{\pi G R_c^4}{4\sqrt{3}L_c d}\left(\frac{3d^2}{L_c^2}\right)$$

$$\frac{\sqrt{3}VdL_c}{H_c\pi R_c^2} \le \sigma_Y \quad \text{(core member yielding)} \tag{11}$$

$$\frac{\sqrt{3}VdL_c}{H_c\pi R_c^2} \le \frac{\pi^2 E R_c^2}{L_c^2} \quad \text{(core member buckling)}$$

$$\sigma_c \le \frac{2\sigma_Y \pi R_c^2 H_c}{\sqrt{3}L_c d^2} \quad \text{(core member crushing yield)}$$

$$\sigma_c \le \frac{2\pi^3 E R_c^4 H_c}{\sqrt{3}L_c^3 d^2} \quad \text{(core member crushing buckle)}$$

The elastic buckling stress of the compressed face sheet is associated with a sinusoidal mode varying only in the compression direction with nodes at the lines where the joints of the core tripods are attached to the face sheets. The κ factor above is used to model the rotational resistance of the core tripods on the face sheets at the nodes. This factor assumes that these tripods are clamped at the lower (tensile) face, based on the accuracy of the equivalent assumption in the earlier 2D problem (see Fig. 3b). No "long wavelength" constraint is present due to the results of the earlier 2D problem – the other core constraints (core yield and buckling) size the core members such that the long wavelength modes are suppressed. These buckling constraints for the core members are valid for members assumed to be clamped at the face sheets.

The weight per unit area and constraints are written in dimensionless form using $\ell = M/V$ and the four design variables $\vec{x} = \left(t_f/\ell, R_c/\ell, H_c/\ell, d/\ell\right)$. The normalized weight per unit area, $W/w\ell$, and the six dimensionless constraints involve only the parameters: σ_Y/E (taken as 0.007 in the calculations), ν (taken as 1/3 in the calculations), $V/\sqrt{EM}$, and the normalized crushing strength, σ_c/σ_Y. The solution to this optimization problem was again found using an IMSL subroutine. The details of the honeycomb core analysis can be found in the earlier study on this topic (Wicks and Hutchinson, 2001).

4.2 *Optimization with no constraint on the crushing stress*

The fully optimized (minimum weight) results for these structures in the absence of any constraint on crushing stress is shown in Fig. 8a. The plots are terminated at $V/\sqrt{EM} \cong 0.0018$, as larger values of $V/\sqrt{EM}$ generate plates that would not be considered thin, and thus the range of $V/\sqrt{EM}$ for which the results have been presented comprise the full range of relevance. The estimate of the face sheet buckling condition for the tetragonal truss core is more accurate than in the earlier study (Wicks and Hutchinson, 2001). However, there is little difference between the earlier results and those presented here. As before, the full honeycomb optimization results in plate thickness H_c of more than 0.10ℓ which is unrealistically thick. Here optimal results are shown both for the case where H_c/ℓ for the honeycomb core is constrained to be less than 0.10 and where H_c/ℓ is constrained to be identical to that of the optimal tetragonal core structure at the same $V/\sqrt{EM}$. Thus, with no crushing stress, the optimal honeycomb core structure is the lighter weight design, over the entire range of transverse shear load parameter, although the relative advantage is not large especially when the two cores have the same thickness.

In Fig. 8b the crushing strength of these optimal structures are plotted. Clearly the optimal tetragonal core structure is far superior in this regard. Indeed, it is seen that the honeycomb core is unusually vulnerable to crushing. The superiority of the tetragonal core is due to two effects – its inherent advantage at low densities, as illustrated in Fig. 7b and the fact that the optimal tetragonal core plate has somewhat higher core density than the optimized honeycomb core plate.

4.3 Optimization with a crushing stress constraint

To illustrate the effect of the crushing stress constraints, the optimization was run at a mid-range load combination corresponding to $V/\sqrt{EM} = 0.001$, over a range of crushing stress from 0 to 2% of the material yield stress, σ_Y. The results from this optimization are shown in Fig. 9. Both the minimum weight and the core relative densities are plotted. At the higher values of prescribed crushing stress (above about 1.4% of the material yield stress), the optimized tetragonal core is the lighter of the two structures. The honeycomb structure has a higher core density at the higher levels of crushing stress in order to counteract its inferior crushing resistance properties.

For the tetragonal core structures, face member yield and buckle are active constraints throughout the load range plotted. At low values of crushing stress (below about 1.5% of the yield stress), core member buckle (from the transverse loads) is an active constraint. At higher values of crushing stress, core member crush buckling becomes active. The core members of the optimized tetragonal core have $H_c > \sqrt{2/3}L_c$ corresponding to members oriented closer to the perpendicular to the face sheet than is the case for a regular tetrahedron. This orientation increases both the crushing strength of the core and the ability of the core to resist face sheet buckling (by decreasing the wavelength of the buckle).

The full honeycomb optimization results in plate thickness H_c of more than 0.10ℓ over the low end of the loading range. This is not a thin plate and such a design would most likely not be considered in an application. In order to make a meaningful comparison between the plates with honeycomb and truss cores, H_c/ℓ for the honeycomb was constrained to be less than 0.10 over the entire optimization. With no crushing stress, the active constraints for the honeycomb plate are face yield, face buckle, and core web buckle. Above low levels of crushing stress (as low as 0.2% of the yield stress), the active constraints switch to face yield and core member crush buckling. These constraints remain active throughout the higher crushing stress levels shown in Fig. 9.

One final optimization comparison is shown in Fig. 10. In this example, the crushing stress is fixed at 2% of the yield stress of the material, while the $V/\sqrt{EM}$ load combination varies over the same range previously plotted. In the presence of this crushing stress, the optimal tetragonal core structure is actually lighter than the optimal honeycomb core structure over the entire range plotted, although the difference between the weights of the two designs is small. A design constraint requiring a crushing strength of 2% of the base material yield stress is not unreasonable. Constraints for certain applications might dictate even larger crushing strengths.

5. Conclusions

Truss core construction appears to be as efficient as honeycomb core construction for sandwich plates optimally designed to carry prescribed combinations of moment and transverse force when a realistic minimum crushing strength is imposed. If the constraint on the crushing strength is relaxed, optimized honeycomb core plates have a slight weight advantage, but their crushing strength is exceptionally low. By contrast, the truss core has an inherent crushing advantage at the low core densities typical of most sandwich plate designs. It is this advantage that wins the day when a design constraint on crushing strength becomes important. Given the very close competition between the two methods of construction from a weight perspective, the advantage outcome is likely to hinge on other issues such as ease of manufacture, vulnerability to delamination or moisture, and multi-functional capabilities. In each of these categories, truss core sandwich construction has distinct possibilities that may tilt the advantage in its favor.

Acknowledgements

This work was supported in part by the Office of Naval Research and in part by the Division of Engineering and Applied Sciences, Harvard University. Nathan Wicks acknowledges the fellowship support of the National Defense Science and Engineering Graduate Fellowship Program.

Appendix A. Bifurcation Buckling Analysis of the Planar Truss under Pure Moment

Figure 11 shows the unit cell for the finite difference analysis. In the j$^{\text{th}}$ cell, there are two types of nodes and four types of members. The force and displacement quantities are expanded in perturbation series about the pre-buckling state in the usual way i.e. $N_j^3 = -P + \xi \tilde{N}_j^3 + \ldots$, $N_j^4 = P + \xi \tilde{N}_j^4 + \ldots$, $w_j^k = \xi \tilde{w}_j^k + \ldots$, etc. The six equations of perturbed nodal equilibrium (force balance in two directions and moment balance, at each node type) can then be written in matrix form:

$$K_{ij}F_j = 0$$

where $\vec{F}$ is a vector of the 22 force-like quantities which enter into the perturbed equilibrium equations. (N_j^k, V_j^k, $M_j^k$are the axial force, shear force, and moment respectively in the k^th^ member of the j^th^ unit and u_j^k, w_j^k, θ_j^k are the displacements and rotation of the k^th^ type node of the j^th^ unit.) Thus, K is a 6 by 22 matrix.

Treating each member as a beam-column, the force quantities are related to the displacement components and rotations at the ends of the members:

$$F_i = B_{ij}U_j$$

where $\vec{U}$ is a vector of the 18 displacements and rotations at the j^th^ joints and the joints adjacent to these joints. B is a 22 by 18 matrix relating these quantities. These relations for a beam of length L with a compressive axial force P are:

$$N(0) = N(L) = -\frac{EA}{L}\left[u(L) - u(0)\right]$$

$$M(0) = -\frac{2EI}{L}\left[2C_{10}\theta(0) + C_{20}\theta(L) - \frac{3C_{30}}{L}\left(w(L) - w(0)\right)\right]$$

$$M(L) = \frac{2EI}{L}\left[2C_{10}\theta(L) + C_{20}\theta(0) - \frac{3C_{30}}{L}\left(w(L) - w(0)\right)\right]$$

$$V(0) = V(L) = \frac{6EI}{L^2}\left[C_{30}\left(\theta(0) + \theta(L)\right) - \frac{2C_{40}}{L}\left(w(L) - w(0)\right)\right]$$

where A is the member cross-sectional area and C_{10}, C_{20}, C_{30}, and C_{40} are the stability functions (Bleich, 1952) defined as:

$$C_{10} = \frac{\overline{P}\left(\sin\overline{P} - \overline{P}\cos\overline{P}\right)}{4\left(2 - 2\cos\overline{P} - \overline{P}\sin\overline{P}\right)} \quad C_{30} = \frac{\overline{P}^2\left(1 - \cos\overline{P}\right)}{6\left(2 - 2\cos\overline{P} - \overline{P}\sin\overline{P}\right)}$$

$$C_{20} = \frac{\overline{P}\left(\overline{P} - \sin\overline{P}\right)}{2\left(2 - 2\cos\overline{P} - \overline{P}\sin\overline{P}\right)} \quad C_{40} = \frac{\overline{P}^3\sin\overline{P}}{12\left(2 - 2\cos\overline{P} - \overline{P}\sin\overline{P}\right)}$$

where $\overline{P} = \left(PL^2/EI\right)^{\frac{1}{2}}$ is the dimensionless load parameter used in the beam analysis. These relations can be analytically continued to cases with tensile or zero axial load.

Solutions are assumed of the periodic form $u_j^1 = e^{i\mu j}C_1$, $w_j^1 = e^{i\mu j}C_2$, etc. Displacement quantities are then expressed as:

$$U_k = e^{i\mu j}D_{km}C_m$$

where the C_m are 6 complex constants that determine the buckling mode. The set of equilibrium equations can then be written:

$$K_{ij}B_{jk}D_{km}C_m = 0$$

In order to find bifurcation solutions, the matrix $K_{ij}B_{jk}D_{km}$ must be singular. In dimensionless form, this matrix is a function of the dimensionless quantities μ, R_f/L, R_c/L, and M/EL^3. Physically, these quantities are the wave-number of the periodic solution, the slenderness ratios of the horizontal and core members, and the dimensionless buckling moment (the eigenvalue of the system).

Computations were performed to calculate the lowest eigenvalue (M/EL^3) for a given set of $(\mu, R_f/L, R_c/L)$. The determinant of the matrix is non-negative, dropping to zero at the eigenvalues and then increasing again. This is due to the fact that in this complex formulation the eigenvalues are double-roots. In the numerical computations, the eigenvalues were found by looking for zero-crossings of the derivative of the matrix determinant.

References

Bleich, F., 1952. Buckling Strength of Metal Structures. McGraw-Hill, New York, pp. 210-211.

Brittain, S., Sugimura, Y., Schueller, O.J.A., Evans, A.G., Whitesides, G.M., 2001. Fabrication and mechanical performance of a mesoscale, space-filling truss system. JMEMS 10, 113-120.

Evans, A.G., Hutchinson, J.W., Fleck, N.A., Ashby, M.F., Wadley, H.N.G., 2001. The topological design of multifunctional cellular metals. Progress in Materials Science 46, 309-327.

Wicks, N., Hutchinson, J.W., 2001. Optimal truss plates. Int. J. Solids Struct. 38, 5165-5183.

FIGURE CAPTIONS

Fig. 1 Geometry of the two-dimensional infinite model truss.

Fig. 2 Eigenvalue spectrum, $M_c(\lambda)$, for $R_f/L = 0.05$, for two core radius values ($R_c/L = 0.02$ and $R_c/L = 0.004$).

Fig. 3 Approximate analysis of the short wavelength buckling mode (a)-(c) and the border between the long and short wavelength buckling (d).

Fig. 4 Weight per unit length (a) and member dimensions (b)-(d) for optimally designed two-dimensional truss carrying moment M and shear force V for $\varepsilon_Y = 0.007$. The results for the truss designed to carry a pure moment M are also included for comparison.

Fig. 5 Loading situation for panels under transverse loading (a) and crushing stress (b).

Fig. 6 Conventions for tetragonal (a)-(b) and honeycomb (c) core structures. Transverse load lines are parallel to $A-A'$. In (b) solid core nodes are at the upper face sheet, and open nodes are at the lower sheet.

Fig. 7 Table of properties of regular tetragonal and honeycomb core sandwich panels (a). Crushing strength of regular tetragonal and honeycomb core sandwich panels as a function of relative density (b).

Fig. 8 Normalized weight per unit area of optimized tetragonal and honeycomb core sandwich panels subject to transverse shear and moment (a). Two cases of honeycomb panels have been considered: the core thickness fixed at $H_c/\ell = 0.1$; and the core thickness taken equal to that of the sandwich plate with truss core at the same value of $V/\sqrt{EM}$. Crushing strength of the optimized tetragonal and honeycomb core structures (b). The honeycomb panel results are for the core thickness fixed at $H_c/\ell = 0.1$. $(\varepsilon_Y = 0.007)$

Fig. 9 Top solid lines are minimum weights for tetragonal and honeycomb core structures subject to crushing stress as well as normalized transverse load value $V/\sqrt{EM} = 0.001$. Bottom dashed lines are the core relative densities for these optimized structures. $(\varepsilon_Y = 0.007)$

Fig. 10 Normalized weight per unit area of optimized tetragonal and honeycomb core sandwich panels subject to a crushing stress of $\sigma_c/\sigma_Y = 0.02$, as well as transverse shear and moment. Here the honeycomb core thickness has been constrained such that $H_c/\ell \leq 0.1$. $(\varepsilon_Y = 0.007)$

Fig. 11 Unit cell for exact 2D finite difference buckling analysis.

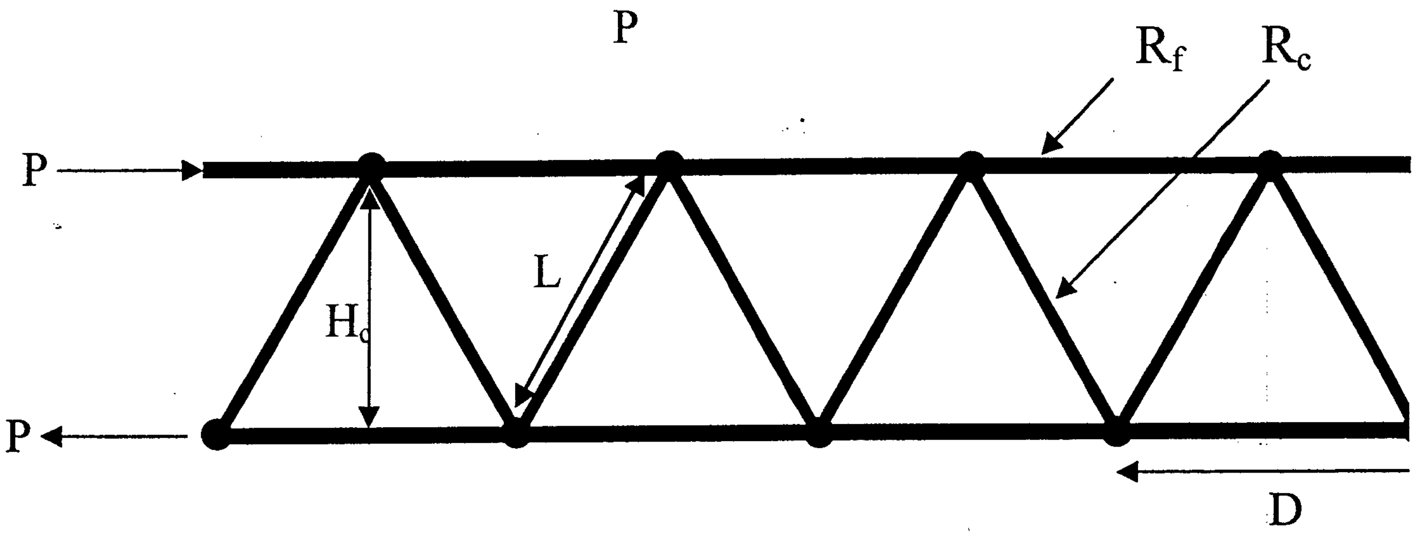

Figure 1

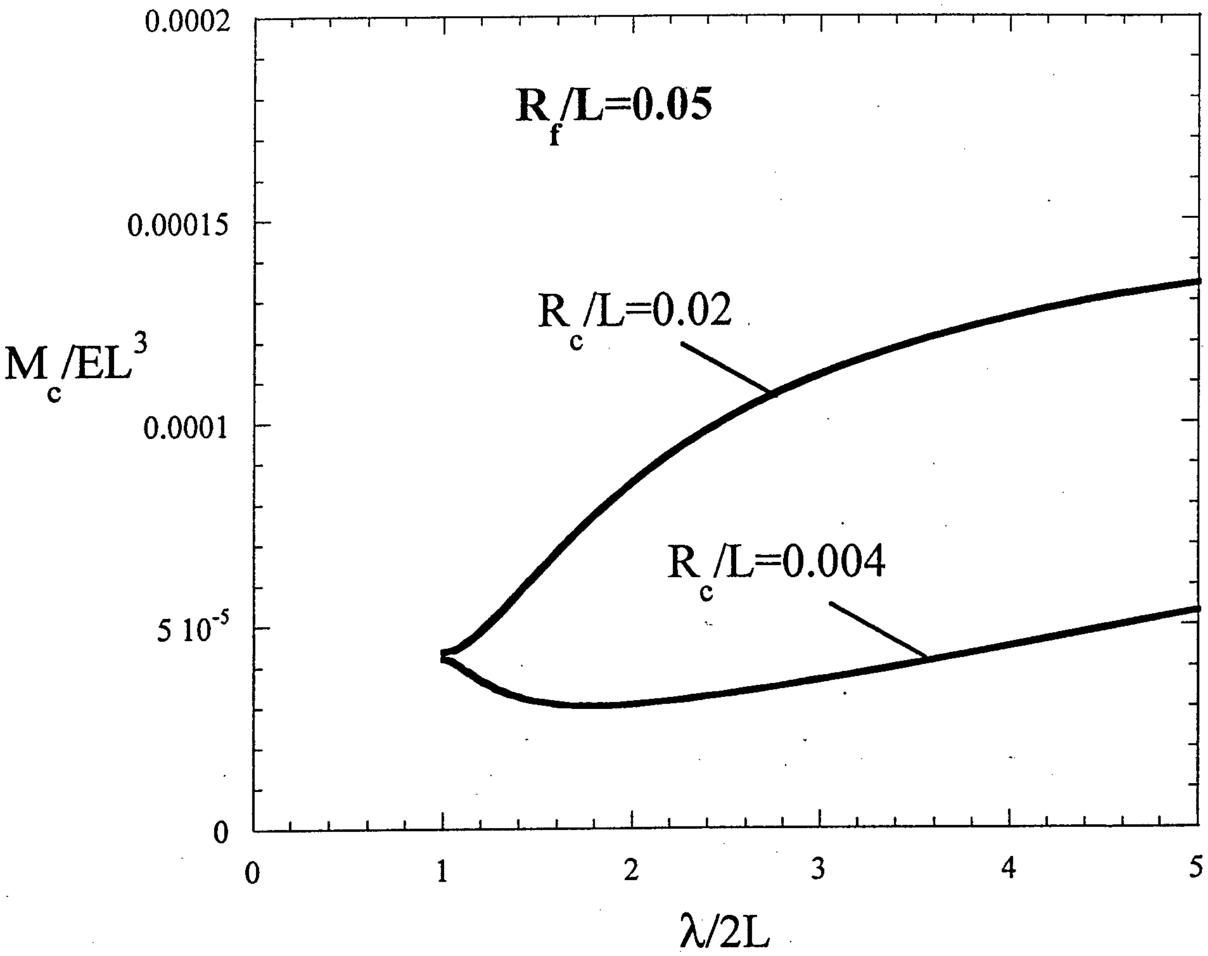
$R_f/L=0.05$
$R_c/L=0.02$
$R_c/L=0.004$
M_c/EL^3
0.0002
0.00015
0.0001
$5\ 10^{-5}$
0
0
1
2
3
4
5
$\lambda/2L$

Figure 2

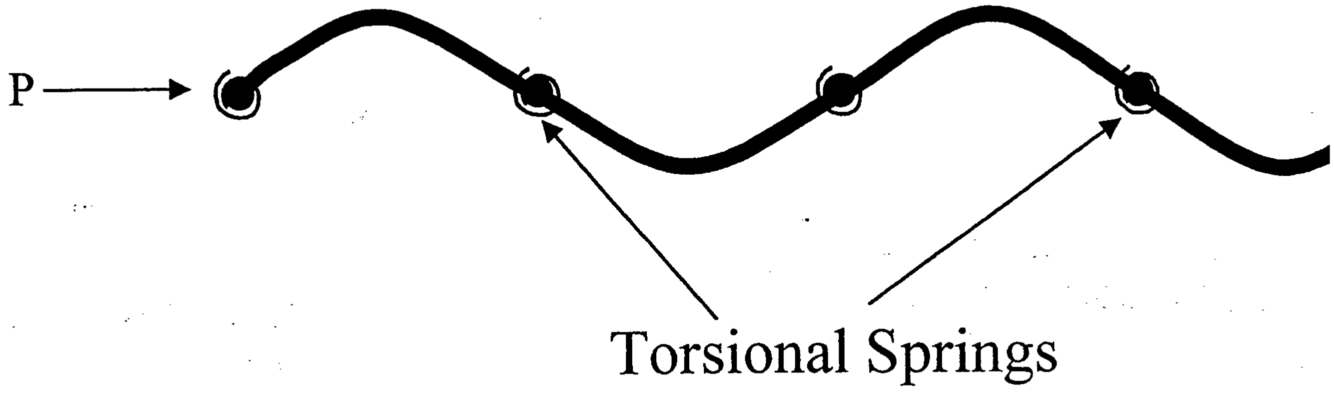
P
Torsional Springs

Figure 3a

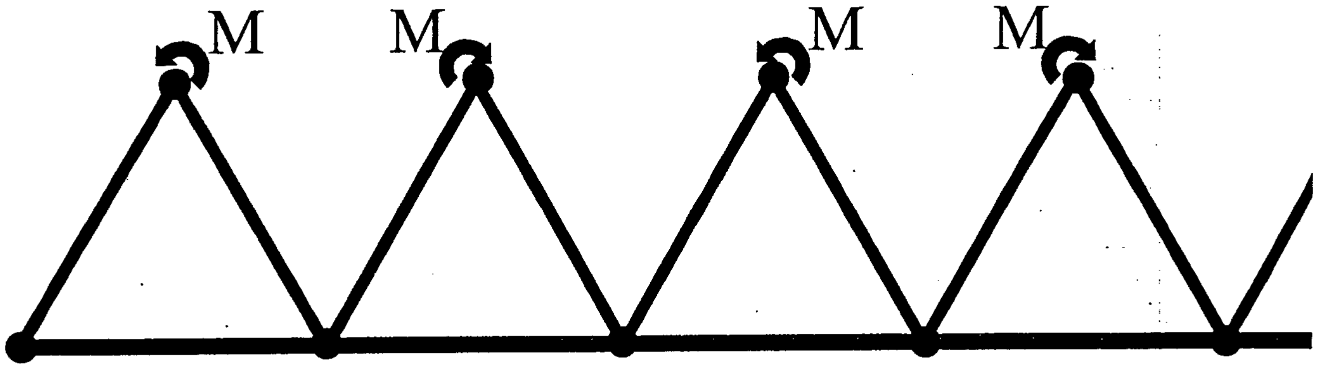

Figure 3b

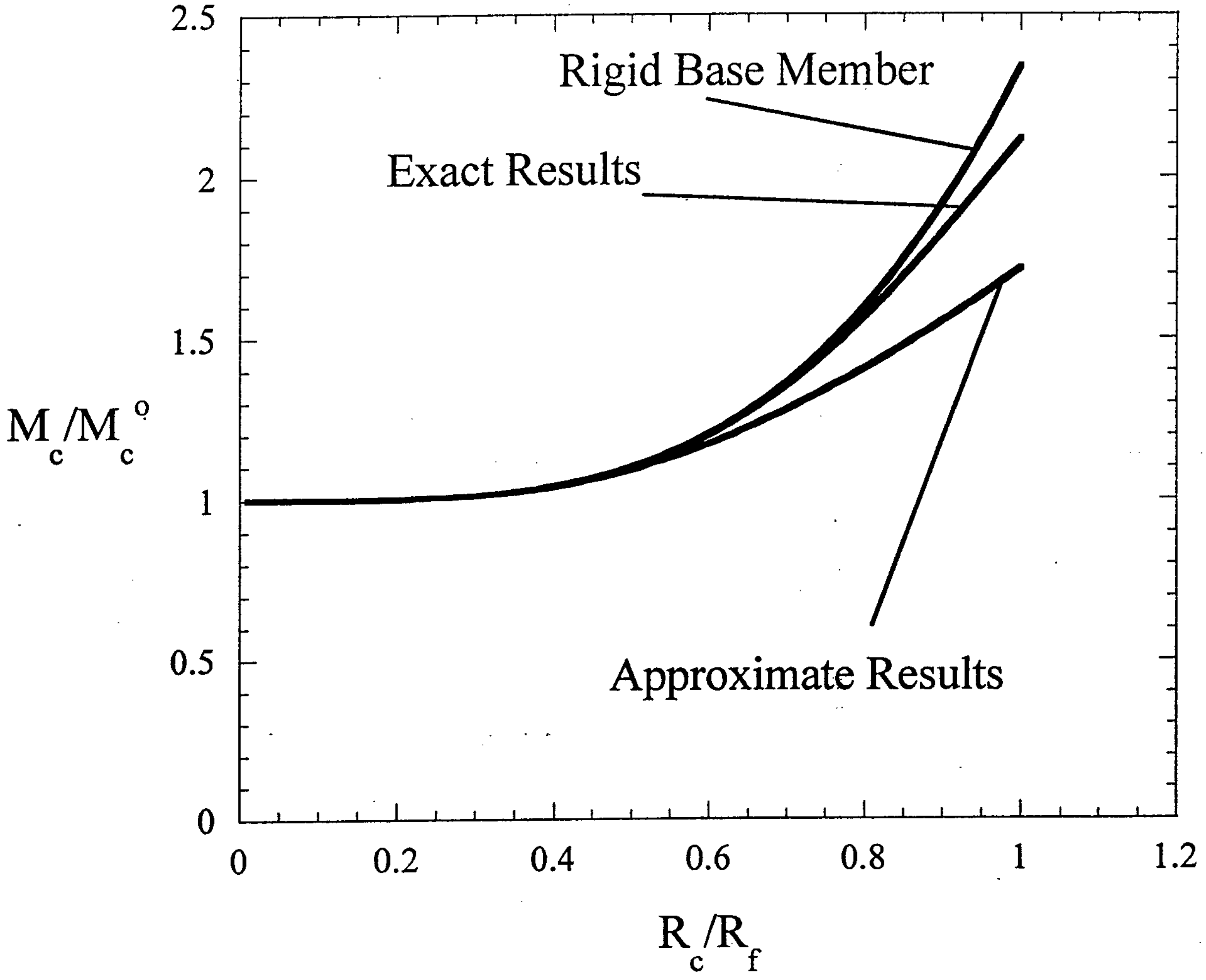

Rigid Base Member
Exact Results
Approximate Results
M_c/M_c^o
R_c/R_f
2.5
2
1.5
1
0.5
0
0
0.2
0.4
0.6
0.8
1
1.2

Figure 3c

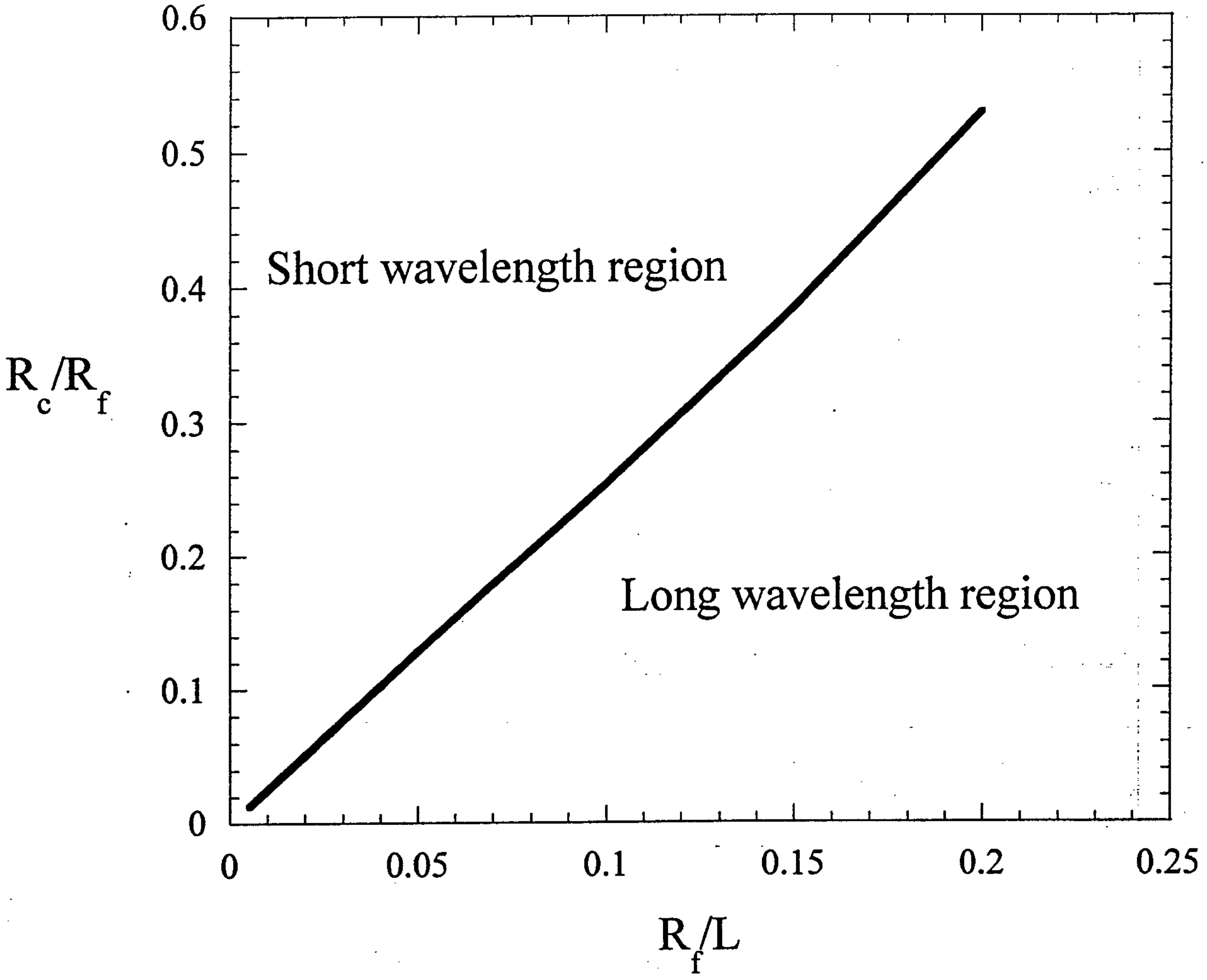
0.6
0.5
0.4
0.3
0.2
0.1
0
R_c/R_f
Short wavelength region
Long wavelength region
0
0.05
0.1
0.15
0.2
0.25
R_f/L

Figure 3d

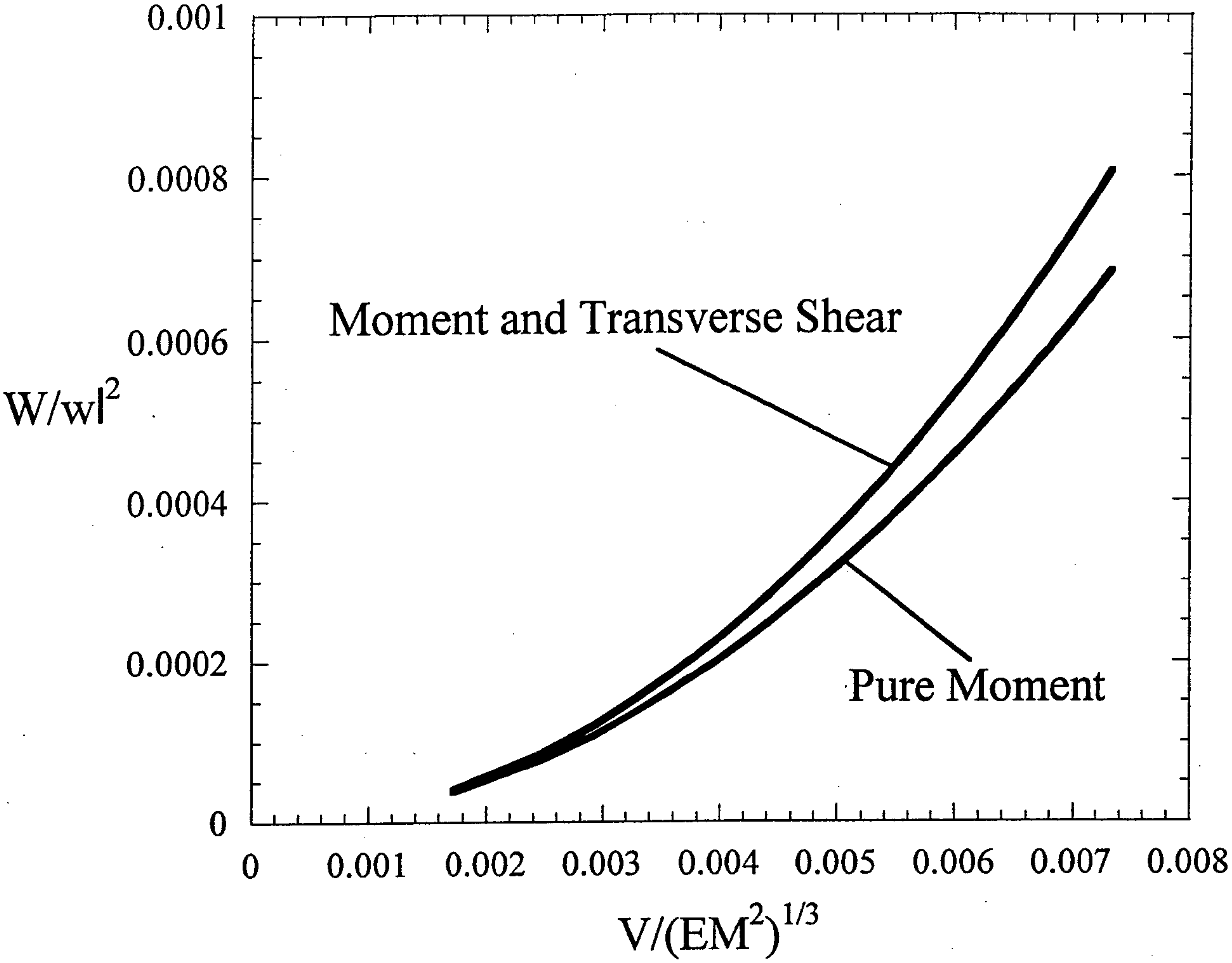
0.001
0.0008
0.0006
0.0004
0.0002
0
W/wl^2
Moment and Transverse Shear
Pure Moment
0
0.001
0.002
0.003
0.004
0.005
0.006
0.007
0.008
V/(EM^2)$^{1/3}$

Figure 4a

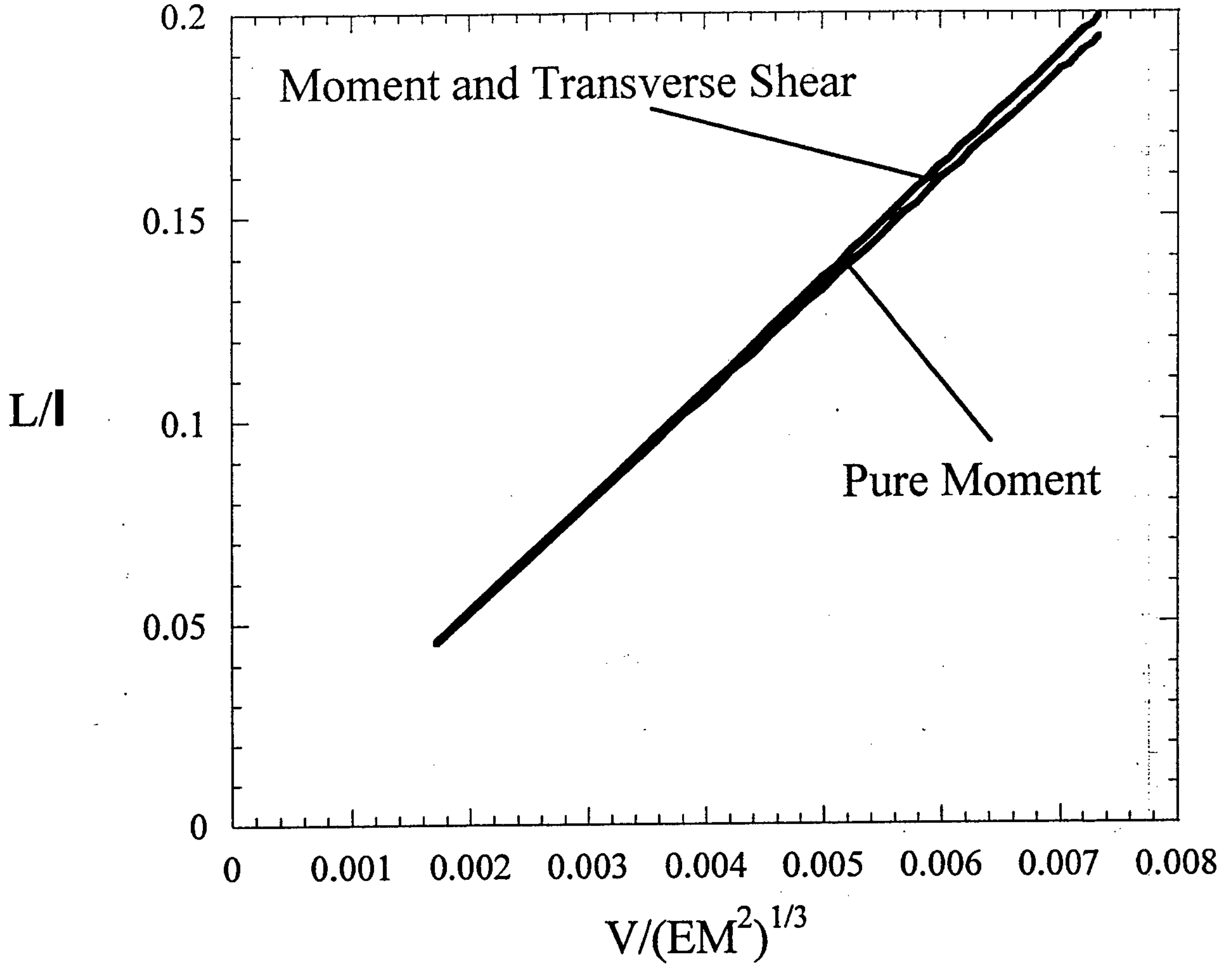

Moment and Transverse Shear
Pure Moment
L/l
0.2
0.15
0.1
0.05
0
0
0.001
0.002
0.003
0.004
0.005
0.006
0.007
0.008
V/(EM2)1/3

Figure 4b

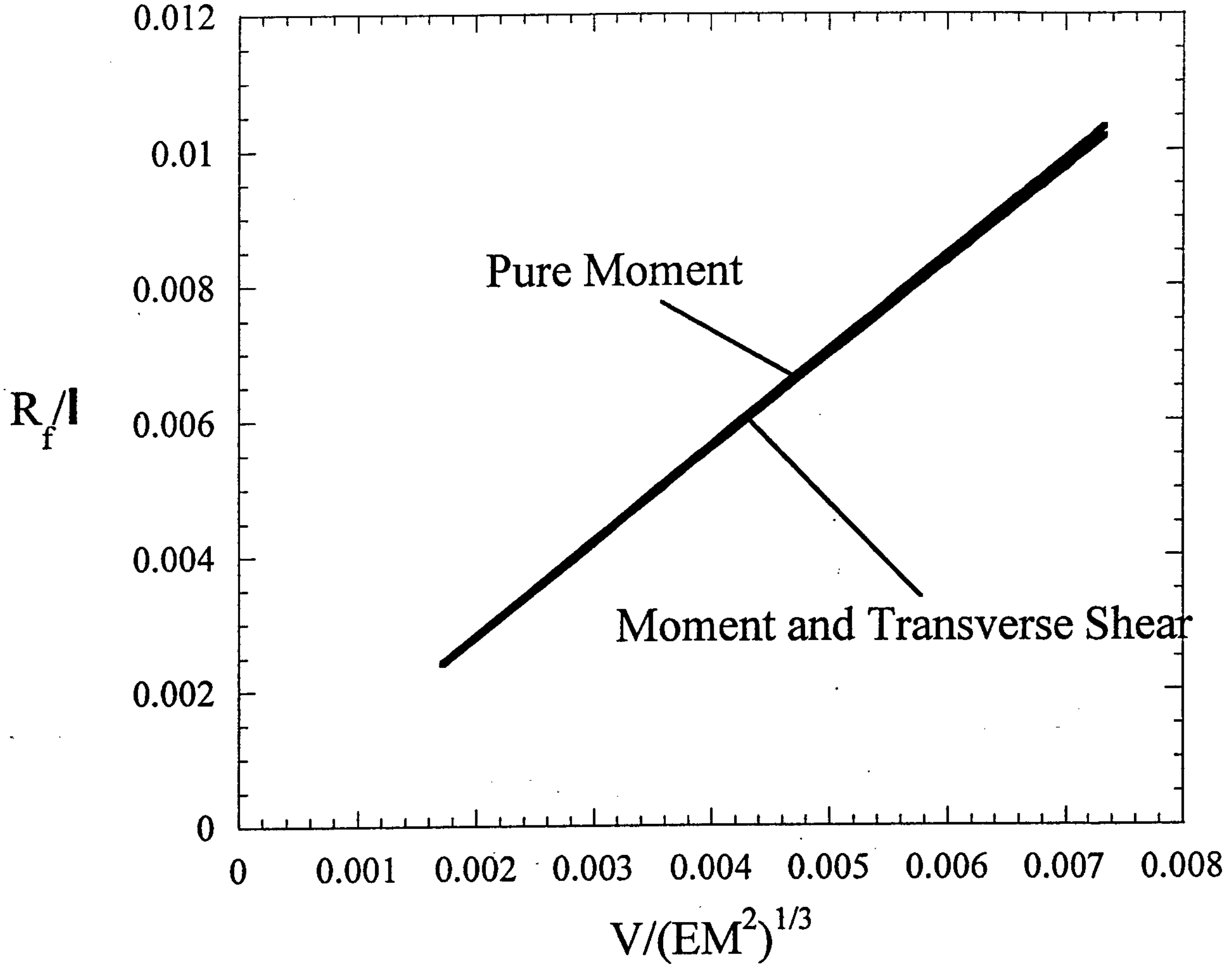
0.012
0.01
0.008
0.006
0.004
0.002
0
R_f/l
0
0.001
0.002
0.003
0.004
0.005
0.006
0.007
0.008
$V/(EM^2)^{1/3}$
Pure Moment
Moment and Transverse Shear

Figure 4c

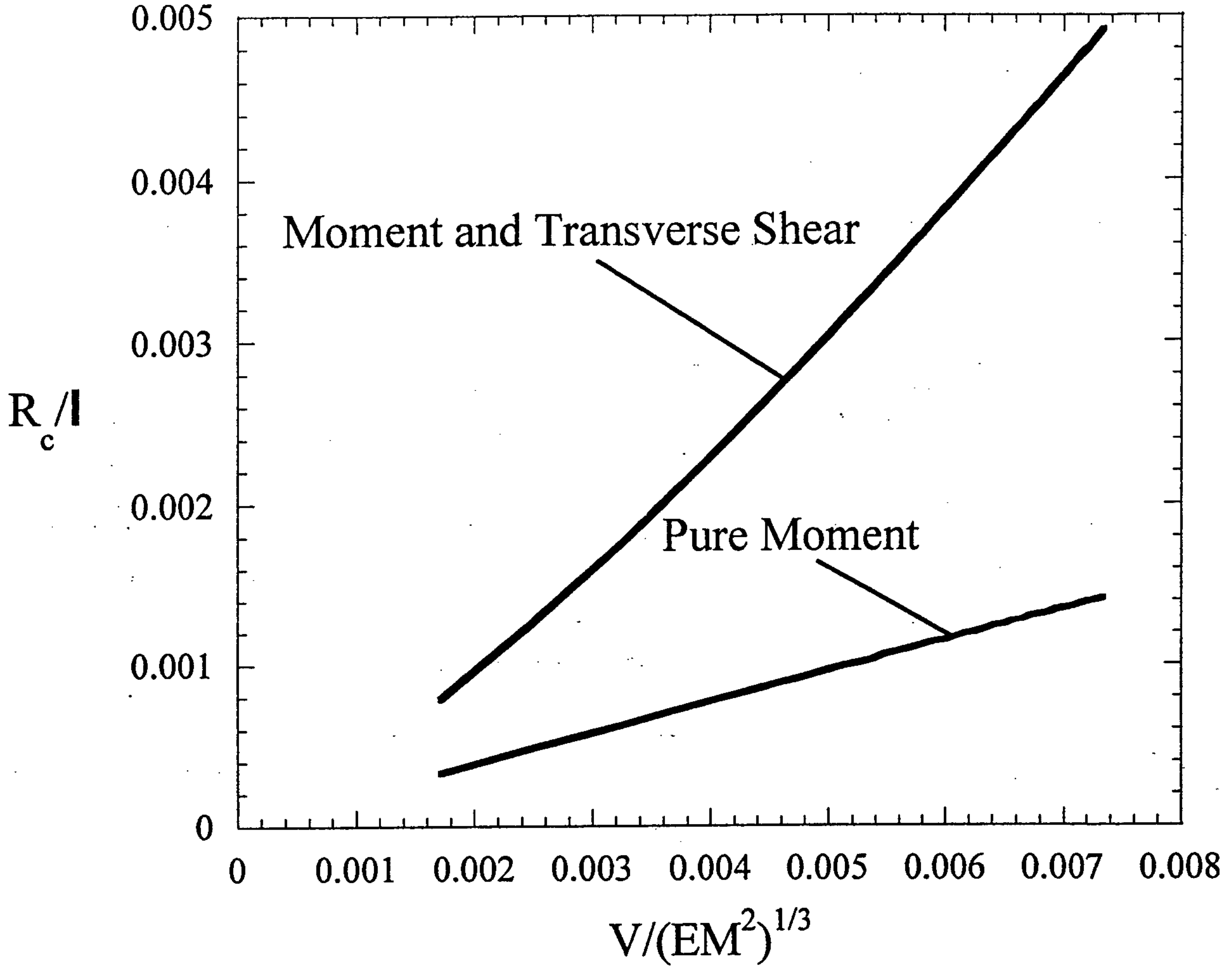
0.005
0.004
0.003
0.002
0.001
0
R_c/l
Moment and Transverse Shear
Pure Moment
0
0.001
0.002
0.003
0.004
0.005
0.006
0.007
0.008
$V/(EM^2)^{1/3}$

Figure 4d

(a)

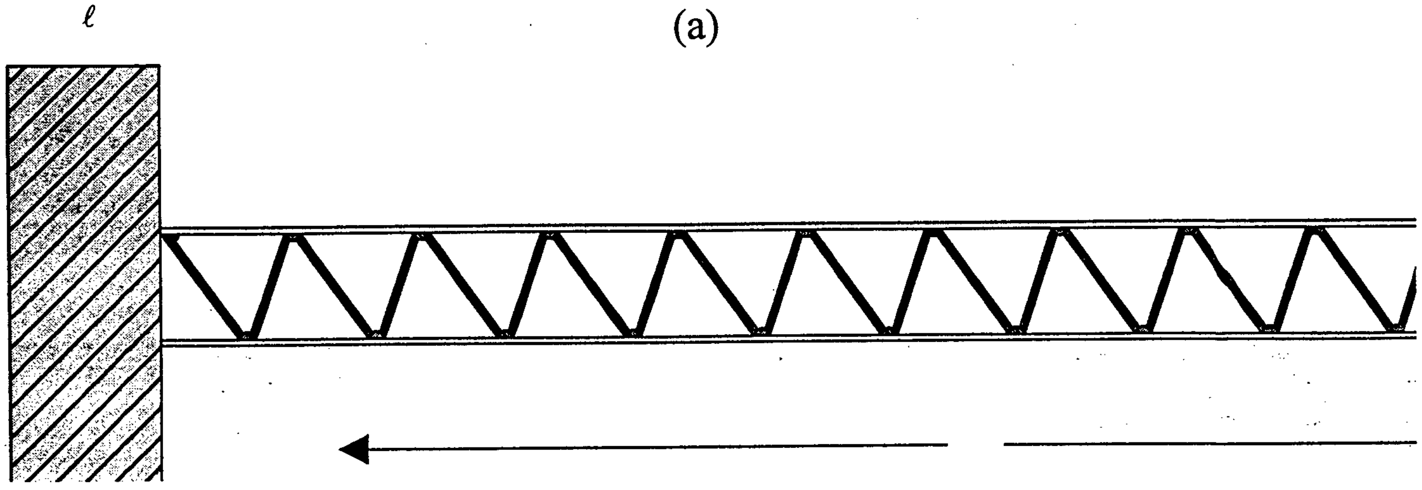
ℓ

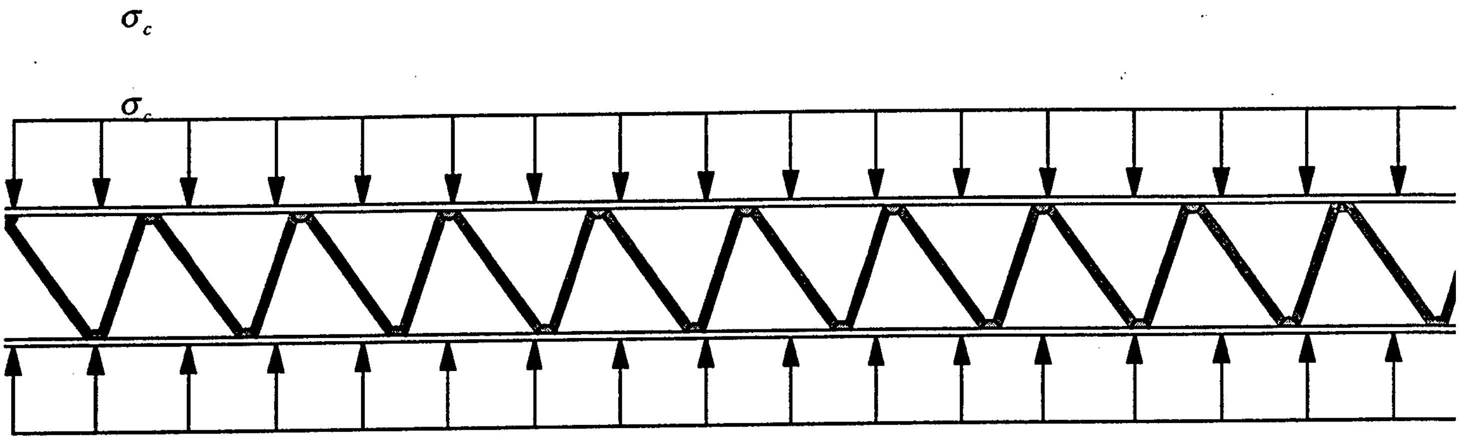

(b)

Figure 5

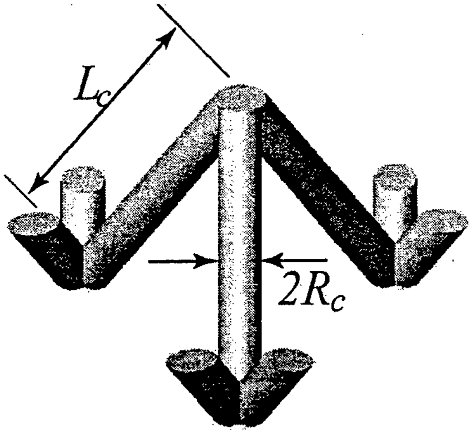
L_c
$2R_c$

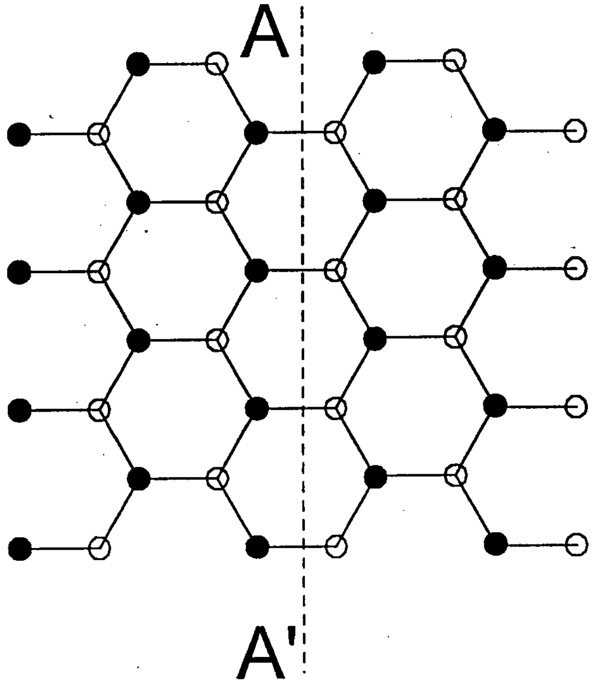
A
A'

Figure 6a

Figure 6b

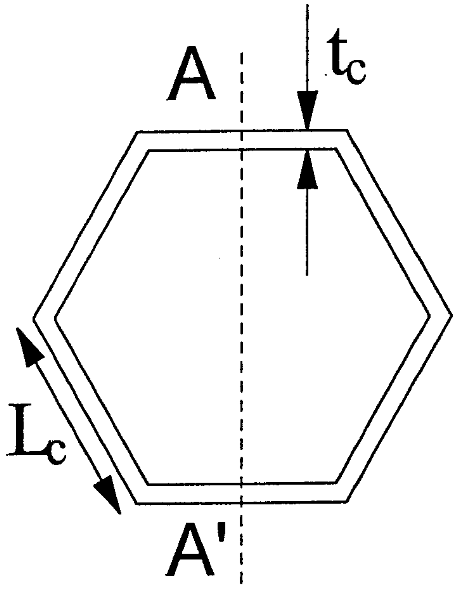

Figure 6c

	Tetragonal Core	Honeycomb core
Elastic shear modulus	$\overline{G} = \frac{1}{9} E\rho_c$	$\overline{G} = \frac{1}{3(1-\nu^2)} E\rho_c$
Crushing strength (plastic yield)	$\overline{\sigma} = \frac{2}{3}\sigma_Y \rho_c$	$\overline{\sigma} = \sigma_Y \rho_c$
Crushing strength (elastic buckling)	$\overline{\sigma} = \frac{\sqrt{2}\pi}{9} E\rho_c{}^2$	$\overline{\sigma} = \frac{\pi^2}{4(1-\nu^2)} E\rho_c{}^3$
Shear strength (plastic yield)	$\overline{\tau} = \frac{1}{3\sqrt{2}}\sigma_Y \rho_c$	$\overline{\tau} = \frac{2}{3\sqrt{3}}\sigma_Y \rho_c$
Shear strength (elastic buckling)	$\overline{\tau} = \frac{1}{18} E\rho_c{}^2$	$\overline{\tau} = \frac{\pi^2 k_s}{24(1-\nu^2)} E\rho_c{}^3$

Figure 7a

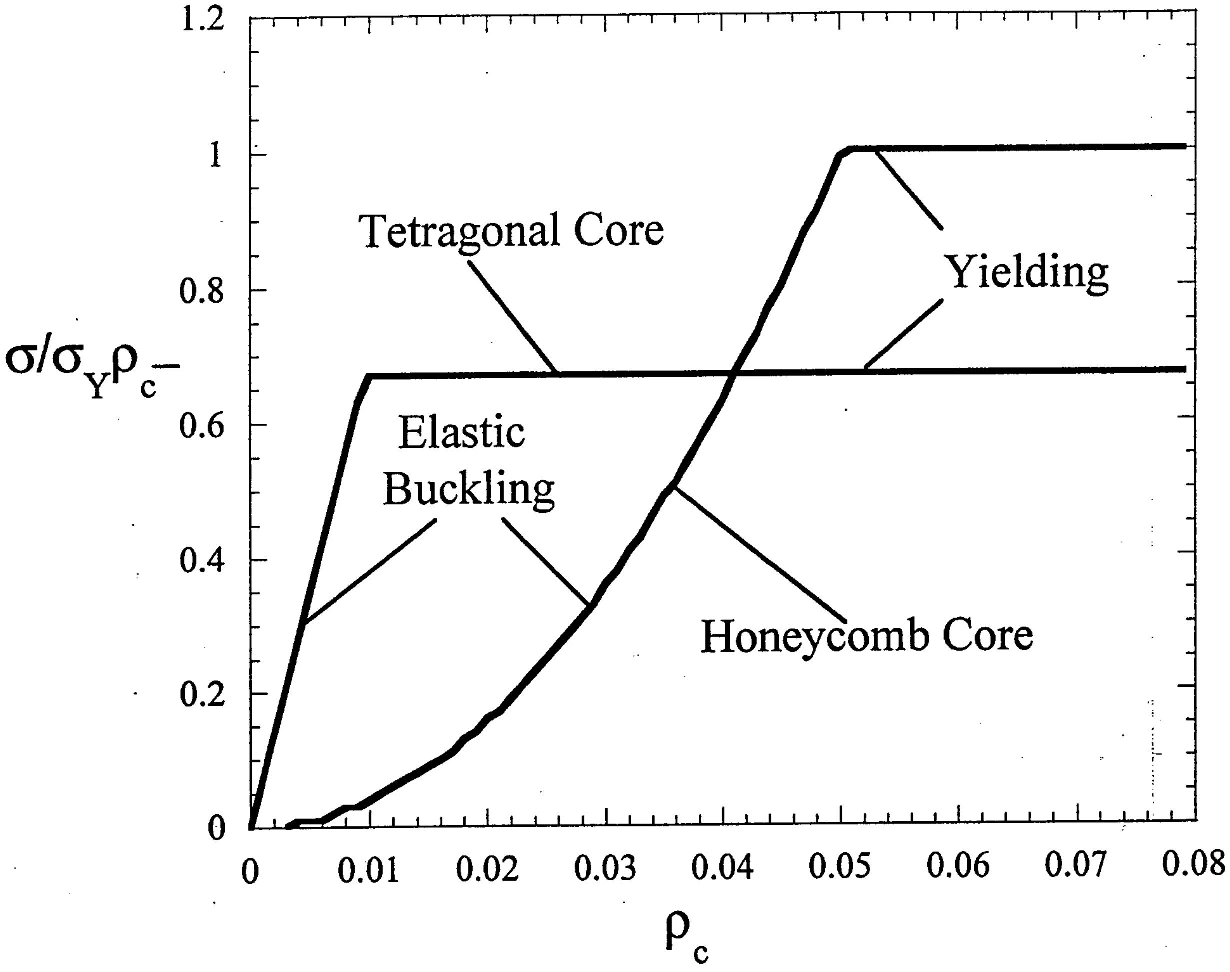

1.2
1
0.8
0.6
0.4
0.2
0
0
0.01
0.02
0.03
0.04
0.05
0.06
0.07
0.08
$\sigma/\sigma_Y \bar{\rho}_c$
$\bar{\rho}_c$
Tetragonal Core
Yielding
Elastic
Buckling
Honeycomb Core

Figure 7b

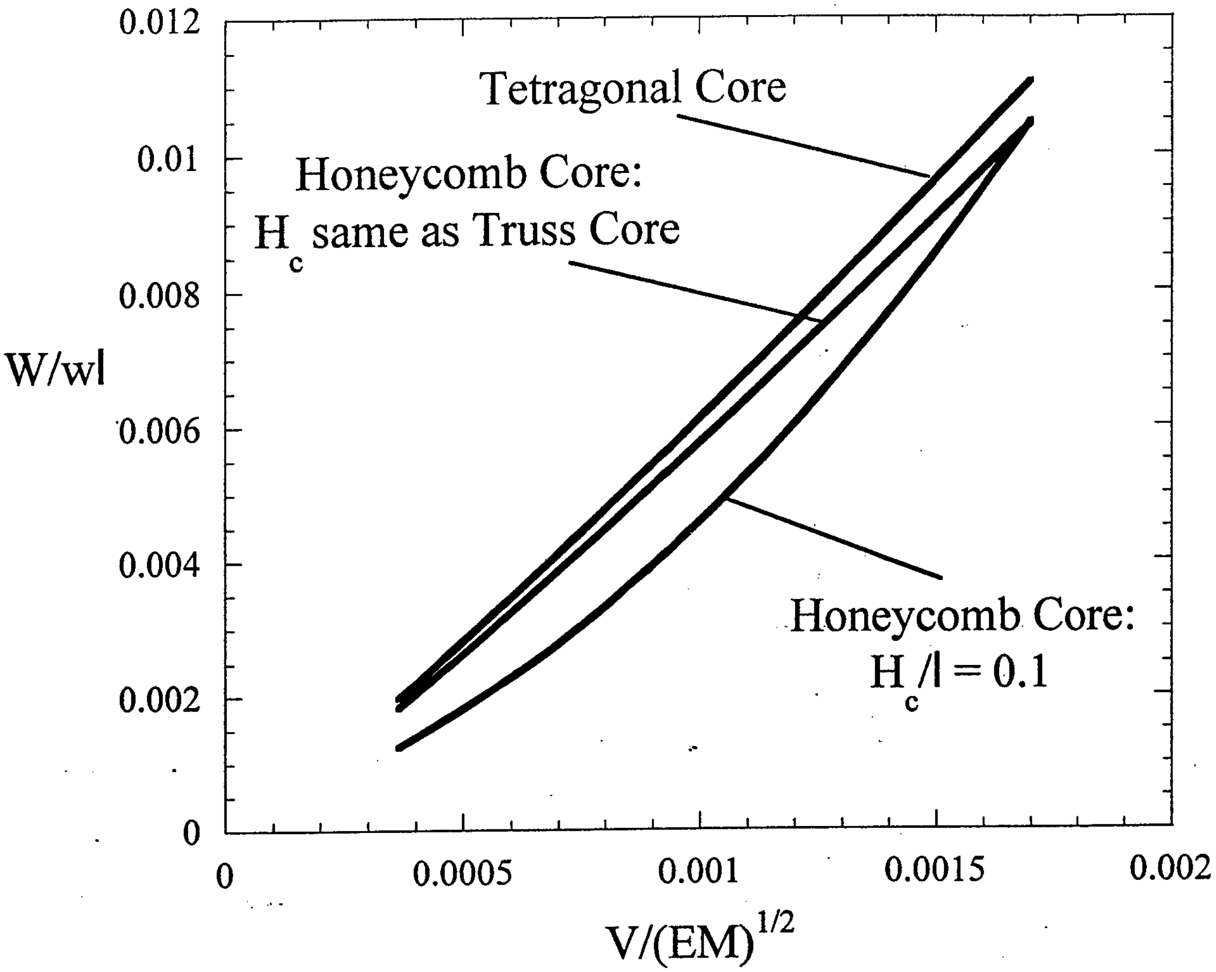
0.012
0.01
0.008
0.006
0.004
0.002
0
W/wl
0
0.0005
0.001
0.0015
0.002
V/(EM)^1/2
Tetragonal Core
Honeycomb Core:
H_c same as Truss Core
Honeycomb Core:
H_c/l = 0.1

Figure 8a

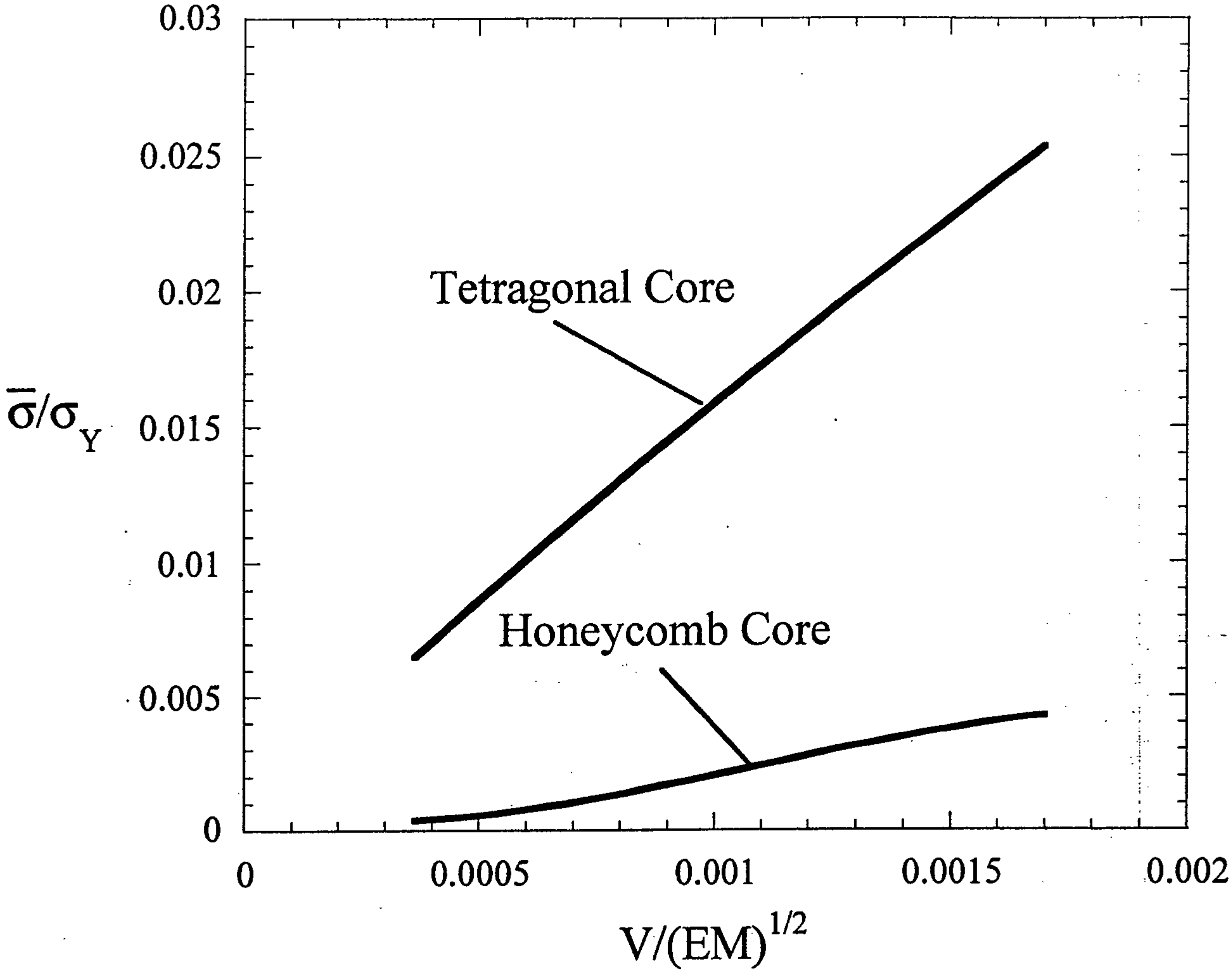

0.03
0.025
0.02
0.015
0.01
0.005
0
$\bar{\sigma}/\sigma_Y$
Tetragonal Core
Honeycomb Core
0
0.0005
0.001
0.0015
0.002
$V/(EM)^{1/2}$

Figure 8b

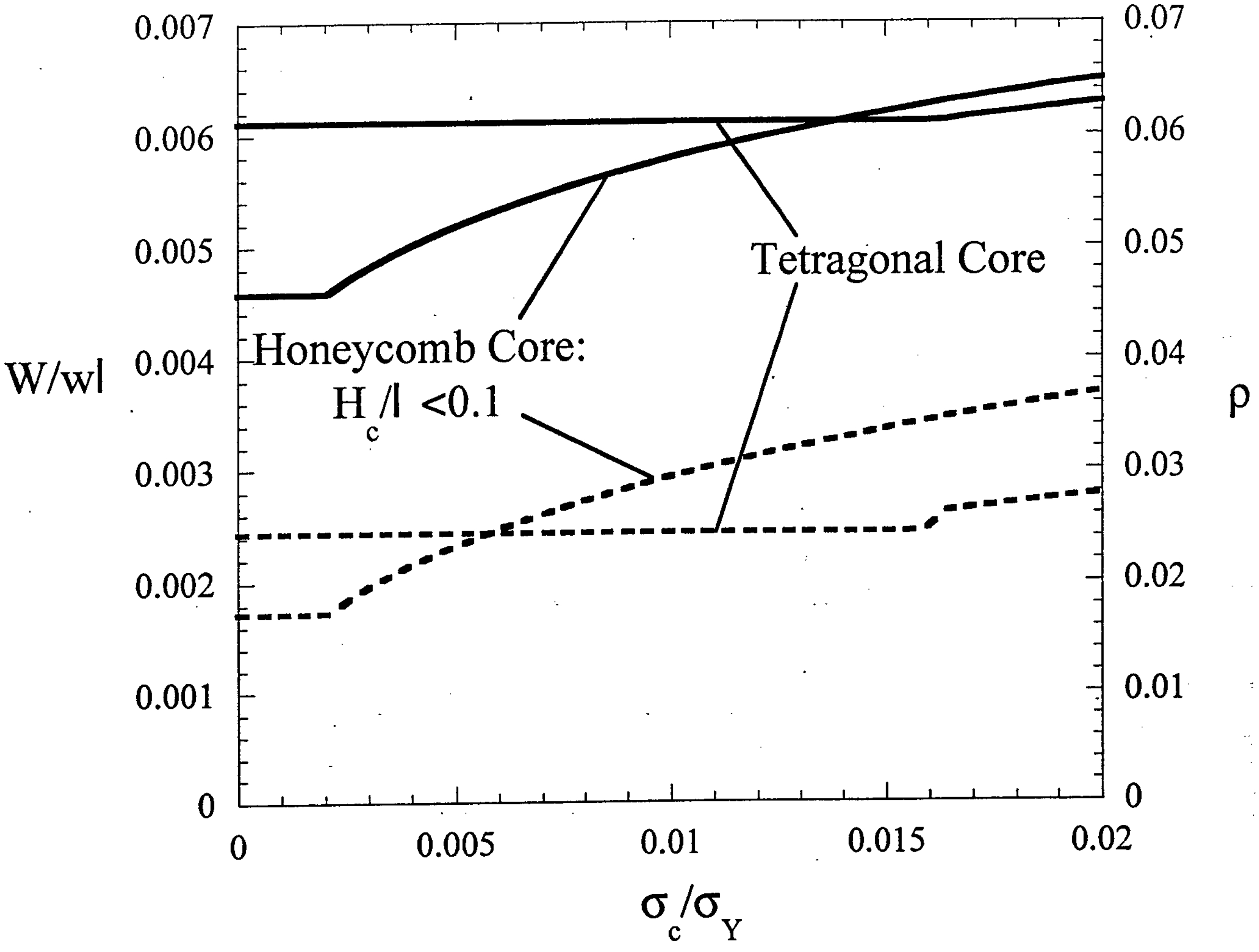
0.007
0.006
0.005
0.004
0.003
0.002
0.001
0
W/wl
0.07
0.06
0.05
0.04
0.03
0.02
0.01
0
ρ
0
0.005
0.01
0.015
0.02
σ_c/σ_Y
Tetragonal Core
Honeycomb Core:
H_c/l <0.1

Figure 9

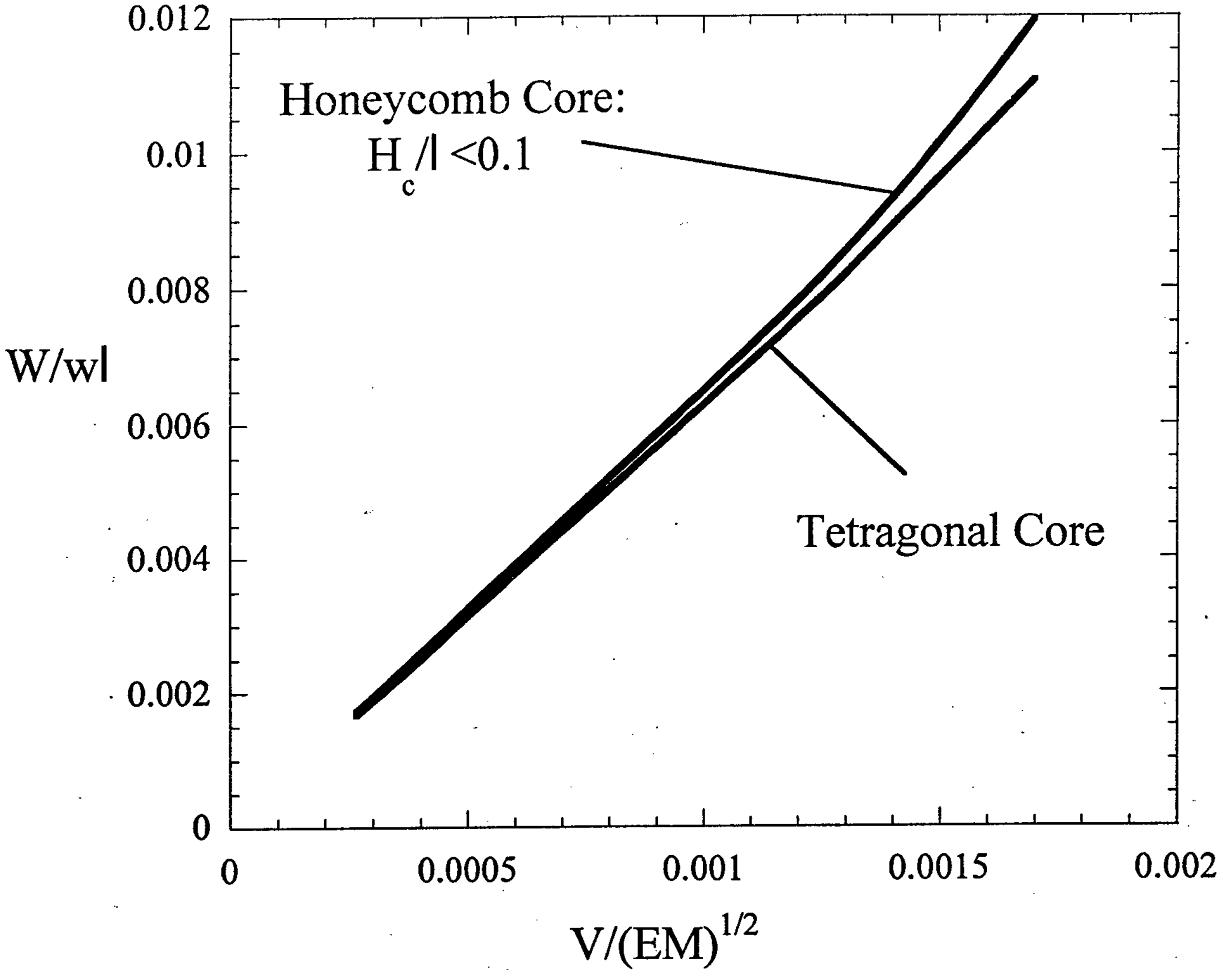

Figure 10

ℓu^{2}_{j+1}

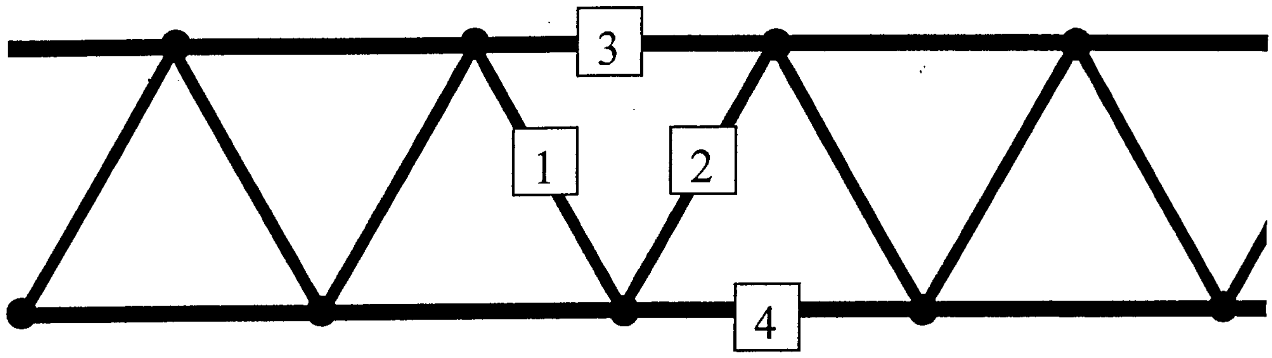

Figure 11

THE STRUCTURAL PERFORMANCE OF NEAR-OPTIMIZED TRUSS CORE PANELS

S. CHIRAS,* D. R. MUMM,
A. G. EVANS,
Princeton Materials Institute
Princeton University
N. WICKS, J. W. HUTCHINSON
Division Of Engineering and Applied Sciences
Harvard University
Cambridge, MA 02138
K. DHARMASENA, H. N. G. WADLEY
Department of Materials Science and Engineering
University of Virginia
Charlottesville, VA 22903
and S. FICHTER
Aurora Casting & Engineering, Inc.
Santa Paula, CA 93050

ABSTRACT

Theoretical studies have indicated that truss core panels with a tetragonal topology support bending and compression loads at lower weight than competing concepts. The goal of this study is to validate this prediction by implementing an experimental protocol that probes the key mechanical characteristics while addressing node eccentricity and structural robustness. For this purpose, panels have been fabricated from a beryllium-copper alloy using a rapid prototyping approach and investment casting. Measurements were performed on these panels in flexure, shear and compression. Numerical simulations were conducted for these same configurations. The measurements reveal complete consistency with the stiffness and limit load predictions, as well as providing a vivid illustration of asymmetric structural responses that arises because the bending behavior of optimized panels is dependent on truss orientation.

1. INTRODUCTION

Truss core panels have been identified as candidates for ultra-light structures that experience predominantly bending or compressive loads [1-5]. Theoretical results have explored truss core and face member topologies that realize the minimum weights. These preferred designs require that, in regions where the core experiences shear, the trusses experience *only compression or tension (no bending).* The octet truss topology has this characteristic [6]. The unit cell for the core is depicted on figure 1b and the plan view on figure 1a.

The shear stress/strain response of the octet truss core is slightly anisotropic [1,3,5], differing in the responses exhibited by panels of type A and B (fig 1). Type A panels are emphasized in this study. When such panels undergo bending, the most highly stressed trusses (AA' on fig. 1a) can experience either

*schiras@princeton.edu, ph. (609)258-0844, fax (609) 258-6878

tension or compression, depending on the sign of the imposed shear force, V. This difference results in asymmetries, vividly demonstrated below. At the optimum, panels made from materials having high yield strain ($\varepsilon_Y = 0.007$), are predicted to fail by simultaneous elastic buckling of the compressed core members, with yielding and wrinkling of the faces [1]. As ε_Y decreases, the failure modes change to simultaneous core yielding with yielding and wrinkling of the faces. Theoretical results reveal that the optimized truss core design is capable of sustaining bending and compression loads at weights at least as low as the lightest competing designs [1,7,8]. The truss design has the additional merit that its open micro-architecture allows secondary functionality, such as cooling and actuation [4,8,9]. When designed for minimum weight, the optimized panels (as well as honeycomb panel analogues) have relatively thin face sheets [1,3]. This thinness causes them to be susceptible to face penetration by sharp objects, and other related damage modes. Accordingly, designs with thicker faces are generally used (subject to a weight penalty), dictating that this study assess panels with thicker-than-optimum faces.

The goal of the present study is to examine the capabilities of near-optimized panels, with the focus on core performance. The approach is to use measurements conducted on fabricated truss core panels to probe the mechanical performance and to correlate with the theoretical expectations. A previous study [3,5] has provided several insights relevant to the design of the present samples. Namely, in the earlier work, in the negative orientation (fig. 1b), susceptible to failure by compressive yielding of core members, while the measured load capacities were in accordance with the analytical results, there were discrepancies in the stiffness. Moreover, in the converse (positive) orientation, governed by yielding of the core members in tension, failure occurred prematurely by rupture of the nodes, rather than by yielding, resulting in a disparity with the predictions. This detrimental failure mode was attributed to the relatively low ductility of the cast aluminum alloy [3,5], in combination with node eccentricity [10]. Accordingly, to realize the range of failure modes, the constituent material should have sufficient ductility to suppress premature rupture and the nodes must be designed to minimize eccentricity. These realizations guided the experimental study reported in the following sections.

In order to correlate with the measurements, new simulations of panel performance are conducted. These are based on the precise topology used in the experiments, as well as the measured stress/strain response of the new casting alloy. In the simulations, the full force/displacement responses of panels in bending and shear are predicted and these results are superposed on the measurements.

2. EXPERIMENTAL PROTOCOL

The underlying concept is to devise bending, shear and compression tests on panels with optimal and sub-optimal core configurations that probe panel load capacity, stiffness and failure mechanisms. The configurations to be tested are designed with thicker-than-optimum face sheets as well as cores ranging in topology from optimal [1] to sub-optimal. A "gap" design was used for the nodes, wherein the intersection of the truss axes was located at the mid-plane of the optimized facesheet. To within $100\mu m$, this geometry was used in all of the fabrication and testing.

Ductility requirements are achieved by selecting a ductile beryllium/copper alloy which exhibits a strain-to-failure in excess of 20% in the as-cast state. The panels were fabricated using a rapid prototyping and investment casting procedure elaborated in the next section. Four fabrication restrictions have enforced some limitations on the panel design. (i) It has not been possible to cast truss members either having an aspect ratio $(L_c / R_c) > 28$ or faces having thickness, $t_f < 1.5mm$. (ii) The largest panel that could be prototyped in the available system had a length, $L \leq 15cm$. (iii) The final samples had dimensions that varied from design specifications by up to 7%, despite rapid prototyping to account for an expected 1.8% shrinkage upon casting. (iv) Some warping of the panels during casting was unavoidable. Deviations from planarity are about 0.3mm over the length, L.

The casting limitation on the truss radius, when considered in combination with the optimal truss aspect ratio for a chosen loading condition $[(V / \sqrt{EM} = 0.002, (L_c / R_c)_{opt} = 22.4]$ determined the core dimensions. The corresponding optimal face sheet was much thinner than casting procedures could produce. Furthermore, due to warping, the faces could not be ground to the optimal thickness. Accordingly, all of the tests were performed with panels having faces up to 7 times thicker than the optimum, consistent with the dictates of commercial practice. For this purpose, panels were fabricated with constant face thickness, $t_f = 1.5mm$, truss length, $L_c = 14.01mm$ and core thickness, $H_c = 11.44mm$, but three different truss radii: $R_c = 0.58, 0.69, 0.83mm$. For these three radii, the relative core densities are, respectively (see equation A5): 2.25%, 3.24% and 4.64%. The smallest radius gave a truss aspect ratio closest to the optimum [1].

3. FABRICATION

3.1 Rapid Prototyping

Integrated face sheet and truss core sandwich panels were made by using rapid prototyping to fabricate ABS (acrylonitrile-butadiene-styrene) patterns, which were then used for investment casting from a high thermal conductivity berryllium/copper casting alloy (Cu-2%Be). Rapid prototyping has gained wide interest in the design community since it provides a means of: (a) visualizing new product ideas and, (b) fabricating parts for functional testing. Since the basis is a computer generated three-dimensional solid model of the object, it provides the convenience of creating panels of optimal, near optimal and sub-optimal designs for performance evaluation. A slicing algorithm defines tool paths for the outer boundaries of each layer and the areas in which material needs to be filled. This information is downloaded to a rapid prototyping machine to generate the part. In this work, an extrusion-based, fused deposition modeling (FDM) process commercialized by Stratasys Inc., Eden Prairie, Minnesota was used [11].

The FDM process chosen uses ABS in filamentary form as the modeling material. The material is fed into a temperature-controlled heater/liquifier through counter-rotating rollers, and is then extruded through a fine nozzle in a semi-liquid state (fig.2). A second liquifier and nozzle system is used to extrude an easily dissolved material for a support structure, which can be removed upon build completion. Prior to applying the slicing algorithm, the part is rotated to the orientation that minimizes the support structure. The feeding system is contained in a head whose movement is numerically controlled in the X-Y horizontal plane. A constraint on the overall panel dimensions was imposed based on the space available in the rapid prototyping machine.

The CAD model was built as an assembly of two face sheets and a truss core design. The panel length was selected to provide adequate overhang beyond the spacing of the outer load supports ($2l$ = 148.8 mm) and the panel width to accommodate four cells (fig. 1). For beryllium-copper, a shrinkage allowance of 1.8%

was added to the final pattern dimensions. After rapid prototyping, the parts were placed in a soluble concentrate and water solution at 70°C to dissolve the support structure. After the parts were sufficiently dry, a coat of clear acrylic spray was applied to fill-in gaps between the individual layers of the model.

3.2. Investment Casting

The ABS patterns were coated with a liquid wax and cleaned with isopropyl alcohol. Seven wax gates were placed in a staggered arrangement to ensure a quick molten metal feed into the two face sheets (fig. 3). Casting wax runners were then placed connecting the seven gates. Three vent channels were provided at the center and two ends of the sandwich panel to allow gases to escape from the mold during ABS burn-out (fig. 4). The gated patterns were dipped in a ceramic slurry containing colloidal silica (supplier, Ransom and Randolph), and Zircon ($ZrSiO_4$). After allowing the slurry to drain, the patterns were then coated with a fine-grained Zircon. The shells were allowed to air dry at approximately 23°C for about a day and a half. A second dip was done in a slurry containing colloidal silica (Nyacol) and Zircon. After draining the excess slurry the patterns were again coated with Zircon and allowed to dry. The procedure was repeated for 2 more layers of the second slurry mix (3rd and 4th overall layers) and medium grain fused silica. The last three layers (5th-7th) used the second slurry mix followed by a coarse grained fused silica in order to add strength to the shell. After the 7th layer had dried, the patterns were dipped one last time (referred to as the "seal" coat) in the second slurry mix to prevent the sand from the previous coats from falling off the shell and getting inside the cavity at the burnout stage. After the seal coat was dry, the tips of the vents were ground to allow gases to escape during the ABS burnout process.

The ceramic shelled ABS panels were preheated to 900°C, placed in a furnace, the temperature ramped up to 1066°C and held for 1.5h. The hollow shell molds were removed and allowed to cool to room temperature for inspection of cracks. Residual ash in the shells was removed by rinsing with water and a high pressure air jet. The vents were plugged with a refractory cement and the shells placed back in the furnace and heated to ~980°C. The alloy was induction melted in a 14 kg crucible and poured in to the mold at 1425°C.

When the shells had cooled after casting, the shell material was removed using a high pressure water jet. The runner system was cut-off at the gates and ground flush with the surface of the face sheets using a two-stage grinding operation.

3.3 Microstructure and Defects

After fabrication and before testing, metallurgical sections were made at various locations in the panels. A random section (fig. 5) shows the dendritic structure expected for this alloy. Sections made through several of the nodes (fig. 6) revealed casting porosity.

4. TEST DESIGN

4.1 Constituent Properties

The basic stress/strain behavior for the Cu/Be alloy has been measured in the following manner. A face sheet from one of the cast panels was cut away from the core and a flat coupon tensile specimen prepared. The reduced gage section had dimensions, 6x2x45mm. The specimen was tested in a servo-hydraulic machine by using friction grips, with strain gages centered on both sides of the mid-section. The stress/strain curve obtained on the as-cast material is plotted on figure 7. In this condition, the material has a tensile ductility exceeding 20%. It has a 0.2% offset yield strength of 300MPa. The unload/reload lines confirm a Young's modulus, $E = 130GPa$. The considerable strain hardening can be captured using the Ramberg-Osgood formulation:

$$\varepsilon = \sigma / E + \alpha\varepsilon_Y(\sigma / \sigma_Y)^N \qquad (4.1)$$

The measurements afford an excellent fit to (4.1), as evident from fig.7, with: $\alpha \approx 1, N = 7.4, \sigma_Y = 291MPa, \varepsilon_Y = 2.23x10^{-3}$.

4.2 Three-Point Bending

The panels were tested in three-point bending by using a procedure similar to that described elsewhere [12], and as depicted in figure 8. Flat-faced loading platens 16mm wide were adhesively-bonded to the faces of the panels. The loads were applied through lubricated rollers inset into the platens that allowed the specimen to rotate upon bending, with minimal friction. Strain gages were bonded to the tensile face at two locations. One set was attached to the face immediately opposite the inner platen. Strains were monitored in both 0° and 90° orientations. A second set was attached to the same face mid-way between the center and outer platens. The tests were performed in a servo-electric test frame. The load, load-point displacements and strains were measured simultaneously.

An assessment of the expected failure mechanisms for each of the panels described in section 2 provides perspective prior to testing. By inserting the properties of the as–cast alloy (figure 7) into the beam theory formulae in the Appendix, the limit load, P_{max}, needed to cause failure by core and face yielding can be estimated for each configuration, as plotted on figure 9. (Face wrinkling is another possible mechanism [1,13]. But, at the face thickness achievable in the fabricated panels, it always occurs at a much higher force than the two yielding mechanisms). Note that panels with all three core radii are predicted to fail by core yielding, although the largest approaches the transition from core yield to face yield.

4.3 Shear and Compression Tests

The configuration used to obtain shear stress/strain curves for the core is shown in figure 10. Three guidelines were used in the design. (i) The avoidance of significant tensile stress normal to the core to prevent premature rupture of the nodes. (ii) Minimization of the normal stresses induced near the ends. (iii) Sufficient rigidity to minimize rotation of the nodes at the face sheet. The resultant design comprised a static frame rigidly attached to a thick base and a moving element with the freedom to displace vertically but not horizontally. The parts interact through two 6cm linear bearings (circulating ball guide blocks and rails) that assure rigid linear motion with minimal friction. The test specimen was rigidly attached to the sliding component by means of holes tapped into the face. In some cases, a steel spacer was used to assure that the loads were aligned with the center of the sample. The load was applied in a servo-electric test frame.

Since transverse displacements are induced during shear, as elaborated in section 6, a means for accommodation that minimizes the induced stresses was incorporated. This was achieved by embedding an array of pins into the face of the static frame. These were inserted into matching holes in the panel face. The lateral movement occurred by displacement of the holes in the plate relative to the pins. Friction was reduced by polishing and lubricating the contact surfaces. Samples were designed to minimize the development of a moment by arranging a singular row of nodes on the face sheet displacing through the pins.

In order to explore the crushing characteristics, compression tests were conducted in the orientation normal to the panel faces by simply compressing a reduced panel (4x4cm) between large flat platens within a servo-electric test frame.

4.4 Observations

During the above bending and shear tests, a high resolution digital camera was connected to the testing frame in order to capture side-view images of the core, while the tests were being conducted. These images were used to identify the failure mechanisms and to determine the shear strains.

5. MEASUREMENTS

5.1 Panel Bending

The load/displacement curves measured in bending are summarized on figure 11a. A peak load, P_{max} is attained, at displacement, δ_{max}, followed by softening. The panels with the two smaller truss radii fail by *core shear* (see figure 3) and the softening is *gradual.* The panel with the largest truss radius fails by *face yielding* (see figure 8) and the softening occurs *rapidly.* All panels experience inelastic strain at small loads (see unload/reload lines on figure 11b), with strong strain hardening prior to the load maximum.

The variation in P_{max} with the truss radius is indicated on figure 9. The bending stiffness, S_B is ascertained from the unloading compliance determined at displacements $\leq \delta_{max}$, and plotted on figure 12. The "initial loading stiffness", $S_{Initial}$ denoted on figure 11b, is about a factor 2 lower than S_B. A similar disparity arises in metal foams and foam core panels, because of local yielding at nodal stress concentrations [7].

Images of the test performed on the panel with the smallest truss radius (fig. 8) indicate that it fails by core shear and that the response beyond the load maximum is asymmetric. This happens because the trusses that experience the largest stresses are in compression on one side and in tension on the other. On the compression side, the trusses buckle plastically, resulting in large inelastic shear strains, causing plastic hinges at both the center and outer load platens. On the tensile side, the trusses stretch and sustain the load at essentially fixed strain, whereupon hinging only occurs at the center platen (that is, the panel remains straight at the outer platen).

The corresponding images obtained on the panels with larger truss radii that fail by face yielding (fig. 8) indicate that, for all intents and purposes, the core remains elastic (undistorted), whereupon the plastic deformation is confined to the face sheet subject to tension. This face begins to neck and tear along the center-line at the load maximum (fig. 8d). The tear extends across the sheet as the displacement increases, but the core continues to support some shear stress, thereby inhibiting abrupt rupture of the panel.

The output of the strain gages for the test on the panel with the smallest radius (depicted on fig.11a) is presented on figure 13a. The axial strains measured beneath the center platen have shape similar to the load point displacement. The unload/reload lines indicate that some face sheet yielding commences at quite small loads (about 2kN) and that, at the load maximum, the plastic strains in the faces are about 0.1%. The transverse strains at the center are consistent with a Poisson contraction of the face: with a Poisson ratio in the elastic range, $\upsilon \approx 0.25$. At the mid-span location, the strain in the elastic range is half that at the center, as expected from beam theory. However, once the core yields (causing the face-sheet beneath the center load platen to become plastic), the face at the mid-span begins to unload, resulting in a compressive residual stress (apparent from extrapolation of the unloading lines). Note that the mid-span gage is on the side of the central platen where the trusses buckle plastically, discussed next.

The center 0° strain measured on one of the specimens that failed by face yielding is indicated on figure 13b. The response up to the load maximum is similar to that for the other panel. At that stage, the central strain gage begins to unload as the tear in the face diminishes the retained load capacity. This occurs at a strain, $\varepsilon_x \approx 0.67\%$.

5.2 Panel Shear

The stress/strain responses measured *in shear* on specimens having the largest aspect ratio trusses are plotted on figure 14a. The strains were obtained from the optical images. They establish that the shear load capacity differs appreciably in the two orientations. That is, the limit load is lower in the negative orientation (defined on the inset) wherein the most heavily stressed trusses are in compression, in contrast to the positive orientation that places the equivalent trusses in tension.

The optical images indicate that, in the negative orientation, plastic buckling occurs at shear strains of about 2.35% (fig. 15). Conversely, in the positive orientation, the most highly stressed trusses stretch plastically and transfer load onto the compressed trusses. Due to a slight curvature of one of the truss members, plastic buckling occurred prematurely, at about 2.0% strain. Nevertheless, the truss under tension partially compensated for the buckling, allowing the sample to continue hardening. After testing it was noted that some of the trusses (about 10%) had ruptured at the nodes, presumably at locations where there is appreciable casting porosity (fig. 6).

5.3 Crushing

A simple compression test has been performed to measure the crushing characteristics of the core with the smallest diameter trusses. The result is plotted on figure 16. Note that the core sustains a peak stress, $P_{crush} = 4.8 MPa$ and then gradually softens. The optical images reveal that the trusses exhibit plastic buckling at the load maximum.

6. SIMULATIONS

Two simulations have been carried out to provide a direct comparison with the tests: (1) the isolated triad loaded by a shear force, and (2) the plate with the truss core loaded in three-point bending. In the plate simulation, a Timoshenko-type theory is developed in which the shearing behavior computed for the triad is used to specify the core stress-strain behavior. Details of the simulations are described below.

6.1 Shear Loading of an Isolated Triad

The triad unit of the octet truss core is depicted in figure 1b, along with the two directions of shear force, F_s. The test fixture is expected to exert some force perpendicular to the direction of the shear force due to frictional sliding. This component is modeled by $F_n = \mu F_s$ where μ is the coefficient of friction, and the sense of F_n is opposite to the direction of sliding. The joints are modeled as pinned such that bending of the members is ignored in computing the relation between F_s and u. This approximation is standard in truss analysis and fully justified because the stretching forces parallel to the members completely dominate the forces generated by bending prior to buckling. The two equations of equilibrium in the current configuration are

$$\begin{aligned} 2F_A \vec{t}_A \vec{i}_x - F_B \vec{t}_B \vec{i}_x &= F_s, \\ 2F_A \vec{t}_A \vec{i}_y + F_B \vec{t}_B \vec{i}_y &= \pm\mu F_s \end{aligned} \tag{6.1}$$

where F_A and F_B are the forces in the X and Y members and the sign of the friction force must be consistent with the sliding direction. The strains in the members are computed exactly from the relation between their change in length and the two displacement components, u and v, of the top joint relative to the bottom face of the fixture. The stress in a member, $\sigma = F / (\pi R_c^2)$, is related to the strain by (4.1).

Member Y is compressed for loading in the negative orientation, and will buckle when F_B attains the plastic buckling load. This member is taken to be clamped at each end such that the critical stress at the onset of plastic buckling is given by, $\sigma_{crit} = -\pi^2 E_t (R / L)^2$, where E_t is the tangent modulus of the stress-strain curve (4.1). A post-buckling analysis has not been carried out. For plate simulation, the shear force, F_s, is taken to be constant after buckling, ignoring the post-buckling fall-off. Plots of the normalized shear force calculated as a function of the overall shear strain, $\gamma = u / H_c$, are shown in figure17 for a frictionless loading fixture and for $\mu = 0.2$. The asymmetry associated with loading in the positive and negative orientations is apparent. The influence of friction is relatively small. These calculated results have been superposed on the measurements in figure 14b. The comparison will be discussed below.

6.2 Three-point Bending of a Sandwich Plate with the Octet Truss Core

To appropriately simulate the load/deflection response in bending, note that the contribution of the shear stiffness of the core must be taken into account in predicting elastic deflections. Moreover, once the core yields, the non-linearity of the load/deflection response becomes compounded by the asymmetry attributable to plastic buckling of core members on the right side of the beam. A Timoshenko-type plate theory that fully accounts for these aspects of core shear is introduced. The model is restricted to loads wherein the face sheets remain elastic. Conventions related to the theory are shown in figure 18. The displacement components of the center-line are denoted by $[u(x), w(x)]$, and the core shear relating the displacement of the top face sheet (+) relative to the lower sheet (-) is $\gamma(x)$. The stretching strains in the top and bottom sheets are

$$\varepsilon_+ = u' + \omega' H_c / 2, \quad \varepsilon_- = u' - \omega' H_c / 2 \tag{6.2}$$

where $\omega = \gamma - w'$ and $()' = d() / dx$. The average stresses in the elastic face sheets are, $\sigma_+ = \overline{E}\varepsilon_+$ and $\sigma_- = \overline{E}\varepsilon_-$, with $\overline{E} = E / (1 - \nu^2)$. The bending moments carried by the individual sheets are $M_+ = M_- = (\overline{E}t_f^{\,3} / 12) w''$. The contribution from the truss core to the net in-plane force per unit length, N, is neglected: whereupon, $N = \sigma_+ t_f + \sigma_- t_f \equiv 0$ and thus: $\sigma_+ = -\sigma_- \equiv \sigma$. It follows immediately from (6.2) that $u' = 0$.

The net moment carried by the plate (again neglecting the very small contribution of the core) is

$$M = M_+ + M_- - \sigma H_c t_f = (\overline{E}t_f^{\,3} / 6) w'' - \overline{E}t_f H_c^2 \omega' / 2 \tag{6.3}$$

Denote the nonlinear shear stress-strain behavior of the truss core by $S(\gamma)$, taken directly from the force-displacement relation of the triad, $F_s(\gamma)$, in figure 17 by dividing the force by the area of the unit triad cell, $S = F_s / (\sqrt{3} L_c^2 / 2)$. Equilibrium of the face sheets requires

$$t_f \sigma' = S(\gamma) \tag{6.4}$$

The overall equilibrium equations are the standard for any beam theory,

$$V' = p(x), \quad M' = -V \tag{6.5}$$

The distributed lateral load per unit length vanishes: $p = 0$. The three-point bend problem is statically determinant such that

$$\begin{aligned} M \equiv M_0(x) &= 0 && -\ell - \Delta\ell < x < -\ell \\ &= P\ell(1 + x/\ell)/2 && -\ell < x < 0 \\ &= P\ell(1 - x/\ell)/2 && 0 < x < \ell \\ &= 0 && \ell < x < \ell + \Delta\ell \end{aligned} \tag{6.6}$$

where the length of the overhang is denoted by $\Delta\ell$ and the loads are idealized as point forces applied at the center of the loading platens.

The two ordinary differential equations governing $\omega(x)$ and $w(x)$ (with $\gamma = \omega + w'$) are thus

$$\begin{aligned} &\frac{\bar{E}t_f^{\,3}}{6} w'' - \frac{\bar{E}H_c^{\,2}t_f}{2}\omega' = M_0(x) \\ &\frac{\bar{E}H_c t_f}{2}\omega'' = S(\omega + w') \end{aligned} \tag{6.7}$$

Continuity across the points of application of the concentrated loads requires that all of w, w', μ and μ' be continuous: the latter two ensuring that γ and σ are also continuous. The jump conditions at the concentrated loads are satisfied because the two equations in (6.7) are based on the statically determinant distribution. The boundary conditions are $w = 0$ at $x = \pm\ell$ and $\omega' = 0$ at $x = \pm(\ell + \Delta\ell)$: the second of these ensures that $\sigma = 0$ at the free ends. The conditions that M and V vanish at the ends follow directly from (6.7). The equations in (6.7) can be put in non-dimensional form by letting $z = x/\ell$, $(\;)' = d(\;)/dz$ and $\bar{w} = w/\ell$ such that

$$\begin{aligned} &\bar{w} - 3(H_c/t_f)^2\omega' = 6\bar{M}_0(x) \\ &\omega'' = 2\bar{S}(\omega + \bar{w}) \end{aligned} \tag{6.8}$$

where $\bar{M}_0 = \ell M_0/\bar{E}t_f^{\,3}$ and $\bar{S} = \ell^2 S/\bar{E}t_f H_c$. A parameterized function, $\bar{S}(\gamma)$, was chosen to fit the computed curves for the triad in figure 17 (with $\bar{S} < 0$ for $\gamma < 0$, and $\bar{S} > 0$ for $\gamma > 0$). Because the computed prediction for the triad in figure 17 slightly underestimates the experimentally measured maximum load (fig. 14), the value of $\bar{S}$ associated with onset of buckling in the present simulation was chosen consistent with $F_s/(\pi R_c^{\,2}\sigma_Y) = 1$, in better accord with the experimental value.

The system of equations (6.8) has been solved for the specific parameters associated with the three-point bend test in figure 8. This specimen has $R_c = 0.575mm$, and the overhang was taken as $20mm$. At each load P the system (6.8) is solved using standard numerical techniques for ordinary differential equations with Newton iteration to deal with the non-linearity due to $\bar{S}(\gamma)$.

The plot of load against maximum downward displacement is shown in figure 19. Prior to the onset of buckling in the core, the deflection of the beam is symmetric with respect to its center. However, once buckling starts on the right side of the beam, that side has less incremental stiffness and there is a tendency for slightly larger deflection than on the left, as has also been observed in the test (fig. 8). The deflection in the overhang on the right is also affected because it resists shearing displacements at that end of the beam. The beam deflection shortly before and after the onset of buckling is shown in figure 20.

7. INTERPRETATION

7.1. Analytical

The stress/strain response for the alloy (fig. 7) is used as input to the formulae in the Appendix in order to predict properties that can be compared with the measured values. The *bending stiffness*, S_B, is determined by evaluating the shear modulus of the core, G^c, from (A5) and inserting into the Timoshenko beam theory result (A9). The measured stiffness values exceed these predictions (fig. 12), again exposing the limitations of this version of beam theory [12].

Assessment of the *limit load*, $P_{\max}$ is performed in the following manner. When the failure occurs by *core shear*, the contribution of the core to $P_{\max}$ is obtained by evaluating τ_Y^c from (A6), upon equating σ_Y^{core} to the stress for plastic buckling, σ_{pb}(A8), upon assuming fully-clamped end conditions. To determine the contribution of face yielding, the strain at which the load attains the maximum (fig. 13) is superposed on the stress/strain curve (fig. 7) and the associated flow stress taken as σ_Y^{face}. With these specifications for σ_Y^{core} and σ_Y^{face}, the load maximum may be estimated from (A10), with and without hinges. The load maxima calculated in this way are compared with the measured values, both in table I and on figure 9 (using averages from table I). The corresponding results for failure by *face yielding* are determined from (A11) upon using the same procedure for determining σ_Y^{face}. The correspondence is seen to be quite good. The most significant discrepancy occurs for the largest diameter truss in the sense that, whereas core yielding is the expected failure mode, it actually fails by face yielding at a smaller load than predicted.

The maximum stress needed to crush the core is obtained by again using the stress for plastic buckling σ_{pb}(A7), determined for the same end conditions, and inserting into the result for the compressive strength (A7) for the appropriate relative density. This predicts a peak stress, $P_{crush} = 4.3MPa$, somewhat smaller than the measured value, $P_{crush} = 4.8MPa$ (fig. 16).

The shear results are assessed using (A5) governing the shear modulus and (A6) dictating the shear strength, with (A8) as the effective inelastic strength, σ_Y^{core}, in the negative orientation. The modulus is ascertained from performing a curve fit on the load curve and using the linear coefficient. The comparison is summarized on table I. Note that the measured shear modulus is entirely consistent with (A5). Moreover, the shear yield strength measured in the negative orientation is similar to that predicted by (A6). In the positive orientation, (A6) underestimates the measured strength when the offset yield strength is used for σ_Y^{core}, because the strain hardening is not included. The correspondence is much improved when the hardening is introduced, as elaborated in the next section.

7.2. Comparison with Numerical Simulations

The comparison between the measured and calculated shear response for the core is presented on figure 14. The shear modulus ascertained from the unloading measurements is in close agreement with the calculated level. Moreover, the maximum shear forces, as well as the (positive/negative orientation) asymmetry found in the experiments, are accurately duplicated in the calculations. The only disparity is the lower strain hardening obtained in the measurements relative to the calculations. The origin is uncertain, but is tentatively attributed to the difficulty in preventing some rotation at the nodes in the present experimental arrangement (fig. 10).

A comparison between the simulated load/deflection behavior in bending with the curve measured for the same panel is presented on figure 19. The simulation slightly underestimates the stiffness, but appreciably underestimates the strength until the deflection becomes large (8-10mm). This discrepency is attributed to the significant lateral constraint exerted by the supports during bending. While this constraint does not affect results in the linear range, as deflections grow, a stretching force develops in the lower face sheet that is not accounted for in the analysis. Note that the present model has not incorporated the fall-off in core shear expected after buckling is well under way, and therefore does not predict the decline in load at large deflections.

8. CONCLUSION

The present series of experiments validates the performance of truss core panels with tetrahedral coordination, in near-optimum designs. The creation of a "gap node" design, through a rapid prototyping approach, followed by investment casting, has been a critical element in demonstrating the full potential of the truss core panel. This node design has enabled the stiffness to attain expected levels and has suppressed undesirable failure modes [3].

Choosing an alloy that has high ductility when tested in uniaxial tension (greater than about 20%) appears to be necessary if the panel is to achieve its full load carrying potential. This ductility requirement appears to be related to the development of high hydrostatic stress concentrations near the nodes and the presence of casting porosity in the same vicinity. This finding highlights the challenges in manufacturing high performance panels by casting and points toward alternate approaches based on wrought materials, such as woven systems [14].

The present study has highlighted the substantial differences that arise in the responses of trusses that experience tension relative to those in compression. The trusses in tension continue to strain harden beyond yield, such that the load capacity of a panel increases as it shears. Conversely, the trusses in compression exhibit buckling after a small plastic strain, limiting the load capacity. This effect has been most vividly illustrated on panels tested in bending. In such tests, the panel response is asymmetric despite the fact that the trusses yield in the same manner on both sides.

APPENDIX

Analytical Results For Truss Cores and Panels [1,3,5,7,13]

(i) Basic Characteristics

For the type A panels (fig. 1a), upon application of a shear force, V, the trusses designated AA' experience the largest axial stresses, given by [1,3]:

$$\sigma_c = \pm \frac{\sqrt{3} V L_c d}{\pi H_c R_c^2} \qquad \text{(A1)}$$

where $d = \sqrt{L_c^2 - H_c^2}$, with L_c the truss length, R_c its radius and H_c the core thickness. The positive and negative orientations are depicted on figures 1b and 14. The transverse shear stiffness in this orientation is [1,3]:

$$S_c = \frac{\pi E R_c^2 H_c^2}{\sqrt{3} L_c^3} \tag{A2}$$

The stress in the faces is:

$$\sigma_f = \pm \frac{M}{t_f H_c} \tag{A3}$$

where M is the bending moment ($M = \ell V$, where ℓ is the span).

(ii) Core Properties

The preceding results can be used to determine the response of the core, upon relating its dimensions to the relative density, $\bar{\rho}_{core}$, using [3],

$$\bar{\rho}_{core} = \frac{6\pi R_c{}^2}{\sqrt{3} L_c H_c} \tag{A4}$$

The transverse shear modulus of the panel, G^c, is obtained from (A2) and (A4) as [3]:

$$G^c / E = \frac{1}{6}\left(\frac{H_c}{L_c}\right)^2 \bar{\rho}_{core} \tag{A5}$$

The shear yield strength of the core, τ_Y^c, is obtained upon equating the stresses in the truss (A1) to the yield condition for the trusses ($\sigma_c \equiv \sigma_Y^{core}$) [3]:

$$\tau_Y^c / \sigma_Y^{core} = \left(\frac{H_c}{6d}\right) \bar{\rho}_{core} \tag{A6}$$

The corresponding compressive strength, σ_Y^c, is [3]:

$$\sigma_Y^c / \sigma_Y^{core} = \left(\frac{H_c}{L_c}\right)^2 \bar{\rho}_{core} \tag{A7}$$

For cases wherein the most highly stressed trusses are compressed and buckle plastically, σ_Y^{core} becomes the collapse stress, σ_{pb}, given by the implicit formula [3]:

$$\left(\frac{\pi k R_c}{2L_c}\right)^2 \varepsilon_Y^{-1} = \left(\frac{\sigma_{pb}}{\sigma_Y}\right) + \alpha N \left(\frac{\sigma_{pb}}{\sigma_Y}\right)^N \tag{A8}$$

where k is a measure of the rotational stiffness of the nodes (it ranges between 1 and 2), with α, N, ε_Y determined from the Ramberg-Osgood expression for the stress/strain curve (4.1).

(iii) Panel Properties

The results for the core can be used to determine the bending properties of panels. The *bending stiffness*, S_B, is given by [7,13]:

$$\frac{1}{S_B} = \frac{2\ell^3}{C_1 b E t_f c^2} + \frac{H_c \ell}{C_2 b c^2 G^c} \tag{A9}$$

where b is the panel width, $c = H_c + t_f$, and, for three-point bending, $C_1 = 48$ and $C_2 = 4$. Substituting G^c from (A5) into (A9) gives S_B.

The *limit load* $P_{\max}$ ($V_{\max} / 2$) depends on whether the panel fails by face yielding or core shear. When *core shear* predominates, the response at the outer supports has an important influence. If plastic hinges develop, such that the overhang does not contribute to that portion of the load carried by the core, then [7]:

$$P_{\max}^{core} = \frac{4bt_f^2 \sigma_Y^{face}}{\ell} + 2bc\tau_Y^c \tag{A10a}$$

The first term is the contribution from the plastic hinges formed in the faces and the second due to shear yielding of the truss core. Substituting τ_Y^c from (A6) into (A10a) predicts the limit load. Absent hinges at the supports, the corresponding result is [7]:

$$P_{\max}^{core'} = \frac{2bt_f^2 \sigma_Y^{face}}{\ell} + 2bc\tau_Y^c[1 + 2H_{over} / \ell] \tag{A10b}$$

where H_{over} is the overhang (see figure 3).

When the panel fails by *face yielding*, the limit load is [7]:

$$P_{\max}^{face} = \frac{4bt_f(c + t_f)\sigma_Y^{face}}{\ell} + \frac{bc^2 \sigma_Y^c}{\ell} \tag{A11}$$

with σ_Y^c obtained from (A7).

REFERENCES

1. Wicks, N., Hutchinson, J.W., 2001. Optimal truss plates. Int. J. Solids and Structures, to be published.
2. Wallach, J.C., Gibson, L.G., 2001. Mechanical behavior of a three-dimensional truss material. Int. J. Solids and Structures, in press.
3. Deshpande, V., Fleck, N.A., Ashby, M.F., 2001. Effective properties of the octet-truss lattice material. J. Mech. Phys. Solids, in press.
4. Evans, A.G., Hutchinson, J.W., Fleck, N.A., Ashby, M.F., Wadley, H.G.N., 2001. The topological design of multifunctional cellular metals. Progress In Materials Science 46, 311-327.
5. Deshpande, V.S., Fleck, N.A., 2001. Collapse of truss core sandwich beams in 3-point bending. Submitted to Int. J. Solids and Structures.
6. Fuller, R. B., 1961. U.S.Patent, 2,986,241.
7. Ashby, M.F., Evans, A.G., Fleck, N.A., Gibson, L.J., Hutchinson, J.W. , Wadley, H.G.N., 2000. Metal Foams: a Design Guide, Butterworth-Heinemann, Boston.
8. Budiansky, B., 1999. On the minimum weights of compression panels. Int. J. Solids and Structures 36, 3677 - 3708.
9. Evans, A.G., Hutchinson, J.W., Ashby, M.F., 1998. Multifunctionality of cellular metal systems. Progress Material Science 43, 171-221.
10. Karlsson, A., Hyun, S., 2001. unpublished research.
11. Crump, S., 1992. U.S. Patent #5121329 .
12. Bart-Smith, H., Hutchinson, J.W., Evans, A.G., 2001. Measurement and analysis of the structural performance of cellular metal sandwich construction. Int. J. Solids and Structures, in press.
13. Gibson, L.J., Ashby, M.F., 1997. Cellular Solids: Structure and Properties (2^{nd} Edition). Cambridge University Press, New York.
14. Sypeck, D.J., Wadley, H.G.N., 2001. Multifunctional microtruss laminates: Textile synthesis and properties. Jnl. Mater Research 16 (3), 890-897.

FIGURE CAPTIONS

Figure 1. (a) A plan view of the panel with the octet truss core showing the two basic orientations, A and B. In this study only orientation A has been tested.

(b) A schematic of the tetrahedral unit characterizing the core, with the notation used in the analysis incorporated.

Figure 2. Schematic of the fused deposition modeling process.

Figure 3. Attachment of wax runners and burn out vents prior to ceramic shelling process.

Figure 4. Molten metal is poured into the ceramic shell after the ABS burnout process.

Figure 5. As cast microstructure of Cu-2%Be.

Figure 6. (a) Cross-section through face sheet and a node.

(b) defects at node - face sheet intersection.

(c) casting porosity in face sheet.

Figure 7. The tensile stress/strain response of the as-cast material, showing the Ramberg-Osgood fit. The unload/reload lines indicate a Young's modulus, E =130GPa.

Figure 8. (a) Optical image of the side of one of the panels, truss core radius, $R_1 = 0.65mm$, located in the bending fixture, showing the loading scheme.

(b) Image of the same panel after testing showing the asymmetry of the displacements that occur upon testing. Plastic hinges are apparent at the inner platen as well as at the outer platen on the side that experiences large core shear strains (but not on the other side).

(c) Image of a panel with larger trusses, $R_1 = 0.825mm$, that fails by face yielding.

(d) Note the tear that has extended along the width at the center line of the face in tension.

Figure 9. The limit loads predicted as a function of the truss radius. The measured values are also shown for comparison. For the calculations, the core yield strength was taken to be the average value of the plastic buckling stress calculated using (A8) for the three geometries tested. The face sheet yield strength has been represented by the Ramberg-Osgood fit.

Figure 10. The configuration used to determine the shear stress/strain response for the truss cores.

Figure 11. (a) The load/deflection responses measured on the panels with the three truss radii.

(b) The result for the panel having the smallest truss core radius highlighting the existence of a load maximum, followed by softening, as well as the difference between the unloading stiffness and the initial loading stiffness.

Figure 12. The effects of truss radius on the bending stiffness. Results expected from beam theory are shown for comparison, as elaborated in the text.

Figure 13. The face layer strains as a function of bending load

(a) The panel having the smallest truss radius that fails by plastic buckling of the core. The mid-span gage is located on the side that experiences plastic buckling.

(b) The panel with the largest truss that fails by face yielding.

Figure 14. (a)The shear stress/strain curves for the panels measured in the two principal orientations indicated on the insets conducted on panels having the smallest truss radius. Note the substantially larger limit load obtained for the positive orientation defined on the inset (most highly stressed trusses in tension). The strains were determined from the optical images.

(b) The corresponding dependence of the shear force on the displacement relative to the core thickness, with the results calculated numerically superposed.

Figure 15. Optical images of the trusses after shear testing.

(a) Positive orientation.

(b) Negative orientation.

Figure 16. The stress/strain response of the core measured in compression.

Figure 17. The shear force/deflection response calculated for the core showing the asymmetry (refer to fig. 14) and the effect of a friction coefficient (μ) operating at the loading fixture.

Figure 18. The stresses and bending moments used for the analysis of the load/deflection response of the panel in bending.

Figure 19. The simulated load/deflection response in bending for the beam having the smallest truss diameter with the measured curve taken from figure 11a superposed.

Figure 20. The calculated deflections of the panel in bending, presented at two of the load levels from figure 19.

a Plan View Of Core

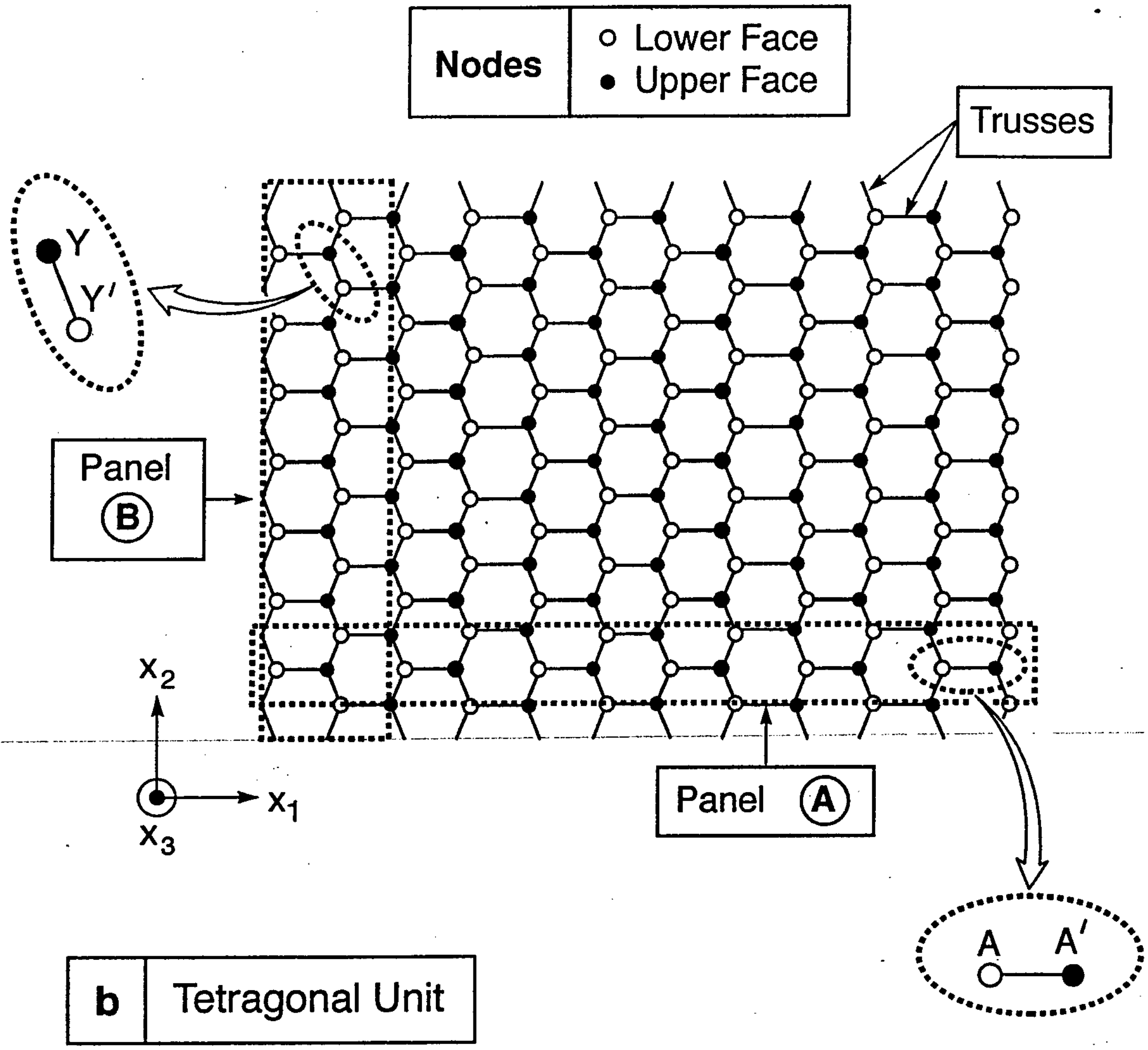

b Tetragonal Unit

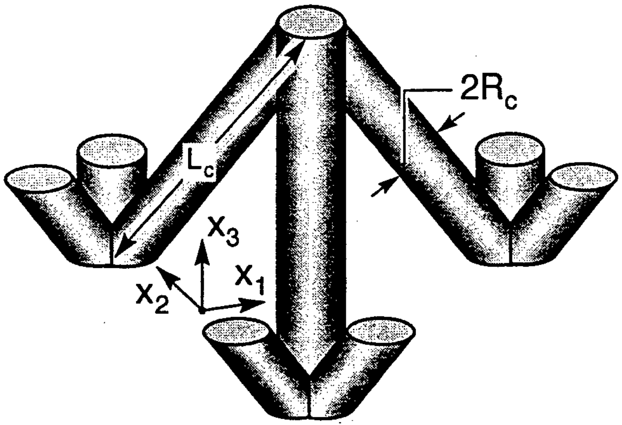

Figure 1

Truss.Chiras.Fig.#1

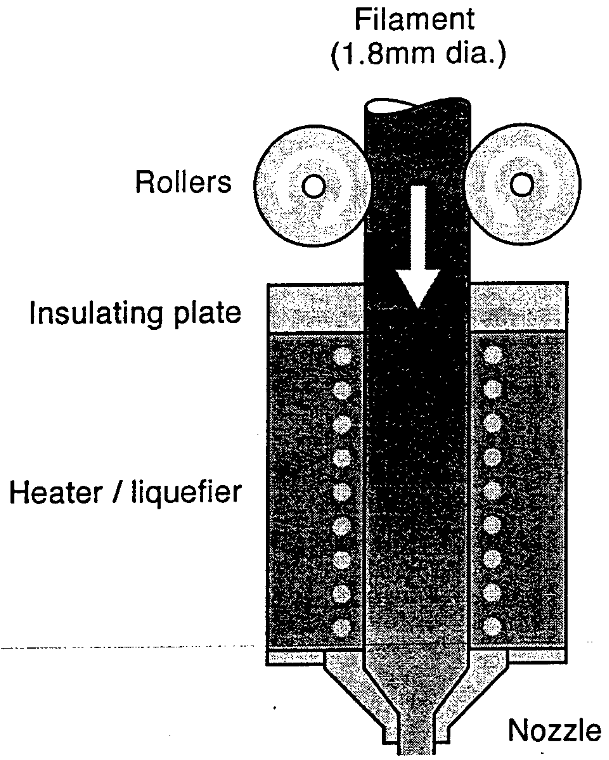

Figure 2

Truss.Chiras.Fig.#2

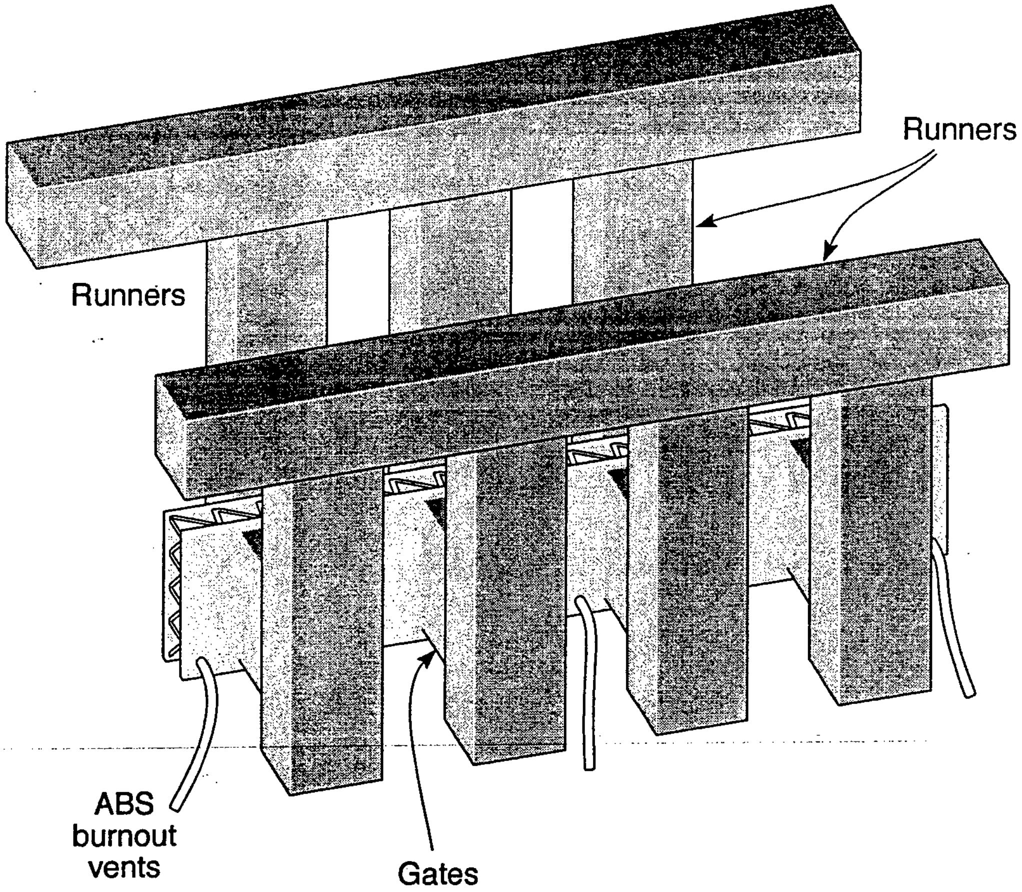

Figure 3

Truss.Chiras.Fig.#3

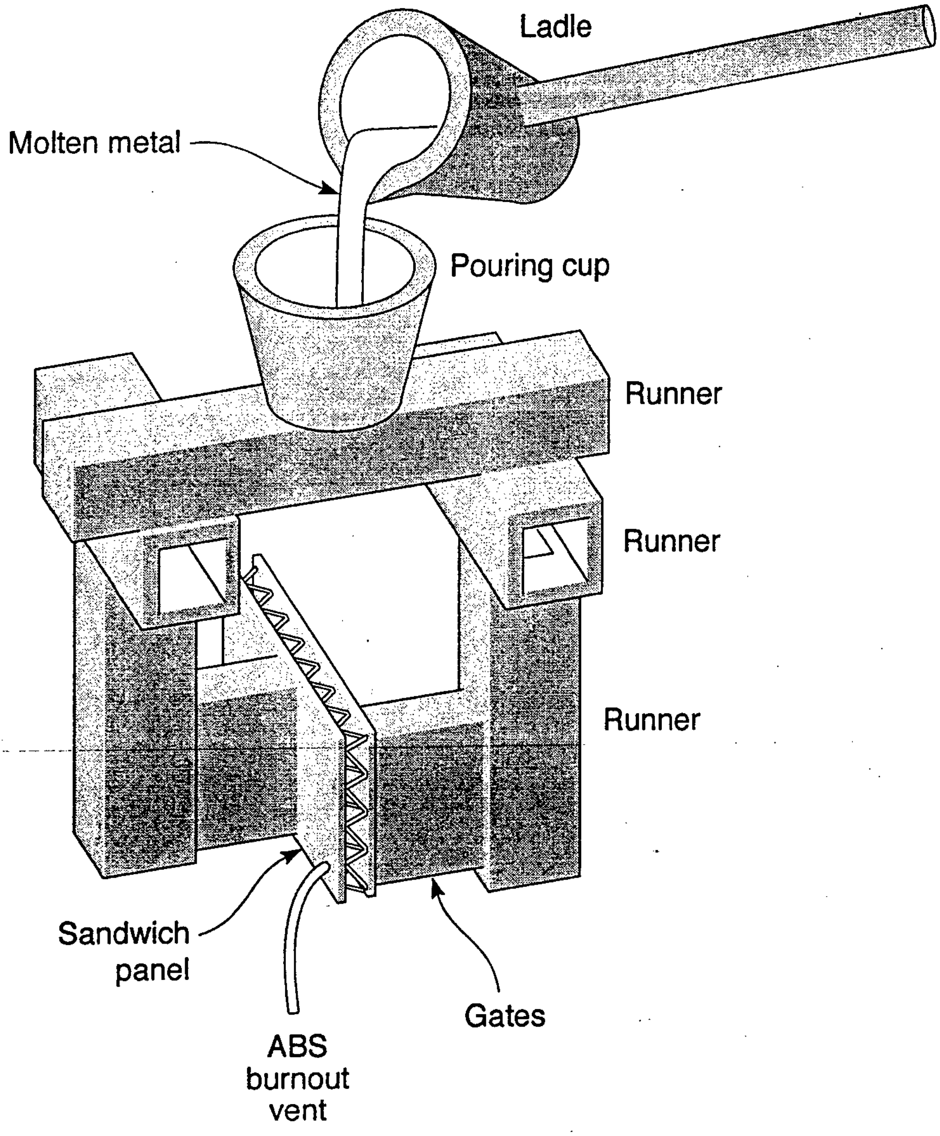

Figure 4

Truss.Chiras.Fig.#4

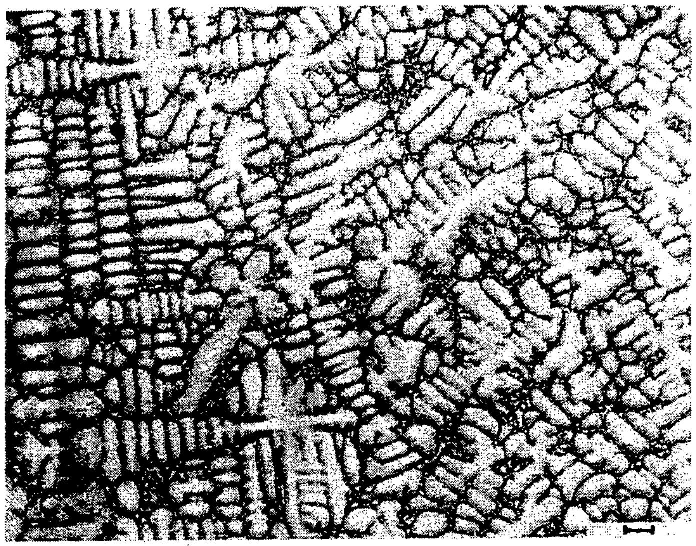

Figure 5

Truss.Chiras.Fig.#5

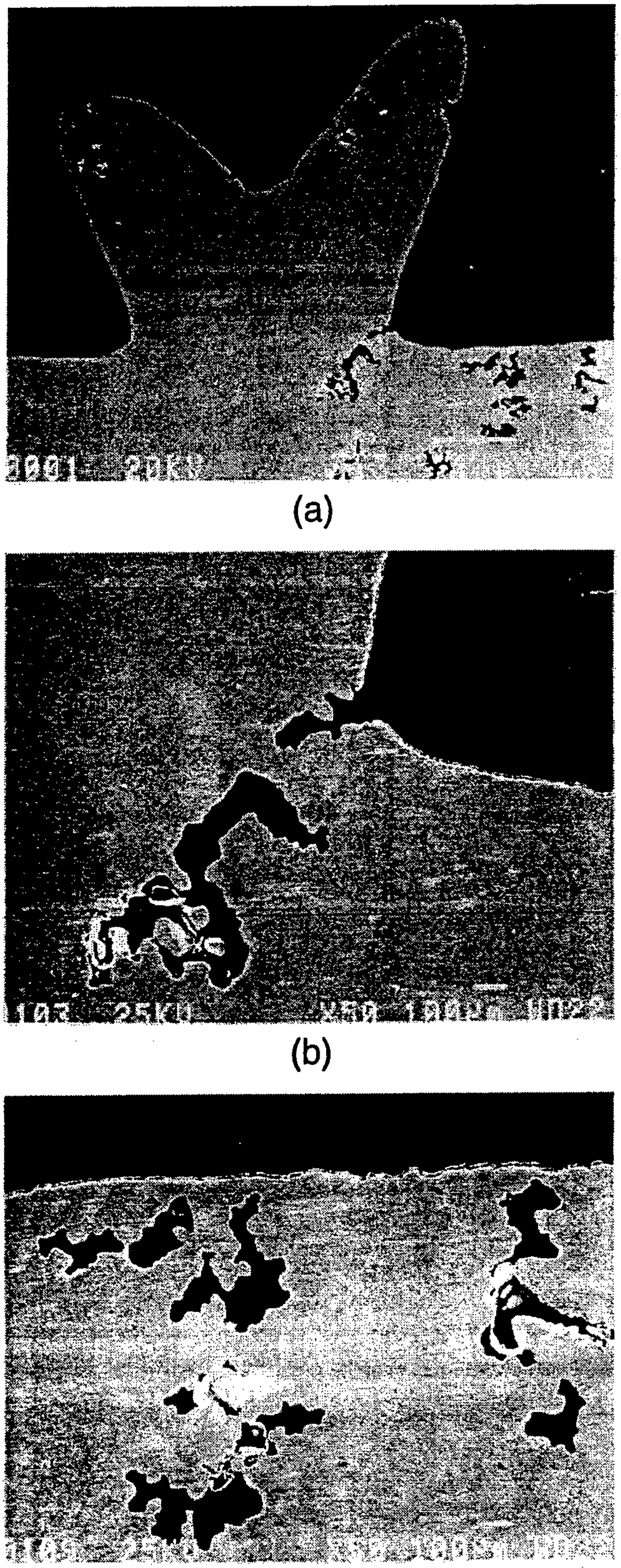

(a)

(b)

(c)

Figure 6

Truss.Chiras.Fig.#6

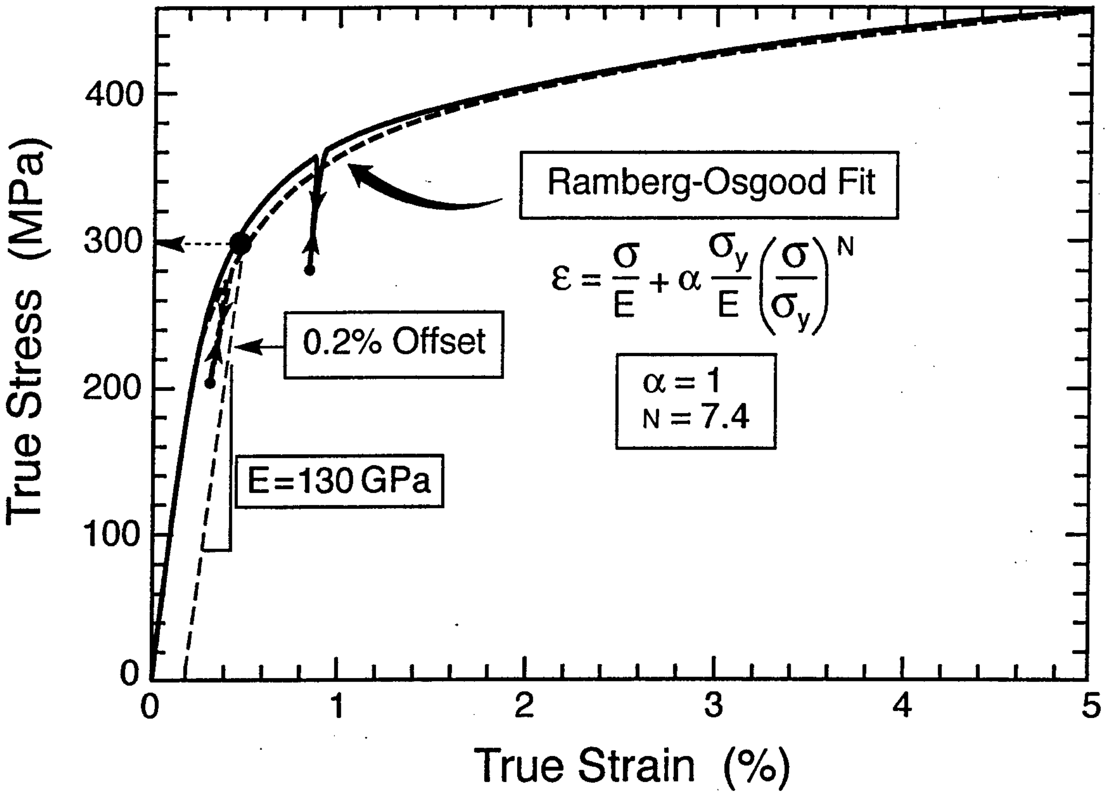

Figure 7

Chiras.Fig.#7

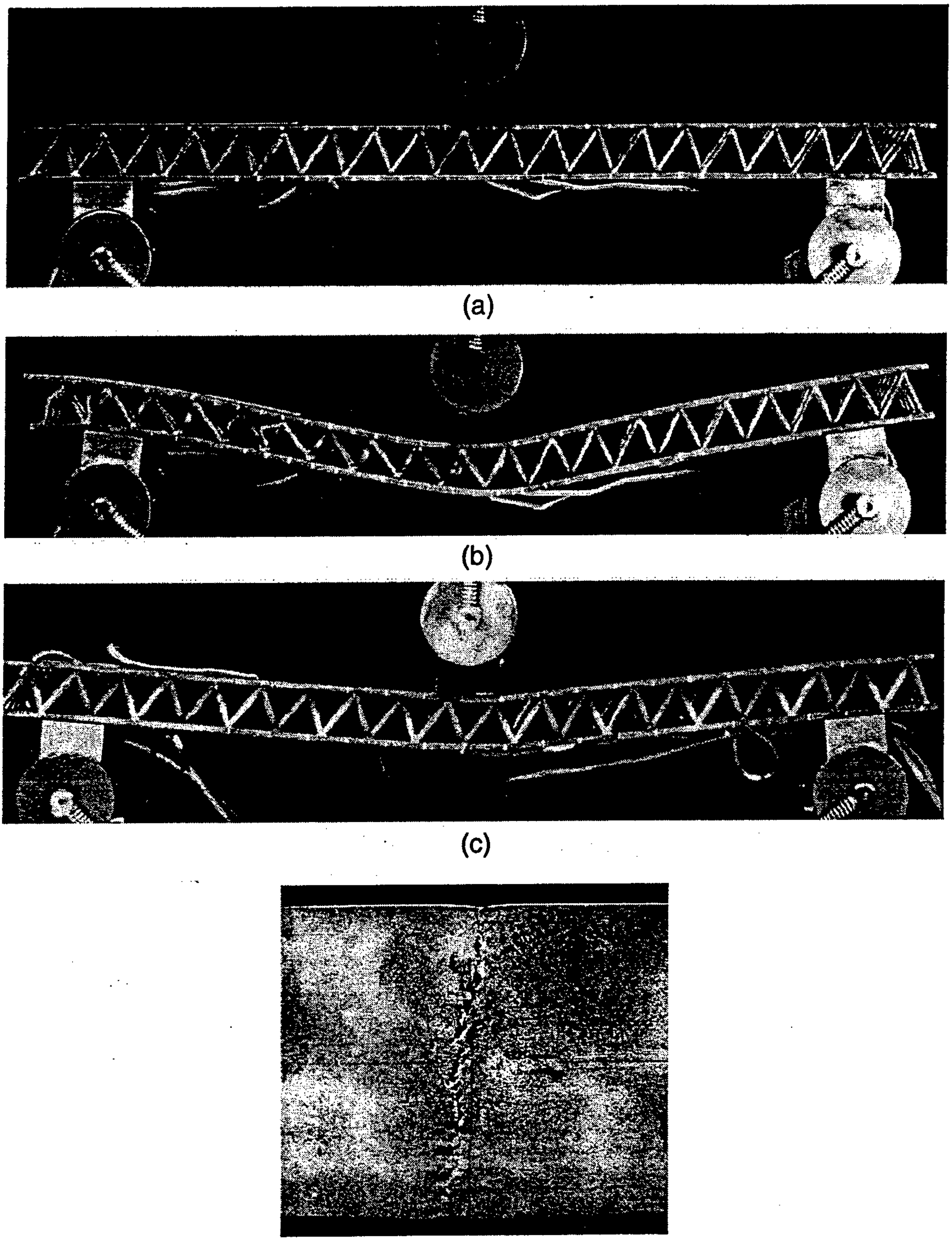

(a)

(b)

(c)

(d)

Figure 8

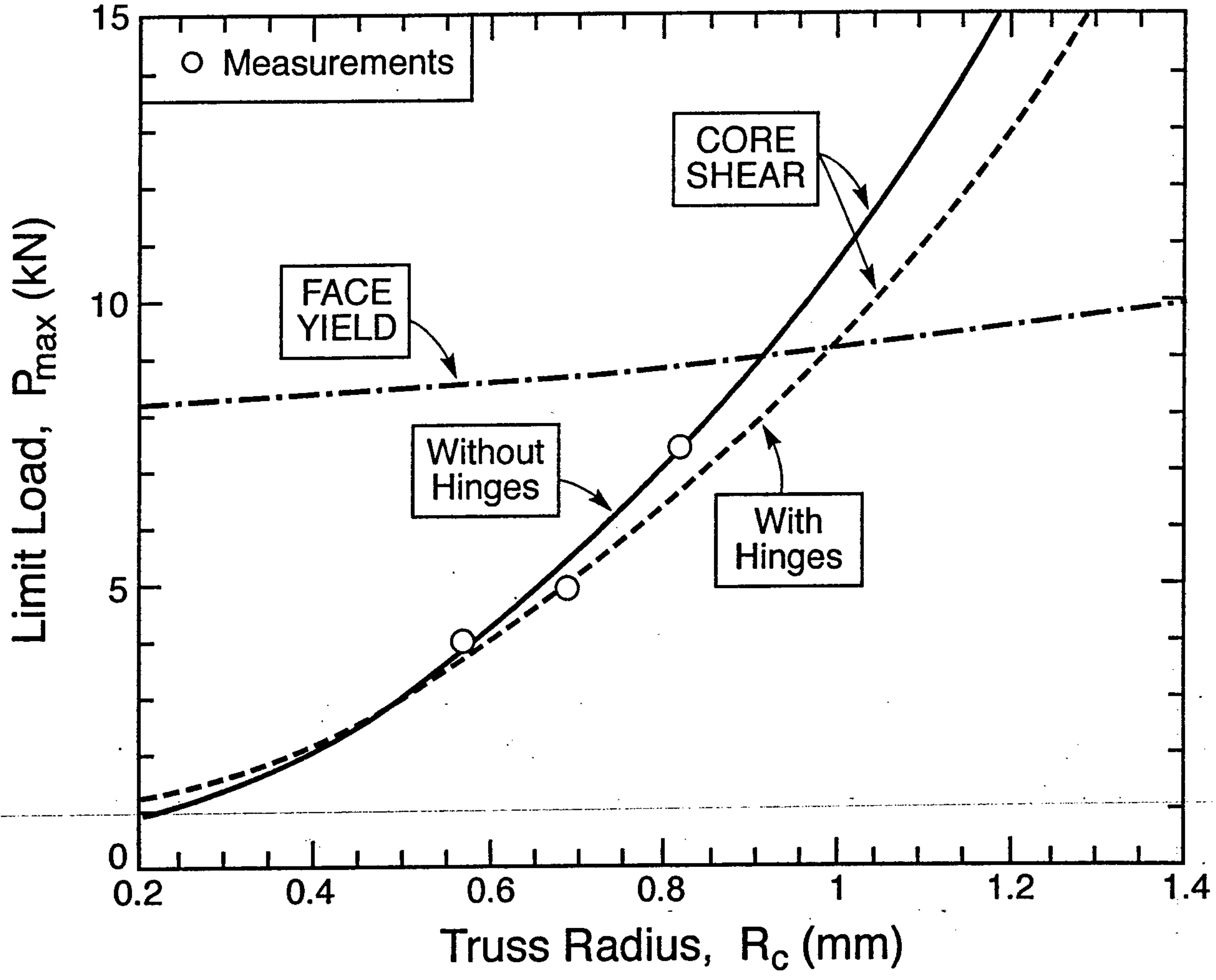

Figure 9

Chiras.Fig.#9

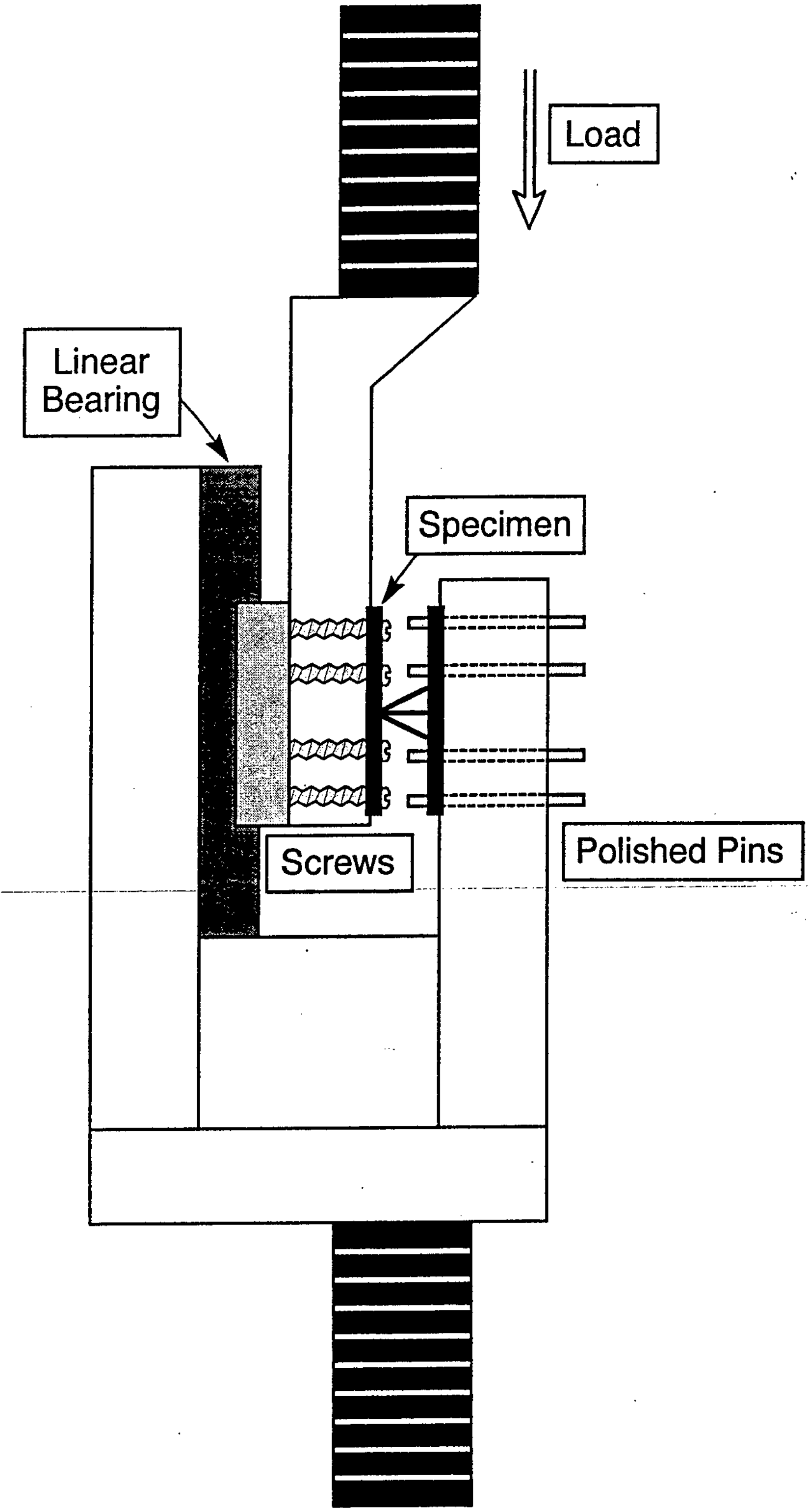

Figure 10

Chiras.Fig.#10

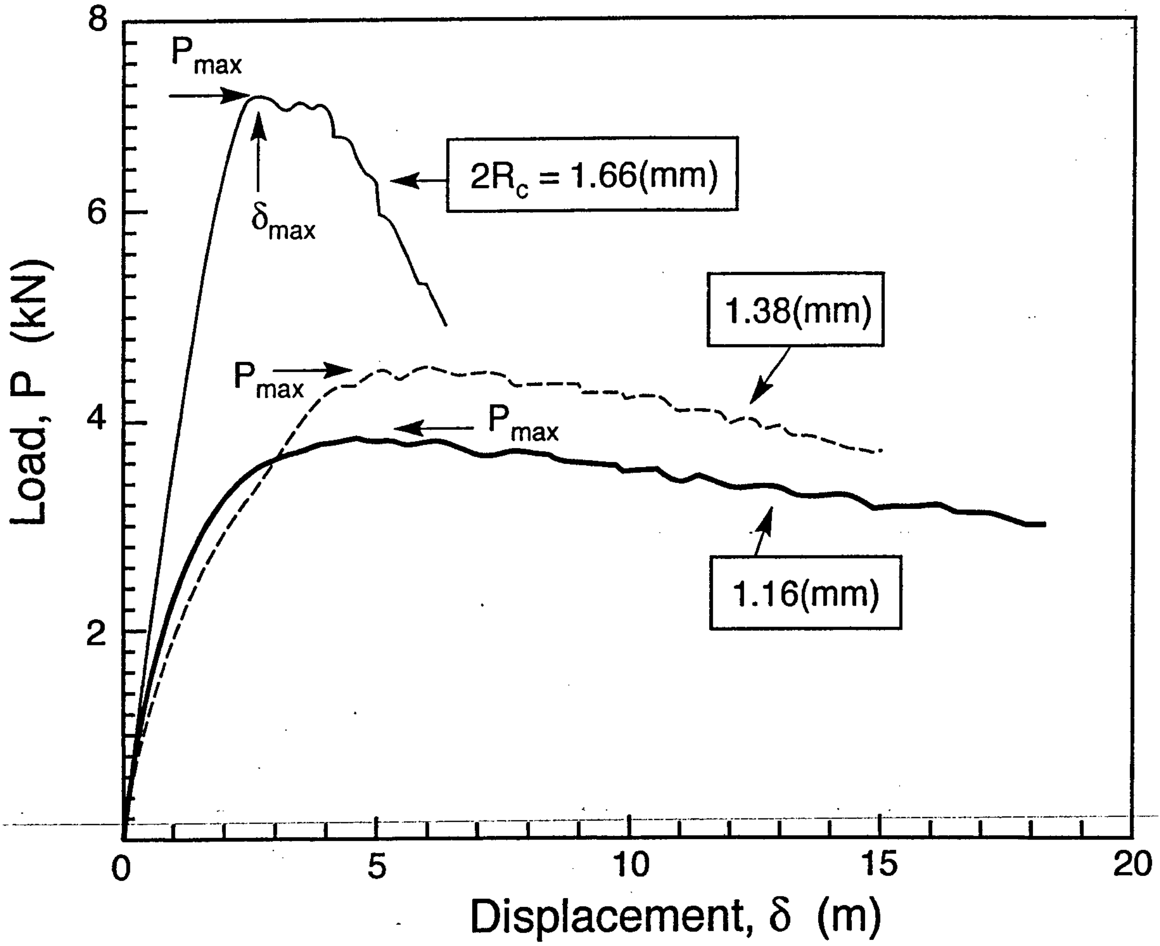

Figure 11a

Chiras.Fig.#11a

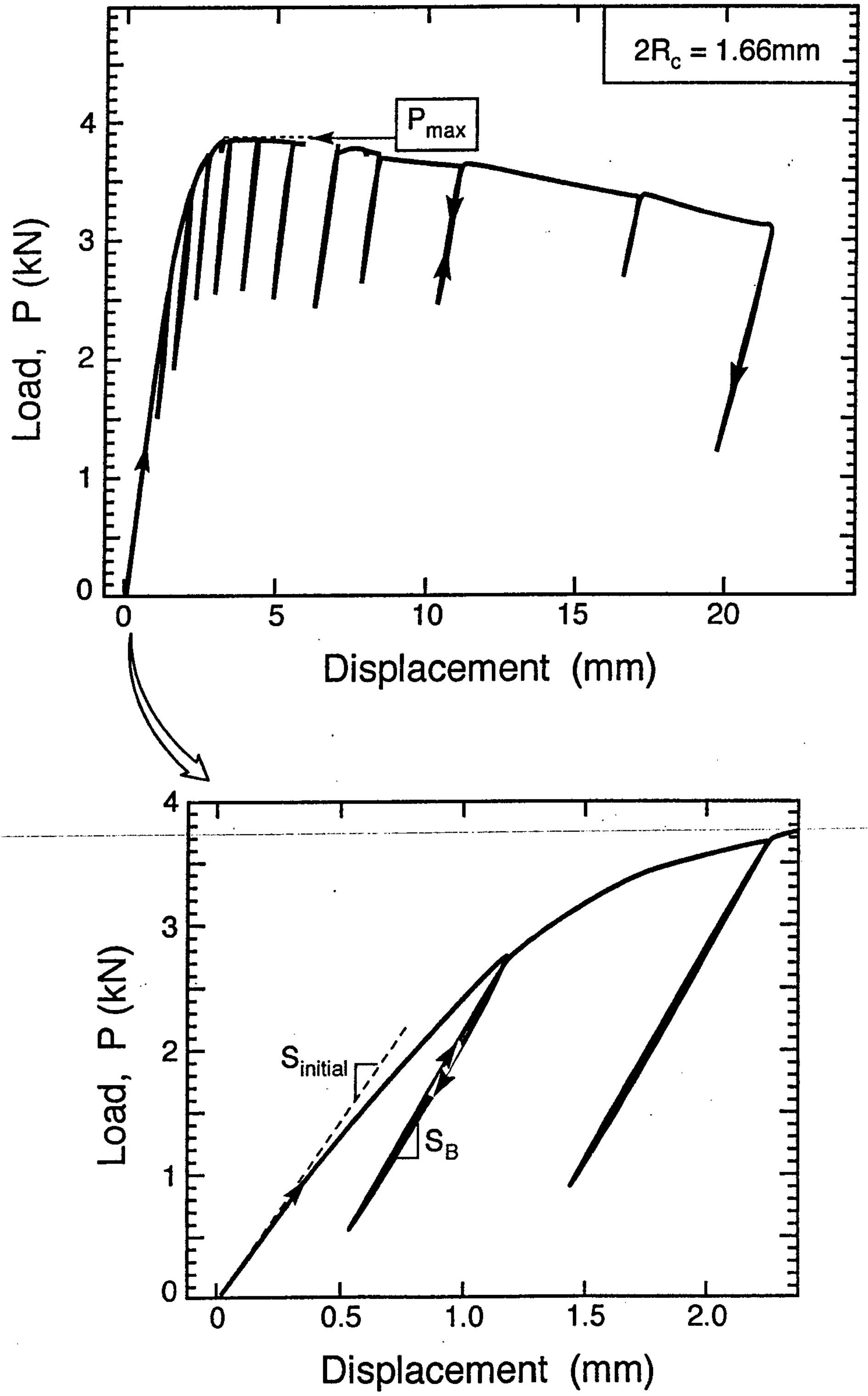

Figure 11b

Chiras.Fig.#11b

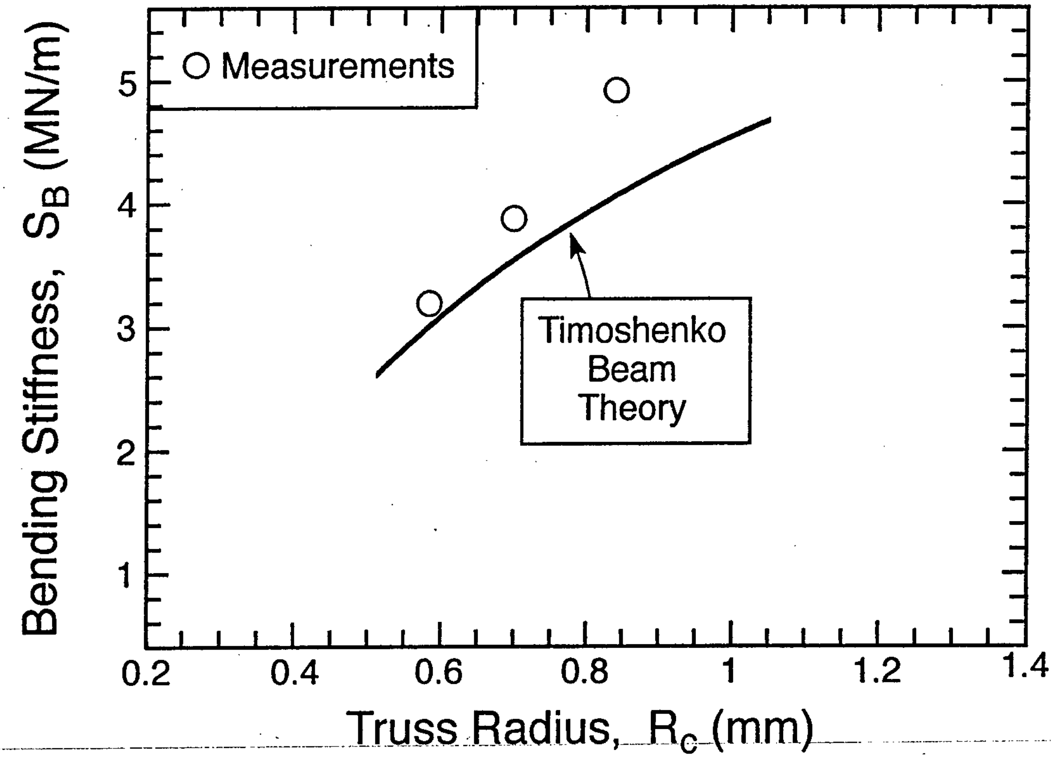

○ Measurements
Timoshenko Beam Theory
Bending Stiffness, S_B (MN/m)
1
2
3
4
5
0.2
0.4
0.6
0.8
1
1.2
1.4
Truss Radius, R_c (mm)

Figure 12

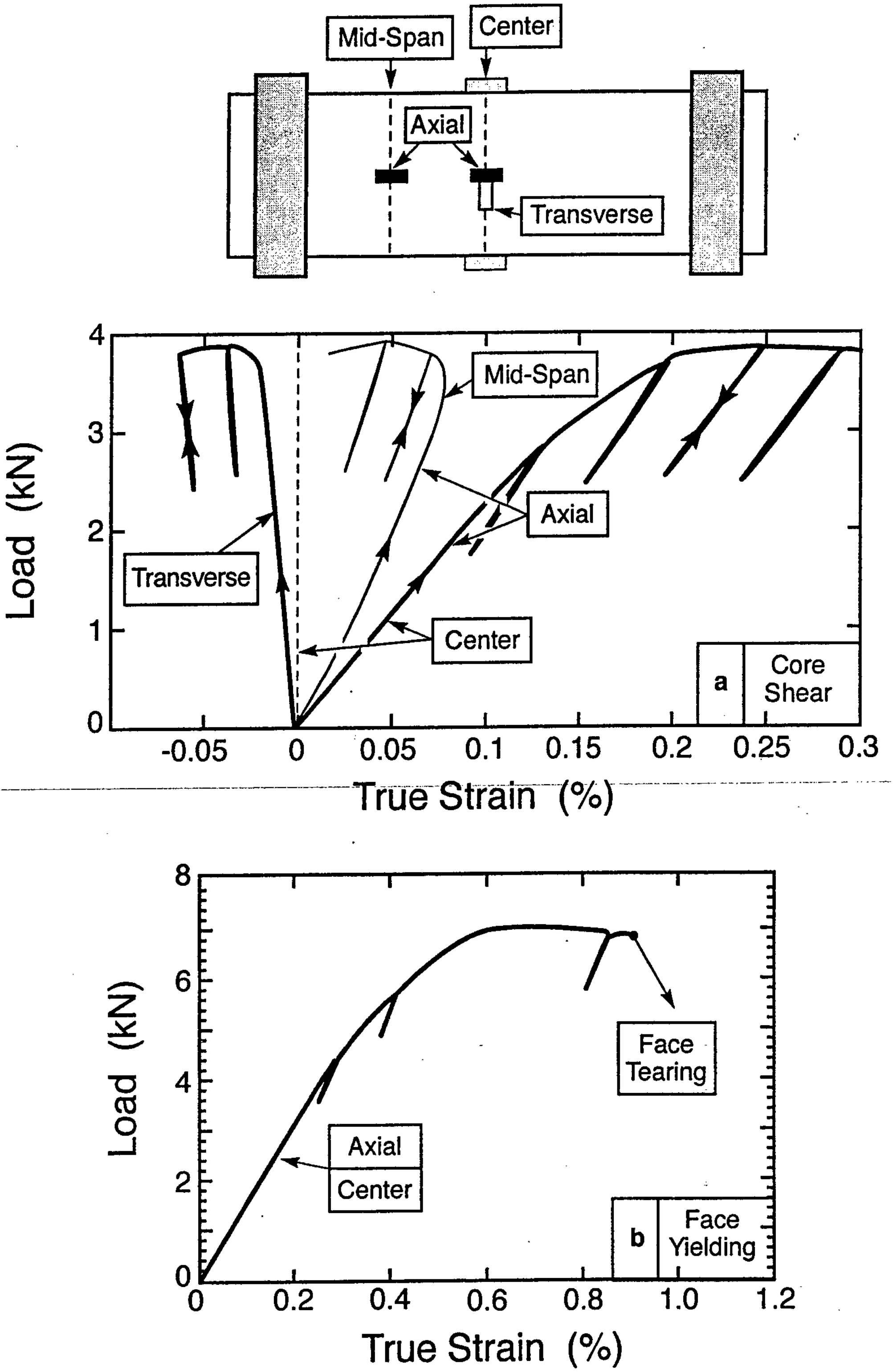

Figure 13

Chiras.Fig.#13

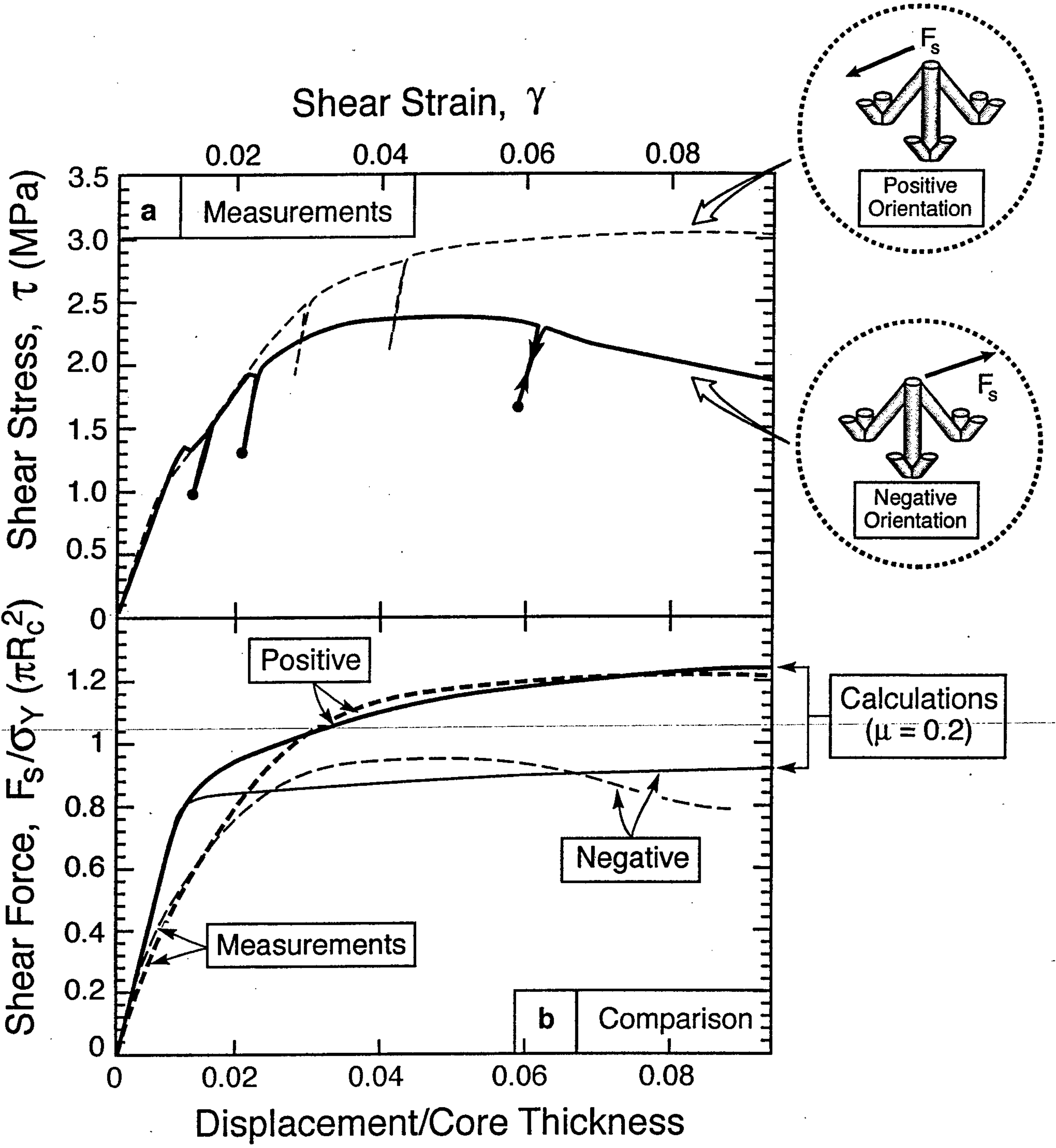

Figure 14

ChirasFig..#14

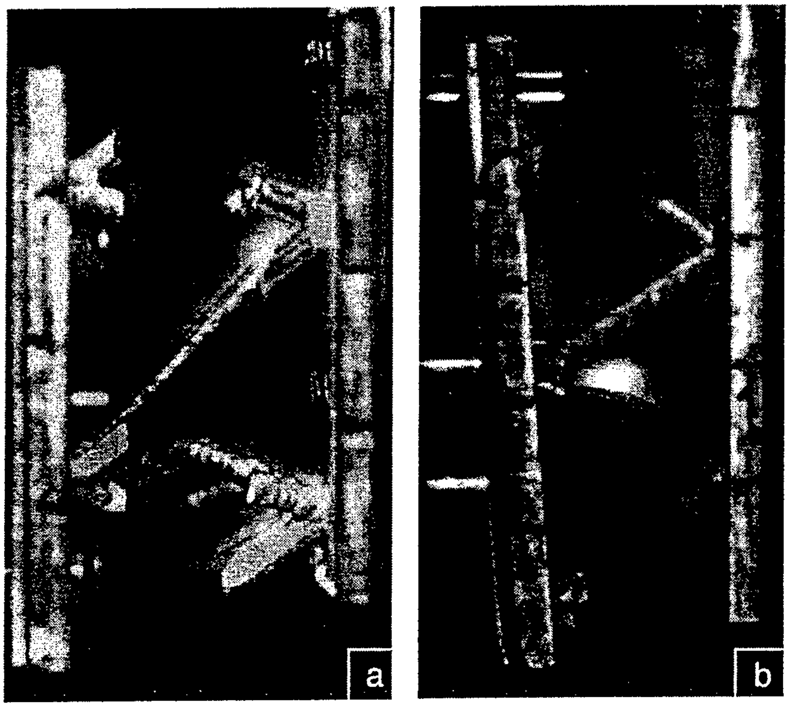

Figure 15

ChirasFig.#15

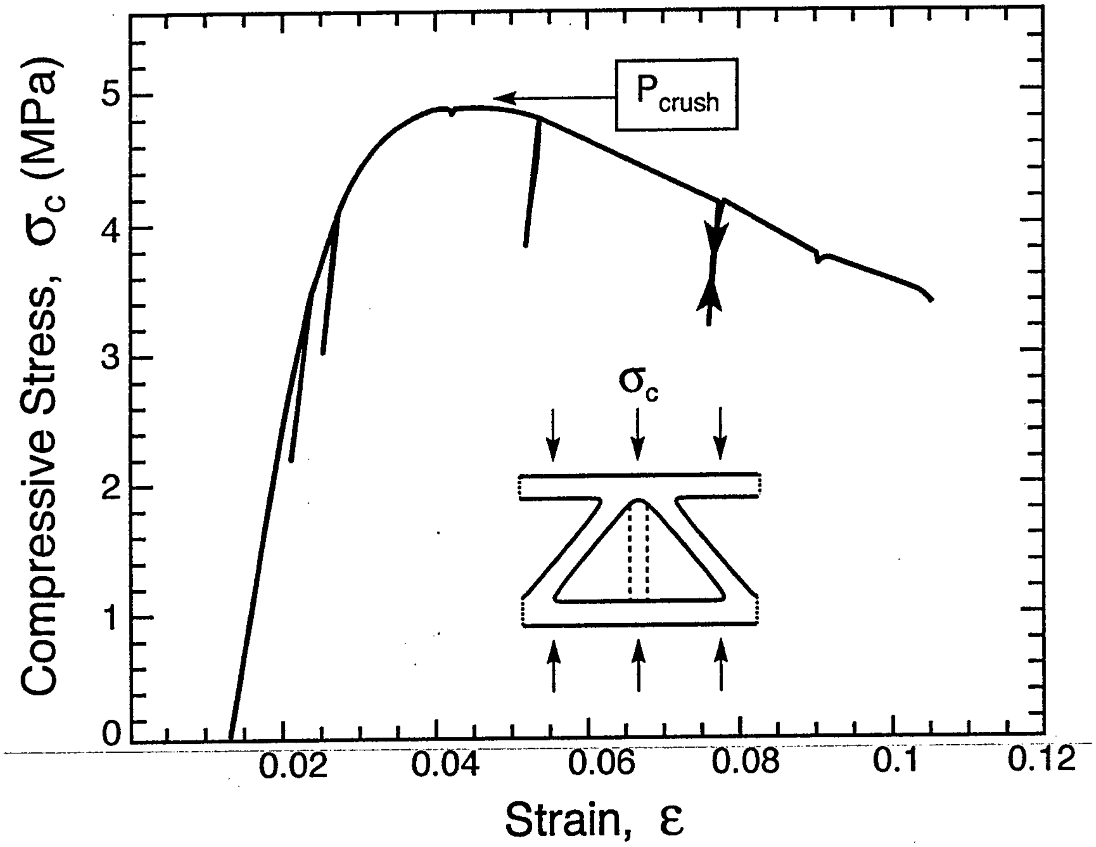

Figure 16

ChirasFig.#16.

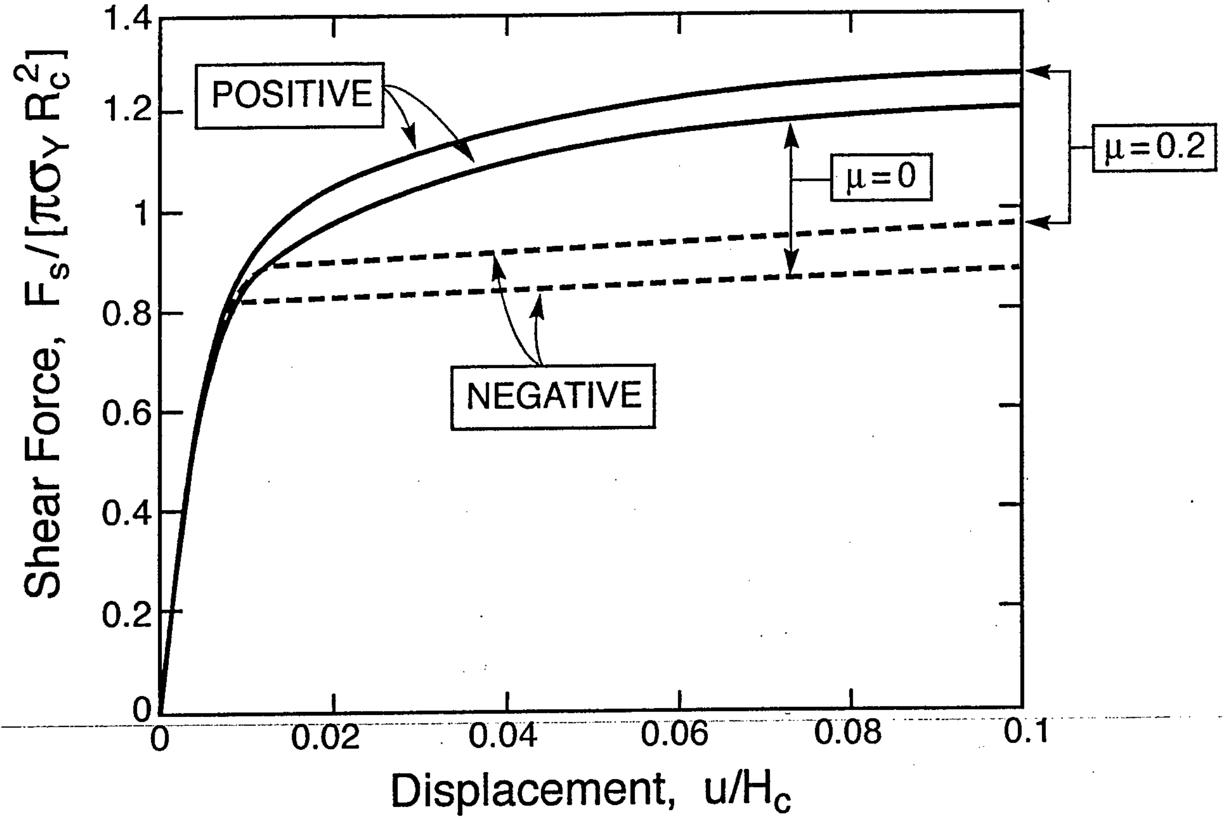

Figure 17

Chiras.Fig.#17.

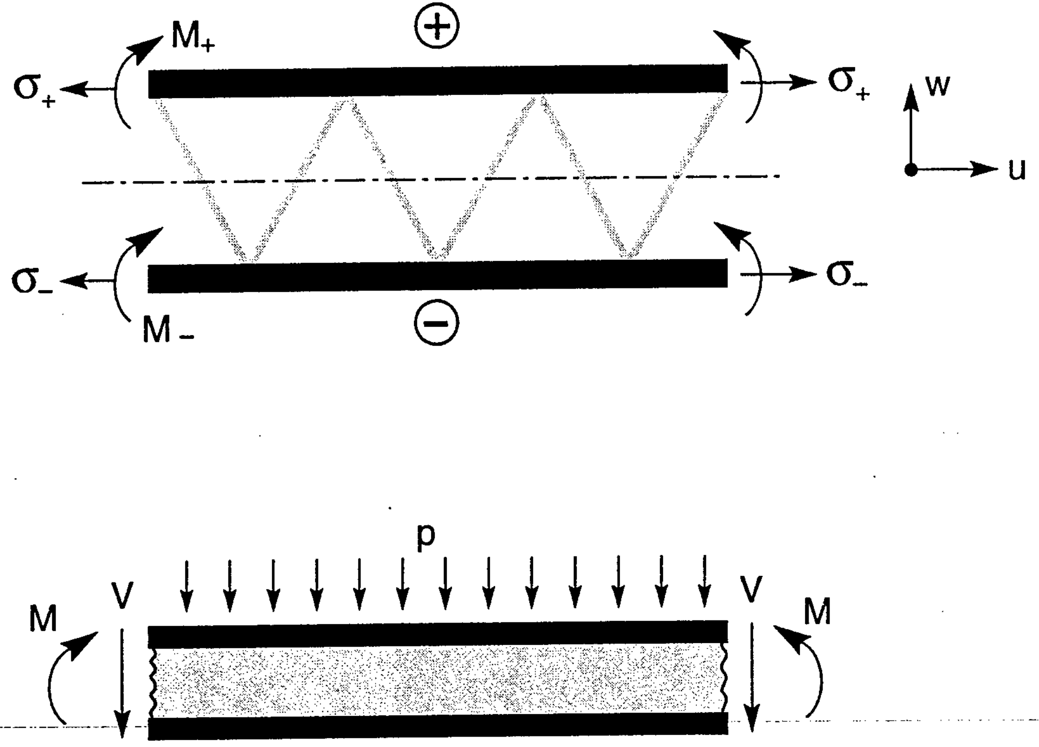

Figure 18

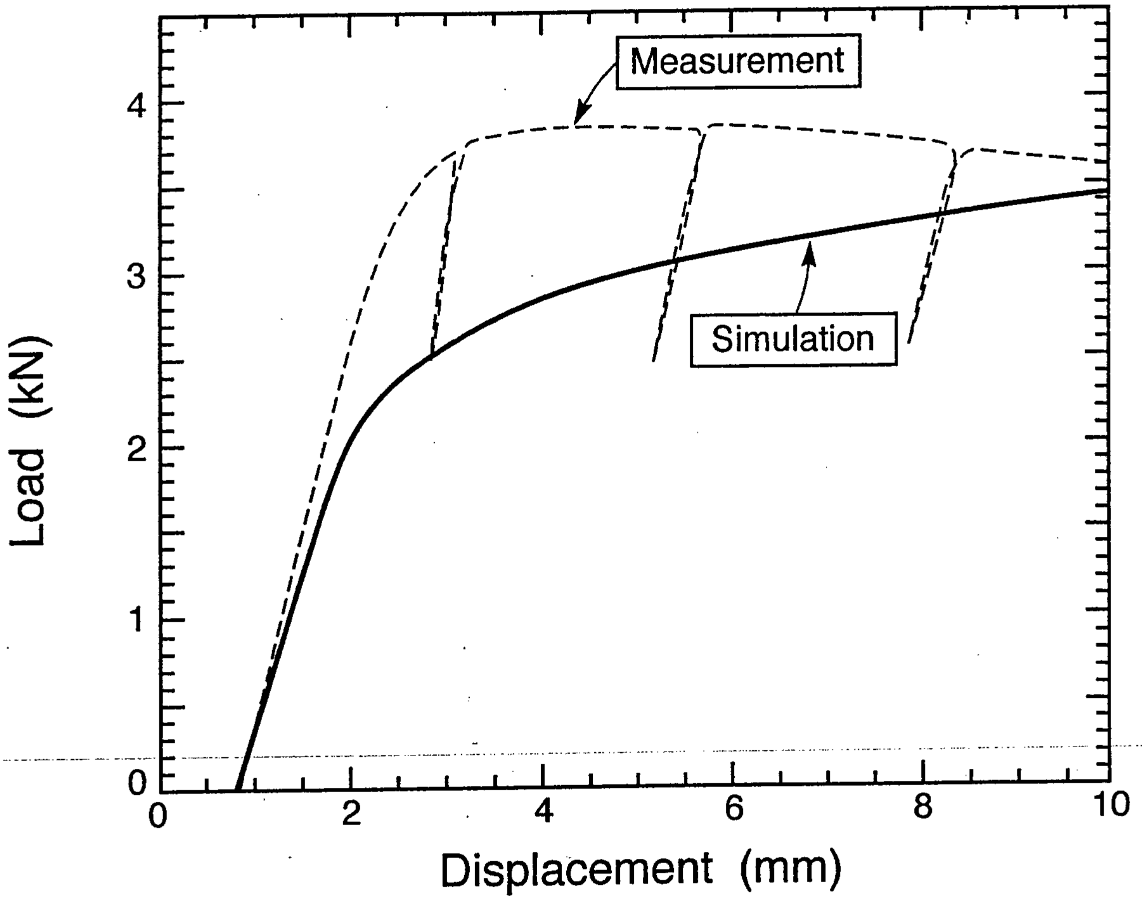

Figure 19

Chiras.Fig.#19

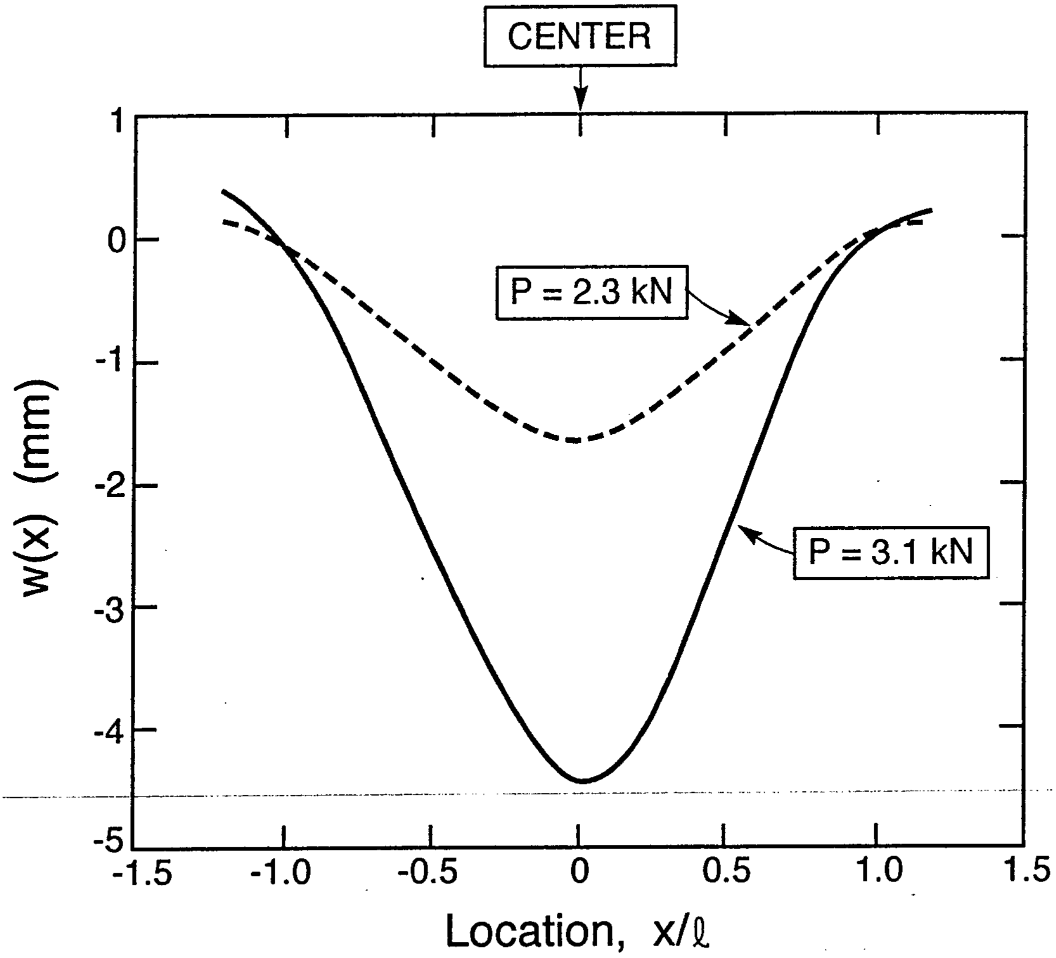

Figure 20

Chiras.Fig.#20

Truss Radius (mm)	Predicted Limit Load due to Core Shear (MPa)		Predicted Limit Load due to Face Yielding (MPa)	Measured Limit Load (MPa)	Calculated Shear Modulus (MPa)	Measured Shear Modulus (MPa)	
	With Hinges	Without Hinges				Positive	Negative
0.58	3280	3480	7110	3870	323	337	323
0.69	4790	5200	8970	4680			
0.83	6810	7630	9680	7260			

Table 1

Truss.Chiras.Table1